Controlled Assembly of 1-D and 2-D Nanomaterials: from Static to Dynamic Junctions

A thesis submitted in partial fulfilment of the requirements of the Degree of Doctor of Philosophy

Giuseppe Amoroso

School of Biological and Chemical Science,
Queen Mary University of London

Supervisor: Dr. Matteo Palma

September 2020

Statement of originality

I, Giuseppe Amoroso, confirm that the research included within this thesis is my own work or that where it has been carried out in collaboration with, or supported by others, that this is duly acknowledged below and my contribution indicated. Previously published material is also acknowledged below.

I attest that I have exercised reasonable care to ensure that the work is original, and does not to the best of my knowledge break any UK law, infringe any third party's copyright or other Intellectual Property Right, or contain any confidential material.

I accept that the College has the right to use plagiarism detection software to check the electronic version of the thesis.

I confirm that this thesis has not been previously submitted for the award of a degree by this or any other university.

The copyright of this thesis rests with the author and no quotation from it or information derived from it may be published without the prior written consent of the author.

Signature:

Date: 16/09/2020

Publications list

Giuseppe Amoroso, Andrei Sapelkin, Qingyu Ye, Vicente Araullo-Peters, Cecconello, Alessandro Fernández Gustavo, Matteo Palma "DNA-Driven Dynamic Assembly of MoS_2 Nanosheets" *Faraday Discussions* (**2020**), DOI: 10.1039/C9FD00118B

Giuseppe Amoroso, Qingyu Ye, Keitel Cervantes-Salguero, Gustavo Fernandez, Alessandro Cecconello, Matteo Palma "DNA-Powered Stimuli-Responsive Single-Walled Carbon Nanotube Junctions" *Chemistry of Materials* (**2019**), 31 (5), 1537–1542

Mark Freeley, Antonio Attanzio, Alessandro Cecconello, Giuseppe Amoroso, Pierrick Clement, Gustavo Fernandez, Felice Gesuele, Matteo Palma "Tuning the Coupling in Single-Molecule Heterostructures" *Advanced Science* (**2018**), 5, 1800596

Abstract

Nanotechnology refers to a field of research and innovation aimed at fabricating functional materials and devices at the supramolecular, molecular and atomic scale. Whether the nanostructured devices will constitute the basis for new technologies relies on the ability to precisely manipulate nanomaterials properties. In this context, controlling the assembly of individual nano-objects directly in solution paves the way for the development of solution-processable nano-devices.

This thesis presents a bottom-up approach to assemble single-walled carbon nanotubes in aqueous solution by means of the formation of either static or dynamic junctions. Furthermore, it will be demonstrated how this approach can be extended to exfoliated molybdenum disulphide.

Initially, pertinent works performed in the field to date will be introduced. Specifically, carbon nanotubes and molybdenum disulphide materials will be described focusing on their structure and properties, synthesis and functionalisation methods, as well as self-assembly ability. Subsequently, the chemical and characterisation techniques that underpin all the results presented in this work will be discussed.

The results presented in this study report the formation of static and dynamic junctions. First, it will be described how a DNA-wrapping strategy allows the dispersion of single-walled carbon nanotubes in aqueous solution and how this protects their side-walls leaving the nanotube tips available for further functionalisation. We will then discuss how the functionalisation of carbon nanotube ends with diverse molecular linkers leads to the formation of static linear junctions, and how the use of DNA as molecular linker may drive the formation of dynamic junctions under different stimuli. Moreover, it will be demonstrated how this DNA-driven approach can also lead the assembly of exfoliated molybdenum disulphide by the formation of static and dynamic junctions.

The strategies developed in this thesis are of interest for the fabrication of solution-processable and stimuli-responsive nano-systems. In particular, junctions between single-walled carbon nanotubes can be employed as sensing platforms with the nanotubes working as nano-electrodes in molecular transport junctions and single-molecule investigations. Furthermore, controlling the assembly of exfoliated molybdenum disulphide holds great potential in optoelectronic and biotechnology applications, and their assembly into laminar membranes can be of interest for energy conversion/storage.

Acknowledgements

First and foremost, I would like to thank my supervisor, Dr Matteo Palma, for believing in me and for giving me the opportunity to work on a research field that is of great technological interest. You have always been very supportive, emotionally and professionally. I grew up a lot since we met four years ago – you pushed me to become a *Researcher*. Thank you!

A great thanks goes also to my co-supervisor, Dr Gustavo Fernández, from University of Münster. I have appreciated your help and support during my doctorate course. I will definitely visit you in Münster.

A big THANK YOU is for Dr Alessandro Cecconello, my mentor and dear friend. You introduced me to the field of DNA nanotechnology and taught me much about scientific rigour. I will never forget our Friday nights of alcohol and science.

Next, I would like to thank "The Palma Group": Mark, Keitel, Xinzhao, Qingyu, Caoimhe, William G., Joey, Da, Jingyuan, Antonio, Pierrick, Marina, Nasir, Sandra, Zamaan and William. It was amazing working with you guys.

I also would like those people I had the privilege to meet during my time at QMUL: Chiara, Luca, Martina, Jacopo, Fosca, Nolwenn, Piera, John, Giorgio, Angelo, Rosemarie, Cecile, Yasel and Shaima. I look forward to having another beer with you.

A special thanks goes to my *Sassy Friend* Andrea, whose friendship is priceless!

A great thanks to my London friends who have helped me in their own special ways.
The *Limehouse Crew*: Roxy and Anna. I will never forget our nights out.
The *Eatalians*: Chiara, Elena, Elisa, Emanuela, Nicolino and Ornella. My second family.
My "*Housemates*": Rashed, Towsif, Suman, Arafat, Rebs, Sam and Avin.

I thanks my *Forever Friends:* Annalisa, Elisa, Francesco, Giorgia, Ivana and Stefania. Physically distant, but close with the heart. I miss you so badly!

An endless thanks to *my partner in crime*, Andrea. Your support has been incredible. If I made it, it is also your merit. Thank you!

Most importantly, I want to thank my Family. In particular, *Mamma e Papà*, I couldn't have asked for better parents than you. You have always encouraged me, even in all my crazy ideas. You gave me the freedom of choosing my own path. You have always been supportive. Even when no one believed in me. Even when I did not believe in myself. I will never be able to repay you for what you have done for me. I love you! My no-little-anymore *Brother*, I will always be by your side. I will fight for your future. You deserve whatever splendid and amazing this life has to give to you. You do not need a big brother anymore, but remember that you can always count on me.

Last but not least, I want to thank Tsukino Usagi. You were, you are and you will always be my role model. You taught me about Freedom, Friendships, Hope and Love. *Tsuki no Hikari wa Ai no Message!*

Table of Contents

Table of Figures

List of Figures in **CHAPTER 1**:

List of Figures in **CHAPTER 2:**

List of Figures in **CHAPTER 3**:

List of Figures in **CHAPTER 4**:

List of Tables

List of Abbreviations and Acronyms

SI: International System

0-D: Zero-dimensional

1-D: One-dimensional

2-D: Two-dimensional

3-D: Three-dimensional

CNT: Carbon Nanotube

SWCNT: Single-Walled Carbon Nanotube

MWCNT: Multi-Walled Carbon Nanotube

CVD: - Chemical Vapour Deposition

DOS: Density of States

VB: Valence Band

CB: Conduction Band

BSA: Bovine Serum Albumin

PEG: Polyethylene Glycol

PmPV: Poly(m-phenylenevinylene-co-2,5-dioctyloxy-p-phenylenevinylene)

DNA: Deoxyribonucleic Acid

ssDNA: single strand DNA

A: Adenine

T: Thymine

C: Cytosine

G: Guanine

dsDNA: double strand DNA

SEC-HPLC: Size-Exclusion High-Performance Liquid Chromatography

IEX: Ion Exchange Chromatography

ATP: Aqueous Two-Phase

***h*-BN:** Hexagonal Boron Nitride

***g*-C_3N_4:** Graphitic Carbon Nitride

BP: Black Phosphorus

LDHs: Layered Double Hydroxides

TMOs: Transition Metal Oxides

TMDs: Transition Metal Dichalcogenides

MoS_2: Molybdenum Disulphide

VBM: Valence Band Maximum

CBM: Valence Band Minimum

PAA: Polyacrylic Acid

PAM: Polyacrylamide

IDT: Integrated DNA Technologies

HiPco: High Pressure Carbon Monoxide

MES: 2-(N-morpholino) ethanesulfonic acid

EDC: 1-ethyl-3-[3-dimethylaminopropyl] carbodiimide hydrochloride

Sulfo-NHS: N-hydroxysulfosuccinimide sodium salt

DPBS: Dulbecco's phosphate buffered saline

CuAAC: Copper-catalysed Reaction

MOPS: 3-(N-Morpholino)propanesulfonic acid, 4-Morpholinepropanesulfonic acid

TAE: tris(hydroxymethyl)aminomethane-acetate-ethylenediaminetetraacetic acid

PCR: Polymerase Chain Reaction

TCEP: Tris[2-carboxyethyl] phosphine

AFM: Atomic Force Microscopy

SPM: Scanning Probe Microscopy

TEM: Transmission Electron Microscopy

UV-Vis: Ultraviolet-Visible

NIR: Near-Infrared

PL: Photoluminescence

DI water: De-ionised water

SD: Standard Deviation

OD: Optical Density

G4: G-quadruplex

Q: Quencher

Cy3: Cyanine 3

MW: Molecular Weight

A reminder to myself:
Never give up!
You are stronger than you think

CHAPTER 1: Introduction

The word “nano” derives from the Latin word “nanus” and the Ancient Greek word “νᾶνος”, which meant "little old man" or "dwarf". The International System (SI) of units considers nano a unit prefix indicating "one billionth", i.e. a billionth of a metre, a billionth of a litre and a billionth of a kilogram. When used as a prefix for something other than a unit of measure, nano refers to nanotechnology.

Technology scaling is the primary driving factor for industrial development, following the predictions of Moore’s law.[1] In this context, the concept of nanotechnology is of fundamental importance for the next generation devices.[2] Nanotechnology is the manipulation of matter on an atomic, molecular, and supramolecular scale and has received enormous attention over the last 50 years due to the scientific and technological progress. Its idea was first proposed in the talk “There is plenty of room at the bottom” given by the Nobel Laureate Richard Feynman at the American Physical Society meeting in 1959. However, the term was defined by Norio Taniguchi in 1974 as follows: “Nano-technology mainly consists of the processing of separation, consolidation and deformation of materials by one atom or by one molecule”.[3]

More generally , the term nanotechnology refers to the particular field of technology and applied science aimed at controlling material properties at the nanoscale, normally from 1 to 100 nanometres, where properties differ significantly from those at a larger scale. The manipulation of matter within this size range is linked to the concept of nanomaterial, described as the "material with any external dimension in the nanoscale or having internal structure or surface structure in the nanoscale" by the International Organization for Standardization. Nanosized materials possess unique optical, electronic and mechanical properties[4–10] due to the higher surface area over volume ratio and quantum effects at the nanoscale. These emergent properties have the potential for great impacts in several applications, such as electronics,[11] sensing[12] and medicine.[13]

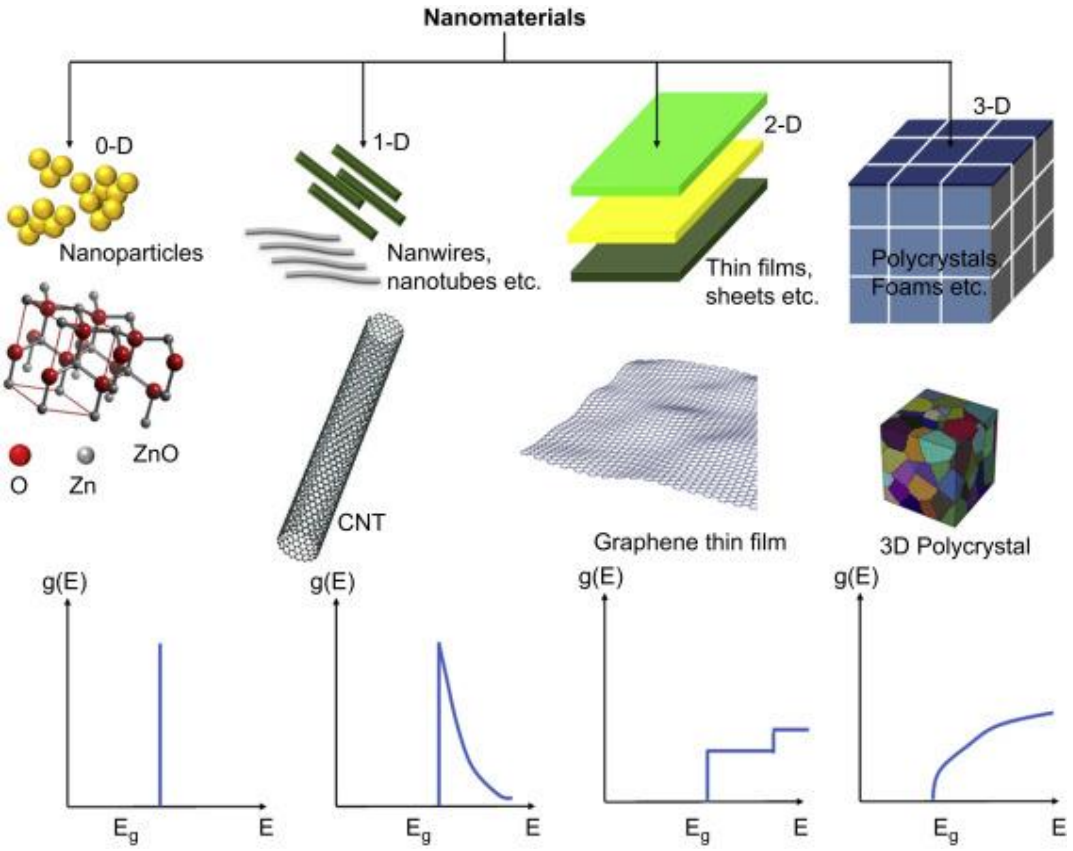

Figure 1 - 1 *Schematic representation of zero-dimensional (0-D), one-dimensional (1-D), two-dimensional (2-D), and three-dimensional (3-D) nanomaterials with associated density of electron states. Taken from reference 14.*[14]

Depending on the number of dimensions not confined to the nanoscale range, nanomaterials can be classified as shown in Figure 1 – 1.[14]

- Zero-dimensional (0-D): wherein all the dimensions are within the nanoscale. 0-D nanomaterials include nanoparticles, fullerenes and clusters.
- One-dimensional (1-D): one dimension is not confined to the nanoscale, such as in nanotubes, nanorods and nanowires.
- Two-dimensional (2-D): two of the dimensions are outside the nanoscale. These materials exhibit plate-like shapes, like nanofilms and nanosheets.
- Three-dimensional (3-D): all the dimensions confined to the macroscale (> 100 nm). Bulk materials are 3-D nanomaterials that are composed of individual blocks which may exist in nanoscale. This class contains bulk powders, dispersions of nanoparticles, bundles of nanotubes and multi-nanosheets.

The bulk physical properties can be described as a collective contribution of a very large number of atoms in the material. This theory falls apart when the size of the material is reduced to the nanoscale and the materials starts to exhibit new properties.[15] These properties are highly dependent on the electrons and holes (charge carries) movement along the dimensions. This dimensionality denotes the number of degrees of freedom in the particle momentum. Indeed, in 0-D systems (quantum dots), the charge carries are confined to all the three directions wherein the electrons show a spectrum of discrete energy. In 1-D systems, quantum wires can be obtained when charge carries are free to travel in one direction and confined in the other two directions. The charge carries are confined in one direction and are free to move in two directions in a 2-D system (quantum well). Finally, in a 3-D system, there is no confinement and the electrons are free to move in all the directions.

The main approaches for the synthesis and the fabrication of devices at the nanoscale are top-down and bottom-up, or a combination of both. The top-down approach[16] involves slicing or successive cutting bulk material to form the nanoscale structure. Differently, the bottom-up approach[17,18] refers to the building up of a material from the bottom: particles self-assemble to form larger structures. The latter, when compared to the top-down method, is less time-consuming and costly, as it allows to work in parallel, but it also produces nanostructures with less defects, more homogenous chemical composition, and better short- and long-range ordering.

1.1 CARBON NANOTUBES

1.1.1 Structure, Synthesis and Properties

Carbon (from Latin: carbo "coal") belongs to the group 14 of the periodic table. It is a non-metallic element with the symbol C, atomic number six and four electrons in the outer electron layer. Carbon atoms possess exceptional properties, due to their electron structure and smaller size compared with other elements of group IV, and have the ability to hybridise in sp, sp^2 and sp^3 configurations. This electronic configuration allows atoms of carbon to stabilise in different atomic structures with diverse molecular configurations called allotropes.[19] Additional allotropic forms have been added, such as fullerenes, carbon nanotubes (CNTs) and graphene,[20] to the two well-known carbon allotropes, diamond and graphite (Figure 1 – 2) .

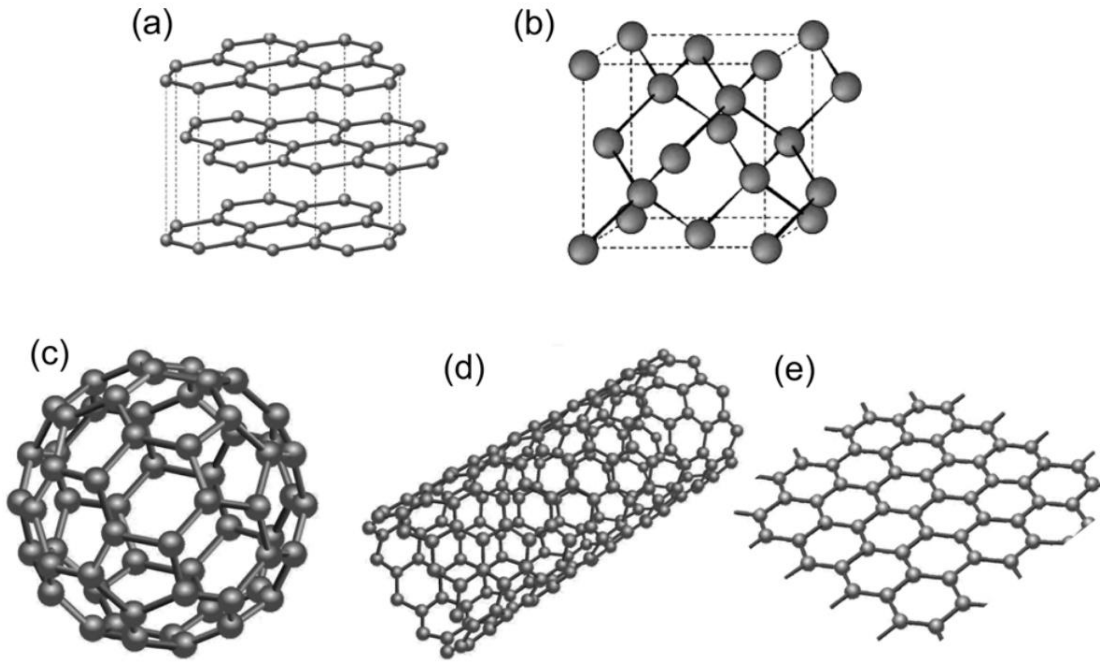

Figure 1 - 2 *Carbon allotropes including (a) 3-D graphite, (b) 3-D diamond, (c) 0-D buckminsterfullerene (d) 1-D CNT, and (e) 2-D graphene. Taken from reference 20.*[20]

Among the carbon allotropes, the study of carbon nanotubes is evolving at rapid pace. They are cylindrical one-dimensional structures, where the carbon atoms are arranged in a hexagonal pattern, like in a graphene sheet, while the closed ends of the nanotubes resemble half a buckyball. Their structure can be conceptualised by rolling up a single sheet of sp^2 bonded carbon atoms (single-walled carbon nanotube, SWCNT)[21,22] or several sheets (multi-walled carbon nanotube, MWCNT)[23] into a seamless tube (Figure 1 – 3). Generally, SWCNTs are around 1-3 nm in diameter with lengths varying from tens of nanometres to few micrometres, while MWCNTs have a diameter of 5-40 nm and a length around 10 µm.

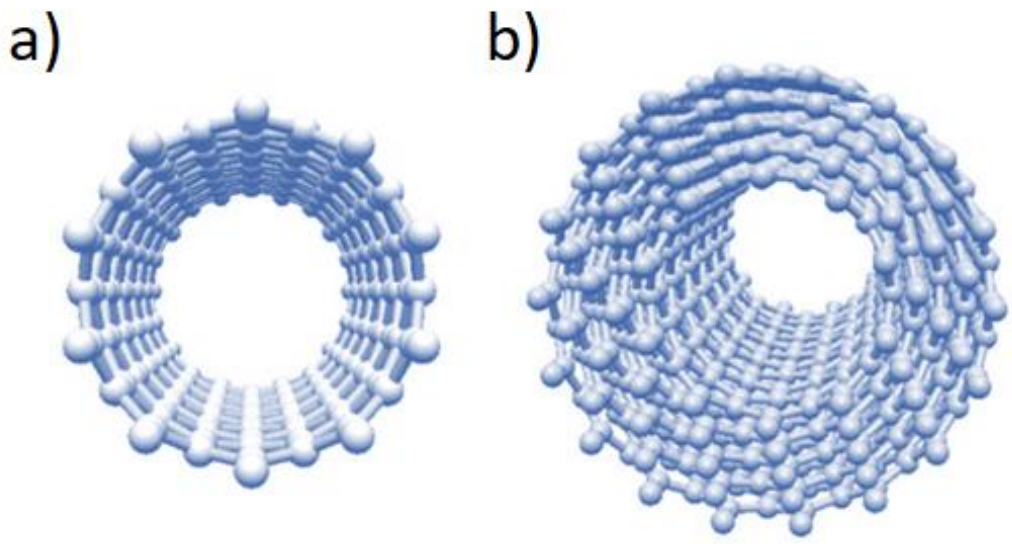

Figure 1 - 3 *Schematic illustration showing (a) SWCNT and (b) MWCNT.*

The common methods for the production of carbon nanotubes are[24]

- Arch discharge:[25] it is the easiest way for making CNTs, but it originates a mixture of components. The method consists in applying a direct-current arc voltage between two graphite electrodes, which are immersed in an inert gas. The discharge consumes one of the carbon electrodes, creating a deposit on the opposing electrode. While using a pure graphite anode results in the synthesis of fullerenes and MWCNTs, a graphite anode containing Fe or Co catalysts generates pure SWCNTs.
- Laser ablation:[26] in this method, laser pulses vaporise a graphite rod in a high-temperature furnace, filled with an inert gas. The rod is a composite of graphite and metal catalyst particles (Co and Ni mixture). This method produces a mat of ropes and each rope contains a bundle of SWCNTs.
- Chemical vapour deposition (CVD):[27,28] it is the most common method due to the continuous mass production and low cost. The CVD methods involve the decomposition of carbon atom-containing gas (such as acetylene, ethylene, ethanol or methane) with the presence of catalytic nanoparticles. Then, carbon nanotubes can grow at the sites of the metal catalyst.

Since their discovery in 1991 by Sumio Iijima,[23] carbon nanotubes have attracted researchers for their notable properties.[4,29–38] The density of carbon nanotubes is about one quarter that of steel, but their mechanical properties make them one of the strongest and stiffest known materials in terms of tensile strength and elastic modulus. This strength is due to the strong covalent sp^2 bonds formed between carbon atoms, resulting in a tensile strength of up to 63 GPa for MWCNTs. Despite they have a tensile strength over 100 times that of the steel and a Young's modulus value estimated on the order of TPa, carbon nanotubes are rather soft because of their elasticity in the radial direction. The high flexibility and strong in-plane coupling against non-axial strains are related to the thermal properties of CNTs. All carbon nanotubes are good thermal conductors along the tube, with a thermal conductivity about 3,500 $W \cdot m^{-1} \cdot K^{-1}$ at room temperature for SWCNTs, but good insulators lateral to the tube axis, with thermal conductivity about 1.52 $W \cdot m^{-1} \cdot K^{-1}$ at room temperature for SWCNTs. They also possess good temperature stability, which is estimated to be up to 2,800 °C in vacuum and about 750 °C in air. Nevertheless, carbon nanotubes are of great interest especially for their electrical properties. Indeed, depending on their atomic structure, they can possess either semiconducting or metallic character.[4]

The atomic structure of SWCNTs can be defined by a chiral angle, θ, and a roll-up vector, C_h.[39] Both are obtained by the combination of structural parameters indicating how the tube is twisted, as shown in the equations below:

$$\boldsymbol{C_h = na_1 + ma_2} \text{ and } \boldsymbol{\theta = tan^{-1}\left[\frac{\sqrt{3}\,m}{2n+m}\right]}$$

where a_1 and a_2 are the unit vectors in the graphene space, while the integers *m* and *n* are called chiral indices and describe how the graphene sheet is rolled up. The diameter (*d*) of the CNTs is also related to (*n*,*m*) indices as follows.

$$\boldsymbol{d = \frac{a_{cc}}{\pi}\sqrt{(n^2 + nm + m^2)}}$$

Where a_{cc} is the carbon atoms bond length.

Carbon nanotubes can be classified in three types based on the chiral indices (*n*,*m*) that define their geometry:[20,40] zigzag, armchair and chiral (Figure 1 – 4). If either *n* or *m* is equal to zero, the nanotube is zigzag type; when *n* = *m* the tube orientation is known as armchair; in all the other cases when *n* ≠ *m* the resultant carbon nanotubes are chiral.

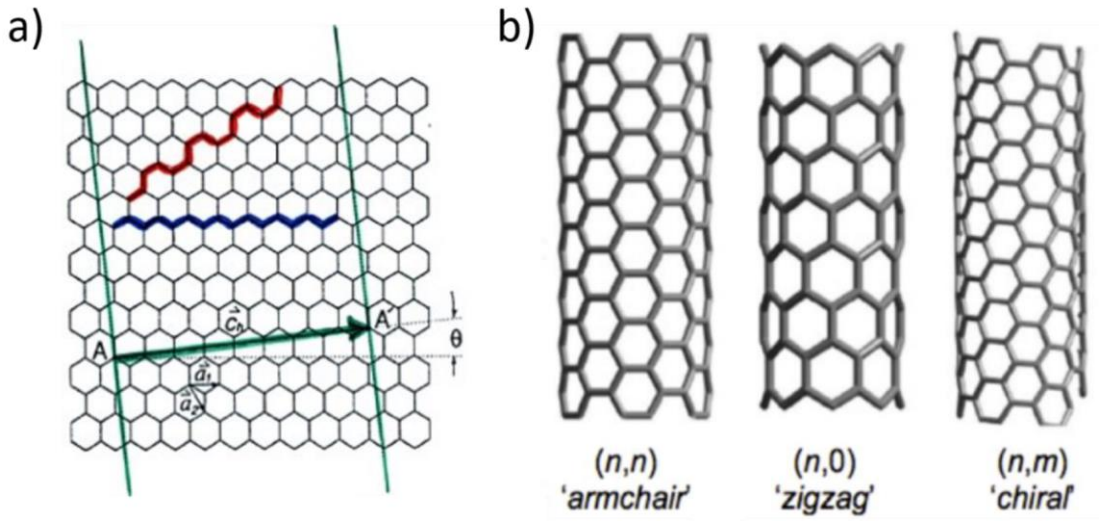

Figure 1 - 4 *(a) Graphene honeycomb network and (b) structure of SWCNTs exhibiting different configurations: armchair, zigzag and (c) chiral. Taken (adapted) from reference 20.*[20]

The (*n*,*m*) indices also define whether SWCNTs possess semiconducting or metallic behaviour. Armchair nanotubes are metallic; carbon nanotubes for which $n - m = 3i$ and *i* an integer are metallic; while all other combinations are semiconducting.

Although this “rule” identifies the electrical nature of CNTs, exceptions must be made as the nanotube diameter strongly influence their band gaps. A theoretical graph based on CNT band structure calculations was designed in 1999 by Hiromichi Kataura.[41] The Kataura plot relates nanotube diameter and bandgap energies: carbon nanotubes of certain diameter range can be metallic or semiconducting as shown in Figure 1 – 5.[42]

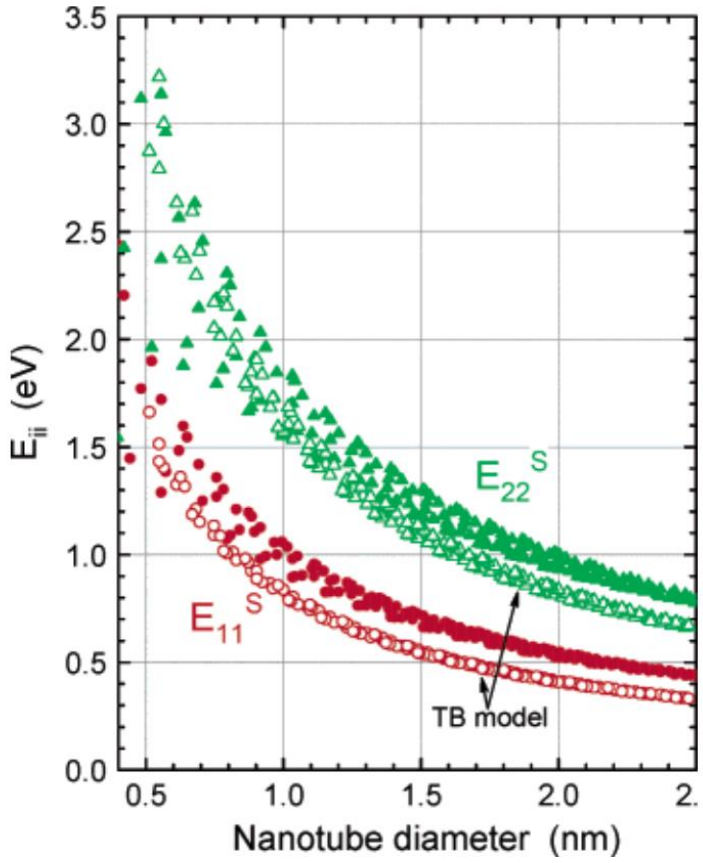

Figure 1 - 5 *Comparison between model-based and empirical values of optical transition energies vs diameter for semiconducting SWCNT. Taken from reference 42.*[42]

The band gap is inversely proportional to the diameter of the nanotube as shown in the following equation:

$$E_g = \frac{2\gamma_0 a_{cc}}{d} = \frac{0.84}{d(nm)}\ eV$$

where γ_0 is the carbon-carbon tight-binding overlap energy. Generally, a semiconducting SWCNT has a band gap of about 0.5-0.65 eV; as consequence, chiral and zig-zag carbon nanotubes with small diameters that should be metallic have a finite gap.

The optical properties of CNTs are determined by their electronic structure. A bulk material has continuous density of states (DOS), but a one-dimensional crystal has van Hove singularities. As the energies between van Hove singularities depend on CNT structure, their optoelectronic properties can be tuned by varying this structure.[43] In van Hove singularities, DOS descends gradually and then increases in a discontinuous spike; optical transitions occur between van Hove singularities. In this regard, UV-Vis-NIR absorption spectroscopy is a powerful tool for the characterisation of SWCNTs.[44] For semiconducting SWCNTs, the electrons present in the valence band (VB) can jump up into the corresponding energy levels of the conduction band (CB) when excited. Semiconducting transitions are indicated as S_{11} for transitions from VB_1 to CB_1, as S_{22} for transitions from VB_2 to CB_2, etc. In the case of metallic SWCNTs, the spacing between the van Hove singularities is larger and only transitions from VB_1 to CB_1, termed M_{11}, can be probed in the UV-Vis region (see Figure 1 – 6).

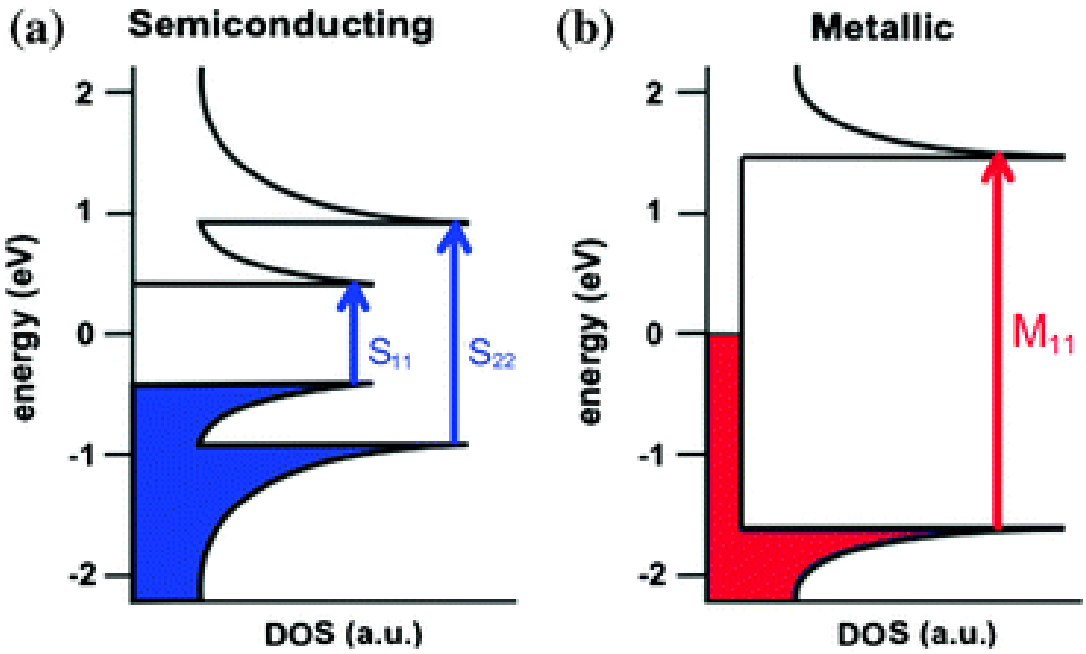

Figure 1 - 6 *Plot of the electronic density of states for (a) semiconducting and (b) metallic SWCNTs and the possible transitions between the van Hove singularities. Taken (adapted) from reference 43.*[43]

While the transitions of metallic SWCNTs are probed in the UV-Vis region, semiconducting SWCNTs are observed in the Vis-NIR region, as shown in the absorbance spectrum in Figure 1 – 7. The peaks in the spectrum arise from specific SWCNT chiralities; as shown for (7,5)-SWCNT,[45] in the case of semiconducting SWCNTs, one specific chirality has one peak in the S_{11}-regime and another one in the S_{22}-regime.

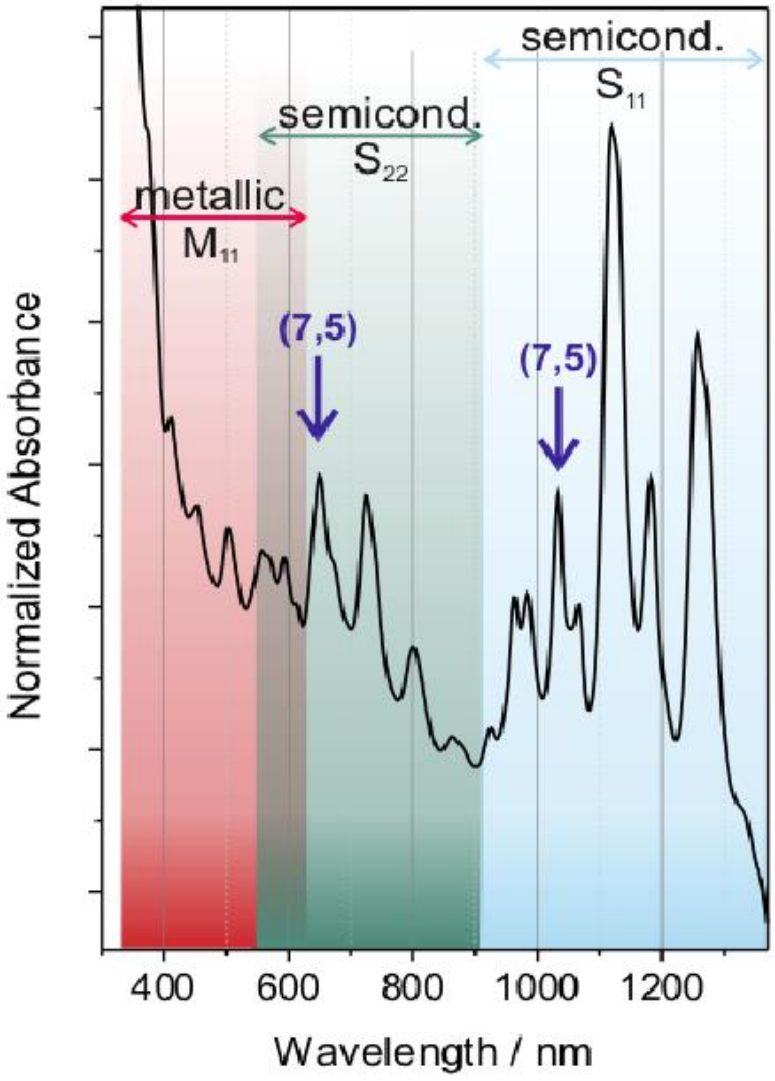

Figure 1 - 7 *Typical absorbance spectrum of a mixture of single-walled carbon nanotubes with different chiralities. The M_{11}, S_{11} and S_{22} transitions of metallic and semiconducting SWCNTs are highlighted in red, blue and green, respectively. The purple arrows in the figure indicate that the (7,5)-SWCNT yields one peak in the S_{11}-regime and another one in the S_{22}-regime. Taken (adapted) from reference 45.*[45]

1.1.2 Chemical Functionalisation

Thanks to their unique properties, carbon nanotubes can be employed for many nanotechnological applications, such as scanning probes,[46] hydrogen storage[47] and sensor/biosensors.[12] In order to employ CNTs in a diverse range of applications,[11,38,48–58] it is essential to disperse and purify them. Unfortunately, their poor dispersibility in both aqueous and non-aqueous solution makes hard their manipulation. They can be dispersed in some solvents by sonication, but precipitation occurs once the process is ended. However, carbon nanotubes can react with various compounds through chemical functionalisation.[59] The chemical functionalisation of carbon nanotubes helps their dispersion in solvents, by converting them into more manageable materials. The main approaches for CNT modification can be grouped into two categories: covalent and non-covalent functionalisations.

1.1.2.1 Covalent Functionalisation

The covalent functionalisation of carbon nanotubes[34] can disrupt their π-conjugated networks and thus modify their mechanical and electronic properties. Although it is important to covalent functionalise CNTs for specific applications, it is also essential that their electronic structure is not diminished.[60] An example of covalent functionalisation is the oxidative cutting of SWCNTs *via* acid treatment.[61–63] As a result, the open-ends and the sidewall of the carbon nanotubes are covered with oxygen-containing groups (Figure 1 – 8), which can be exploited for further functionalisation.

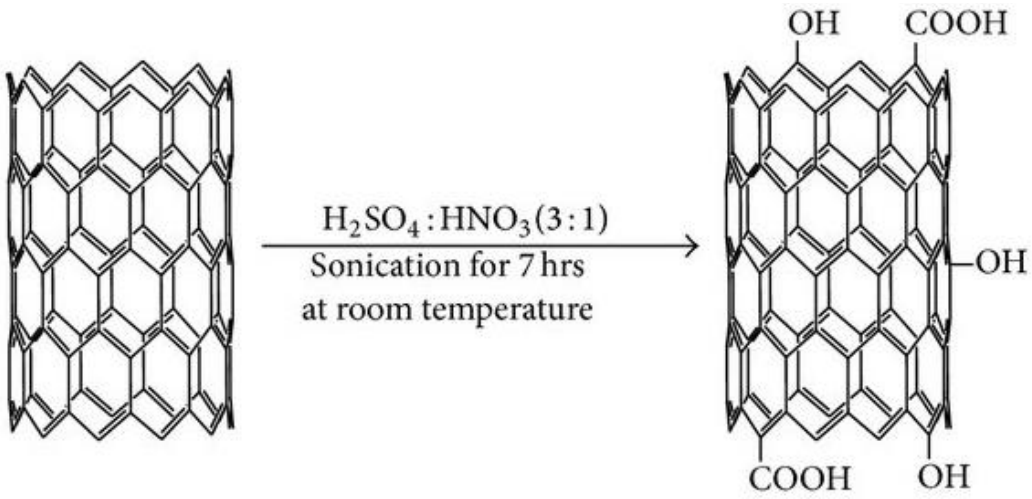

Figure 1 - 8 *Oxidative cutting of the CNTs by H_2SO_4 : HNO_3. Taken from reference 63.*[63]

After oxidation of pristine carbon nanotubes, it is possible to further functionalise the tubes *via* amidation or esterification of the carboxylic groups. The amidation strategy has been used to assemble SWNTs and to link SWCNTs other moieties, such as fullerenes.[64] In the same way, esterification reactions have been used to link carbon nanotubes to porphyrins[65] and alkyl pyrrole derivatives.[66]

In 1998, Chen *et al.*[67] treated carboxylated CNTs with long chain alkylamines *via* acylation and made carbon nanotubes dispersible in organic solvents for the first time (see Figure 1 – 9).

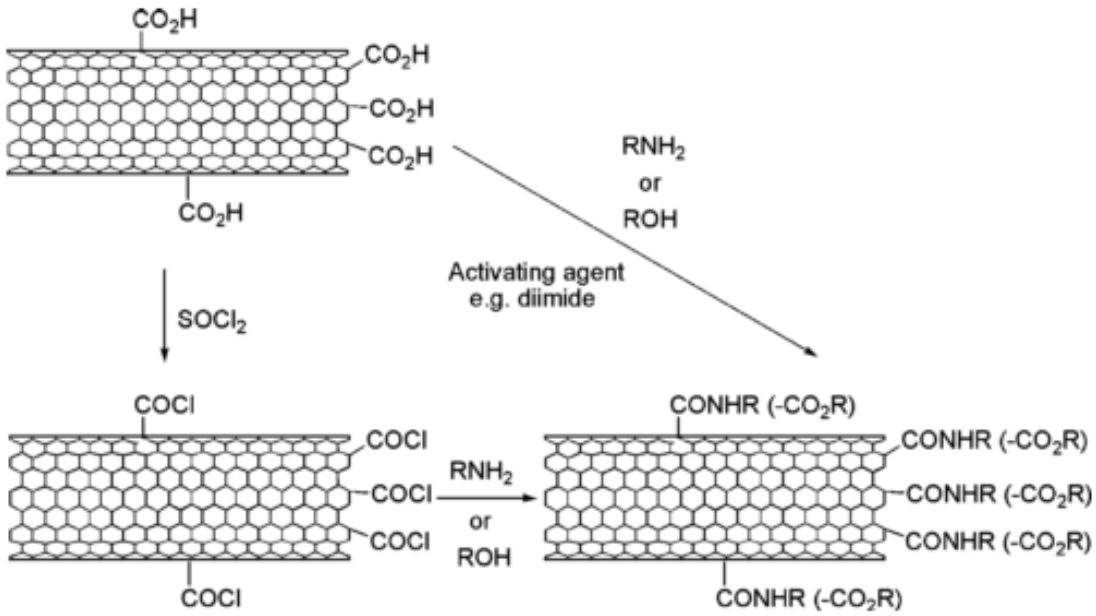

Figure 1 - 9 *Derivatisation reactions of acid-cut CNTs. Taken from reference 59.*[59]

Another example of covalent modification is the nitrene [2+1] cycloaddition to the CNTs.[68] This method consists in the decomposition of an organic azide, which gives rise to a very reactive nitrene group *via* nitrogen elimination, and then in the [2+1] cycloaddition of the nitrene to the nanotube *via* aziridine adducts formation, as shown in Figure 1 – 10. This allows to attach a variety of functional groups onto CNTs.

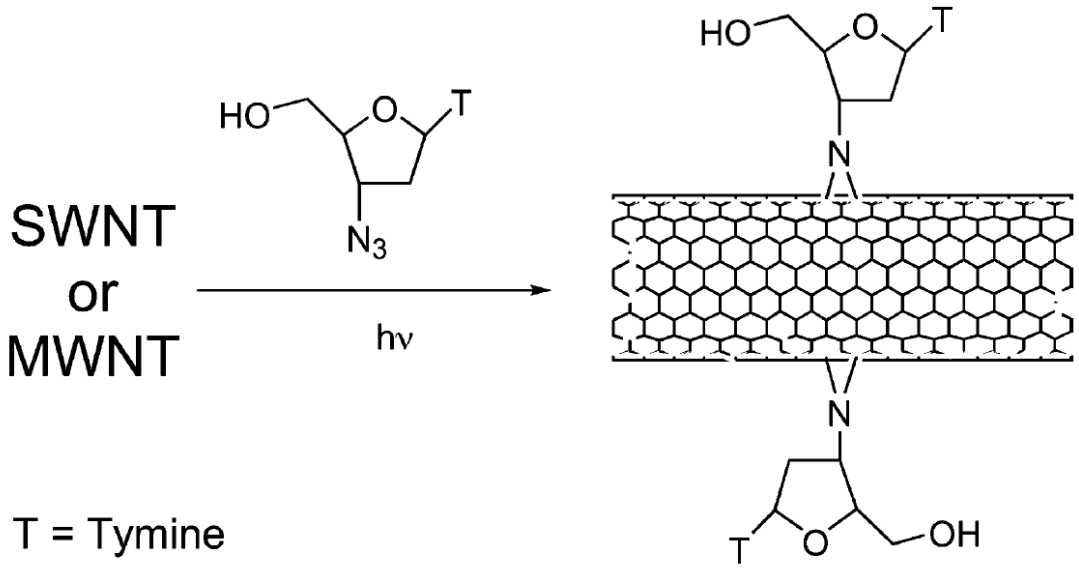

Figure 1 - 10 *Photoinduced nitrene [2+1] cycloaddition to CNTs. Taken from reference 59.*[59]

The CNT covalent functionalisation opens the doors to the integration of biological systems to form functional assemblies.[69–71] In fact, the combination of the carbon nanotube electronic properties and the biomaterial recognition properties can be exploited for the fabrication of new bioelectronic systems. In 2002, Huang *et al.*[69] prepared CNT-protein conjugates *via* diimide-activated amidation reaction. The nanotubes were functionalised with bovine serum albumin (BSA) proteins and the CNT-BSA conjugates were found to be highly dispersible in aqueous media, as shown in Figure 1 – 11.

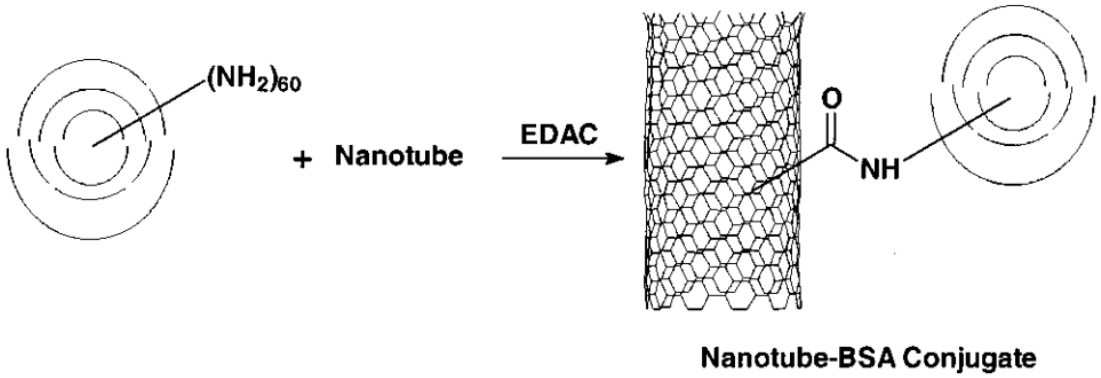

Figure 1 - 11 *Scheme of CNT-protein conjugates via diimide-activated amidation reaction Taken from reference 69.*[69]

Another strategy relies on the use of radicals to covalent functionalise carbon nanotubes. Some examples are with diazonium salts, where the reactive species were aryl radicals and the formation of this reactive molecules was triggered by electron transfer between the nanotube and the diazonium salts.[72–76] In other examples, alkyl or aryl peroxides were thermally decomposed and subsequently the resulting phenyl or lauyl radicals reacted with the nanotubes.[77,78]

1.1.2.2 Non-covalent Functionalisation

Conversely to the covalent functionalisation, non-covalent interactions conserve the π-conjugated skeleton of CNTs. This preserves their unique properties and allows their dispersion in solvents, which could enhance the adsorption of biomolecules on their surfaces. The main forces that drive the non-covalent functionalisation are van der Waals or π-π stacking interactions.[79] It consists in the interaction between the nanotube surface and various dispersants,[80] such as polymers,[81] surfactants[82,83] and biomolecules.[84,85]

Carbon nanotubes are considered ideal reinforcing agent for polymer composites, due to their electrical and mechanical properties. Therefore, CNT-polymer nanocomposites are great candidates for organic optoelectronics and structural applications. In 1999, Tang *et al.*[86] prepared the first CNT-polymer nanocomposites by in situ polymerisation of phenylacetylene in presence of carbon nanotubes. This procedure allowed the wrapping of the polymer chain around the nanotube, increasing its dispersibility in common organic solvents. Carbon nanotubes have been dispersed in a variety of polymers, such as polystyrene, polypropylene, and polyethylene glycol (PEG). The first CNT-PEG composites was first fabricated by Goh and co-workers[87,88] and exhibited enhanced mechanical properties due to hydrogen bond interactions between the nanotube defect sites and the PEG oxygen atoms. Poly(m-phenylenevinylene-co-2,5-dioctyloxy-p-phenylenevinylene)(PmPV) is a polymer widely employed for the fabrication of optoelectronic applications due to its luminescent properties. The research work of Blau and co-workers[89,90] explains the importance of producing CNT-PmPV composites since the integration of CNT in PmPV improves the electrical conductivity of the conjugated polymer by 8 orders of magnitude.

Another approach for the non-covalent modification of CNT is shown in Figure 1 – 12 and involves the use of pyrene derivatives.[91–93] In this process, the pyrene molecules are irreversibly adsorbed onto the nanotube sidewall due to π-π stacking interactions and can be used as linker to covalently attach biomolecules.[92,93]

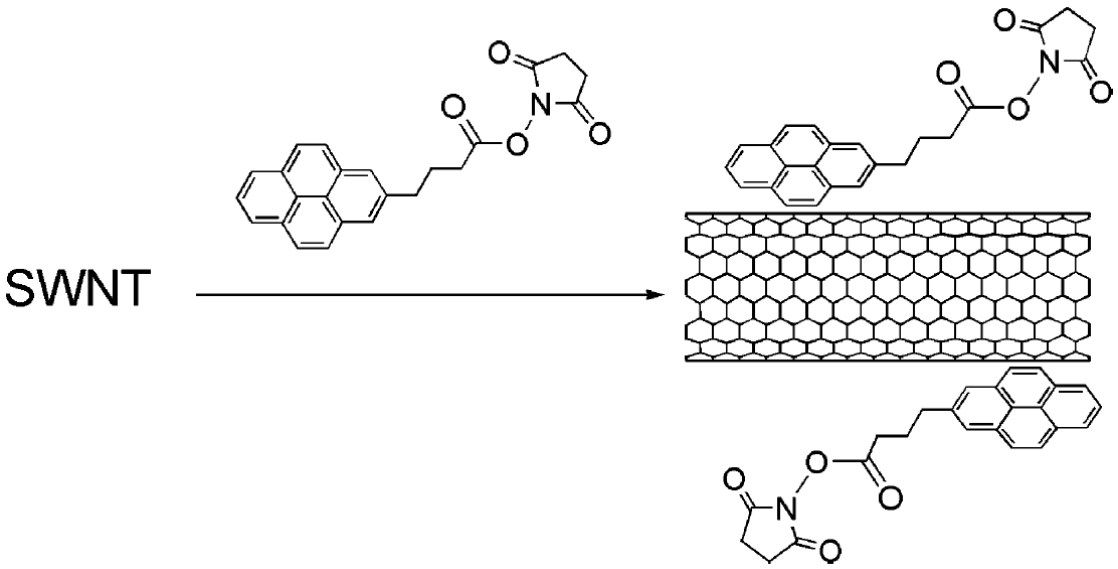

Figure 1 - 12 *Interactions of CNTs with pyrene derivatives. Taken from reference 59.*[59]

Carbon nanotubes can also interact directly with biomolecules in appropriate conditions. An example is streptavidin, a water-soluble protein that can be absorbed on MWCNTs after incubation (Figure 1 – 13).[85]

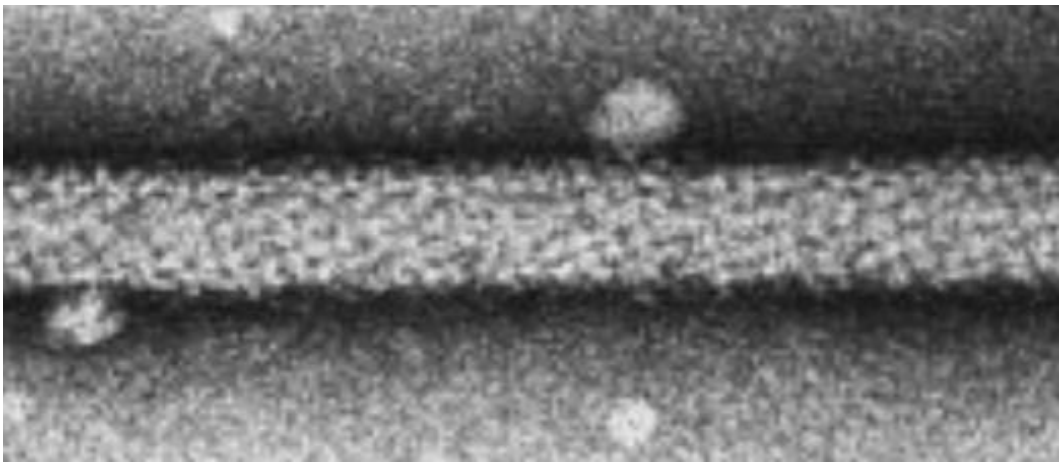

Figure 1 - 13 *Electron micrograph of MWCNTs coated with streptavidin molecules. Taken (adapted) from reference 85.*[85]

Among the biomolecules able to interact with carbon nanotubes, deoxyribonucleic acid (DNA) has drawn great attention due to its capability to bind to CNTs with high affinity and form dispersible hybrids, solving the problem of nanotube dispersion and separation. The DNA-wrapping around the sidewalls of the CNT is the main driving force[94] and offers a high dispersion efficiency (up to 4 mg/mL), while maintaining the unique CNT properties.[84,95] This thesis is focused on DNA-wrapped SWCNTs and they will be further discussed in the following section.

1.1.3 DNA-wrapped SWCNTs

1.1.3.1 Dispersion

Deoxyribonucleic acid is an organic polymer that plays a central role in biology and due to its properties has inspired a search for non-biological applications. It is made from four different monomers, called nucleotides, and polymerisation of nucleotides forms the backbone of a single strand DNA (ssDNA). Each nucleotide contains a phosphate group, a 2-deoxyribose and a nucleobase [adenine (A), thymine (T), cytosine (C) or guanine (G)] attached to the sugar. Adenine and thymine are known as purine, while cytosine and guanine as pyrimidines. A double strand DNA (dsDNA) is composed of two helical chains, connected to each other by specific and complementary hydrogen bonds between either adenine and thymine, or guanine and cytosine, as shown in Figure 1 – 14. DNA is polar due to its negative charged phosphate backbone and its polarity makes it water-soluble according to the principle "like dissolves like".

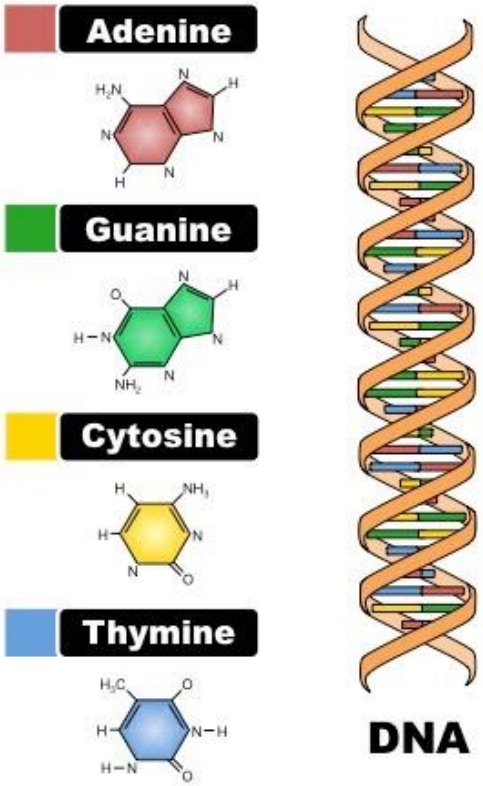

Figure 1 - 14 *Schematic representation of DNA molecule. Taken (adapted) from https://ib.bioninja.com.au/*

The molecular recognition between complementary strands of DNA has been exploited for the fabrication of geometric nano-objects, and for controlling the assembly of colloidal particles. In addition, the π-π stacking interactions and the electronic properties of DNA bases have been investigated for possible use in molecular electronics. In this context, joining the unique properties of SWCNTs and DNA opens the doors to a new class of materials with exceptional properties and diverse range of applications.[96–105]

In 2003, Zheng *et al.*[84] had successfully obtained DNA-wrapped SWCNTs in aqueous environment (Figure 1 – 15). The wrapping process[84,106] consists in sonicating, in a water ice bath, an aqueous solution containing carbon nanotubes and ssDNA. In the process, DNA acts as a dispersing agent:[84,99] the flexible hydrophilic phosphate backbone is exposed to the aqueous media and allows low-energy conformations for the π-π stacking interactions between its aromatic hydrophobic bases and CNT sidewalls.

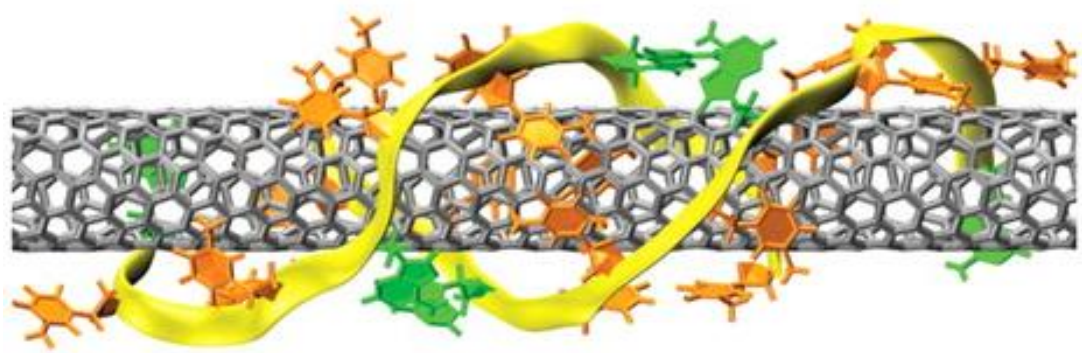

Figure 1 - 15 *Schematic model of DNA-wrapped single-walled carbon nanotube. Taken (adapted) from reference 107.*[107]

In order to optimise the dispersion of carbon nanotubes by DNA, several studies have been conducted to find the best wrapping conditions. In particular, several parameters have been investigated: length and sequence of the DNA strands; sonication time; carbon nanotube type; and salt concentration.

In this regard, thymine-rich DNA sequences result in the highest dispersion efficiency for SWCNTs.[84] In particular, Zheng *et al*.[84] found that, among DNA/SWCNT hybrids containing different lengths (60-, 30-, 21- and 15-mer) of poly(T), T_{30} DNA sequence has the highest yield.[106]

In addition, a search of the ssDNA library showed that DNA sequences containing $d(GT)_n$, with n = 10 to 45, have a high dispersion yield and also enable CNT separation by anion exchange chromatography.[106]

Generally, the kinetic stability of DNA-wrapped SWCNTs increases with the length of the DNA sequence.[108] However, in the work of Vogel *et al.,*[109] shorter DNA sequences have displayed high dispersion efficiency: DNA sequences $d(GT)_n$ and $d(AC)_n$, with n equals to 2, 3, 5, 10, 20, or 40, were employed both individually and as equimolar mixtures of the complementary DNA strands; unexpectedly, the highest dispersion yield was found for the DNA mixture $d(GT)_3$:$d(AC)_3$.

The absorption of nucleobases on the SWCNT sidewall strongly depends on the ionic strength of the medium. The work of Ghosh *et al.*[110] shows that while in low salt concentration the wrapping of ssDNA on the nanotube surface is due to the π–π stacking interactions between the DNA bases and the sp^2-hybridised SWCNT surface, at elevated salt concentration the DNA bases self-stack and DNA molecule adopts a partially folded structure, weakening the interaction between DNA and SWCNT. Moreover, the force between DNA-wrapped SWCNTs is a function of their interaxial distance in low monovalent salts, where electrostatic repulsion dominates. The research work of Qiu *et al.*[111] shows that while DNA-SWCNTs forces resemble that of dsDNA in low salt concentration, a different behaviour rises at high monovalent salts: DNA/CNT hybrids aggregate spontaneously, whereas dsDNA remains soluble. The traditional wrapping process is not very effective for large diameter (>1 nm) tubes and do not preserve secondary and tertiary structural and functional domains present in certain DNA sequences. To overcome this problem, Streit *et al.*[112] developed a low energy strategy to DNA-wrap single-walled carbon nanotubes by replacing strong binding bile salt surfactants (Figure 1 – 16). This simple method allows to produce DNA-wrapped SWCNTs with tubes of broad diameter range and DNA of arbitrary sequence.

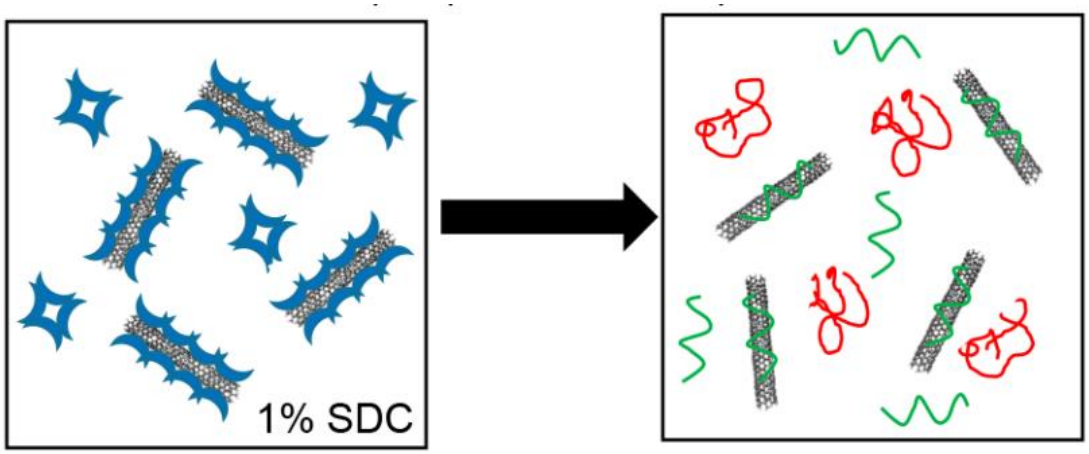

Figure 1 - 16 *Schematic DNA/SDC exchange process. Taken from reference 112.*[112]

1.1.3.2 Separation Methods

Device applications require both size and properties control of carbon nanotubes. Different strategies have been reported to sort CNTs by diameter, chirality, electronic behaviour and length.

The dominant physical dimension of a SWCNT is its length. Although the carbon nanotube electronic band structure is not dependent on its length,[113] device applications need nanotube length control for an easy and reproducible fabrication. Several studies about CNT length sorting have been reported, such as capillary electrophoresis[114,115] and gel electrophoresis.[116] In 2005, Huang *et al.*[117] demonstrated that DNA-wrapped SWCNTs can be fractionated by size-exclusion high-performance liquid chromatography (SEC-HPLC) to yield populations of nanotubes with uniform length. In addition, UV-Vis-NIR analysis of the SEC-HPLC fractions, shown in Figure 1 – 17, revealed the effective removal of graphitic impurities and excess of DNA.

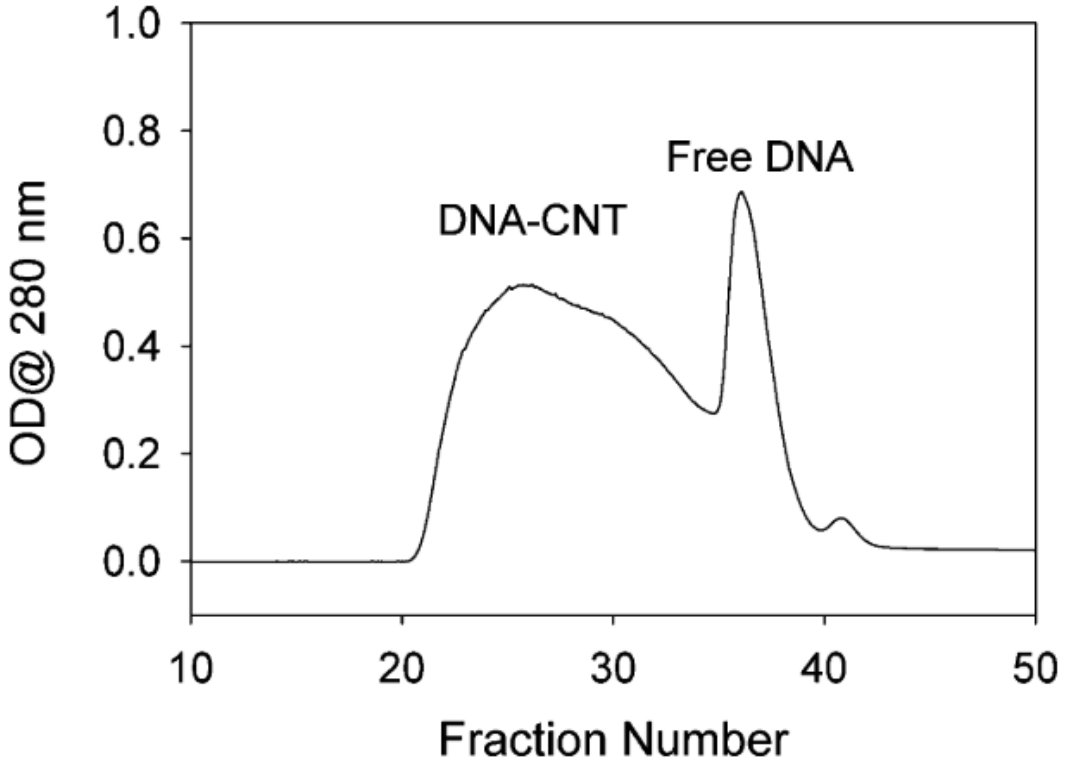

Figure 1 - 17 *Chromatogram of size-exclusion column separation of DNA-wrapped SWCNT, showing a broad peak at ~20 min retention time and a relatively narrower peak at ~37 min retention time, corresponding to DNA-wrapped SWCNTs of different length and free DNA in solution, respectively. Taken from reference 117.*[117]

Since DNA/SWCNT hybrids are found to be negatively charged, due to the exposed phosphate backbone, another chromatography technique that allows their separation is ion exchange chromatography (IEX).[106] Ion exchange chromatography is a chromatography technique that usually separates ions and polar molecules based on their affinity to the ion exchanger. It is used for almost any charged molecule as well as proteins, nucleotides, and amino acids. There are two types of ion chromatography: cation-exchange chromatography, used when positively charged molecules are attracted to the negatively charged stationary phase; and anion-exchange chromatography, employed when the stationary phase is positively charged and negatively charged molecules are loaded to be attracted to it. Zheng *et al.*[106] found that anion-exchange chromatography provides a useful tool to separate DNA-wrapped SWCNTs by their diameter and electronic properties. The separation is linked to the DNA sequence as the nanotubes behaviour depends on their linear charge density. This results in early fractions enriched in smaller diameter and metallic SWCNTs, whereas late fractions are enriched in larger diameter and semiconducting nanotubes.

As previously mentioned, the electronic structure of SWNTs is not dependent on their length, but it is a key factor during a separation process. In fact, a broad length distribution reduces their separation resolution. To overcome this problem, Zheng *et al.*[95] developed an effective length sorting method, by combining IEX and SEC-HPLC. In the experiment, first the SWNTs length distribution was narrowed by SEC-HPLC separation, then IEX separation was conducted. This combination resulted in the production of a few single chirality enriched SWNTs

The structure of DNA-wrapped SWCNTs depends on both DNA sequence and SWNT chirality. This allows to select DNA sequences for specific SWNT structure recognition. In this context, Tu *et al.*[107] designed an effective search of a ssDNA library, and identified short DNA sequences that enabled nanotube separation by chirality (see Figure 1 – 18). In particular, the study showed a periodic purine–pyrimidines pattern, which can form a 2-D sheet *via* hydrogen bonding, and fold selectively on SWCNT into a well-ordered 3-D barrel.

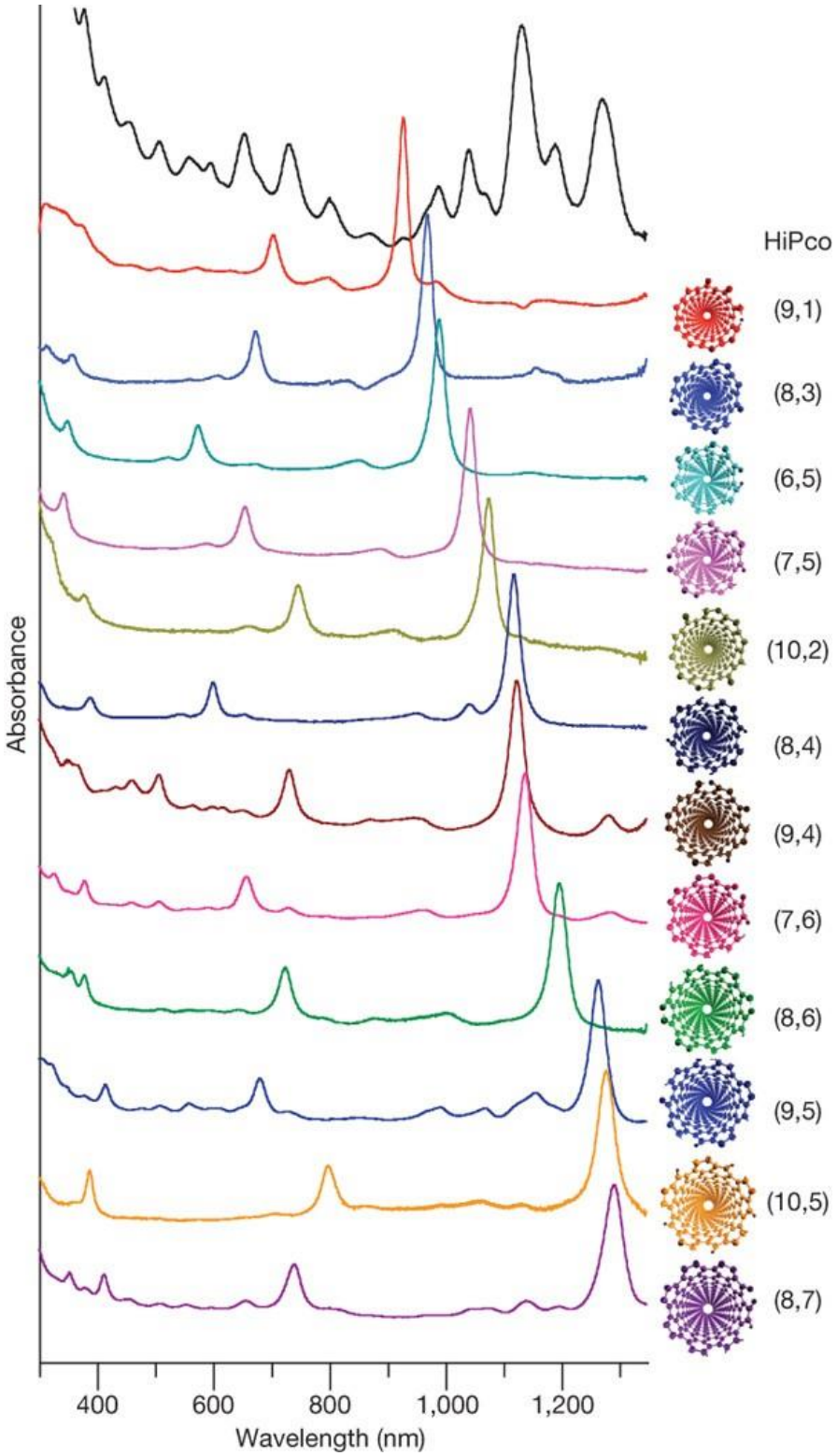

Figure 1 - 18 *Comparison of ultraviolet–visible–near-infrared absorption spectra of SWNTs. The black spectrum shows the absorbance peaks of HiPco SWCNTs and the coloured spectra show the two characteristic peaks, one in the S_{11}-regime and the other one in the S_{22}-regime, for semiconducting SWNTs sorted by chirality. Taken from reference 107.*[107]

Another efficient method for the purification of SWCNTs is by means of a polymer aqueous two-phase (ATP) system. The ATP system consists of a polymer-polymer phase separation to generate two immiscible aqueous phases having slightly different physical properties. The difference in solvation energy of diverse SWCNT chiralities results in their distribution between the two phases. The work of Ao *et al.*[118] shows how the partition of DNA-wrapped SWCNTs in a given ATP system strongly depends on the DNA sequence and can be modulated by salt and polymer additives. In particular, with the proper combination of ATP system, DNA sequence and salt concentration, they separated 15 single-chirality nanotube species from a synthetic mixture, as shown in figure 1 – 19.

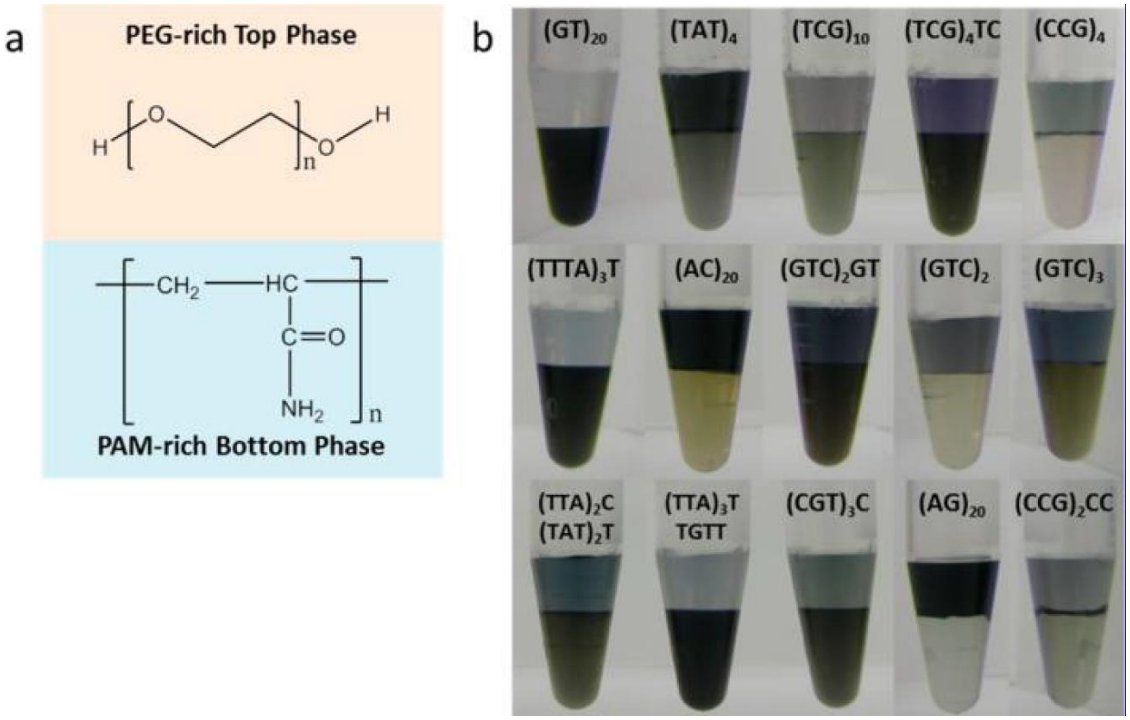

Figure 1 - 19 *Sequence-dependent partition of DNA-SWCNTs in the PEG/PAM ATP system. Taken from reference 118.*[118]

1.1.3.3 Controlled Assembly

Control of the geometry, orientation and structure of carbon nanotubes is needed to optimise their performance for a given application. The use of bottom-up approaches, in which a disordered system of pre-existing components forms an organised structure or pattern, allows to control the assembly of SWCNTs. In this context, DNA-wrapped SWCNTs are a promising material for the construction of organised structures with applications into the "nano-field".

In the work of Eskelinen *et al.*,[119] carbon nanotubes were assembled on DNA-origami templates exploiting the streptavidin-biotin interaction. As shown in Figure 1 – 20, rectangular DNA-origami, with a precise pattern of biotin modifications, were fabricated and streptavidin molecules were assembled on the DNA-origami structure to define the binding sites for SWCNT attachment. Then, SWCNTs, wrapped with biotin-modified ssDNA, were immobilised on the origami templates.

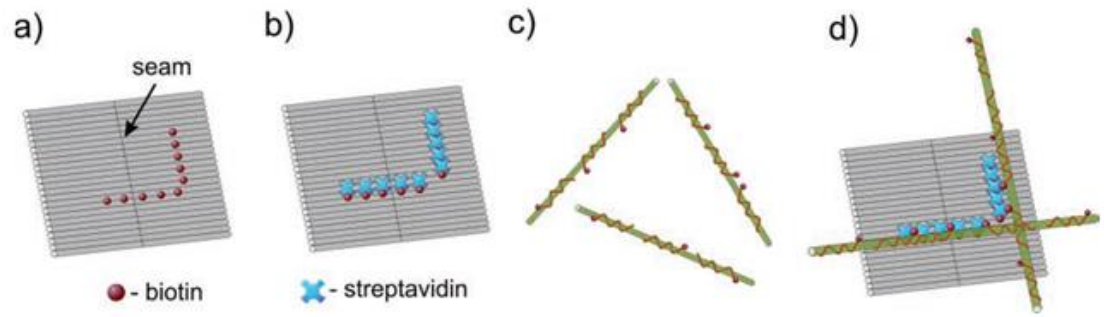

Figure 1 - 20 *Schematic of SWCNT assembly on DNA origami templates using streptavidin-biotin interaction: (a) DNA-origami with a certain pattern of biotin modifications, (b) After that, streptavidin assembly on the origami, (c) biotin-modified DNA-wrapped SWCNTs , and (d) SWCNTs immobilised on the origami templates. Taken from reference 119.*[119]

In the work of McMorrow *et al.*,[120] SWCNTs were wrapped with modified-DNA sequences exhibiting specific chemical functionalities for metal coordination and cycloaddition reactions. The SWCNTs assembly was controlled *via* side-to-side interactions and changes in the reaction conditions led to changes in the structures obtained (Figure 1 – 21).

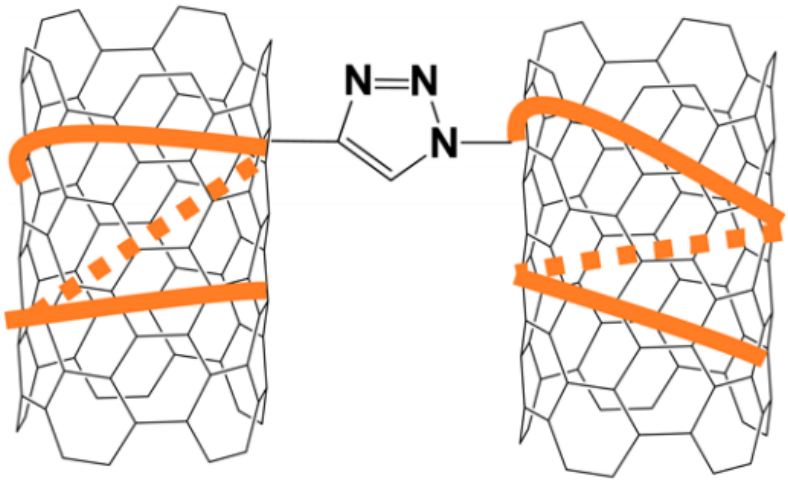

Figure 1 - 21 *Schematic of a junction between parallel SWCNTs. Taken (adapted) from reference 120.*[120]

Another strategy consists in assembling single-walled carbon nanotubes by means of DNA linkers. Han *et al.*[121] use multidomain DNA linkers that cooperatively disperse each nanotube *via* DNA-wrapping; the resulting dispersion is stable under ambient conditions, but it assembles into parallel arrays on charged surfaces in the presence of divalent counterions, which form salt bridges between the SWCNT-anchored DNA linkers and the surface charge groups, as shown in Figure 1 – 22.

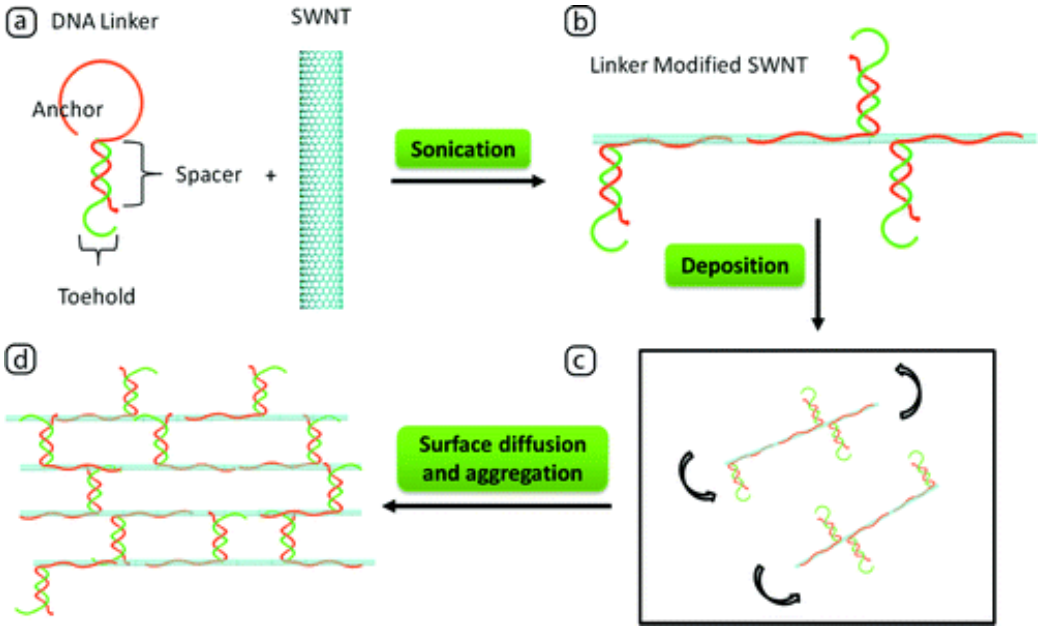

Figure 1 - 22 *(a) DNA linkers and SWCNTs are sonicated to give (b) anchored DNA linkers modified SWNTs. (c) After deposition, (d) nanotubes assemble into parallel arrays. Taken from reference 121.*[121]

In 2010, Weizmann *et al.*[122] used DNA linkers for joining the ends of single-walled carbon nanotubes (Figure 1 – 23). In this work, the authors linked SWCNTs *via* amidation reaction exploiting the carboxylic acid groups on the ends of nanotubes and the amino groups of amino-functionalised oligonucleotides.

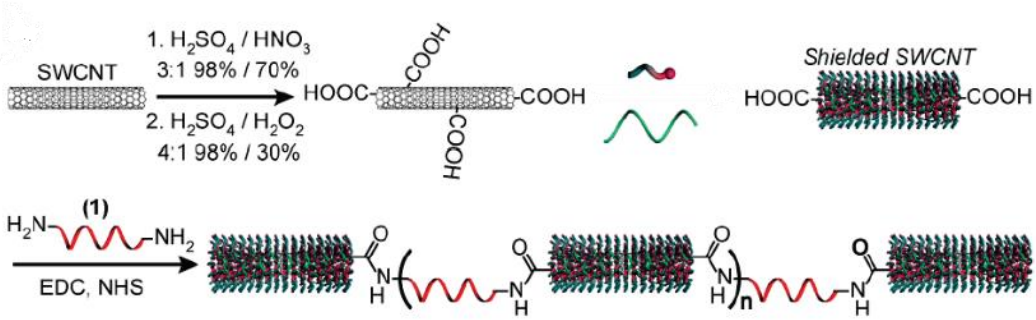

Figure 1 - 23 *Schematic of end-to-end assembly of DNA-wrapped SWCNT via amidation reaction. Taken (adapted) from reference 122.*[122]

In a similar approach, Palma and co-workers[123] assembled DNA/SWCNT hybrids using non-conjugated diamine linkers (Figure 1 – 24). This approach is a novel strategy for the fabrication of solution-processable molecular transport junctions.[124]

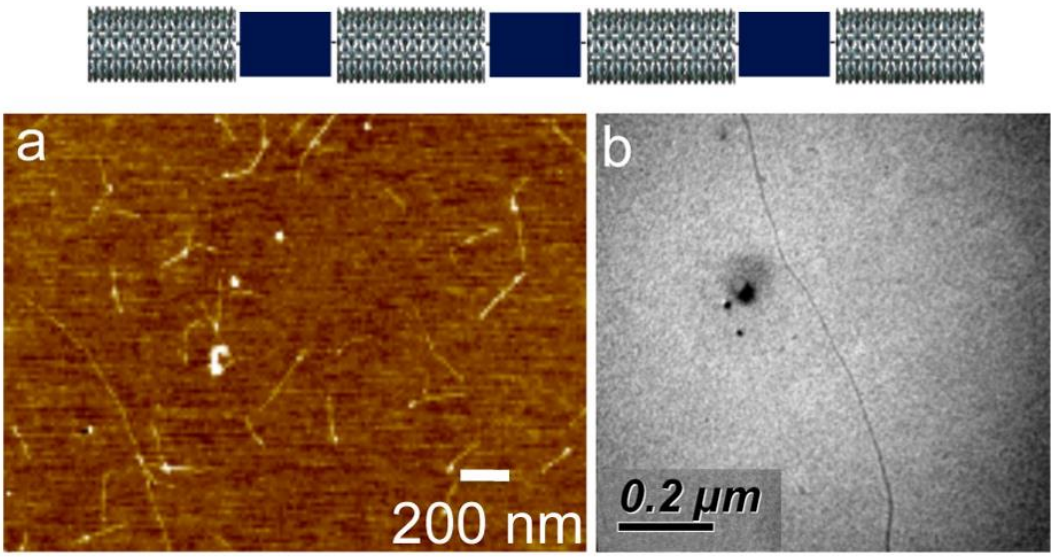

Figure 1 - 24 *(top) Schematic of linear SWCNT junctions. (a) AFM and (b) TEM images of SWCNT junctions formed using molecular linker. Taken (adapted) from reference 123.*[123]

In another work, Clément *et al.*[125] employed a three-terminal diazonium salt molecule to link in a single-step strategy DNA-wrapped SWCNTs tips in water at room temperature. Moreover, they observed that upon increasing the concentration of the diazonium molecular linker, side-to-end and side-to-side SWCNT molecular junctions were formed. This strategy demonstrates the possibility of controlling the formation of linear and branched SWCNT junctions in function of the linker concentration, which is of paramount importance for the fabrication of SWCNT-based devices.

Reversible assembly and disassembly of SWCNTs has an important function in the controllable construction of nanodevices.[126,127] There are several methods to achieve the reversible assembly/disassembly of DNA/SWCNT conjugates. Li *et al.*[128] employed hybridisable DNA sequences onto the DNA-wrapped SWNTs to construct an assembled system *via* DNA hybridisation, and demonstrated the disassembly of SWCNTs *via* strand-displacement mechanism, as shown in Figure 1 – 25.

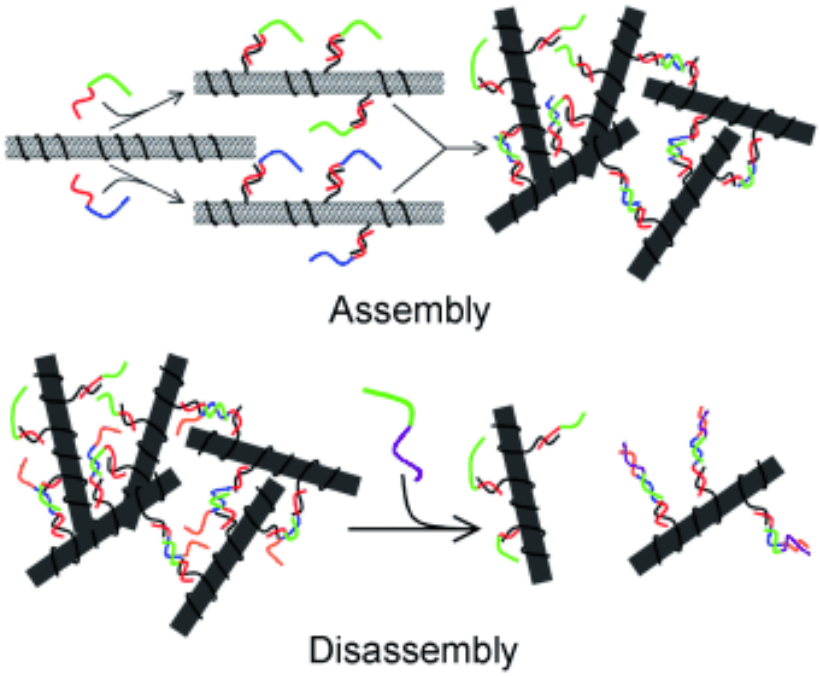

Figure 1 - 25 *Disassembly of linked SWNT by DNA-strand-displacement mechanism. Taken from reference 128.*[128]

In the work of Wan *et al.*,[129] SWCNTs were dispersed with two different ssDNA: one containing an *i*-motif sequence and the other its complemental DNA sequence. The resulting DNA-wrapped SWCNTs can assemble as the two DNA terminals hybridise under slightly basic conditions, while they disassemble under slightly acid conditions as an *i*-motif DNA structure is formed (Figure 1 – 26).

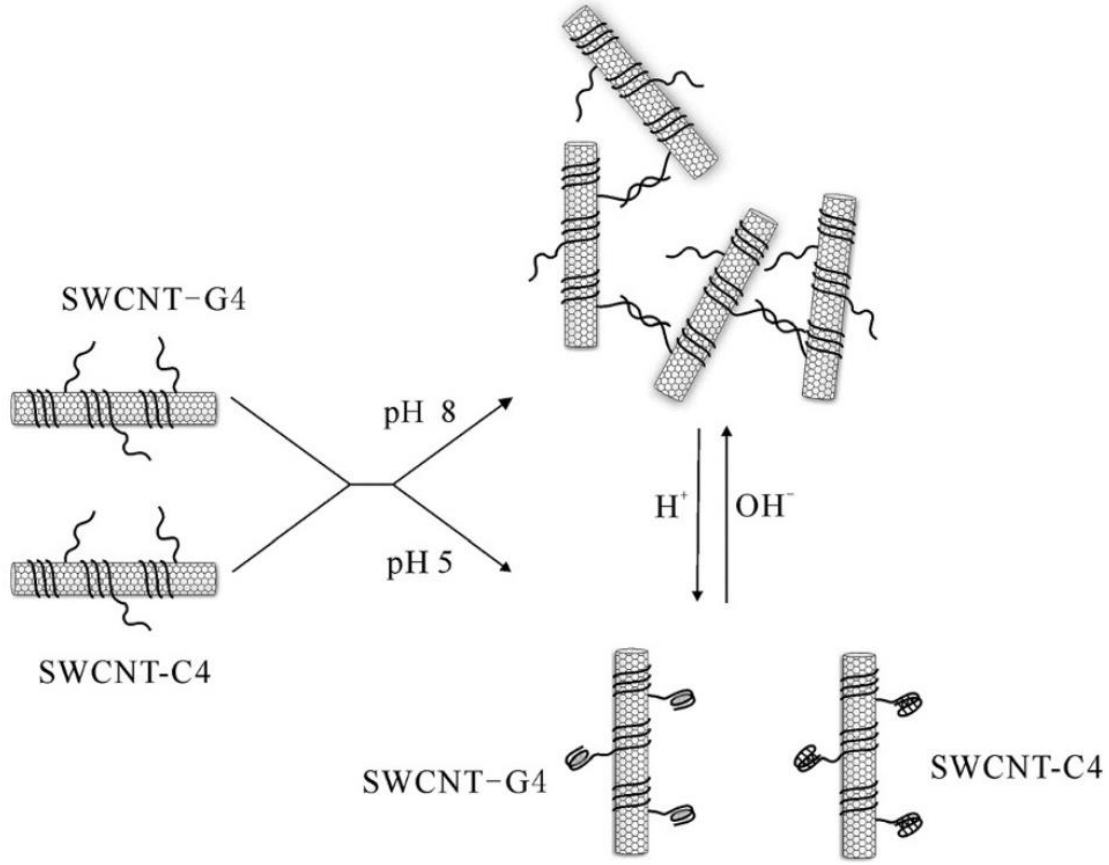

Figure 1 - 26 *Reversible assembly/disassembly of DNA-wrapped single-walled carbon nanotubes. Taken from reference 129.*[129]

1.2 MOLYBDENUM DISULPHIDE

1.2.1 Layered Materials Overviews

Two dimensional (2-D) layered materials[130–132] have gained extensive interest since the discovery of graphene[133] and its properties.[134] They possess a sheet-like structure with a lateral size up to a few micrometres and thickness less than 5 nm.[135] The structure is composed of stacked nanometre-thick layers, which, due to the electron confinement in two dimensions,[136] gives to this materials unique structural,[137,138] mechanical,[139] electrical,[140–142] thermoelectric,[143–146] optical,[147–153] catalytic,[154,155] and sensing properties.[156–161] The layers are linked by weak out-of-plane van der Waals interactions,[162] while they have strong in-plane covalent bonds. Their layered structure allows exfoliation of the bulk material by means of top-down exfoliation methods.

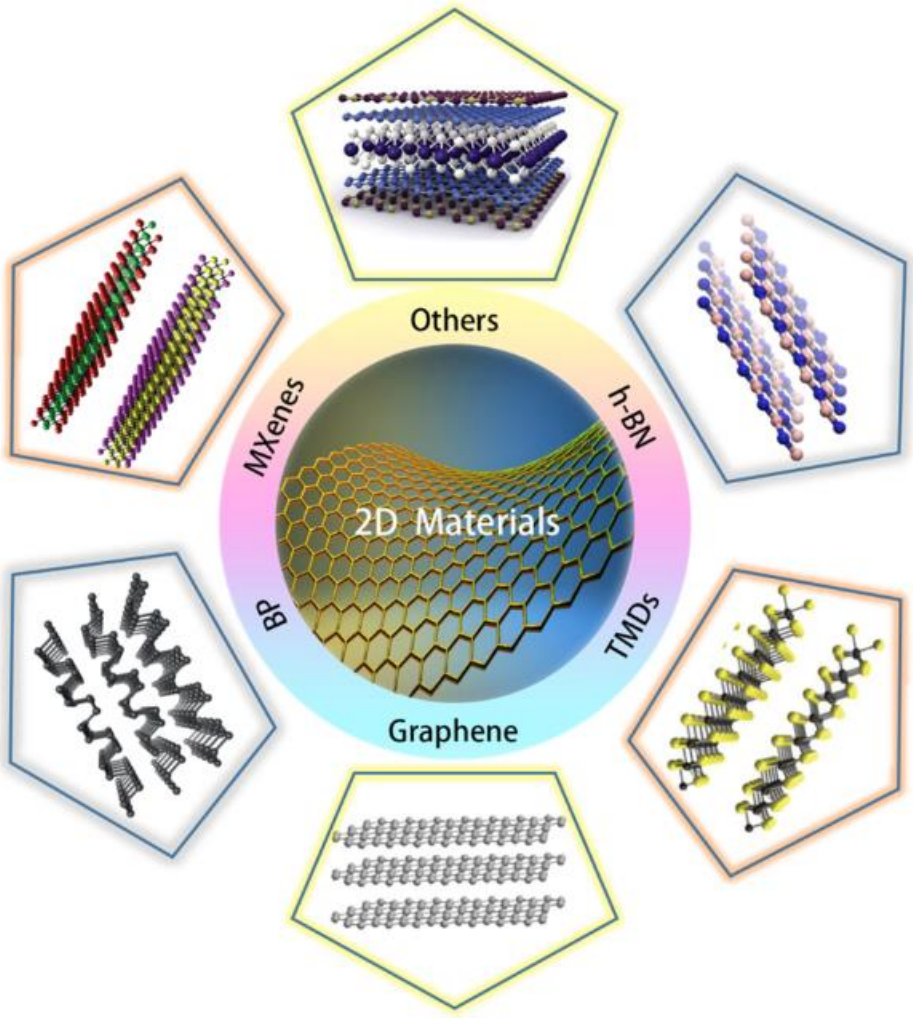

***Figure 1 - 27** 2. Schematic of 2D layered materials. Taken (adapted) from reference 131.*[131]

Besides graphene, there are other 2-D layered materials (Figure 1 – 27) and the main categories are described below:

- Graphene: is the typical example of layered materials in which layers stack together, forming the bulk graphite. It is an allotrope of carbon and can be considered as an indefinitely large polycyclic aromatic hydrocarbon. A single layer of graphene consists of carbon atoms packed into a 2-D hexagonal lattice.[163] For this, it can also be treated as the basic structural element of other graphitic materials, such as fullerenes (0-D), carbon nanotubes (1-D) and graphite (3-D).[136] Graphene is a zero-gap semiconductor with extraordinary properties: a larger theoretical specific surface area (2,630 m^2/g) compared to CNTs (from ≈100 to 1,000 m^2/g);[134,164] an electron mobility of $2.5 \times 10^5\ cm^2\ V^{-1}\ s^{-1}$ at room temperature;[165] a Young's modulus of 1 TPa and intrinsic strength of 130 GPa;[166] a thermal conductivity above 3,000 $W\ m^{-1}K^{-1}$;[167] a complete impermeability to standard gases;[168] and the ability to be chemically functionalised.[169–171] Its structure, combined with its properties, makes graphene an ideal material for several applications.[133,166,172–175]
- Hexagonal Boron Nitride (*h*-BN): is an interesting lubricant and high-temperature ceramic material thanks to its high thermal conductivity, inertness, and tribological properties.[176] The structure of *h*-BN is similar to that of graphene. Indeed, a single-layer *h*-BN consists of equal numbers of boron and nitrogen atoms covalently bonded in a hexagonal structure, while the bulk crystal is formed from these layers stack together by van der Waals force.
- Graphitic Carbon Nitride (*g*-C_3N_4): is another analogue of graphene, with a 2-D layered structure,[177–179] and presents interesting physicochemical properties due to the s-triazine cores. This compound has general formula g-C_3N_4 and its structure can be considered as N-substituted graphene framework formed through the sp^2 hybridisation of carbon and nitrogen atoms. Although electronic applications are limited due to the poor conductivity, its catalytic activity can be exploited for water splitting and pollutant degradation at room temperature.[180]
- Black Phosphorus (BP): is a rising 2-D material because of its electronic structure and bandgap. Indeed, BP is a direct semiconductor regardless of layer number.[181]

The bulk material is constituted of stacked phosphorene monolayers through weak van der Waals forces and each monolayer possesses an honeycomb structure, in which one phosphorus atom bonds the other three in a sp^3 hybridisation. Among the four P atoms, three of them are located in the same plane, while the last one at the parallel adjacent plane.[182–184]

- MXenes: are a class of 2-D layered transition metal carbides and/or nitride typically synthesised by a top-down etching process of the MAX phase. MAX phase has general formula $M_{n+1}AX_n$, where M is a transition metal, A is an element from group 13 or 14, X is carbon and/or nitrogen, and n = 1-4. They have a layered hexagonal structure, where M layers are nearly closed packed and X atoms fill octahedral sites. Therefore, $M_{n+1}X_n$ layers are interleaved with A, which is metallically bonded to M. MXenes are conductive layered materials with tunable surface terminations and can be exploited for diverse applications.[185–195]
- Layered Double Hydroxides (LDHs): are lamellar inorganic solids with general formula $[M^{z+}_{1-x}M^{3+}_x(OH)_2]^{m+}[A^{n-}]_{m/n}\cdot yH_2O$, in which A^{n-} is an intercalating anion and M^{z+} and M^{3+}, giving m = x, are a divalent and trivalent metal ions respectively. The anions are located in the interlayer regions and can be easily replaced. The incorporated anions are weakly bound and their intercalation properties have use for advanced applications.[196] Diverse anions can be intercalated in this materials, ranging from inorganic and organic anions, such as CO^{2-}_3 and benzoate, to complex biomolecules, including DNA.
- Transition Metal Oxides (TMOs): are a class of layered materials that can undergo to chemical transformations without disrupting the covalent bonding within layers.[197] They have chemical formula MO_3 (M = Mo, Ta, W, etc.)[198,199] and the bulk crystal is composed of different layers stacked together along the y-axis through the van der Waals force. The properties of TMOs are governed by the oxygen ions, which generate remarkable properties on their surface, as well as the cationic species and their flexibility in changing oxidation state.[199] Promising application of TMOs are presented in photodetection, gas sensing, light emission, energy storage, and photocurrent generation.[200–203]
- Transition Metal Dichalcogenides (TMDs): this class of layered materials will be deeply discussed in the next paragraph.

1.2.2 Transition Metal Dichalcogenides

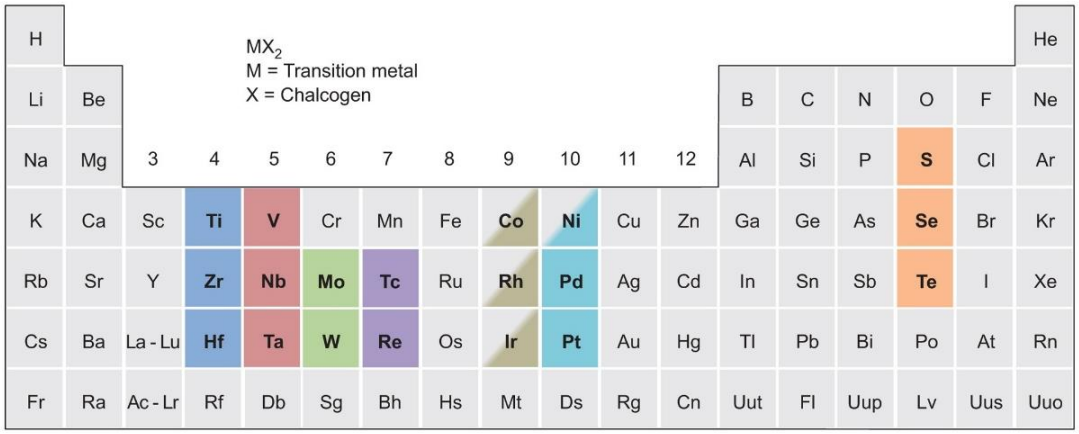

Figure 1 - 28 *Periodic table with highlighted elements able to form TMDs. Taken from reference 132.*[132]

Chalcogen elements are highly reactive to metals, creating various metal chalcogenide combinations with diverse stoichiometric ratios (Figure 1 – 28). Among them, TMDs are an emerging class of two-dimensional layered materials with applications in diverse research areas, such as catalysis,[204,205] sensing,[206–208] energy,[209,210] and electronics.[211–213] Their general formula in chemical notation is MX_2, in which M is a transition metal element (e.g. Mo or W) and X is a chalcogen atom (e.g. S, Se, or Te).[214] The length of M-M bond depends on the size of the transition metal and chalcogen ions, ranging from 3.15 Å to 4.03 Å.[132] These values are larger than the bond lengths of the corresponding transition metal solids, indicating a poorest energetic and spatial overlap of the *d* orbitals.

A single TMDs monolayer typically has a thickness of 6 - 7 Å and consists of three atomic layers, in which a transition metal layer is sandwiched between two chalcogen layers.[132] Similar to the graphite structure, the intralayer metal-chalcogen bonds are covalent, while TMDs monolayers are vertically stacked together through van der Waals force.[215]

In contrast to graphite, one of TMDs characteristics is the ability to form a variety of polymorphs.[216] The most common polymorphs are shown in Figure 1 – 29. For 1T, 2H and 3R polytypes, the T stands for trigonal, the H for hexagonal and the R rhombohedral, whereas the digits indicate the number of X-M-X units in the unit cell.[217]

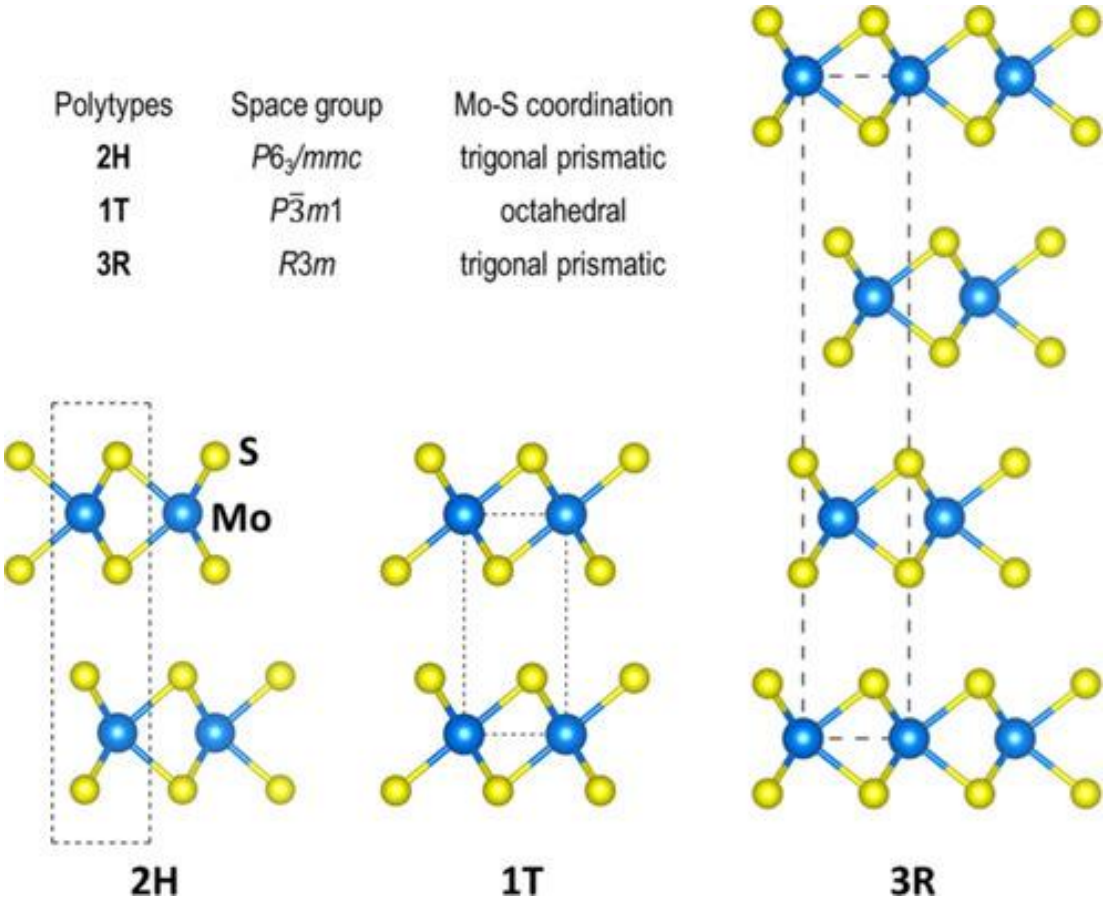

Figure 1 - 29 *Structural polymorphs of MoS_2 bulk, including 2H, 1T and 3R phases. Taken (adapted) from reference 216.*[216] .

The electronic structure of TMDs strongly depends on the coordination environment of the transition metal element and its *d*-electron count. This produces an array of electronic properties for diverse TMDs: HfS_2 is an insulator, MoS_2 and WS_2 are semiconductors, WTe_2 and $TiSe_2$ are semimetals, and NbS_2 and VSe_2 are metals. Exfoliation of this materials into mono- or few-layers can preserve their properties, and lead to new features thanks to quantum confinement effects.[218–220] This thesis is focused on exfoliated MoS_2.

1.2.3 Exfoliated MoS_2

1.2.3.1 Structure and Properties

Amongthe TMD series, molybdenum disulphide (MoS_2) is the most widely studied. MoS_2 has a sandwich-like S-Mo-S structure, where a planar network of molybdenum atoms is covalently linked, in out of-plane directions, between two layers of sulphur atoms. The bond angle between two S atoms and a Mo atom is 82°. However, while in the same layer the Mo-S and S-S distances are 3.16 Å and 2.41 Å, respectively, in different layers the perpendicular Mo-S and S-S distances are 1.58 Å and 3.17 Å, respectively, as shown in Figure 1 – 30.[221]

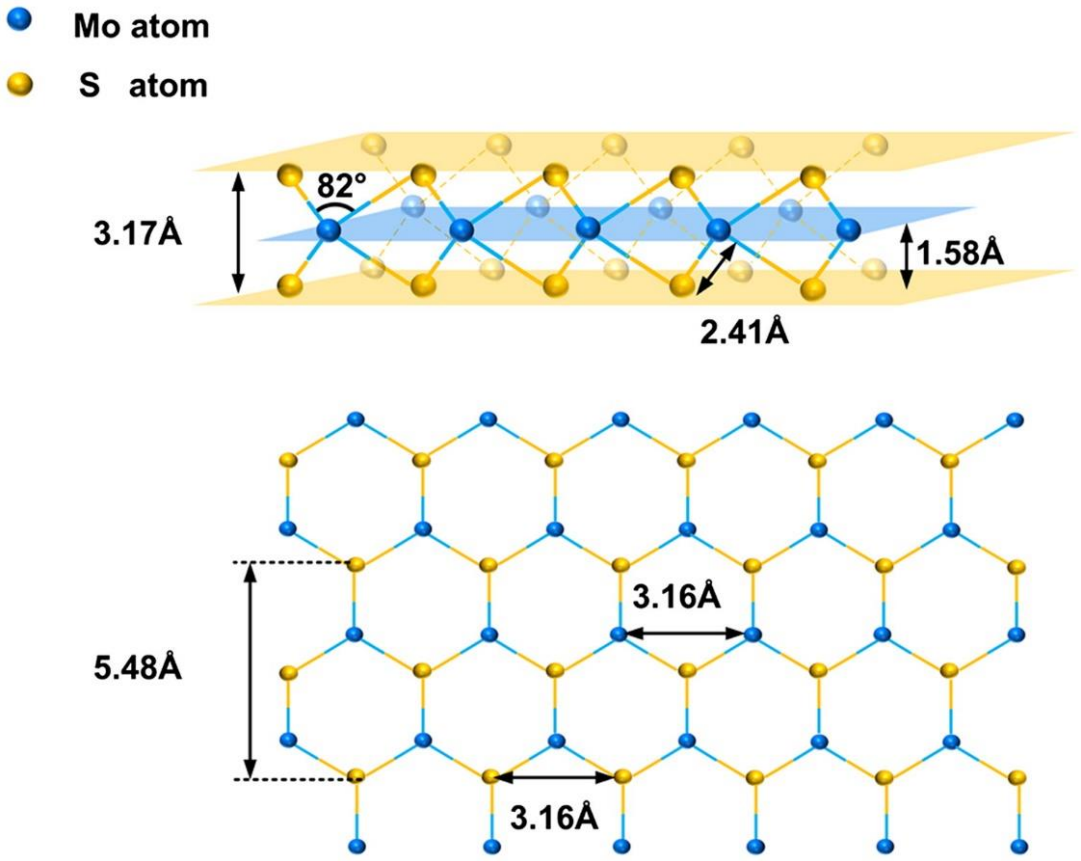

Figure 1 - 30 *The yellow and blue dots indicate S and Mo atoms in MoS_2, respectively. Schematic lateral and top views of MoS_2. Taken from reference 221.*[221]

In the MoS_2 structure, the oxidation states of molybdenum and sulphur atoms are +4 and −2, respectively, such that Mo^{4+} gives four electrons to fill the bonding states. The lone-pair electrons of sulphur atoms are located on the surfaces of the layers, thus the absence of dangling bonds makes MoS_2 surface stable in presence of other surrounding species.

Molybdenum disulphide is present in nature as “molybdenite”. This mineral is extremely soft due to the weak interlayer van der Waals interactions,[215] which allow to layers to slide over one another. It is a dark solid with a metallic lustre, and is similar to graphite, to the point that is hard to distinguish between the two minerals without appropriate laboratory equipment. Like graphite, MoS_2 is employed as dry lubricant[222] and in high-vacuum applications. Unlike graphite, it does not need humid environments, and its lubricative properties enhance in oxygen-deficient environments.[223]

Bulk MoS_2 is a semiconductor with an indirect bandgap of ~1.2 eV,[224,225] and is therefore of limited interest to the optoelectronic applications. Compared to the corresponding bulk, individual layers of MoS_2 have different properties. Indeed, MoS_2 monolayer is a semiconductor with a direct bandgap of ~1.8 eV,[204,225–231] exhibiting strong photoluminescence.[227,229–234] This can be explained through the band structure diagram of bulk and monolayer MoS_2 shown in Figure 1 – 31. The bulk material shows indirect-gap transition from the valence band maximum (VBM), at the Γ point, to the conduction band minimum (CBM), between the K and Γ points. Conversely, the monolayer exhibits direct gap transition at the K points. Indeed, as the number of layers is reduced to single layer, the energy at the Γ point is less than that at the K point in the VBM, and the energy between the K and Γ points is higher than that at the K point in the conduction CBM.[235] This broadly compensates the weakness of gapless graphene, showing promise in the next generation of optoelectronic devices.[208,213,228,229,231,234]

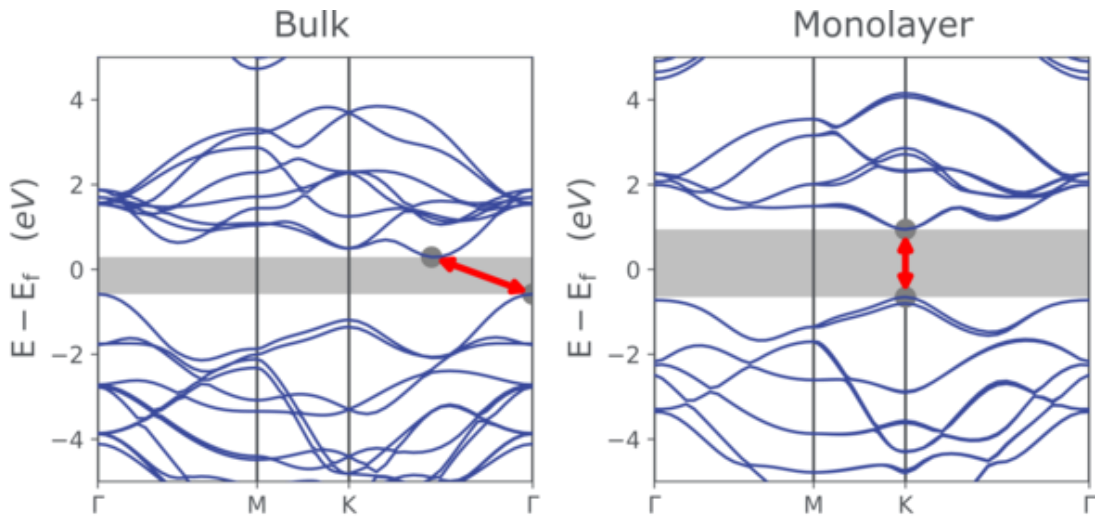

Figure 1 - 31 *Band structure diagram of (left) bulk and (right) monolayer MoS_2. The red arrows indicate the indirect-gap transition for the bulk material from the Γ point of the VBM, to the CBM between the K and Γ points, and the direct-gap transition for the monolayer from the VBM to the CBM at the K points. Taken from Ossila Ltd website.*

Depending on the coordination environments and stacking orders, MoS_2 has different crystal phases. The two most common phases are the thermodynamically stable 2H phase[236] and the metastable 1T phase,[237] though synthetic MoS_2 often contains the 3R phase.[132] The MoS_2 electronic properties change drastically between polymorphs.[217,230] In particular, while the 2H-MoS_2 polymorph is a photoluminescent semiconductor,[211] the 1T-MoS_2 phase possesses a metallic behaviour.[238] Structural crystal phases with the corresponding band structures of bulk 1T and 2H MoS_2 are shown in Figure 1 – 32.

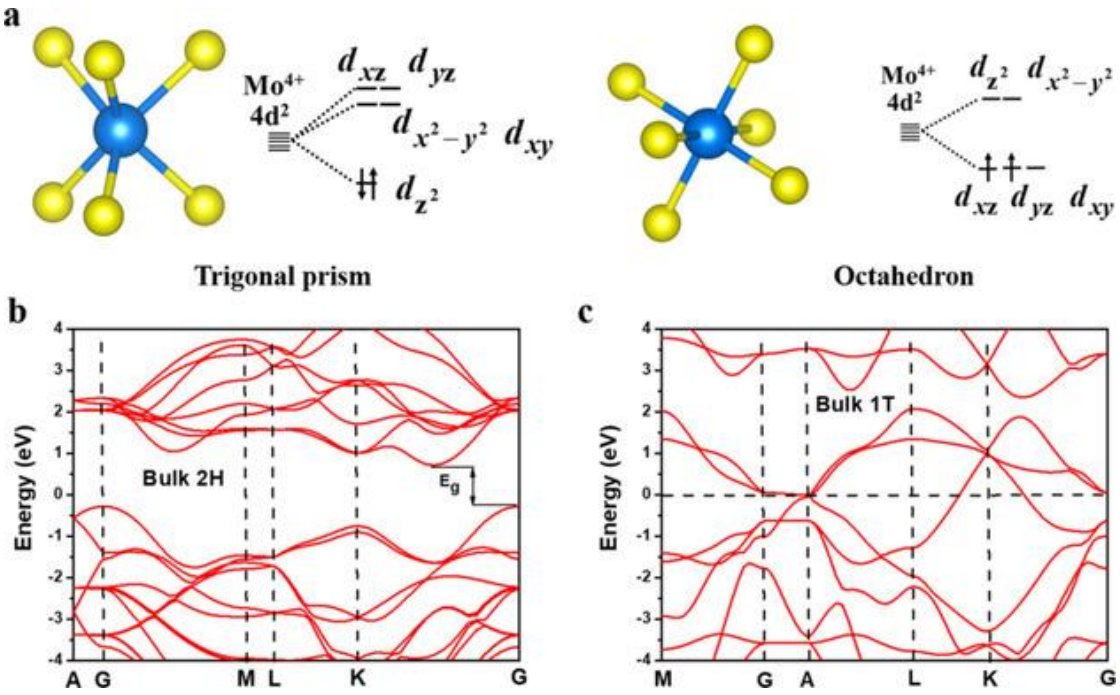

Figure 1 - 32 *(a) Structural polymorphs, with corresponding Mo^{4+} 4d orbital splitting, and (b, c) associate band structures of bulk 1T and 2H MoS_2 phases. Taken from reference 216.*[216]

The diverse crystal phases can be differentiated by several techniques. For example, the Raman spectrum of bulk 2H-MoS_2 in Figure 1 – 33 shows two strong peaks:[239–241] the E_{2g}^1 peak, corresponding to the in-plane vibration mode of Mo and S atoms in the basal plane, and the A_{1g} peak, corresponding to the out-of-plane mode of S atoms; whereas, the Raman spectrum of bulk 1T-MoS_2 shows four additional peaks: the three distinct peaks J_1, J_2 and J_3, attributed to the longitudinal acoustic phonon modes of the S-Mo-S bonds in the 1T phase, and the E_{1g} peak, arisen from the in-plane optical vibration of S atoms in the basal plane. In addition, shift of these peaks is employed to study the grade of exfoliation and the number of layers.[240]

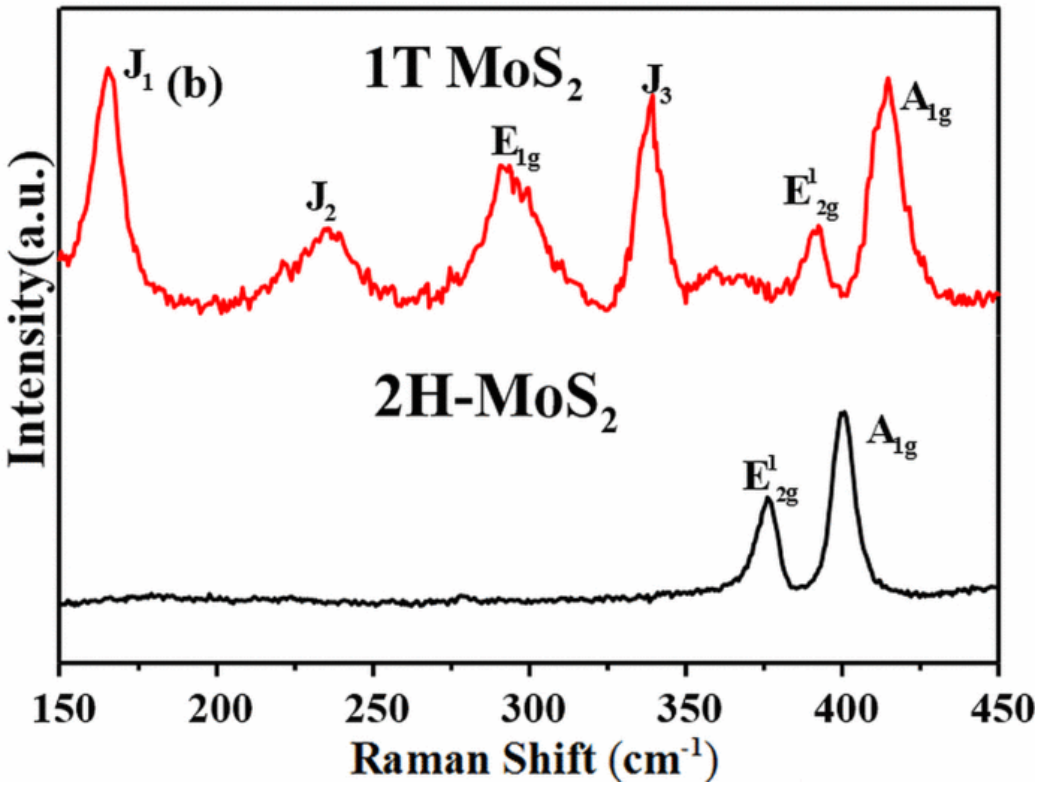

Figure 1 - 33 *Comparison of Raman spectra of (a) 1T and 2H MoS_2. The Raman spectrum of bulk 2H-MoS_2 shows two strong peaks, E_{2g}^1 and A_{1g}; while, in the case of 1T-MoS_2 the distinct J_1, J_2, J_3 and E_{1g} peaks appear. Taken from reference 241.*[241]

Molybdenum disulphide also exhibits characteristic absorption peaks.[242] In the UV-Vis spectra of MoS_2 (see Figure 1 – 34), the A and B peaks, characteristic for MoS_2 dispersions, arise from the interband excitonic transitions at the K point of the Brillouin zone, while the C and D peaks can be assigned to the direct excitonic transition at the M point.

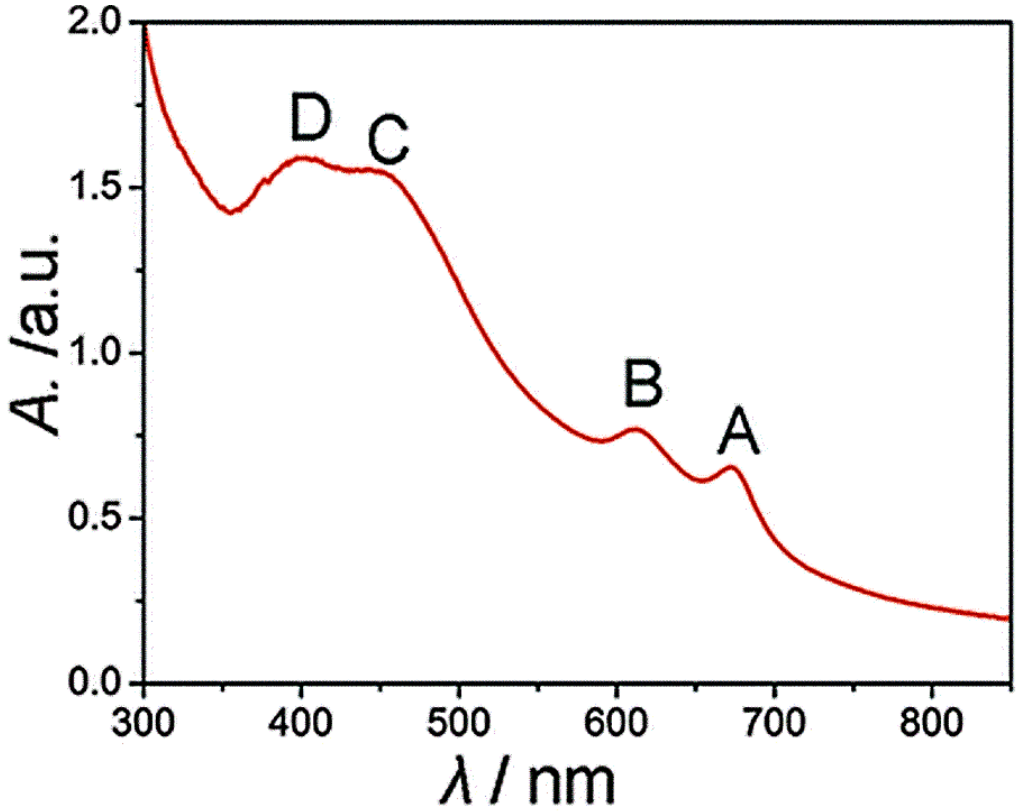

Figure 1 - 34 *UV-Vis spectrum of exfoliated 2H-MoS_2. The A and B peaks correspond to the interband transitions at the K point of the Brillouin zone, whereas the C and D peaks to the direct transition at the M point. Taken from reference 242.*[242]

MoS_2 monolayers also possess good mechanical properties: they are flexible,[243] and have a stiffness comparable to steel and a high breaking strength.[244] Moreover, their thermal conductivity at room temperature results to be 34.5 W/mK, which is 100 times lower than that of graphene.[245]

1.2.3.2 Preparation Methods

Various methods have been used for the synthesis of single-layer and few-layers of MoS_2.[246] Among the bottom-up approaches, chemical vapour deposition is the most reliable technique for controllable fabrication of nanoscopic MoS_2 with high quality, scale-up capability and efficiency. It involves a chemical reaction to convert a precursor to the final MoS_2 material. For example, in the work of Zhang *et al.*,[247] a series of bilayer MoS_2 were synthesised with variable structural configurations and tunable electronic and optical properties through a two-stage thermal CVD process (Figure 1 – 35). In the experiment, the Si substrates was placed facing down above the MoO_3 powder in heating zone 2, while S powder was placed in the heating zone 1. In the A-B stage, for the growth of the first MoS_2 layer, the heating zone 2 was heated to 700 °C and the heating zone 1 become hotter due to the thermal radiation. In the C-D stage, for the growth of the second MoS_2 layer, the temperature of heating zone 2 was further increased to 750 or 800 °C.

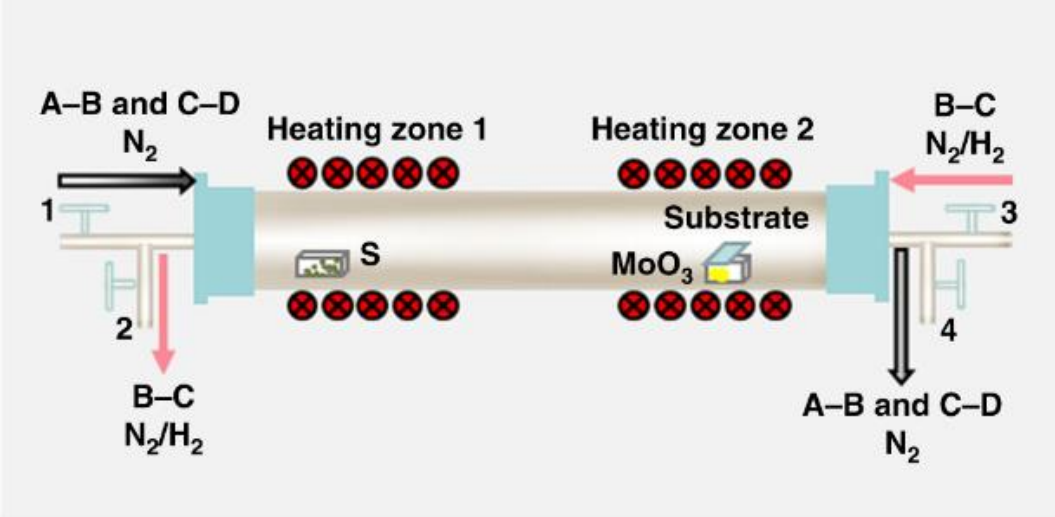

Figure 1 - 35 *Experimental setup of the two-stage thermal CVD process. Taken (adapted) from reference 247.*[247]

Among the top-down approaches, the mechanical exfoliation of bulk MoS_2 has the advantages of scalable production capability and less cost. For example, in the work of Lopez-Sanchez *et al.,*[248] single layers of MoS_2 were exfoliated from crystals of molybdenite using the scotch-tape technique pioneered for the production of graphene.[133] This sticking-and-peeling process can be repeated until single MoS_2 monolayers are obtained. It produces high-quality crystalline monolayers, but the disadvantage is the low yield of monolayer products.

Another top-down approach is the chemical exfoliation of MoS_2 and consists in the ion intercalation between layers. This method is time consuming and removal of the ions results in reaggregation of the layers. Furthermore, the resulting layers tend to change its phase from 2H to 1T. However, Fan *et al.*[249] provided an efficient route to obtain exfoliated 2H MoS_2 by combining sonication-assisted lithium intercalation and infrared laser-induced phase reversion, as shown in Figure 1 – 36.

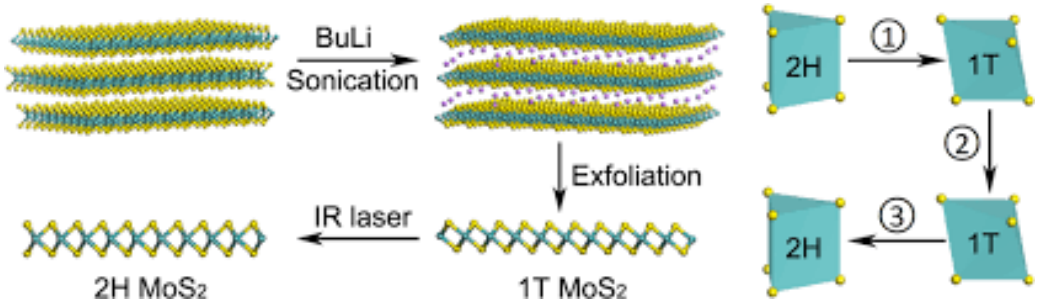

Figure 1 - 36 *Reaction scheme of chemically exfoliated 2H MoS_2. Taken from reference* [249]

Liquid-phase exfoliation also starts from the bulk material and consists in its sonication in solvents. This method breaks the bulk MoS_2 down, producing small MoS_2 flakes with random number of layers. To prevent the layers restacking over each other, a surfactant is often added to the solution.[250] For example, Li *et al.*[251] obtained few-layer MoS_2 by sonicating the MoS_2 bulk in an aqueous sodium cholate solution (Figure 1 – 37).

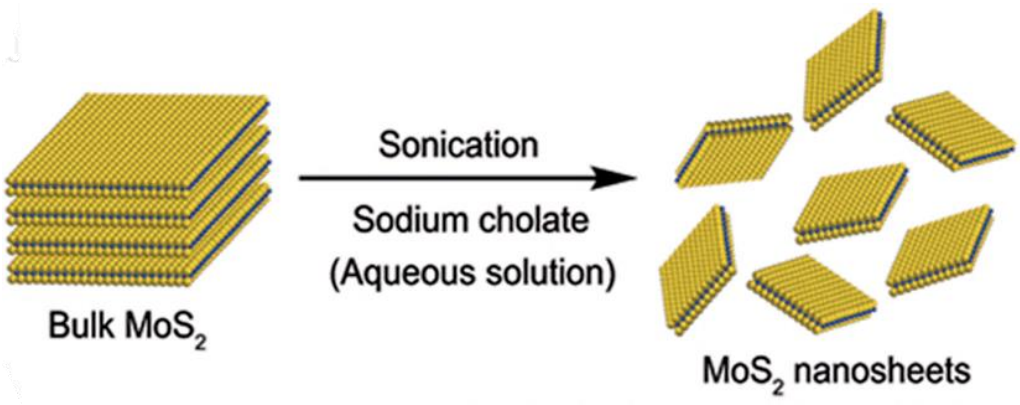

Figure 1 - 37 *Schematic of the liquid-phase exfoliation of MoS_2 bulk in presence of sodium cholate. Taken (adapted) from reference 251.*[251]

1.2.3.3 Surface Modification

As already mentioned, exfoliated MoS_2 materials have been used extensively in diverse research areas due to their extraordinary properties, which are often determined by the method of preparation. Tailoring colloidal stability, specific interactions and further reactivity of this layered material are typically obtained by surface modification. Chemical functionalisation at the surface of this 2-D material includes the interaction between a molecule and the unsaturated metal or chalcogen atoms at the edges, or defects of the basal plane.

Intrinsic and extrinsic defects such as vacancies, point defects, and grain boundaries on MoS_2 are inevitable during the production process. In this context, defects provide new opportunities to fine tune the physical and chemical properties of MoS_2. On this background, surface functionalisation of MoS_2 using sulphur vacancies and thiolated molecules has been reported.[227,252] Chou *et al.*[253] exploited the sulphur atom defect sites present on the exfoliated MoS_2 surface to attach diverse thiolated ligands, as shown in Figure 1 – 38. This allowed to modulate the ζ-potential and colloidal stability of MoS_2 layers, enabling its usage as selective protein receptor.

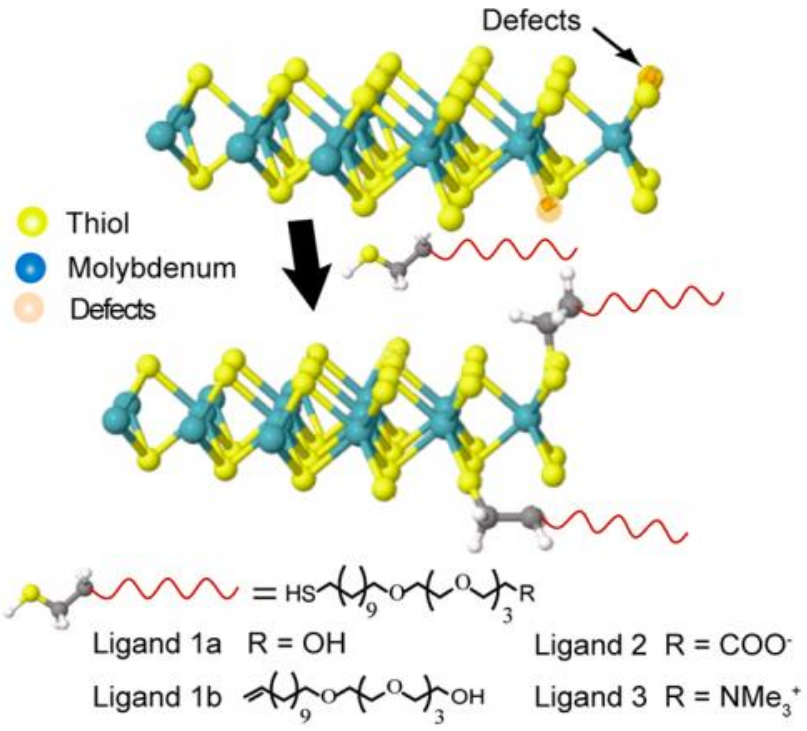

Figure 1 - 38 *Structural models showing functionalisation of MoS_2 with and thiolated ligand exploiting MoS_2 sulphur vacancies. Taken from reference 253.*[253]

Voiry *et al.*[232] describe a method for the covalent functionalisation of exfoliated MoS_2 by electron transfer between the negatively charged 1T MoS_2 surface and an electrophilic organohalide reactant. As shown in Figure 1 – 39, this results in chemical groups that are covalently attached to the S atoms. This attachment on MoS_2 surface changes the optoelectronic properties of the layered material. In particular, the authors demonstrated that the metallic 1T MoS_2 is now semiconducting and possess strong and tunable photoluminescence.

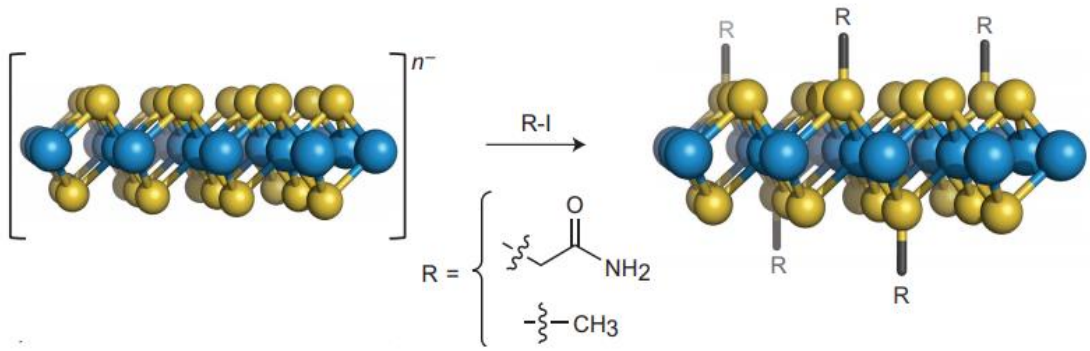

Figure 1 - 39 *Chemical functionalisation of 2H MoS_2 with organohalide reactant. Taken (adapted) from reference 232.*[232]

In a similar experiment, Knirsch et al.[254] functionalised MoS_2, exfoliated through lithium intercalation, with electrophilic aromatic diazonium salts, exploiting the negative charges presents on MoS_2 surface (Figure 1 – 40).

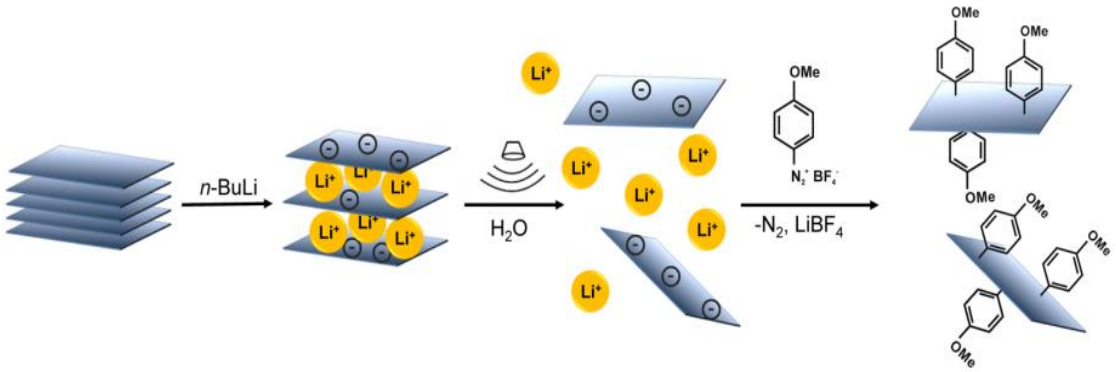

Figure 1 - 40 *Functionalization of n-BuLi-exfoliated MoS_2 with diazonium salt. Taken from reference 254.*[254]

In another work, Tuci *et al.*[255] efficiently decorated lithium-exfoliated MoS_2 with phenyl-azido groups, as shown in Figure 1 – 41. The presence of azido groups allowed, for the first time, the possibility to further functionalise MoS_2 surface through Cu-catalysed azide alkyne cycloaddition (CuAAC) "click" chemistry.

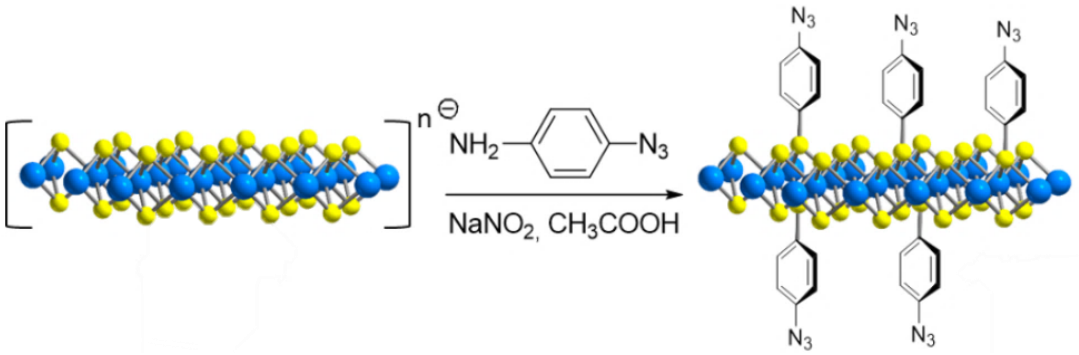

Figure 1 - 41 *Chemical Functionalization of lithium-exfoliated MoS_2 with aryl-azido groups. Taken (adapted) from reference 255.*[255]

The methods previously mentioned showed the chemical modification of 1T MoS_2. The first successful chemical functionalisation of 2H MoS_2 was reported by McDonald and co-workers.[256] They found that the reaction of liquid-exfoliated MoS_2 with different metal complexes led to the functionalisation of its surface, as shown in Figure 1 – 42. Functionalisation occurred through the coordination of the sulphur atoms on MoS_2 surface with the metal atom of the metal complexes, and the grade of functionalisation depends on the metal.

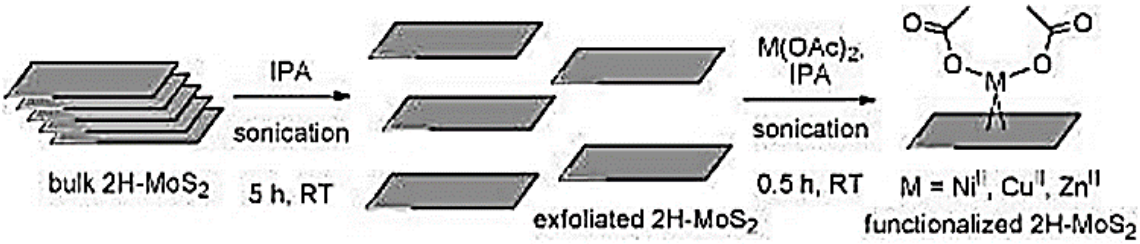

Figure 1 - 42 *Schematic representation of the and functionalization of 2H-MoS_2 metal complexes. Taken from reference 256.*[256]

Recently, Vera-Hidalgo *et al.*,[257] exploited the nucleophilic character of sulphur atoms to functionalise 2H-MoS_2 with maleimide derivatives at room temperature *via* Michael addition (Figure 1 – 43). This opens the doors to new ways to further chemically functionalise exfoliated MoS_2 surface, for example by thiol-Michael addition reaction.

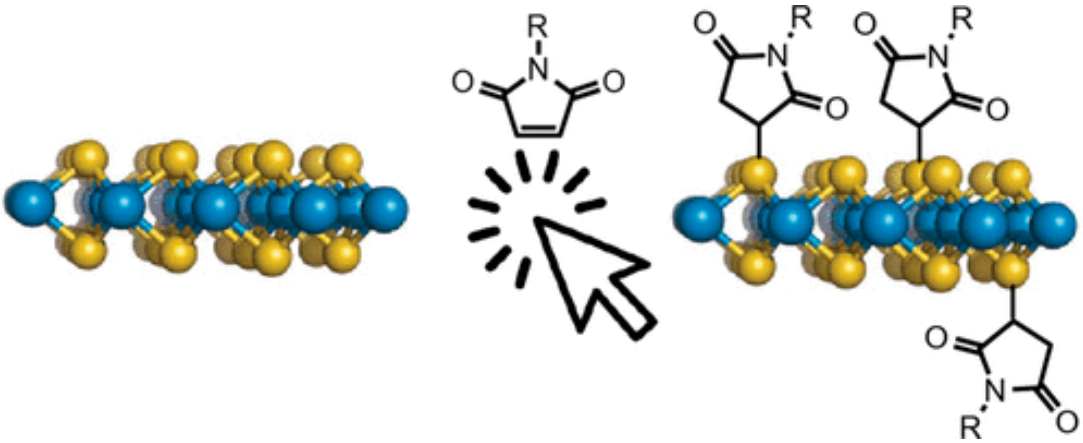

Figure 1 - 43 *General scheme for the functionalization of 2H-MoS_2 with maleimide derivatives. Taken from reference 257.*[257]

1.2.3.4 Layer-by-layer Assembly

Layer-by-layer (LbL) self-assembly is a versatile technique for fabricating multilayer nanomaterials with controlled architecture.[258–260] As previously mentioned, the tunable MoS_2 properties mainly depend on the numbers of layers, thus thickness control of exfoliated MoS_2 is fundamental in device fabrication and biological research.

The first successful fabrication of multi-layer MoS_2 architecture by layer-by-layer assembly was reported by Joo *et al*.[261] The assembled MoS_2 structure was obtained by subsequentially mixing a positively charged polymers and the negatively charged exfoliated MoS_2, followed by thermal treatment (Figure 1 – 44). The use of a polymeric spacer allowed to preserve the direct band gap of MoS_2 as well as to improve its photoluminescence properties.

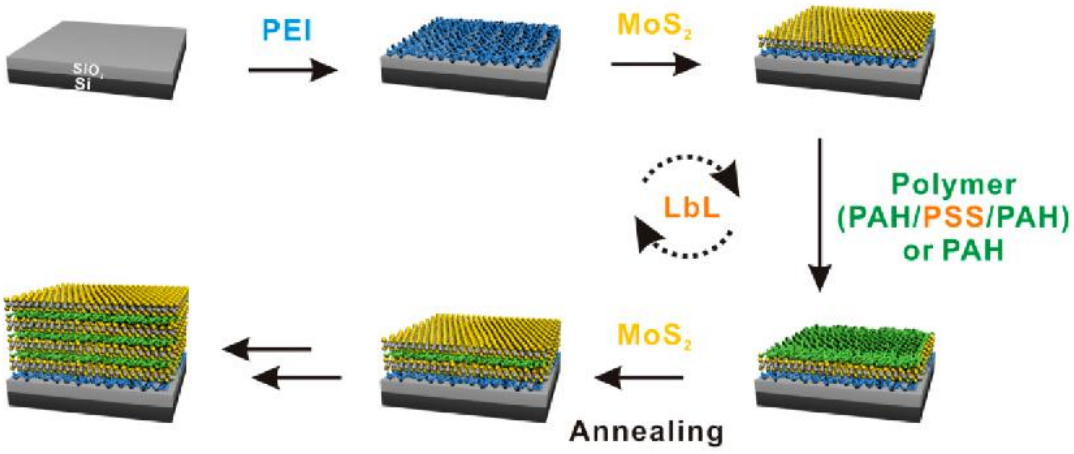

Figure 1 - 44 *Schematic representation of layer-by-layer assembly of MoS_2 with polymer spacings. Taken (adapted) from reference 261.*[261]

In another experiment, Ye and co-workers[262] directed the assembly of exfoliated MoS_2, functionalised with polyacrylic acid (PAA) and polyacrylamide (PAM), as shown in Figure 1 – 45. Multi-layered MoS_2 were produced by immersing in a positively charged solution of PDDA, first a negatively charged solution of PAA-functionalised MoS_2, then a positively charged solution of PAM-functionalised MoS_2, and ultimately a negatively charged solution of PEDT-PSS.

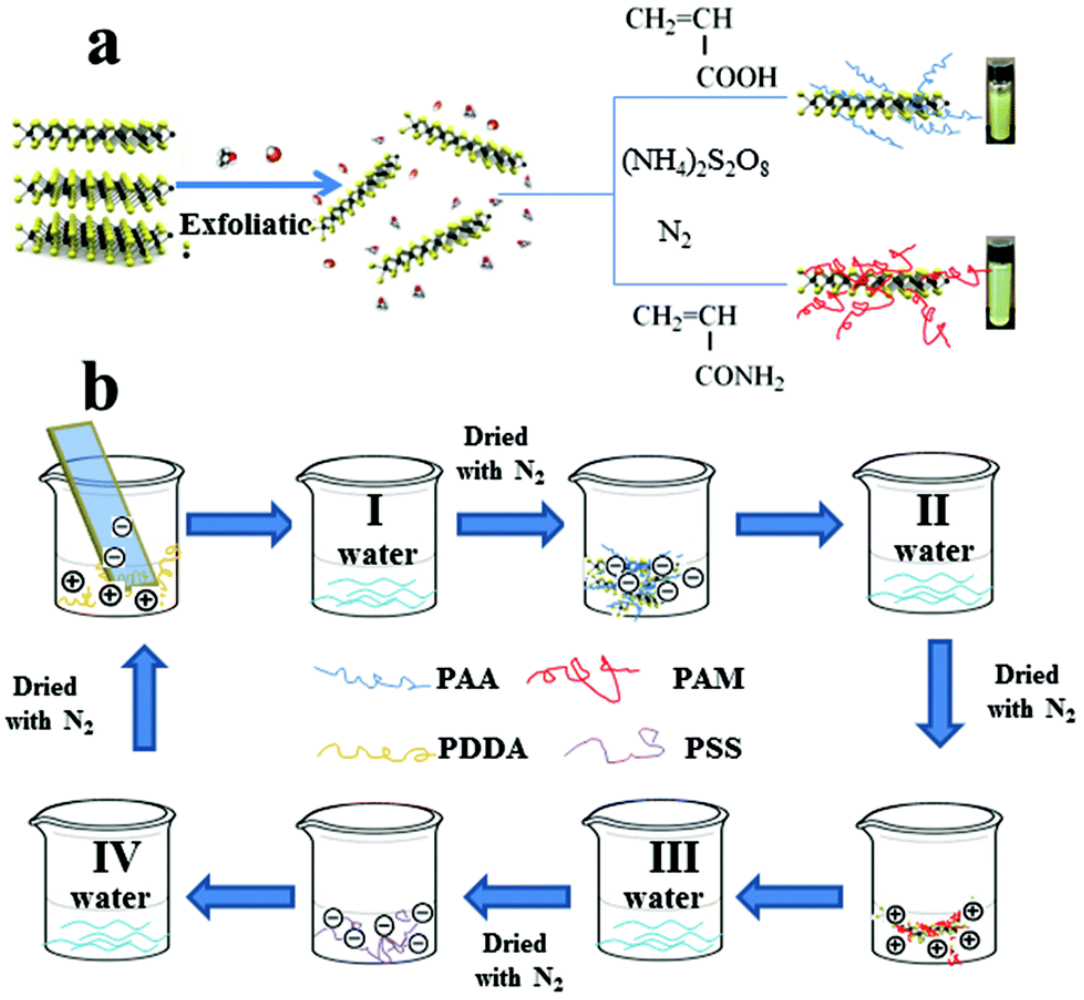

Figure 1 - 45 *(a) Preparation of PAA-MoS_2 and PAM-MoS_2; (b) Lbl assembly of MoS_2 films. Taken from reference 262.*[262]

Ushakov *et al.*[263] assembled liquid-phase exfoliated MoS_2 monolayers with alkyldiammonium ions in solution. The assembled MoS_2 architecture was formed exploiting the strong NH···S hydrogen bonding interactions and stabilised by the weaker but more numerous CH···S interactions, as shown in Figure 1 – 46.

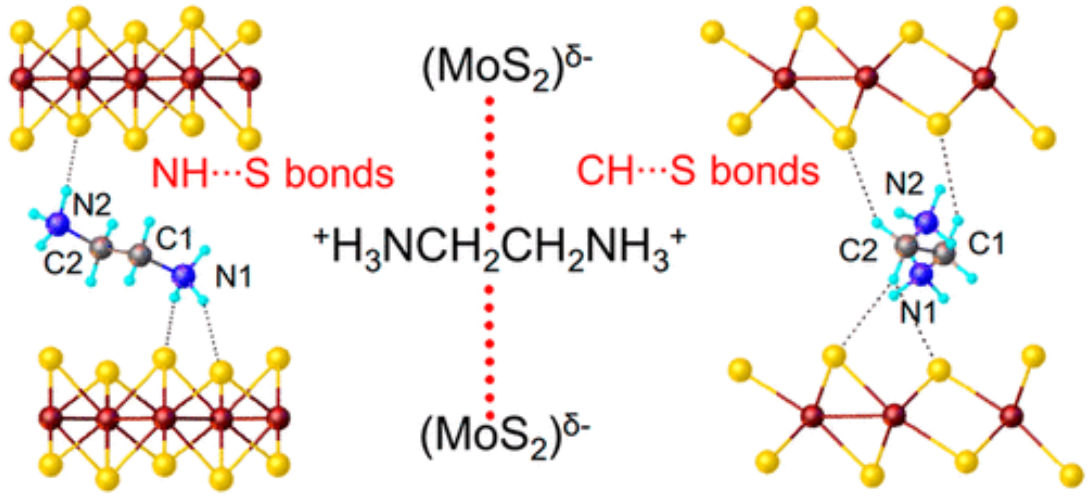

Figure 1 - 46 *Schematic of assembled MoS_2 monolayers with alkyldiammonium ion. Taken from reference 263.*[263]

In another work, Pramoda *et al.*[264] employed the Sonogashira coupling strategy to covalently assemble *n*-BuLi-exfoliated MoS_2 layers, enhancing their hydrogen evolution activity. This strategy is of particular interest since it also allowed to covalently link MoS_2 with reduced graphene oxide, displaying a high surface area and good CO_2 storage capacity (Figure 1 – 47).

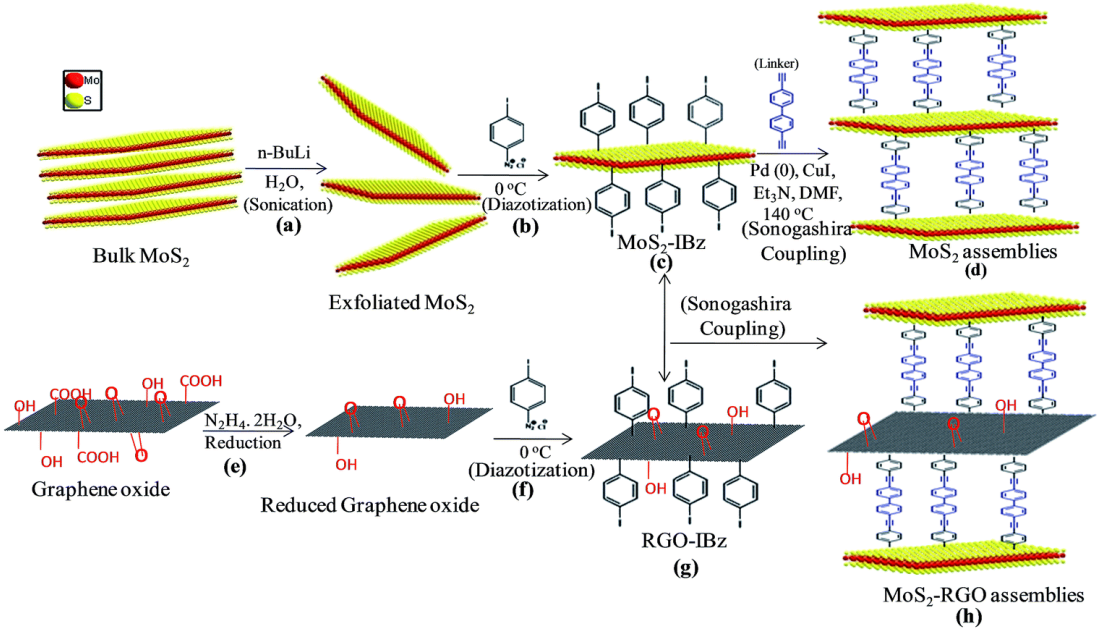

Figure 1 - 47 *Schematic representation of MoS_2 and MoS_2-RGO assemblies through Sonogashira coupling. Taken from reference 264.*[264]

It is fundamental to mention that the reversible assembly of exfoliated MoS_2 nanolayers opens new frontiers to smart MoS_2-based applications. In this regard, Leong and co-workers[265] linked DNA-functionalised MoS_2 *via* DNA hybridisation of the thiolated DNA oligonucleotides anchored on MoS_2 and an ATP aptamer, as shown in Figure 1 – 48. However, in the presence of target ATP molecules, the MoS_2 superstructure disassembled as a consequence of the stronger binding of ATP molecules with the linking aptamers.

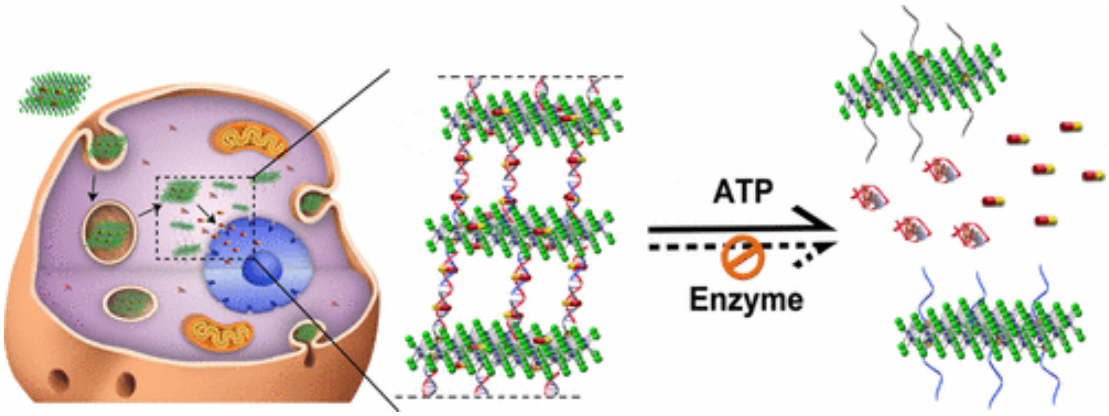

Figure 1 - 48 *ATP-induced disassembly of MoS_2 assemblies. Taken from reference 265.*[265]

1.3 Thesis Aims

This thesis is organised in three main sections, with the shared aim of controlling the self-assembly of 1-D and 2-D nanomaterials in aqueous solution. Optical and microscopy-based characterisation were used to verify the dispersion in solution of the nanomaterials and to confirm their assembly by length/height increment.

The first section focuses on single-walled carbon nanotubes (SWCNTs) and their non-covalent functionalisation *via* a DNA-wrapping strategy, which allows them to be dispersed in aqueous solution. Subsequently, the dispersed DNA-wrapped SWCNTs were separated by length through size-exclusion high-resolution chromatography and covalently functionalised with organic molecules at their terminal ends. This demonstrates how diverse chemical groups at the end of single walled carbon nanotubes can lead to the formation of static linear junctions, linking the nanotubes through covalent bonds.

In the second section, I present the covalent functionalisation of DNA-wrapped carbon nanotubes at their terminal ends with single stranded DNA oligonucleotides. By carefully designing the DNA sequences, it is possible to take advantage of the self-recognition properties of DNA and form carbon nanotubes junctions through non-covalent interaction. Indeed, the functionalisation of nanotubes with complementary DNA sequences at the SWCNT terminal ends forms linear nanotube junctions by DNA hybridisation. In addition, SWCNTs dynamic linear junctions have been obtained, exploiting the stimuli-responsive behaviour of specific DNA sequences. This allows to reversibly assemble and disassemble DNA-wrapped single-walled carbon nanotubes by changes in the environment.

In the last section, a similar strategy was applied to exfoliated TMDs materials to confirm the versatility of the approach. In particular, few-layer MoS_2 were obtained from the bulk material by its sonication in an aqueous sodium cholate solution. Liquid-phase exfoliated MoS_2 were then functionalised with DNA strands and layer-by-layer assembled by complementary base pairing. Finally, the disassembly of MoS_2 architecture was achieved by disrupting the DNA duplex forming the junction under different stimuli.

The last chapter of this thesis will draw the general conclusions of the work, summarising the main results obtained and outlining future challenges in the field.

CHAPTER 2: Materials and Methods

2.1 DNA OLIGOMERS

DNA sequences were designed with the help of "*NUPAK*" and "*IDT OligoAnalyzer 3,1*" online softwares. All DNA strands were purchased from IDT (Integrated DNA Technologies, Inc.). DNA strands were processed by desalted purification and functionalised DNA strands were processed by HPLC purification.

Table 1 *DNA strands (all sequences are reported from 5' to 3')*

(**GT**)$_{20}$	GTG TGT GTG TGT GTG TGT GTG TGT GTG TGT GTG TGT GTG T
(**1**)	TTT TTT TTT TTT CC CAA TCC CAA TCC CAA TCC C
(**1'**)	TTT TTT TTT TTT CAC AAT CAC AAT CAC AAT CAC AAA AAA AAA
(**2**)	TTT TTT TTT TTT GT GAT TGT GAT TGT GAT TGT G
(**3**)	Biotin- AAA AAA AAA AAA
(**4**)	IowaBlackFQ- AAA AAA AAA AAA
(**5**)	CAATCACA -Cy3
(**6**)	ACA AGA AAG CAA GCA AAT CAG ATA ACA GCC ATA TTA TTT ACC TGA GCC TGC TGC ATA
(**SD1**)	TGG TGG GAT TGG GAT TGG GTG GTA TA
(**SD2**)	TAT ACC ACC CAA TCC CAA TCC CAC CA
(**I**)	Amine- CAG GCT CAG G
(**II**)	Biotin- CCT GAG CCT G
(**III**)	Amine- TGC TAT GCA GCA GGC TCA GG
(**IV**)	Biotin- CCT GAG CCT GCT GCA TAG CA
(**V**)	Amine- TGC TAT GCA GCG GTC AAC TAC AGG CTC AGG
(**VI**)	Biotin- CCT GAG CCT GTA GTT GAC CGC TGC ATA GCA
(**VII**)	TGC TAT GCA GCG GTC AAC TAC AGG CTC AGG CTG GGT AAG GGT AAG GGT AAG GGT AA -Amine
(**VIII**)	TTA CCC TTA CCC TTA

2.2 CHEMICAL TECHNIQUES

2.2.1 SWCNT Oxidative Cutting *via* Acid Treatment

For the experiments, HiPco carbon nanotubes (Carbon Nanotechnologies Inc.), H_2SO_4 (95-98 wt %; SigmaAldrich) and HNO_3 (69 wt %; VWR) were employed to cut SWNTs into open-ended tubes. Generally, 8 mg SWCNTs were suspended into 10 mL of a 3:1 mixture of concentrated H_2SO_4/HNO_3 and sonicated in a water bath (Sonics, VC130PB) for 15 min at a power of 3W and a temperature of 30 °C. Then, the SWCNT suspension was collected on 0.1 µm centrifugal filters (Merck Millipore Ltd.), washed with DI water and allowed to dry.

2.2.2 DNA-wrapping SWCNT Procedure

Single-walled carbon nanotubes were dispersed in aqueous solution according to published DNA-wrapping procedure.[106] Typically, 1 mL solution containing HiPco nanotube (1 mg/mL), DNA oligomer $(GT)_{20}$ (1 mg/mL) and NaCl (0.1 M, Fisher Scientific™) was sonicated in an ice water bath for 90 min at a power of 3W. After sonication, the solution was divided into 0.1 mL aliquots, centrifuged for 90 min at 15,000 × g to remove insoluble materials, and the supernatant collected.

2.2.3 SWCNT Linear Junctions

2.2.3.1 Direct Amidation

Molecular junctions were obtained *via* amide bonds formation between the carboxylic functional groups present at the ends of DNA-wrapped SWCNTs and polyamine-terminated molecular linkers. Activation of SWCNT carboxyl groups in aqueous conditions was performed with the aid of coupling reagents in a buffer solution made with BupH™ 2-(N-morpholino) ethanesulfonic acid (MES) Buffered Saline Packs (ThermoScientific): 1-ethyl-3-[3-dimethylaminopropyl] carbodiimide hydrochloride (EDC, Sigma Aldrich) and N-hydroxysulfosuccinimide sodium salt (Sulfo-NHS, Sigma Aldrich). The activation of carboxylic groups by EDC is most efficient at acidic pH (pH= 4 – 5), and the Sulfo-NHS forms a more stable NHS ester with the acid for amidation reaction with primary amines. Then, the amidation reaction between the NHS ester and a polyamine-terminated linker is carried out with Dulbecco's phosphate buffered saline (DPBS) at physiological conditions, as shown in Figure 2 – 1.

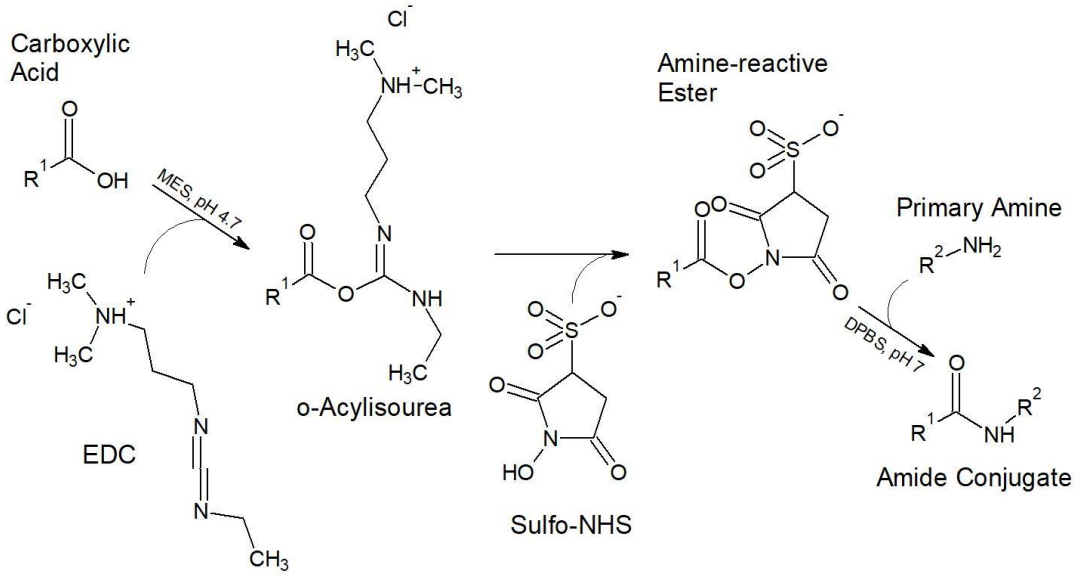

Figure 2 - 1 *Mechanism of amidation reaction activated by EDC and sulfo-NHS.*

In the experiment, the junction formation procedure follows that carried out by Palma *et al*.[123] Typically, DNA-wrapped SWCNTs solution was added in a 1:1 ratio to a pH= 4.7 MES buffer solution (0.2 M) containing EDC (4mM) and Sulfo-NHS (10mM). The resultant solution was shaken and incubated at room temperature for 30 minutes. Then, the solution was diluted with DPBS in a 1:1 ratio (final pH= 7.2) and left incubating for 1 hour. Finally, to form end-to-end SWCNT junctions, a solution containing a polyamino-linker (10nM) was added and incubated overnight. To increase linker coupling, a new solution of activated DNA-wrapped SWCNTs was subsequently added to the reaction mixture in 1:1 ratio and incubated overnight.

2.2.3.2 Copper-free Click Chemistry

An improvement of the amidation reaction to form SWCNT junctions relies on the use of "click" chemistry. The term click chemistry was introduced by K. B. Sharpless in 2001 to describe a class of biocompatible reactions commonly used in bioconjugation.[266] The classic click reaction is the copper-catalysed reaction (CuAAC), where Cu(I) can complex to a terminal alkyne and promote the reaction with an azide resulting in the formation of a 1,2,3-triazole. However, a strain promoted alkyne-azide cycloaddition can be employed to enable the formation of 1,2,3-triazole isomers as shown in Figure 2 – 2. This strain promoted alkyne-azide cycloaddition, also termed as the "Copper-free Click Chemistry" reaction, uses a ring strain-activated cyclooctyne molecule that exclusively and efficiently react with an azide.

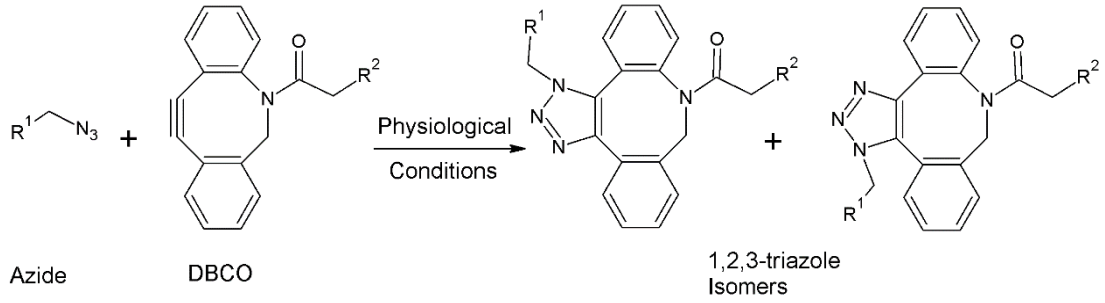

Figure 2 - 2 *Schematic representation of the Copper-free Click Chemistry reaction between an azide-molecule and a DBCO-molecule.*

In this work, 1,2,3-triazole linked SWCNTs were obtained by the reaction of SWCNT terminal-ends functionalised with cyclooctyne and azide functional groups, respectively. To introduce the appropriate biomolecules at the nanotube tips, the carboxylic defects present at the end of DNA-wrapped SWCNTs were exploited and reacted with amino-functionalised cyclooctynes or azide *via* amidation reaction as described in paragraph *2.2.3.1*. Then, cyclooctyne and azide functionalised SWCNTs were mixed 1:1 ratio and incubated overnight at physiological conditions. This allowed the formation of 1,2,3-triazole that linked SWCNT ends

2.2.3.3 DNA Hybridisation

Nitrene [2+1] Cycloaddition. To functionalise DNA-wrapped single-walled carbon nanotubes, 50 µL of DNA-wrapped SWCNTs solution were mixed with methanol (at a final volume of 1 mL) and divided into two equal aliquots. The first aliquot was mixed with (**1**) or (**1'**) 5'-azido-modified DNA strands (at a final concentration of 2 µM), the second with (**2**) 5'-azido-functionalised DNA strands (at a final concentration of 2 µM), and then both UV-irradiated for 10 min with a 400W medium pressure immersion mercury lamp (Photochemical Reactors Ltd). After irradiation, the free DNA in the samples was removed by 3 min centrifugation at 15,000 × g with centrifugal filters (Amicon Ultra 100 kDa, Millipore). The centrifugation process was then repeated three times and finally the samples were re-dispersed in 100 µL NaCl (0.1 M) solution.

DNA-linked SWCNT Junctions Formation. Samples (150µL volume) at pH= 7 were prepared as follows: 10 µL of (**1**)-functionalised or (**1'**)-functionalised SWCNTs and 10 µL of (**2**)-functionalised SWCNTs were mixed in a buffered solution (2 mM MOPS, Sigma-Aldrich, 400 mM NaCl, pH= 7) and incubated for 1 hour at room temperature.

SWCNT Junctions Labelling. 10 µL of the previously made (**1**)/(**2**)-linked SWCNT junctions solution and (**3**) (at a final concentration of 100 nM) were mixed and incubated for 1 hour at room temperature. Afterwards, the solution was drop-cast on mica (Agar Scientific) pre-treated with $MgCl_2$ solution and incubated for 10 min. Finally, 10 µL of streptavidin solution (500 nM, Invitrogen™) was deposited on the mica substrate, incubated for 10 minutes, rinsed with MilliQ water and blown-dried with compressed air.

pH-controlled Disassembly. 50 µL of the (**1**)/(**2**)-linked SWCNT junctions solution was acidified (pH= 5) by addition of acetic acid (10% vol/vol, VWR Chemicals) and incubated for 1 hour at room temperature.

SWCNT junctions disassembly *via* strand-displacement. 50µL of (**1**)/(**2**)-linked SWCNT junctions solution was mixed with 2µL of (**SD1**) (at a final concentration of 100 µM) and incubated for 1 hour at room temperature.

2.2.4 SWCNT-QD Nanohybrid Assembly

DNA-wrapped SWCNTs were functionalised dsDNA linkers bearing amino functional groups *via* amidation reaction as described in Paragraph 2.2.3.1. The (**I**)/(**II**), (**III**)/(**IV**) or (**V**)/(**VI**) dsDNAs were hybridised in DPBS at a concentration of 2.5×10^{-6} M. The dsDNAs were added in a tenth of the total reaction volume giving a final concentration of 250×10^{-9} M, and the solutions were shaken at room temperature overnight. Excess linker was removed by dialysis against 1 × TAE buffer with 0.1 M NaCl using Slide-A-Lyzer MINI Dialysis Devices with a 20 kDa cut-off (ThermoScientific). To conjugate QD to SWCNT, a solution of Qdot 585 Streptavidin Conjugate (100×10^{-9} M) was added to freshly dialysed SWCNT−DNA solution (10, 20, or 30 bp) to give a final concentration of 5×10^{-9} M. The reaction was shaken for 40 hours at room temperature in the absence of light. This QD concentration was found to be optimum for maximising the functionalisation of DNA-wrapped SWCNTs while minimising the number of free QDs in solution.

For the dynamic system, the partial (**VII**)/(**VIII**) dsDNA linker employed was attached to the ends of DNA-wrapped SWCNTs as for the 10, 20, and 30 bp DNA linkers. The QDs were conjugated with (**VI**) by mixing the QDs (100×10^{-9} M) and the DNA strands (10×10^{-6}M) in 1 × TAE with 0.1 M NaCl. This solution was placed in a polymerase chain reaction (PCR) machine (Hybaid PCR Sprint), heated to 47 °C and then cooled (at 0.1 °C per minute) to room temperature. The QD-DNA conjugates were filtered in Amicon Ultra-0.5 mL Centrifugal Filters (100 kDa cut-off) three times at 15,000 × g and mixed with the SWCNT-DNA solution (final QD concentration of ~ 5×10^{-9} M). The solution was then shaken at room temperature for 40 h in the absence of light. To contract or extend the SWCNT-QD distance, KCl (40×10^{-3} M) or Cryptand 222 (25×10^{-3} M) were respectively added: upon contraction of the structure due to the formation of the G quadruplex, DNA sequence (**VIII**) de-hybridised from (**VII**).

2.2.5 MoS_2 Liquid-phase Exfoliation

Exfoliated MoS_2 were obtained from the bulk material according to published liquid-phase exfoliation procedure.[265] Generally, 1mL aqueous solution containing bulk MoS_2 powder (5 mg/mL; Sigma-Aldrich) and sodium cholate (1.5 mg/mL; Sigma-Aldrich) was sonicated for 24 hours at a power of 3W. After sonication, the black dispersion was centrifuged at 3,000 × g and the yellow supernatant collected. The supernatant was then centrifuged at 4,000 × g and the sediments were re-dispersed in 1 mL of deionized water. This washing process was repeated three times in order to remove the sodium cholate absorbed on MoS_2 surface.

2.2.6 DNA-functionalisation of MoS_2 Nanosheets

5'-thiolated DNA oligos ordered from IDT are shipped in their oxidised form and require a reduction process to remove the protecting group before their use. The reducing process employed is a TCEP (Tris[2-carboxyethyl] phosphine) treatment, which consists in incubating for two hours an aqueous solution containing 10 mM TCEP and 100 µM thiolated DNA oligos at room temperature.

To functionalise the MoS_2 surface with thiol-modified DNA, 20 µL of exfoliated MoS_2 solution were mixed with 2 µL of 5'-thiolated DNA strands solution (100 µM) and diluted into 200 µL of buffer solution (1 × TAE; Invitrogen™). The resulting solution was then sonicated for 1 min and incubated for 5 h at room temperature. To remove the excess of DNA, the solution was then centrifuged at 4,000 × g for 30 min and the sediments re-dispersed in 100 µL of deionized water.

2.2.7 LbL Assembly of Exfoliated MoS_2

Static Junctions Formation. Equal amounts of (**1'**)-functionalised exfoliated MoS_2 and (**2**)-functionalised exfoliated MoS_2 solutions were combined in a buffer solution, containing MOPS (2mM) and NaCl (400mM). The mixture was then incubated and gently shaken for 1 h.

Dynamic Junctions Formation. To drive the Layer-by-layer assembly of the exfoliated MoS_2, a pH= 8 solution, containing 2mM MOPS, 400 mM NaCl, and equal amounts of (**1**)-functionalised exfoliated MoS_2 and (**2**)-functionalised exfoliated MoS_2, was incubated and shaken for 1 h. To induce the acidic pH-stimulated disassembly, the pH of the solution was changed from 8 to 5.5 by adding 1 mM HCl and incubated for 30 min at room temperature. The disassembly *via* strand displacement mechanism was achieved by adding (**SD1**) DNA strands solution at a final concentration of 30 µM.

2.3 SIZE-EXCLUSION HIGH-PERFORMANCE LIQUID CHROMATOGRAPHY

Size-exclusion high-performance liquid chromatography is a chromatographic method that allows to separate polydisperse solutes by their size at isocratic condition. As previously mentioned in the paragraph *1.1.3.2*, SEC-HPLC is a powerful analytical technique that allows to separate DNA-wrapped SWCNTs by their length.

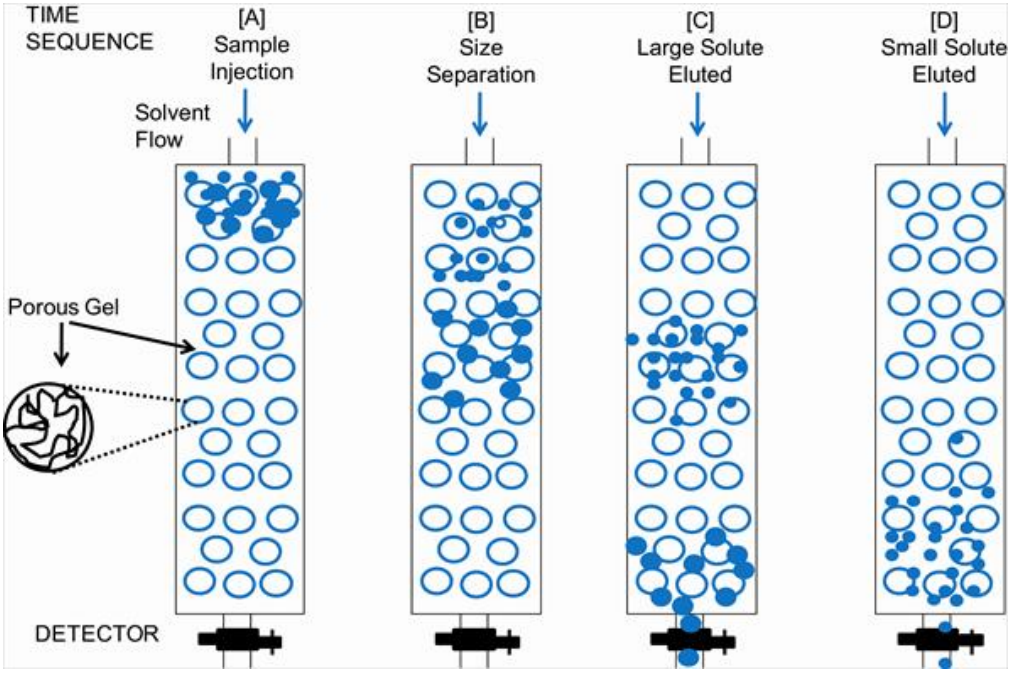

Figure 2 - 3 *Schematic mechanism of SEC-HPLC separation. [A] Sample is injected into the column and forced by a high-pressure solvent flow through the column. [B] As the sample flows through the column, solute is separated by size. [C] Large solute do not interact with the medium and is eluted first, while [D] small solute is trapped into the pores and eluted later. Finally, the solute eluted is analysed by an inline UV-Vis absorption detector and collected. Taken from mychem.ir*

A good visual aid to understand the separation mechanism in SEC-HPLC is shown in Figure 2 – 3. In a typical separation process, the medium, a porous and inert gel matrix of spherical particles, is tightly packed into a hollow column to form a packed bed. The medium is chosen for its lack of reactivity and adsorptive properties toward the sample. A solvent travels down the column at high pressure. The liquid inside the pores, stationary phase, is in equilibrium with the liquid outside the spherical particles, mobile phase. The sample is then injected and forced by the mobile phase through the column. Large solute particles are eluted more quickly than small solute particles. Indeed, smaller solute particles penetrate every region of the mobile phase and are trapped into the pores, while larger solute particles pass through the column

because too large to enter into as many pores. Therefore, as the sample travels down the column, the solute is separated by size and eluted isocratically. Finally, the eluent is collected in constant volumes, known as fractions. More similar the eluted particles are in size, more likely they are in the same fraction. The use of an inline UV-Vis absorption detector allows to determine the concentration of the eluted particles. For a solute, the time from injection to detection is named retention time and it is a measure of the time taken to flow through the chromatography column. The visual output of the detector is termed chromatogram and monitors the signal in the detector over retention time. In the case of an optimal SEC-HPLC separation, different peaks on the chromatogram correspond to different fractions of the separated sample.

In this work, the separation of DNA-wrapped SWCNTs follows an enhanced procedure to that carried out by Huang *et al*.[117] In the experiments, a 1.5 mL seat capillary (Agilent Technologies) and three columns (Sepax technologies, Inc) connected in series, with pore size of 2000 Å, 1000 Å and 300 Å respectively, were mounted on a HPLC system (Agilent 1100 Series). The surface functional groups of the medium, 5 µm silica beads, are negatively charged to prevent the adsorption by the phosphate groups of DNA. In a typical run, 300 µL of DNA-wrapped SWCNTs solution were eluted with a pH= 8 buffer solution, containing MOPS (10 mM) and NaCl (0.2 M), at a flow rate of 0.25 mL/min. Eluent, containing only length sorted DNA-wrapped single-walled carbon nanotubes, was collected from min 33 to min 44 retention time at 0.25 mL/ fraction and stored at room temperature.

2.4 MICROSCOPY TECHNIQUES

2.4.1 Atomic Force Microscopy

Atomic force microscopy (AFM) was developed in 1986 by Binning *et al.*[267] to investigate the surface of samples with low electrical conductivity. It is a very high-resolution scanning probe microscopy (SPM), with resolution on the order of a nanometre.[268] The information is gathered by moving a sharp tip, attached to the end of a spring-like cantilever, with a radius usually ~10 nm over the surface of the sample. A precision positioning device, usually made of a piezoelectric tube, is used to move the sample or the tip. When the probe tip is brought sufficiently close to the sample surface, the forces between the tip and the sample surface cause up and down motions of the cantilever in line with the Hooke's law. Indeed, according to the Hooke's law, the applied force (F_s) equals a constant (k) times, that depends on the material and dimensions of the cantilever, the motion of the cantilever in length (x), as stated by the following formula:

$$\boldsymbol{F_s = kx}$$

By monitoring the warping of the cantilever, it is possible to map surface morphology, as shown in Figure 2 – 4. Cantilever deflections are monitored by using a laser beam that is targeted on the back of the cantilever and reflected by a mirror onto a position-sensitive photo detector. Thus, the motion of the cantilever is directly proportional to the output of the detector. It is the change in positions of the beam in the sensor that allows the mapping of sample surface. A feedback control is commonly introduced to maintain the tip in a "fixed relationship" with the surface during the scan.

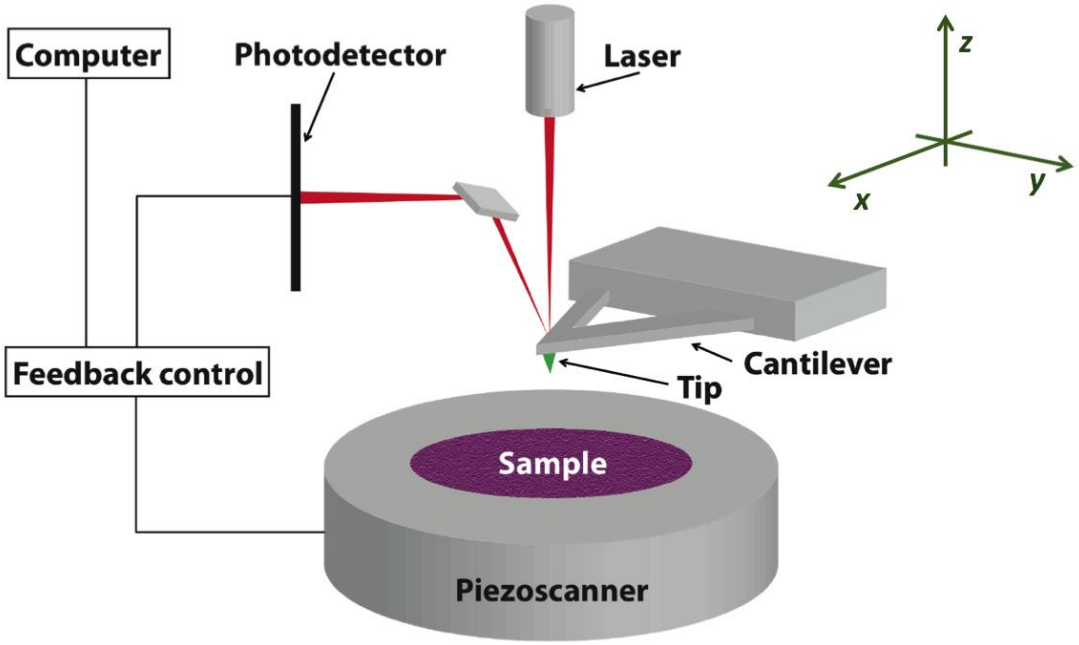

Figure 2 - 4 *Schematic diagram of the principles of an AFM. A probe sharp tip is fixed to the free end of a flexible cantilever. Optionally, a piezoelectric element oscillates the cantilever. The sample is mounted on a stage scanner. The scanner is composed of three piezo components, which control the x, y, and z directions of the sample. The photodetector records the deflection and motion of the cantilever by means of a reflected laser beam from a laser source. Taken from amyhallr.wordpress.com*

The overall interactions between the probe tip and the sample surface can be estimated as van der Waals and repulsive forces. These interactions can be explained by the Lennard – Jones potential:

$$\boldsymbol{U(d) = 4\varepsilon\left[\left(\frac{\sigma}{d}\right)^{12} - \left(\frac{\sigma}{d}\right)^{6}\right]}$$

Where U is the intermolecular potential between two molecules or atoms; ε is the depth of potential well; d is the inter-atomic distance between particles (tip-sample distance); σ is the distance at which the potential is zero; the term proportional to $(1/d)^{12}$ describes the Pauli repulsion at short distances; and the attractive term proportional to $(1/d)^{6}$ dominates at long distance and it models the van der Waals forces (induced dipole, dipole-dipole and permanent-induced dipole interactions).

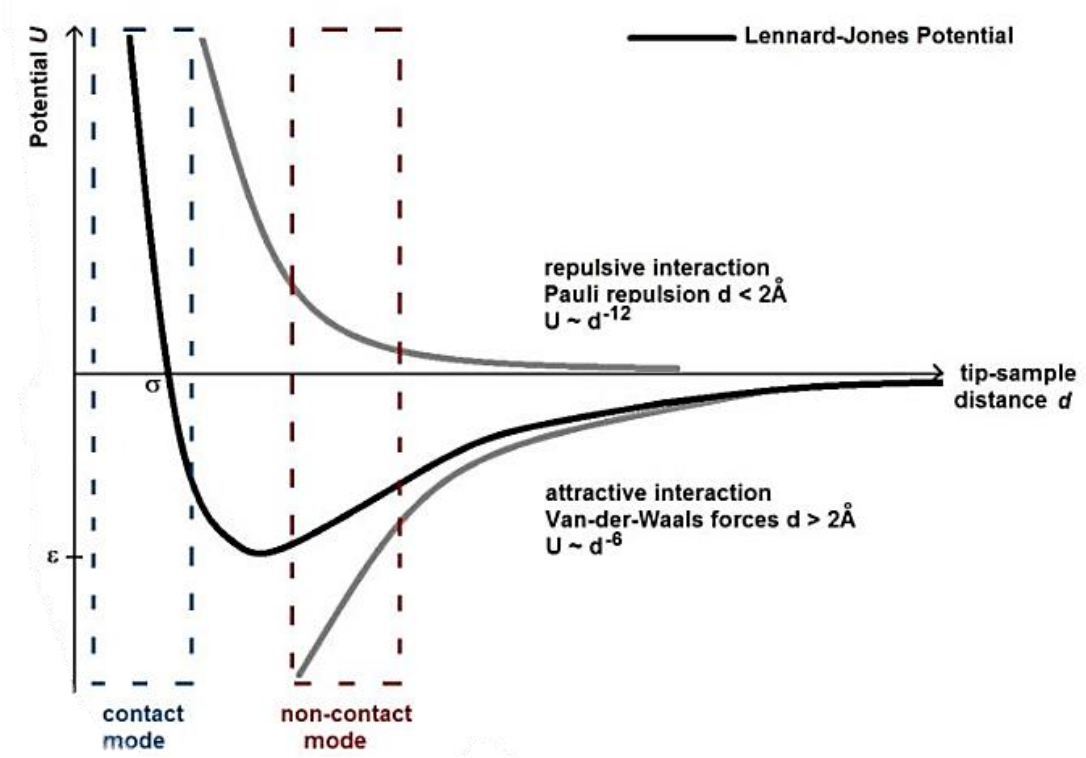

Figure 2 - 5 *Lennard-Jones potential and AFM modes: contact (blue) and non-contact (red). Taken (adapted) from reference 269.*[269]

Figure 2 – 5 displays the relationship between tip-sample forces and distance. The graphic shows two important distance regimes, repulsive and attractive, where different interactions dominate: at small distance (d < 2 Å), a strong repulsive interaction appears due to the overlapping orbitals between the tip and the sample ; as the tip moves away from the sample (d > 2 Å), attractive interaction predominates.

According to the two distance regimes, three main different AFM modes can be described:

- In contact mode, the probe tip is kept in direct contact with the sample surface (repulsive regime). Although this mode is suitable for obtaining high-resolution images, the friction force may cause problems for stable imaging.
- Non-contact mode is employed to measure weak attractive forces between the tip and the sample surface. It does not suffer from tip or sample damage, sometimes observed in contact mode, and makes non-contact mode suitable for the imaging of soft samples, e.g. biological samples and organic thin film.
- Tapping mode is a combination of both contact and non-contact modes, and the AFM tip oscillates at or just below its resonant frequency, while the tip is scanning the surface. Taking advantage from the oscillating contact, this mode acquires an improved lateral resolution compared to non-contact mode, without damaging soft sample surface as contact mode.

PeakForce Tapping, with ScanAsyst image optimisation software, is the method of imaging used in this work. It operates similarly to tapping mode, by intermittently contacting the sample surface, but the probe tip oscillates well below its resonance frequency. This allows to precisely control the probe-to-sample interaction. The enhanced force control results in the highest resolution AFM imaging for a wider range of samples compared to normal tapping mode.

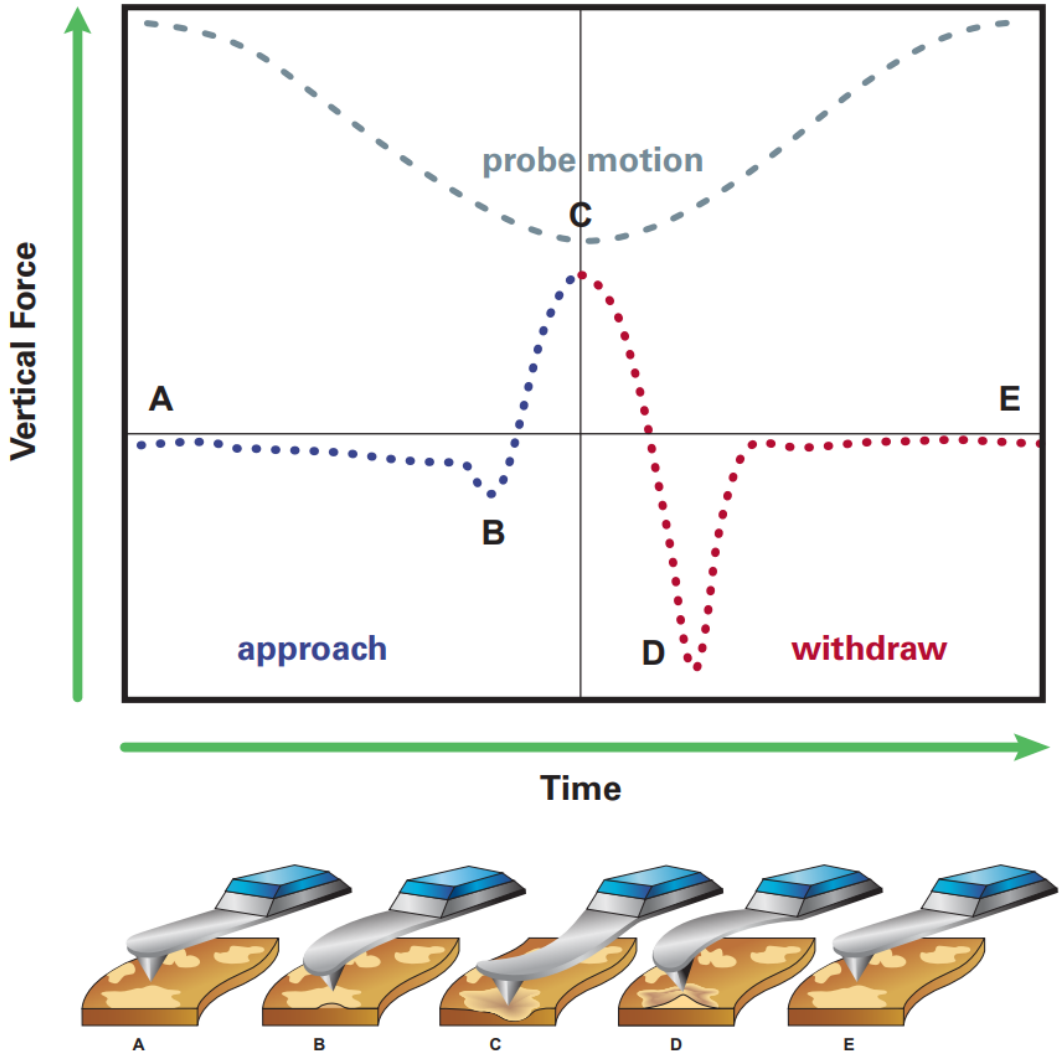

Figure 2 - 6 *Force diagram and schematic of AFM tip deflections in PeakForce Tapping. Taken from Bruker.*

Figure 2 – 6 shows the force versus time diagram and the schematic of when the probe tip interacts with the sample: the top curve describes the probe motion; and the latter represents the forces measured during the approach (blue) and the withdrawal (red) of the probe to the sample surface. In particular, when the probe tip is well distant from the surface, there is no interaction (A). As the probe approaches the sample, the cantilever is deflected toward the sample surface due to the attractive forces (B) and the tip is in contact with the surface until the repulsive forces lead to the peak point at the approaching curve (C). When the probe tip starts to withdraw, the force decreases until it reaches an adhesion minimum (D), usually due to capillary meniscus. Finally, the tip becomes free and far distant from the sample surface (E).

AFM imaging was carried out on a Bruker Dimension Icon system, with a NanoScope IV control unit (Figure 2 – 7). Air measurements were conducted with silicon nitride ScanAsyst probe tips, with a spring constant of 0.4 N/m from Bruke. AFM images were analysed with NanoScope Analysis (version 1.5, Bruker) software.

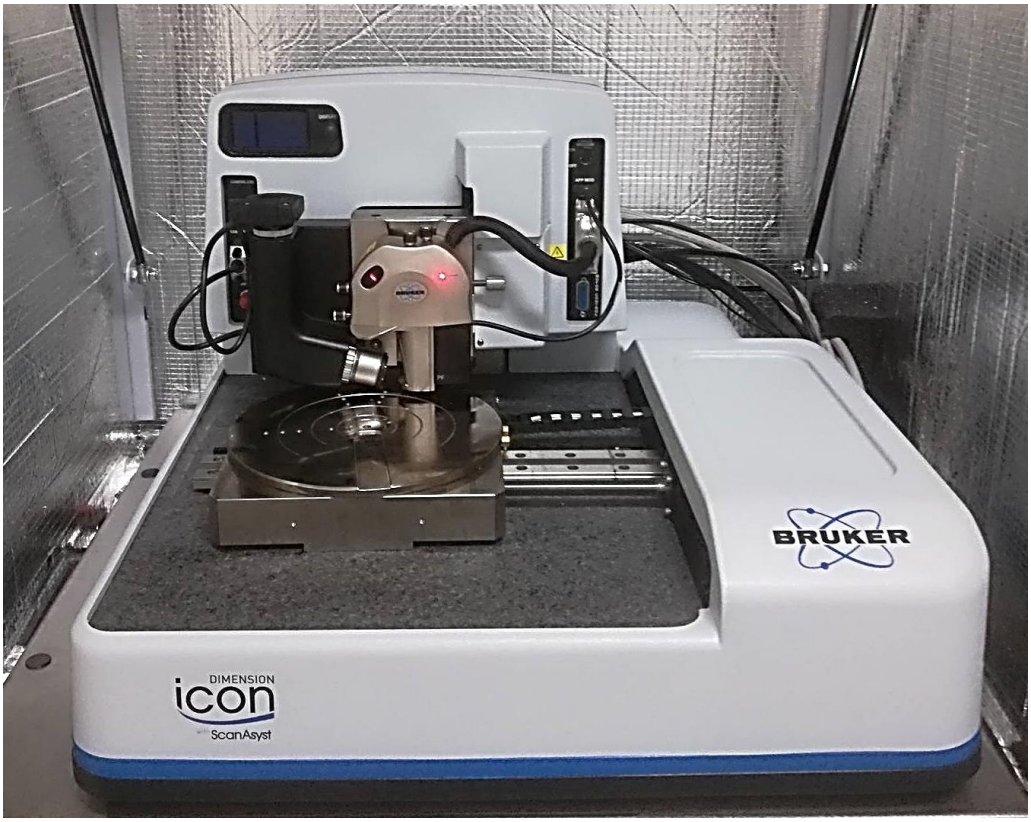

Figure 2 - 7 *Image of the Bruker Dimension Icon AFM system of "The Palma Group".*

2.4.2 Transmission Electron Microscopy

The first transmission electron microscopy (TEM) was demonstrated by Ernst Ruska and his mentor Max Knoll at the Berlin Technische Hochschule in 1931. However, the first commercial TEM was produced in 1939, and Ruska was awarded the Nobel Prize in physics in 1986 for its invention.[270] TEM is a type of microscopy that uses a high energy beam of electrons as a source of illumination. A TEM image is generated from the interaction of the electrons and a very thin sample as the electron beam transmits through. Since the de Broglie wavelength of electrons is smaller than the wavelength of photons, the resolution for TEM images is greater than that from a light microscope.

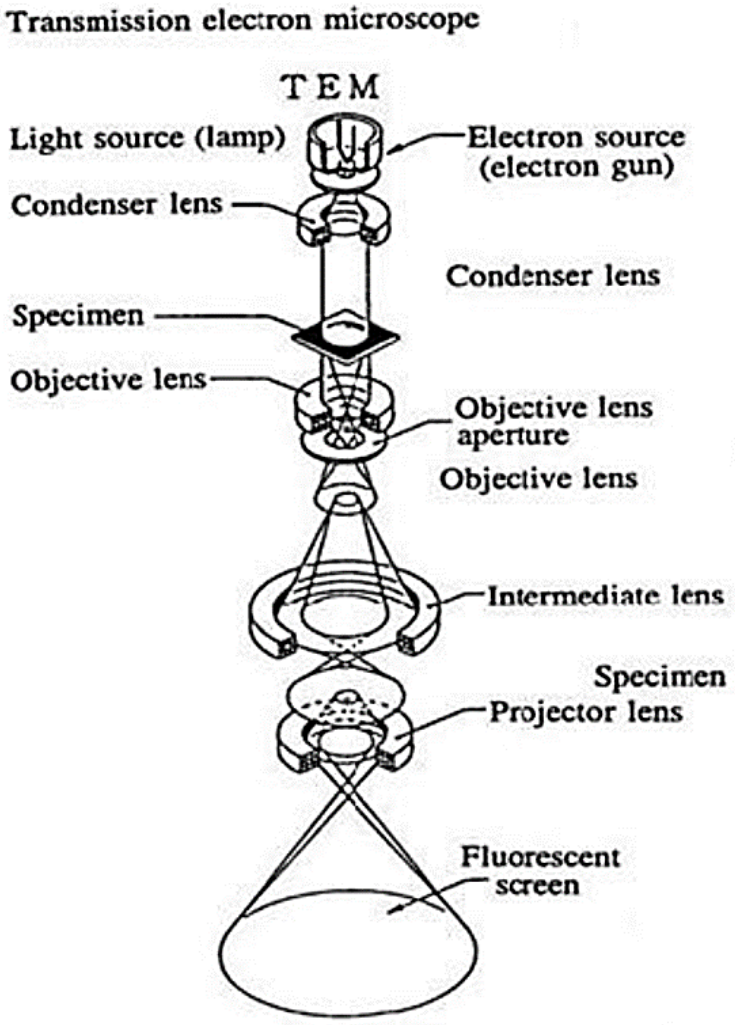

Figure 2 - 8 *A schematic diagram of the transmission electron microscope. Taken from JEOL 2000FX Handbook*

Figure 2 – 8 describes the general principle of TEM imaging. An electron gun generates a beam of electrons, which is focused into a thin and coherent beam by condenser lens. The electron beam is then restricted by a condenser aperture, excluding high angle electrons, hit the specimen and part of it is transmitted through. Generally, the specimen is an ultrathin section less than 100 nm thick or a suspension on a customised grid. The transmitted part is focused by objective lens into an image. Objective apertures can be employed to enhanced the contrast by blocking out high-angle diffracted electrons from forming the image. Finally, the image is magnified by intermediate and projector lens and focused on a fluorescent screen. As some regions of the sample can absorb or scatter electrons, fewer electrons are transmitted and appear darker in a TEM image. Heavier atoms scatter electrons more intensely than lighter atoms, thus the areas with heavier atoms are the darker ones.

TEM imaging of the samples was carried out by Qingyu Ye, PhD student in the group of Dr Matteo Palma, on a Jeol JEM 1230 TEM equipped with a 200 kV field emission gun, a Morada CCD camera and iTEM software.

2.5 SPECTROSCOPIC TECHNIQUES

2.5.1 Ultraviolet-Visible Spectroscopy

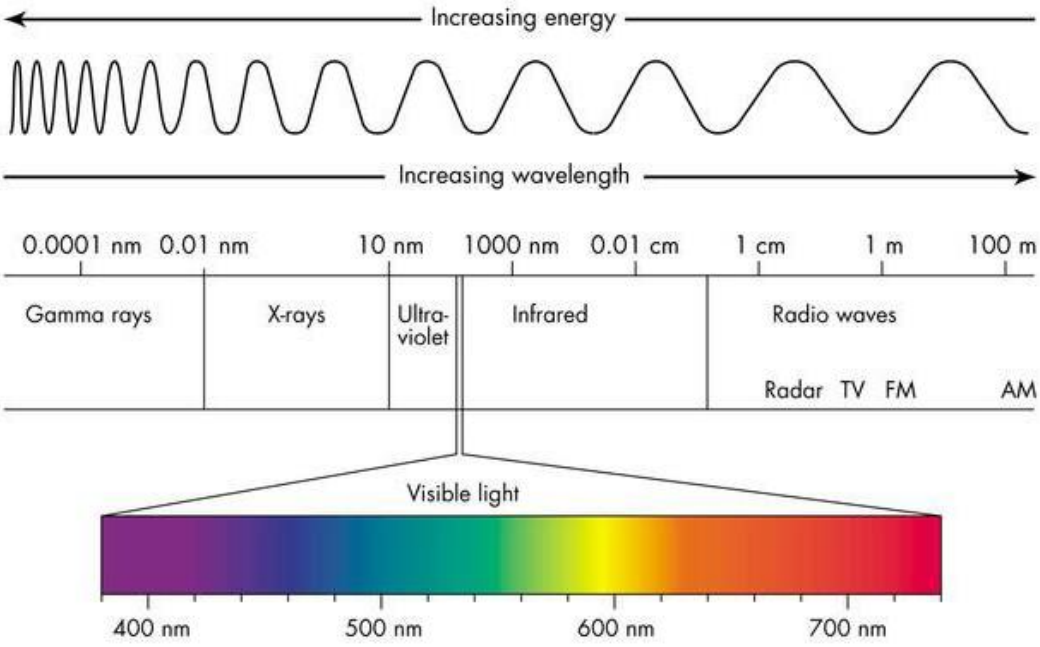

Figure 2 - 9 *Electromagnetic spectrum. Taken from Cyberphysics.*

The electromagnetic spectrum in Figure 2 – 9 shows the range of energies of electromagnetic radiation and their respective wavelengths and frequencies. The energy associated with a given segment of the spectrum is proportional to its frequency, as follow:

$$\boldsymbol{E = h\nu} \quad \text{with} \quad \boldsymbol{\nu} = {}^{\boldsymbol{c}}/_{\boldsymbol{\lambda}}$$

Where *E* is energy, *h* is the Planck's constant (6.6×10^{-34} J·s), *v* is the frequency, *c* is the velocity of light (3×10^{8} m/s) and λ is the wavelength.

When an atom absorbs light, one of its electrons can be excited to a higher energy state. This movement of an electron from a lower energy level to a higher energy level, or vice versa, is called electronic transition. In order for a transition to occur, the energy of the photon absorbed must be equal (or greater) to the energy difference between the two levels. There are four possible types of transitions: π–π*, n–π*, σ–σ*, and n–σ*, as shown in Figure 2 – 10.

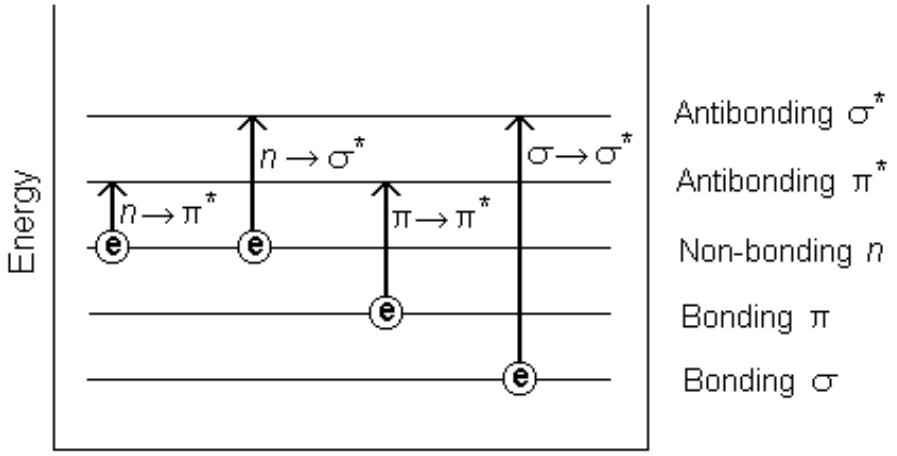

Figure 2 - 10 *Possible electronic transitions of p, s, and n electrons. Taken from Sheffield Hallam University.*

The absorption of a radiation by a substance is called absorbance and obeys to the Beer-Lambert law:

$$\boldsymbol{A = \varepsilon c l}$$

Where *A* is the absorbance, *ε* is a constant known as molar extinction coefficient and it is an intrinsic property of the substance, c is the molar concentration of the species and *l* is the optical path length.

Ultraviolet-Visible (UV-Vis) spectroscopy is a quantitative technique in which light is absorbed by a sample. Despite being named UV-Vis, the wavelength range that is generally used ranges from 190-380 nm (near ultra-violet) to 380-740 nm (visible) to 740-1,100 nm (near-infrared). UV-Vis spectroscopy measures the transmitted intensity of light passing through the sample, I, and compares it to the intensity of incident light at a given wavelength before it passes through the sample, I_0. The ratio I/I_0 is called transmittance, *T*, and it is expressed as a percentage.

The absorbance of a substance is related to the transmittance through the following relation:

$$A = log_{10} \frac{I_0}{I} = -log_{10} T$$

In a typical UV-Vis spectroscopy analysis (Figure 2 – 11), the light emitted by the light source passes through a monochromator, which produces a monochromatic radiation by removing unwanted wavelengths. The monochromator comprises an entrance slit, a collimator mirror, a diffraction grating, a condenser mirror, and an exit slit. When the monochromatic light hit the sample cell, a part of the light is absorbed by the sample. In a single beam instrument, all of the light passes through the sample chamber and the remaining unabsorbed light reaches the detector. Conversely, in a double-beam instrument, the light is split into two beams before it reaches the sample: one beam is used as the reference, while the other beam passes through the sample. When the light reaches the detector, it is converted into an electrical signal.

Optical absorption measurements of samples were carried out on a Cary 100 UV-Visible Spectrophotometer from Agilent Technologies.

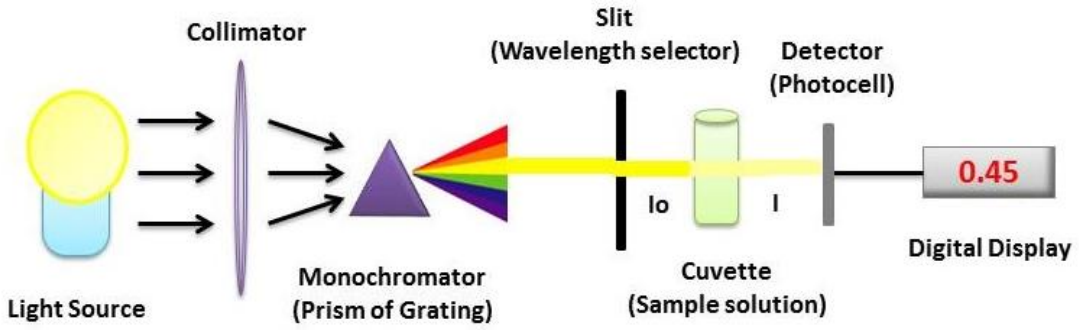

Figure 2 - 11 *Schematic of UV-Vis spectroscopy analysis. Taken from BiochemDen.com*

2.5.2 Fluorescence Spectroscopy

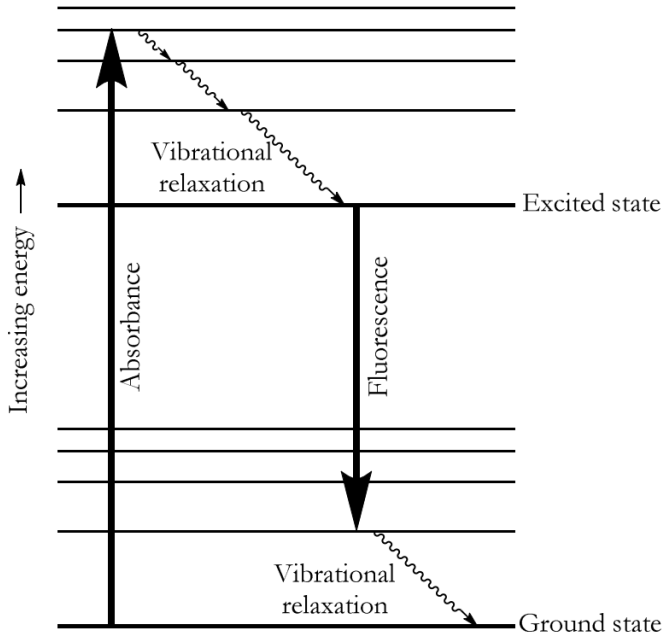

Figure 2 - 12 *Jablonski diagram showing the fluorescence process. The diagram is read from left to right: absorbance, vibrational relaxation and then fluorescence. Taken from the University of Colorado Boulder.*

Fluorescence is a complementary technique to UV-Vis absorption, since absorption is a requirement for the fluorescence process. The physics underlying the fluorescence process is illustrated by the Jablonski diagram in Figure 2 – 12. As mentioned in the previous paragraph, when a substance absorbs a photon, an electron may be excited to a higher energy state, if the energy of the photon absorbed is equal (or greater) to the energy difference between the two states. However, in addition to the electronic orbital levels, a small amount of energy is intended for vibrational sublevels, above each electronic state. Generally, excited electrons relax rapidly to the lowest vibrational sublevel of the excited electronic state. This non-radiative process is called "vibrational relaxation" and causes thermal energy loss. Finally, the electron may drop back to one of the vibrational sublevels of the ground state, emitting a photon with energy equivalent to the energy difference of the transition. Therefore, fluorescence results in the emission of a photon with lower energy than the absorbed photon.

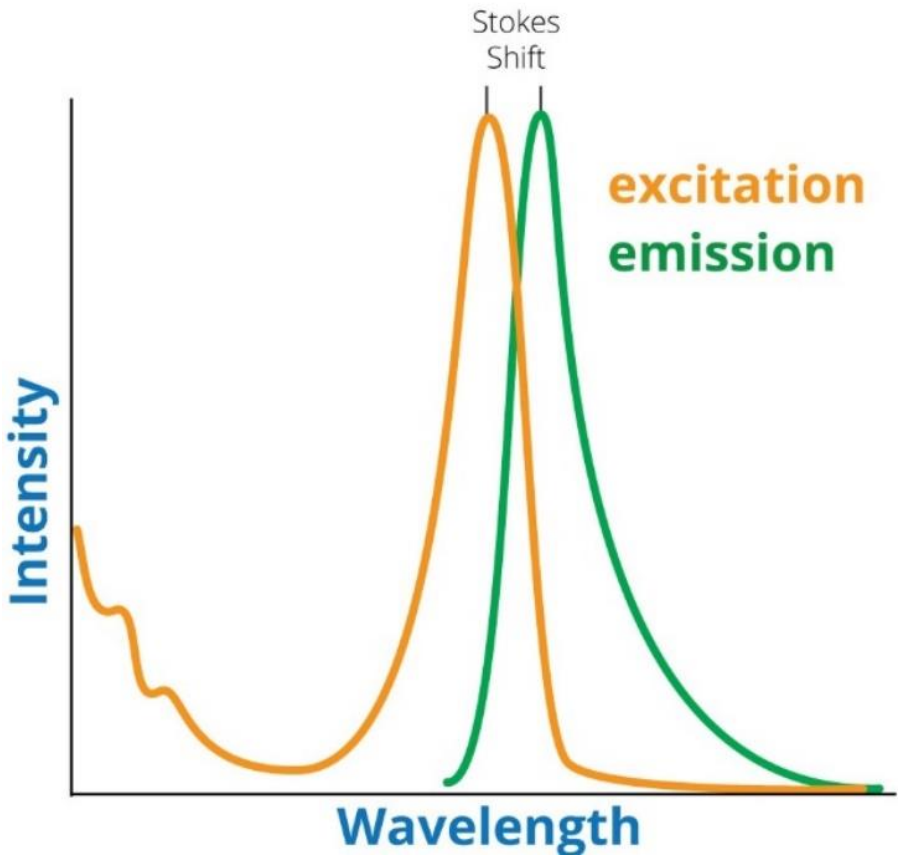

Figure 2 - 13 *Typical excitation-emission diagram, showing in yellow the absorbance spectrum of a substance at shorter wavelength (higher energy) and in green the resultant fluorescence spectrum at longer wavelength (lower energy). Peak intensity and/or wavelength of these two spectra may change with temperature, pH, concentration, and interactions with other molecules. This includes quenchers and molecules that involve an energy transfer. Taken from World Precision Instruments.*

The difference in energy or wavelength of the two photons is called Stokes shift. Figure 2 – 13 shows the Stokes shift between the absorbance spectrum of a substance at shorter wavelength and the resultant fluorescence spectrum at longer wavelength. It is important to note that not all substances electronically excited fluoresce; some just decay to ground state with emission of heat.

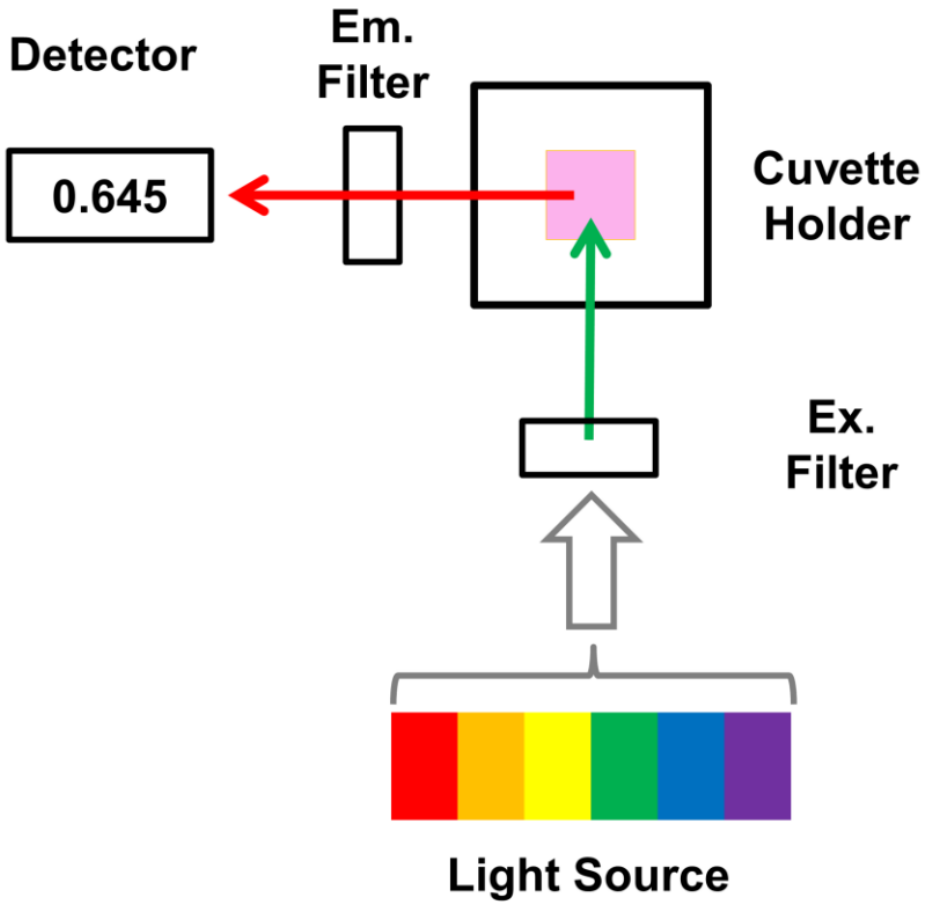

Figure 2 - 14 *A simplistic design of fluorescence analysis. Taken from the OPN Lab created by John Giannini and Chris Stewart.*

Figure 2 – 14 shows a schematic diagram of fluorescence spectroscopy. A high-powered light source transmits light that passes through a filter or monochromator, and hit the sample. A proportion of the incident light is absorbed by the sample and light is emitted in all directions through a fluorescence process. Some of this fluorescent light passes through a second filter or monochromator and reaches a detector. The detector is placed at 90° to the incident light beam to avoid that transmitted or reflected incident light reaches the detector.

Time-dependent fluorescence experiments were performed on an Agilent Cary Eclipse Fluorescence Spectrometer.

Samples (150µL volume) were prepared as follow:

- *Time-dependent fluorescence investigation of pH-switch system*
  10µL of (**1**)-functionalised SWCNTs and 10µL of (**2**)-functionalised SWCNTs were mixed with (**4**)-functionalised IowaBlackFQ (final concentration = 700 nM) and (**5**)-functionalised Cy3 (final concentration = 100 nM) in a pH 7 buffered solution (2 mM MOPS and 300 mM NaCl), and incubated for 1 hour at room temperature. Then, the solution was transferred into a plastic cuvette, the fluorophore (Cy3) excited at 520 nm and the emission signal collected at 562 nm. The temperature was set and maintained at 20°C throughout the whole analysis. The pH of the solution was switched between 5 and 7 by sequential additions of 0.6 µL acetic acid (10% vol/vol) or 0.75 µL of ammonia solution (1M, Sigma-Aldrich).
- *Time-dependent fluorescence investigation of strand-displacement system*
  10 µL of (**1**)-functionalised SWCNTs and 10 µL of (**2**)-functionalised SWCNTs were mixed with (**4**)-functionalised IowaBlackFQ (final concentration = 700 nM) and (**5**)-functionalised Cy3 (final concentration = 100 nM) in a pH 7 buffered solution (2 mM MOPS and 400 mM NaCl), and incubated for 1 hour at room temperature. As for the pH-switch system, the fluorophore (Cy3) was excited at 520 nm into a plastic cuvette and the emission signal collected at 562 nm. The strand-displacement was carried out by sequential additions of (**SD1**) and (**SD2**) at a final concentration of 2 µM.
- *Time-dependent fluorescence control experiment of pH-switch system in the absence of SWCNTs*
  DNA strands (**1**) and (**2**) (both at final concentration of 30 nM) were mixed with (**4**)-functionalised IowaBlackFQ (final concentration = 700 nM) and (**5**) (final concentration = 100 nM) in a pH 7 buffered solution (2 mM MOPS and 300 mM NaCl), and incubated for 1 hour at room temperature. The solution was then transferred into a plastic cuvette, the fluorophore (Cy3) excited at 520 nm and the emission signal collected at 562 nm. The temperature was set and maintained at 20°C throughout the whole analysis. The pH of the solution was switched

between 5 and 7 by sequential additions of 0.6 µL acetic acid (10% vol/vol) or 0.75 µL of ammonia solution (1M, Sigma-Aldrich).

- *Time-dependent fluorescence control experiment of strand-displacement system in the absence of SWCNTs*

  DNA strands (**1**) and (**2**) (both at final concentration of 30 nM) were mixed with (**4**)-functionalised IowaBlackFQ (at a final concentration of 700 nM) and (**5**)-functionalised Cy3 (at a final concentration of 100 nM) in a pH 7 buffered solution (2 mM MOPS and 400 mM NaCl), and incubated for 1 hour at room temperature. Similar as previously described for the pH-switch system, the fluorophore (Cy3) was excited at 520 nm into a plastic cuvette and the emission signal collected at 562 nm. The strand-displacement was carried out by sequential additions of (**SD1**) and (**SD2**) at a final concentration of 2 µM.

2.5.3 Raman Spectroscopy

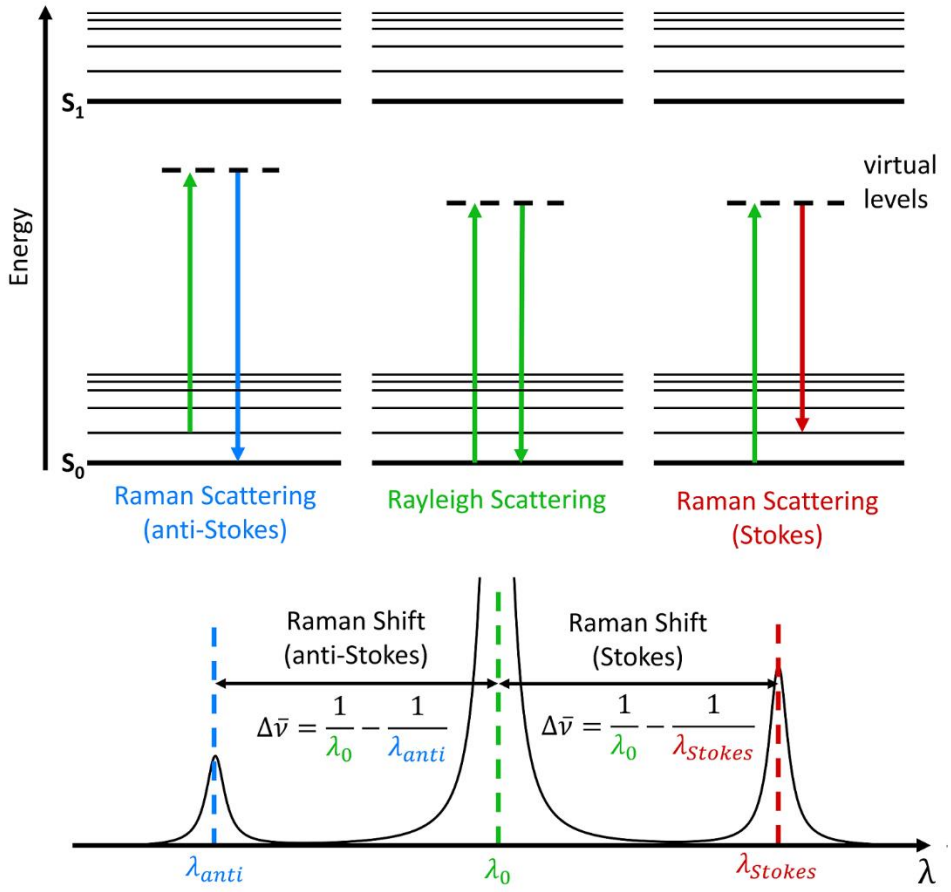

Figure 2 - 15 *Schematic of Rayleigh (green), Stokes (red) and Anti-Stokes (blue) Raman Scattering. Taken from Edinburgh Instrument.*

When light interacts with a substance, it may be absorbed, reflected or scattered. In a scattering process, light energy is absorbed, leaving the molecule in a "virtual" higher state. However, this virtual state is not stable and the photon is re-emitted. Most of the photons are scattered at the same energy, and therefore the same wavelength of the incident light: this process is termed elastic scattering or Rayleigh scattering (Figure 2 – 15). Conversely, about 10^{-7} of the light is scattered at a different energy than the incident light: this process is called inelastic scattering, or the Raman scattering.

The difference between the energy of the incident photon and the energy of the scattered photon is the called the Raman shift, and it is reported in wavenumbers (reciprocal of the wavelength). Raman shift ($\Delta\tilde{\nu}$) is calculated through the following equation, in which λ_0 is the excitation wavelength and λ_s the scattered wavelength:

$$\Delta\tilde{\nu} = \frac{1}{\lambda_0} - \frac{1}{\lambda_s}$$

If the molecule gains energy from the photon when relaxing, the molecule is excited to a higher vibrational level and the energy of the scattered photon is less than that of the incident photon: this is called Stokes Raman scattering. A small number of molecules are already in a higher vibrational level when interact with light and can relax to a lower vibrational level, losing energy; in this case, the scattered photon gains the corresponding energy, resulting in higher energy than that of the incident photon: this is named Anti-Stokes Raman scattering.

Raman spectroscopy was named after the physicist C. V. Raman who first observed Raman scattering in 1928 and won the Nobel prize in Physics in 1930 for its discovery.[271] It is a non-destructive technique where the scattered light is used to measures the energy gap between the vibrational energy states of a sample. In a general Raman spectrum, the peak position provides a unique chemical and structural "fingerprint", which can be used to identify a substance, and the peak intensity is directly proportional to the material concentration. However, calibration is necessary to determine the relationship between peak intensity and concentration.

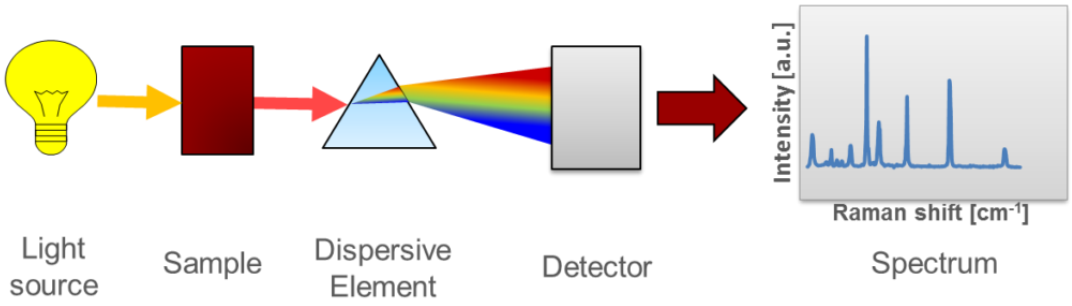

Figure 2 - 16 *Schematic of the measurement principle of a Raman spectroscopy measurement. Taken from Anton Paar.*

In a typical Raman spectroscopy analysis (Figure 2 – 16), a monochromatic light beam, generated by a laser as light source with wavelengths in the visible to near-infrared range, hit the sample. After interaction of the incident light with the sample, the light is scattered in all the directions. The inelastically scattered light is then directed to a dispersive element and separated into different wavelengths. Finally, the dispersed light is analysed by a detector.

Raman analysis of the samples was carried out on a Renishaw inVia confocal Raman microscope. Raman spectra were measured using 442 nm laser line.

2.6 Samples Deposition

For AFM imaging, muscovite mica discs (1 cm diameter; Agar Scientific) were cleaved three times with adhesive tape. Then, 100 µl of an aqueous solution of $MgCl_2$ (1 M; Sigma Aldrich) were drop-cast on the substrate, subsequently wicked with a Kimwipe and blown dry with compressed air. For carbon nanotube samples, 10 µl of 100 times diluted SWCNT solution were drop-cast on mica disc, covered, and incubated for 20 min. For MoS_2 samples, 20 µL of sample solutions were drop-cast on freshly cleaved muscovite mica discs, covered and incubated for 30 min. Finally, the mica discs were rinsed with MilliQ water and dried gently with compressed air.

For TEM imaging, 10 µL of MoS_2 solution were drop-cast on a Holey Carbon Films 400 Mesh Copper Grid (Agar Scientific Ltd) and air-dried at room temperature in a clean fume hood.

For Raman analysis, 2 µL of MoS_2 sample solution were drop-cast on clean silicon wafers (Silicon Quest International, Inc) and allowed to dry under air at room temperature.

2.7 Statistical Analysis

SWCNT length distributions and MoS_2 lateral size were obtained by image-J 1.51j8 software. MoS_2 thickness analysis were obtained by NanoScope Analysis 1.5 software. Histograms and Lognormal curve fitting were generated by OriginPro 2015 (V b9.2.257).

CHAPTER 3: SWCNT Static Linear Junctions

As mentioned in Chapter 1, carbon nanotubes are of (nano)technological interest because of their nanoscale diameter and notable properties.[272,273] The construction of SWCNT junctions[120,123,124,274,275] has been widely explored for the fabrication of nano-electronic devices,[276–278] including their use as nano-electrodes in molecular transport junctions and single molecule investigations.[124,126,279–283] Different methods have been investigated for carbon nanotube junction formation;[123,274,275,284] in this context, the controlled assembly of SWCNT linear (end-to-end) junctions through solution-processable approaches[122–124,285,286] is particularly desirable for the low-cost fabrication[287–289] of SWCNT-based devices.[281,283]

In this chapter, we present a facile bottom-up approach for the in-solution assembly of individual SWCNTs through the formation of static linear junctions. The single-walled carbon nanotubes employed in this study underwent a mild acid treatment and were dispersed in aqueous solution *via* a DNA-wrapping strategy, which also protects the nanotube sidewall; SWCNT dispersion was confirmed by UV-Vis spectroscopy analysis and AFM imaging. DNA-wrapped SWCNTs were then separated by means of SEC-HPLC to yield populations of tubes with well-defined length; this also allows to remove free DNA in solution. To quantify carbon nanotube length distribution in the fractions, DNA-wrapped SWCNTs were deposited on mica substrates and imaged with an atomic force microscope, and the nanotube length was then directly measured. To direct the end-to-end assembly of SWCNTs, chemical reactions were programmed to occur specifically at the carboxylic defects present on SWCNT tips. In particular, di-, tri- and tetra-amino molecular linkers were used for the formation of static linear junctions *via* direct amidation reactions. Junction formation was confirmed by comparing the length of the assembled DNA-wrapped SWCNTs with that of the nanotubes sorted by size-exclusion chromatography.

In addition, we propose an improvement over the direct amidation linking strategy by means of strain-promoted cycloaddition reactions. In this case, two separate batches of DNA-wrapped single-walled carbon nanotubes, from the same fraction, were first in-solution end-functionalised with amino-cyclooctyne and amino-azide molecules, respectively, *via* amide bond formation. This led to the functionalisation of SWCNT ends with cyclooctyne and azido functional groups, respectively. The two solutions were then mixed and SWCNT static linear junctions were obtained by the formation of 1,2,3-triazole molecules that covalently join SWCNT tips.

Finally, as proof of concept, reconfigurable SWCNT/QD hybrids were obtained by using DNA as molecular linker. Here, the SWCNT/QD distance was varied by exploiting the ability of particular DNA sequences able to respond to changes in the environment. Specifically, the formation of G-quadruplex DNA structure allowed to shorten the SWCNT/QD distance in the hybrids, resulting in PL intensity variation.

3.1 DISPERSION AND LENGTH SORTING OF SWCNTs

3.1.1 DNA-wrapping strategy

HiPco single-walled carbon nanotubes were used in this study and dispersed in aqueous sodium chloride solutions *via* DNA-wrapping procedure.[107] This resulted in a homogeneous black aqueous solution of SWCNTs as shown in Figure 3 – 1. The non-covalent wrapping of ssDNA around the carbon nanotube allows the dispersion of the nanotubes in bio-compatible aqueous solutions as well as the protection of nanotube side-wall, leaving their tips available for further functionalisation. The successful dispersion of SWCNTs was verified spectroscopically, and through morphological characterisation.

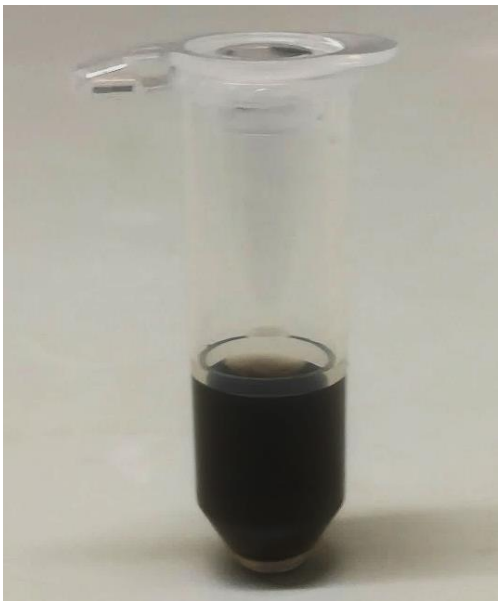

Figure 3 - 1 *Black solution containing DNA-wrapped HiPco SWCNTs.*

Figure 3 – 2 shows the UV-Vis-NIR absorption spectrum of DNA-wrapped HiPco SWCNTs solution diluted 50 times with DI water. The absorption spectrum of SWCNTs usually contains distinct peaks in the dispersion because diverse SWCNT chiralities express peaks at different wavelengths that correspond to an electronic transition. Since HiPco nanotubes contain many different chiralities, the spectrum is a superposition of absorption spectra of different (*n*,*m*)-SWCNTs. The broad peak at around 260 nm is the characteristic absorbance peak of DNA.

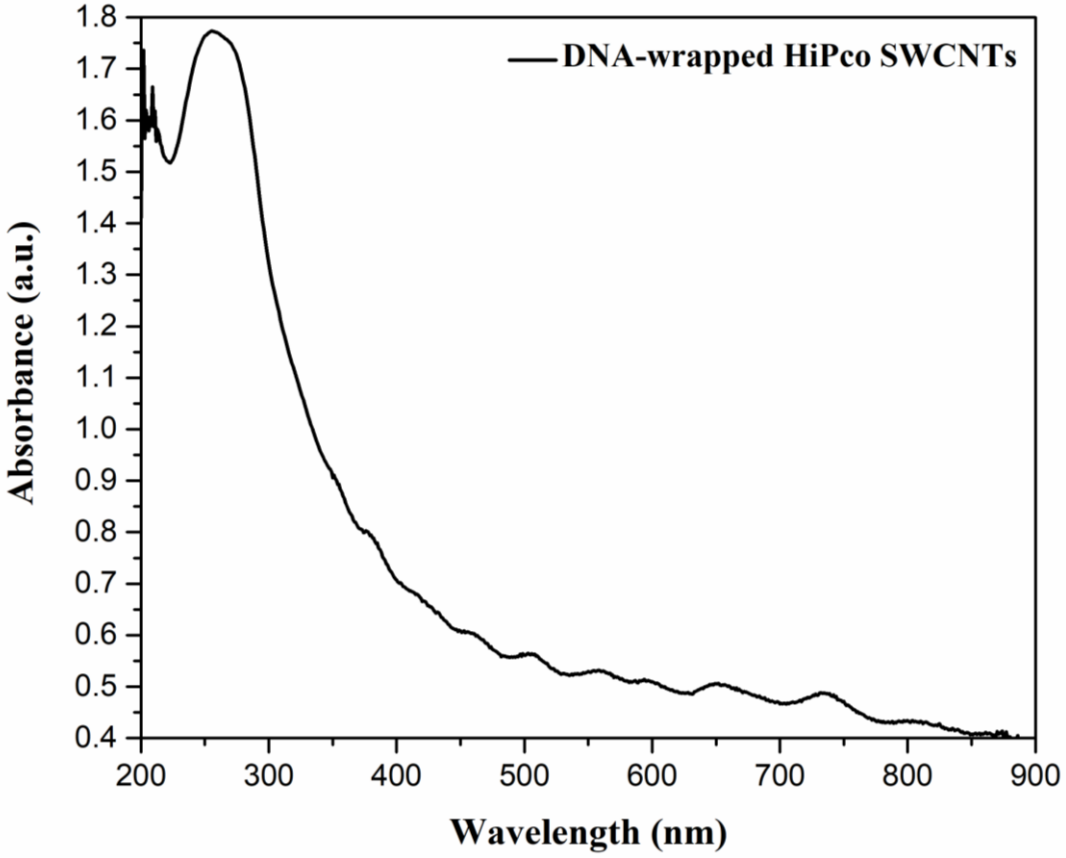

Figure 3 - 2 *Absorption spectrum of HiPco single-walled carbon nanotubes dispersed with ssDNA as dispersant. HiPco SWCNTs contain a mix chiralities, and the spectrum is a superposition of absorption spectra of different chiral-nanotubes. The broad peak at ~260 nm corresponds to the absorbance peak of DNA.*

AFM imaging for the DNA-wrapped HiPco SWCNTs also confirms nanotube dispersion and indicates that the sample exhibits a tube-like structure. The sample does not show a uniform length distribution for DNA-wrapped SWCNTs. However, the helical wrapping of the nanotubes with DNA further enables the separation of SWCNTs by length *via* size-exclusion high-performance liquid chromatography.

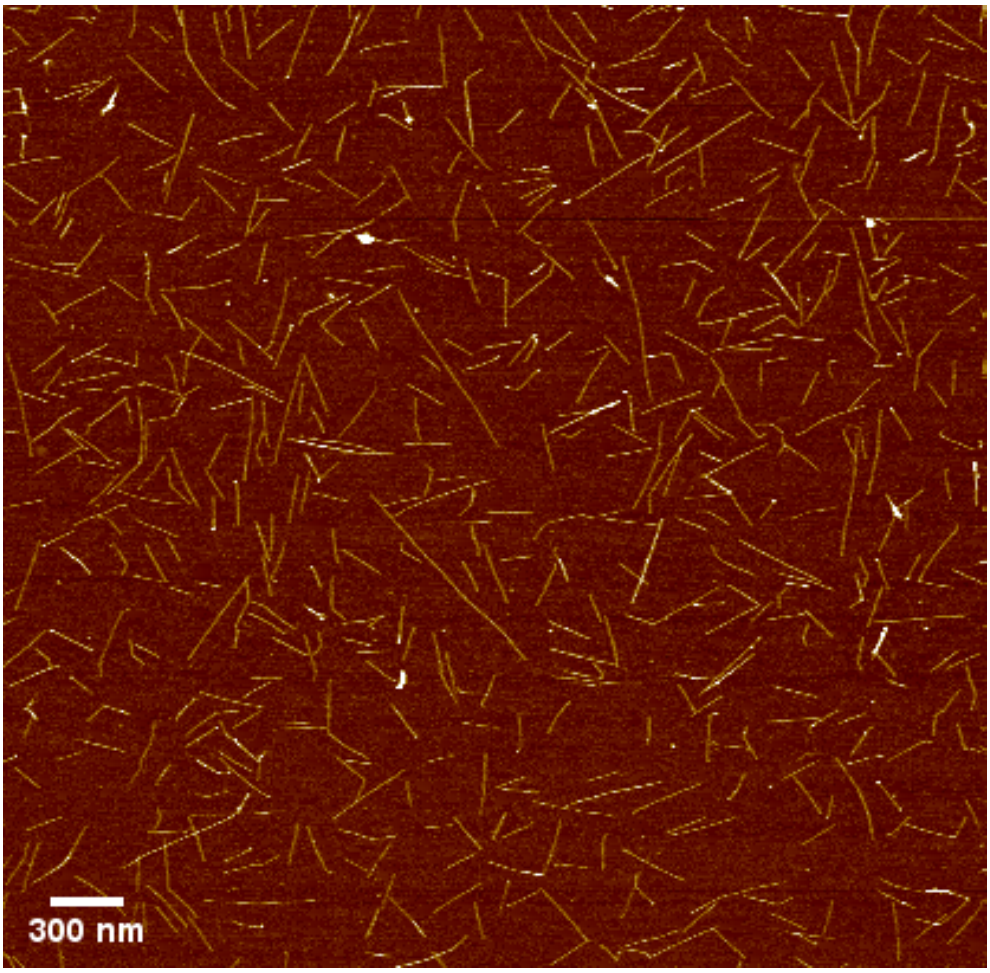

Figure 3 - 3 *AFM image of DNA-wrapped HiPco SWCNTs on mica surface.*

3.1.2 Separation of CNTs by length

Device applications need carbon nanotube length control. Furthermore, SWCNTs with controlled length can be exploited to confirm the formation of nanotube linear junctions, by comparing the length of DNA-wrapped carbon nanotubes before and after the self-assembly process.

In order to obtain an uniform length distribution for both shorter and longer nanotube fractions, three columns in series, with different pore size, were employed in this work. There are many types of SEC-HPLC columns commercially available. Unfortunately, most of them are not suited for DNA-wrapped carbon nanotube separation due to the irreversible adsorption of dispersed nanotubes on the stationary phase. However, the specially designed Sepax CNT-SEC columns are suitable for separating DNA-wrapped carbon nanotubes by length.

In our first experiment, the method follows the procedure carried out by Huang *et al.,*[117] where 100 µL of DNA-wrapped SWCNTs solution were eluted with a pH 8 buffer solution (40 mM Tris, 0.2M NaCl and 0.5 mM EDTA). The chromatogram shown in Figure 3 – 4 exhibits the DNA-wrapped carbon nanotube elution profile obtained by SEC-HPLC. In the elution profile, the peak at around 25 min retention time corresponds to the eluted CNTs, while the peak at around 40 min retention time is identified as free DNA.[117] Therefore, with SEC-HPLC it is also possible to purify the sample solution from free DNA.

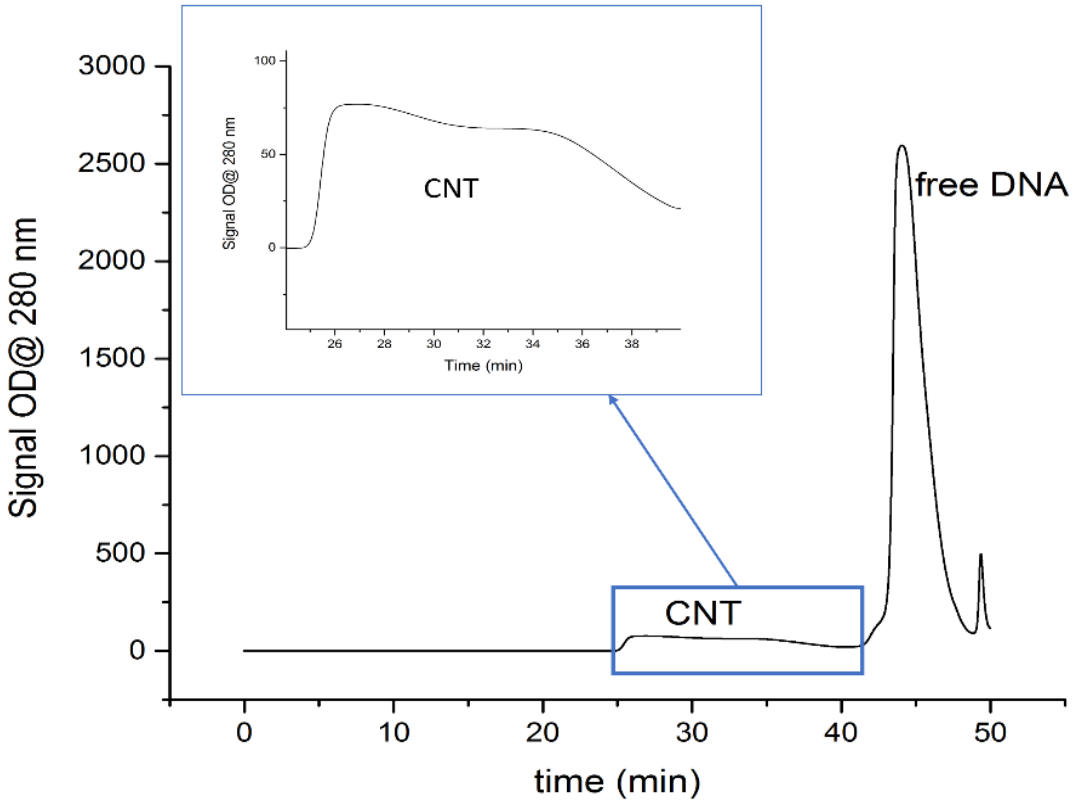

Figure 3 - 4 *Chromatogram of DNA-wrapped carbon nanotubes by SEC-HPLC separation. Injection: 100 µL. Mobile phase: 40 mM Tris + 0.5 mM EDTA + 0.2 M NaCl, pH= 8.*

To verify the length separation of the dispersed nanotubes, each fraction was imaged by AFM and a statistical analysis of the nanotube length distribution was performed from 100 randomly chosen tubes for each fraction. The uncertainty affecting the measured lengths of the nanotube nanostructures was estimated by the standard deviation (SD) values associated with the length distributions, as they appear in the AFM analysis; this is reported for all distributions (average length ± SD). In Table 2 is reported the average length of fractions from minute 25 to minute 33; the nanotube length decreases according to the SEC-HPLC principle: longer SWCNTs are eluted first, while shorter SWCNTs are eluted later. Therefore, the different length distribution in each fraction confirms the possibility of separating the CNTs by length by SEC-HPLC.

Table 2 *Average length and standard deviation of sorted DNA-wrapped carbon nanotubes. Injection: 100 µL. Mobile phase: 40 mM Tris + 0.5 mM EDTA + 0.2 M NaCl, pH= 8.*

Sample	Average length (nm)
Fraction 25	571 ± 139
Fraction 26	381 ± 72
Fraction 27	299 ± 67
Fraction 28	258 ± 51
Fraction 29	211 ± 38
Fraction 30	163 ± 26
Fraction 31	130 ± 24
Fraction 32	105 ± 19
Fraction 33	88 ± 19

In order to increase the sample injection volume, a 1.5 mL seat capillary was then mounted on our HPLC system. This allowed to inject 250 µL of DNA-wrapped SWCNTs solution for SEC-HPLC separation. The chromatogram in Figure 3 – 5 shows a similar elution profile to that in Figure 3 – 4. However, compared to the previous separation experiment, the chromatogram results in a ~5 min retention time shift due to the seat capillary and in a higher optical density (OD) at 280 nm as consequence of the higher volume injected.

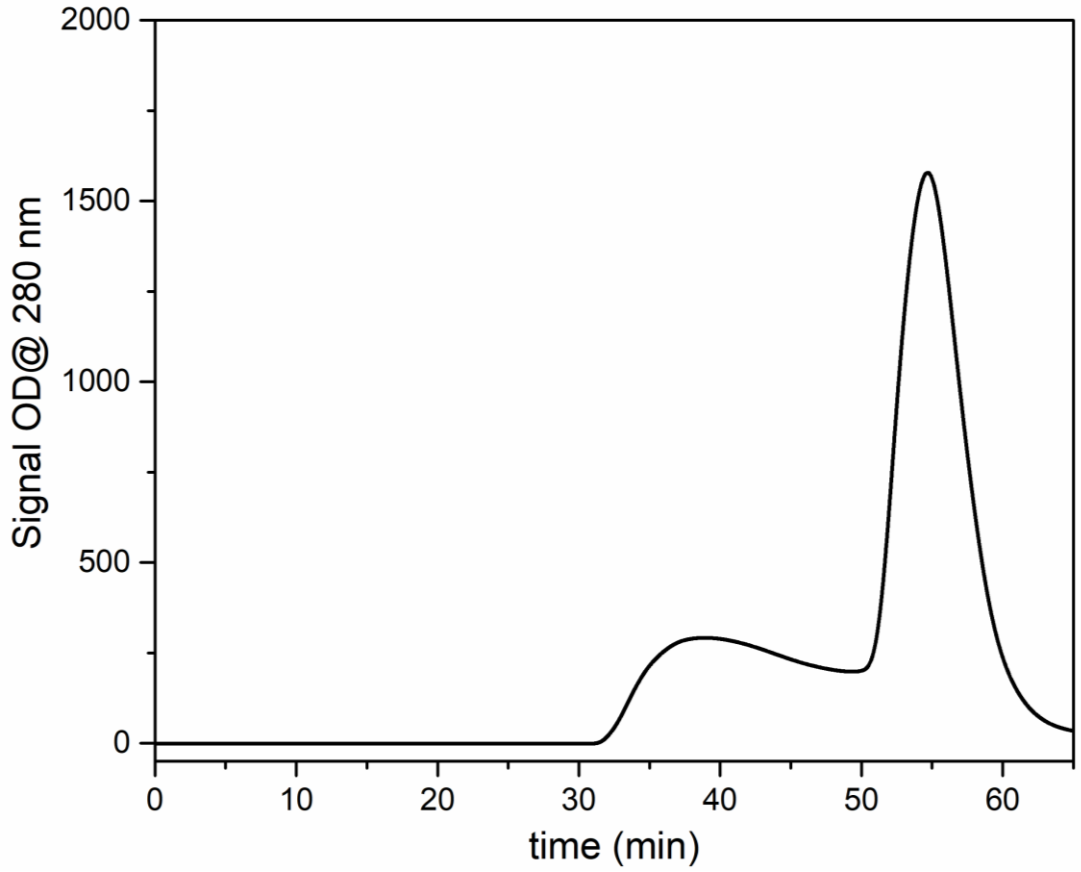

Figure 3 - 5 *Chromatogram of DNA-wrapped carbon nanotubes by SEC-HPLC separation. Injection: 250 µL. Mobile phase: 40 mM Tris + 0.5 mM EDTA + 0.2 M NaCl, pH= 8.*

The strategy employed in this chapter to form linear junctions between SWCNTs consists in exploiting the carboxyl defects present at the end of the carbon nanotubes. As previously mentioned, to disperse the nanotubes in aqueous solution, SWCNTs were sonicated with ssDNA to form DNA/SWCNT hybrids. When carbon nanotubes are sonicated in water, they can present carboxylic functional groups on their surface as a result of the use of ultrasound.[290] Hydrogen and hydroxyl free radicals are in fact generated upon sonication in water and can either combine to form H_2, H_2O_2, and H_2O or oxidise carbon nanotube surface.[291]

However, to increase the chances to have carboxylic groups at the nanotube ends, further oxidative treatments were carried out on the SWCNTs prior their dispersion in aqueous solution.

In the following experiment, SWCNTs were sonicated with a 5 M HNO_3 solution for 6h and we further increased the volume injection to 300 µL of oxidised DNA-wrapped SWCNTs solution. Figure 3 – 6 indicates that a strong acid treatment highly reduces the carbon nanotubes length. In fact, the CNT peak at around 30 min retention time results in a lower OD signal compared to that in Figure 3 – 5 and the broad peak at around 50 min is mostly due to the smallest tubes generated after acid treatment with HNO_3.

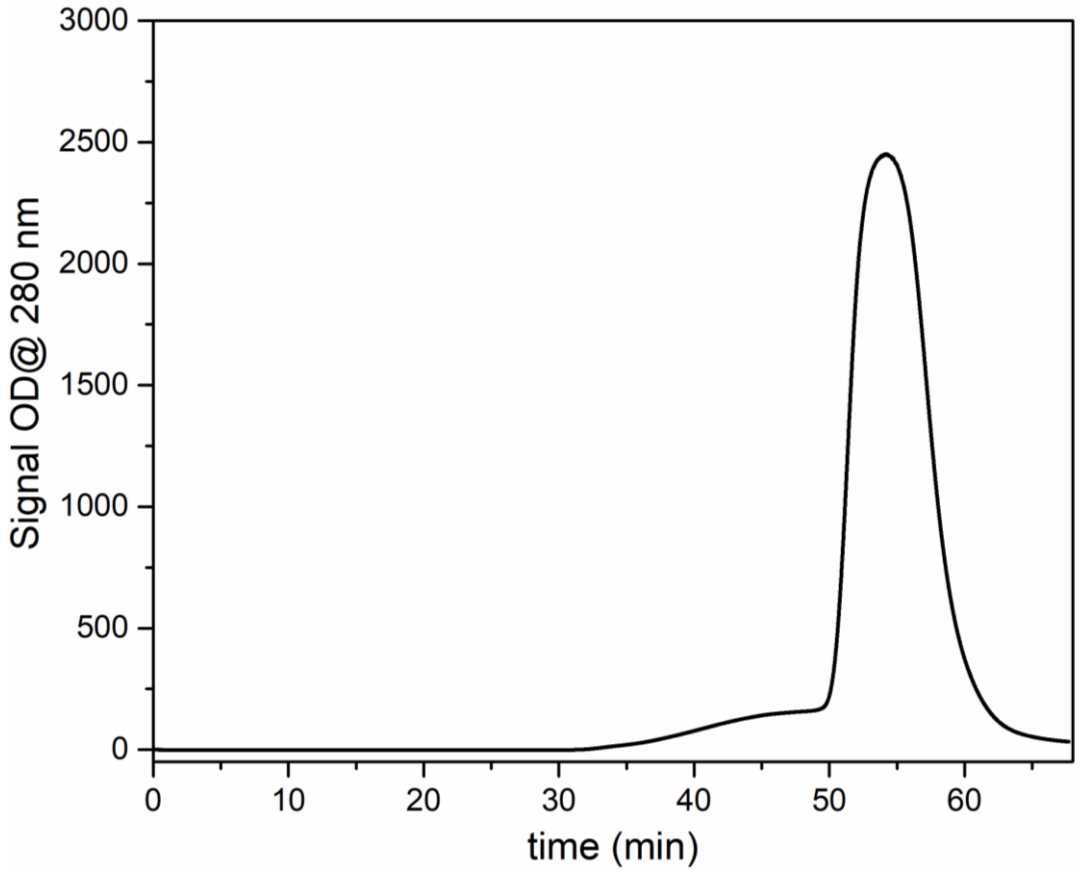

Figure 3 - 6 *Chromatogram of DNA-wrapped carbon nanotubes by SEC-HPLC separation. Injection: 300 µL. Mobile phase: 40 mM Tris + 0.5 mM EDTA + 0.2 M NaCl, pH= 8. Acid treatment: HiPco nanotubes sonicated with 5M HNO_3 for 6 hours.*

In this case, to increase the number of carboxyl defects on SWCNT surface, a different acid treatment was used. Carbon nanotubes were sonicated at 30° C for 45 min with a 3:1 ratio H_2SO_4/HNO_3 solution and then refluxed for 30 min before the wrapping with ssDNA. This allows to functionalise SWCNT tips with diverse molecules through amidation reactions between amino moieties and the carboxyl groups present at the nanotube ends. Unfortunately, the amino group and the four acetic groups in Tris and EDTA, respectively, make the mobile phase employed so far unsuitable for our purpose. A strategy relies on the solvent exchange of the fractions by centrifugal filtration; however, this method reduce the SWCNT concentration as many nanotubes stuck on the filter. Therefore, a different mobile phase is needed for the SEC-HPLC separation. For this, dispersed carbon nanotubes were eluted with a pH 8 DPBS solution. Figure 3 – 7 comes from oxidised DNA/SWCNT solution eluted with DPBS and it distances itself from the reference graph.[117]

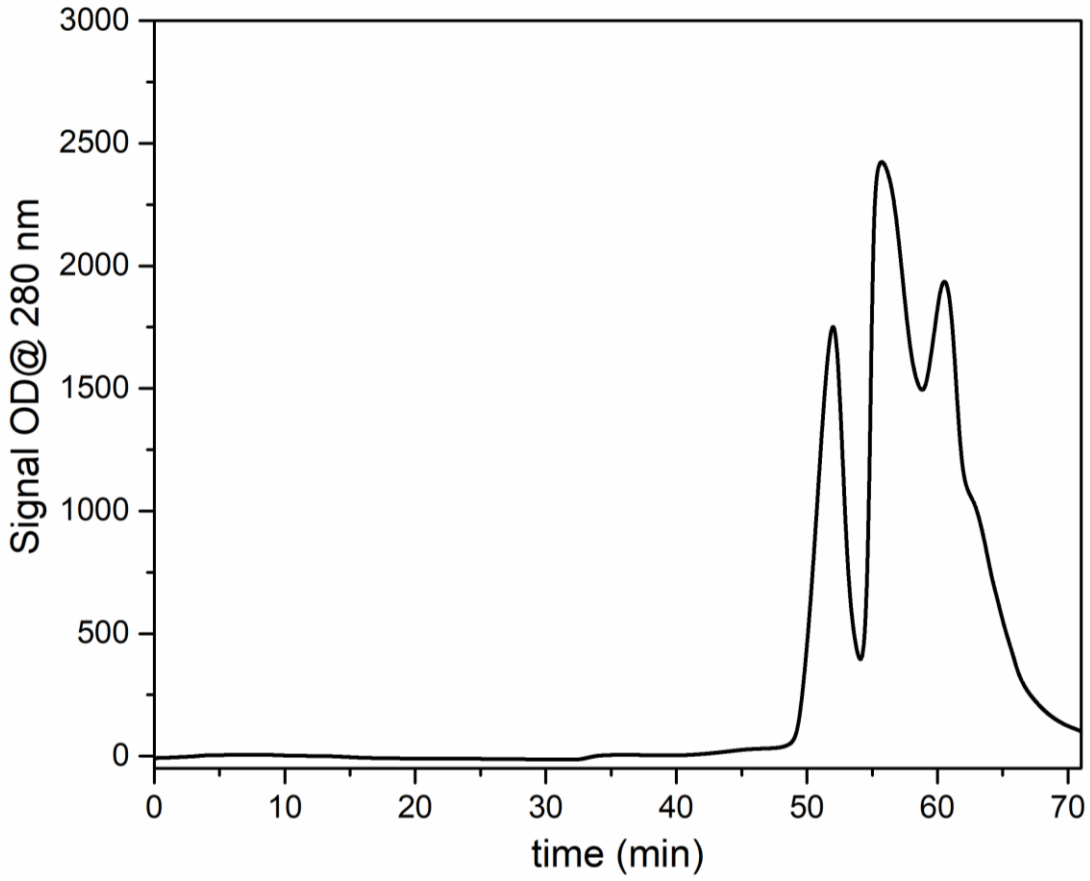

Figure 3 - 7 *Chromatogram of DNA-wrapped carbon nanotubes by SEC-HPLC separation. Injection: 300 µL. Mobile phase: DPBS, pH= 8. Acid treatment: HiPco nanotubes sonicated at 30° C with H_2SO_4/HNO_3 for 45min and then refluxed for 30 min.*

In the following experiment, 300 µL of the same acid treated DNA-wrapped SWCNTs solution were eluted with a new pH 8 buffer solution, containing 10 mM MOPS and 0.2 M NaCl. The chromatogram in Figure 3 – 8, similarly to that in Figure 3 – 6, shows a wide peak at around 50 min retention time, indicating that this acid treatment has highly reduced the tubes length, but overcome the issue of primary amine of Tris interfering with the coupling between SWCNTs and amino moieties.

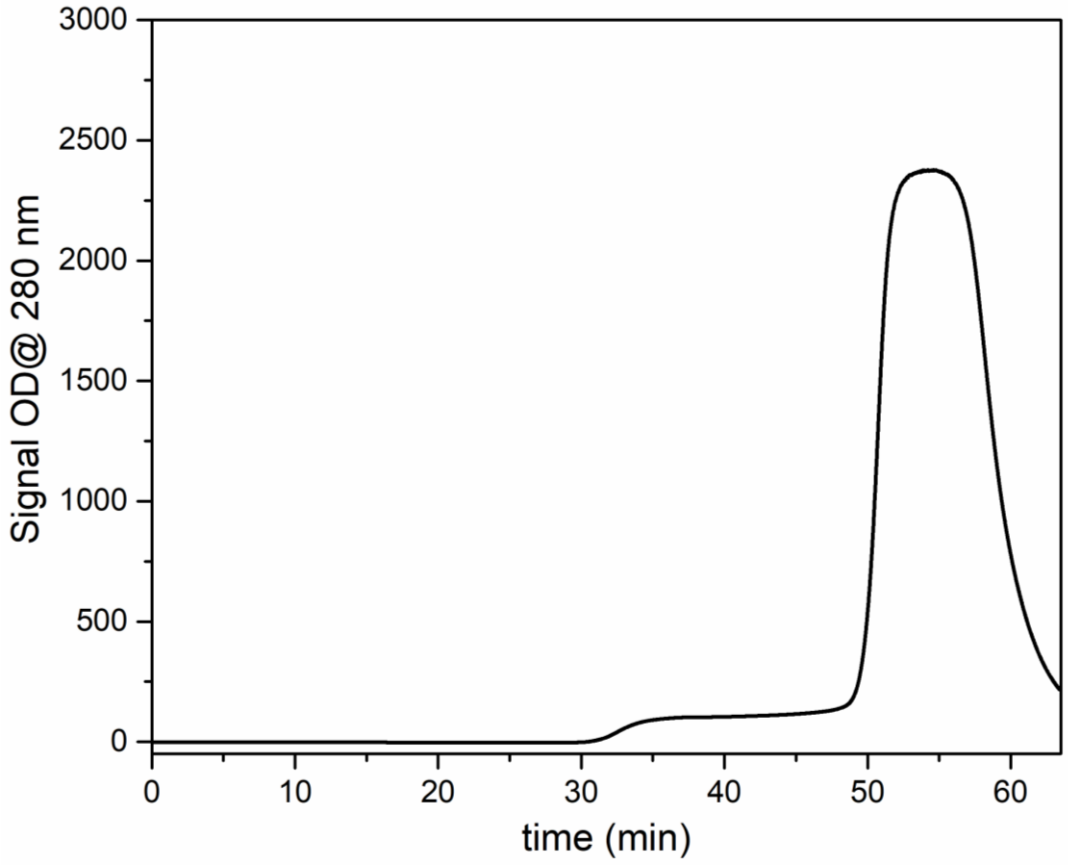

Figure 3 - 8 *Chromatogram of DNA-wrapped carbon nanotubes by SEC-HPLC separation. Injection: 300 µL. Mobile phase: 10mM MOPS + 0.2 M NaCl, pH= 8. Acid treatment: HiPco nanotubes sonicated at 30° C with H_2SO_4/HNO3 for 45min and then refluxed for 30min.*

To avoid an excessive SWCNT cutting, HiPco nanotubes were sonicated at 30° C for 15 min in a 3:1 volume ratio of H_2SO_4:HNO_3 solution without reflux. In Figure 3 – 9 is shown a topographic AFM image of acid-treated DNA-dispersed SWCNTs before length separation by SEC-HPLC. Here, the polydispersed carbon nanotubes suggest that the oxidation process employed does not strongly reduce SWCNT length.

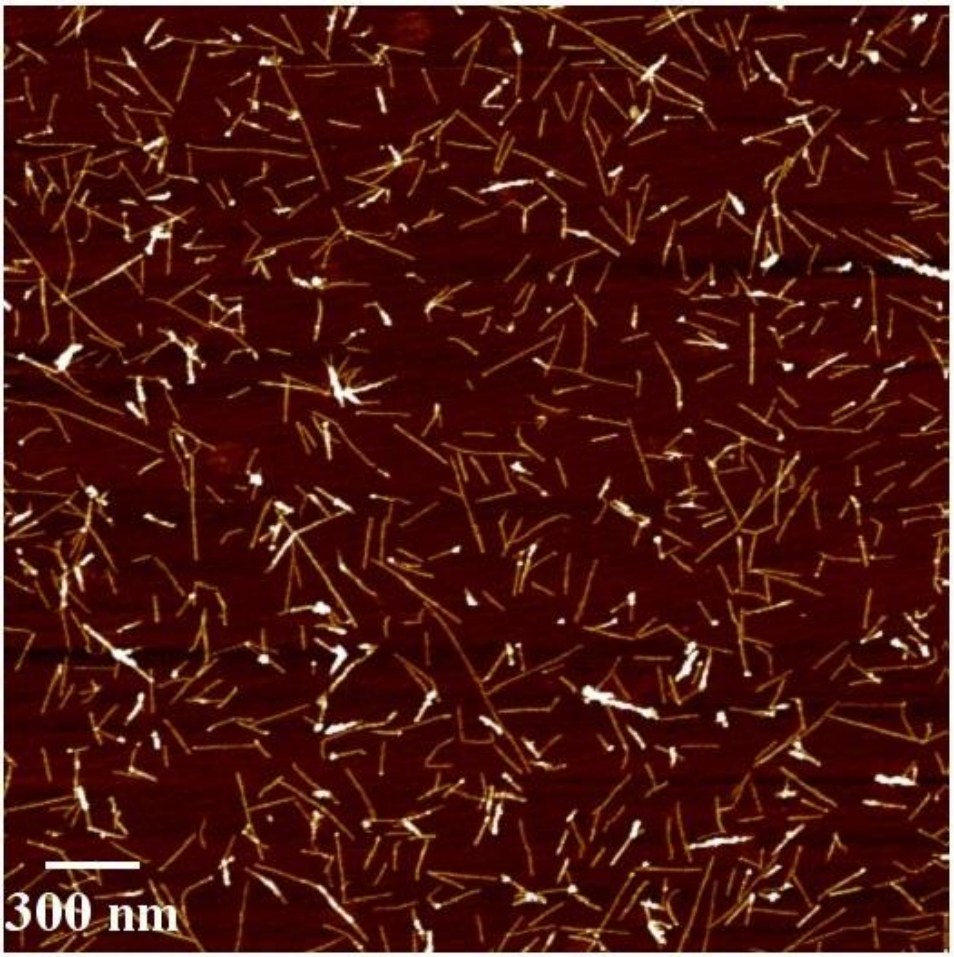

Figure 3 - 9 *AFM image of acid-treated DNA-wrapped HiPco SWCNTs on mica surface.*

To obtain a uniform length distribution of the above acid-treated SWCNTs, the nanotubes were DNA-dispersed and SEC-HPLC separated with a pH 8 mobile phase containing 10mM MOPS + 0.2 M NaCl. Figure 3 – 10 shows a chromatogram with a similar elution profile to that shown in Figure 3 – 5, which suggests a uniform SWCNT length distribution in the fractions.

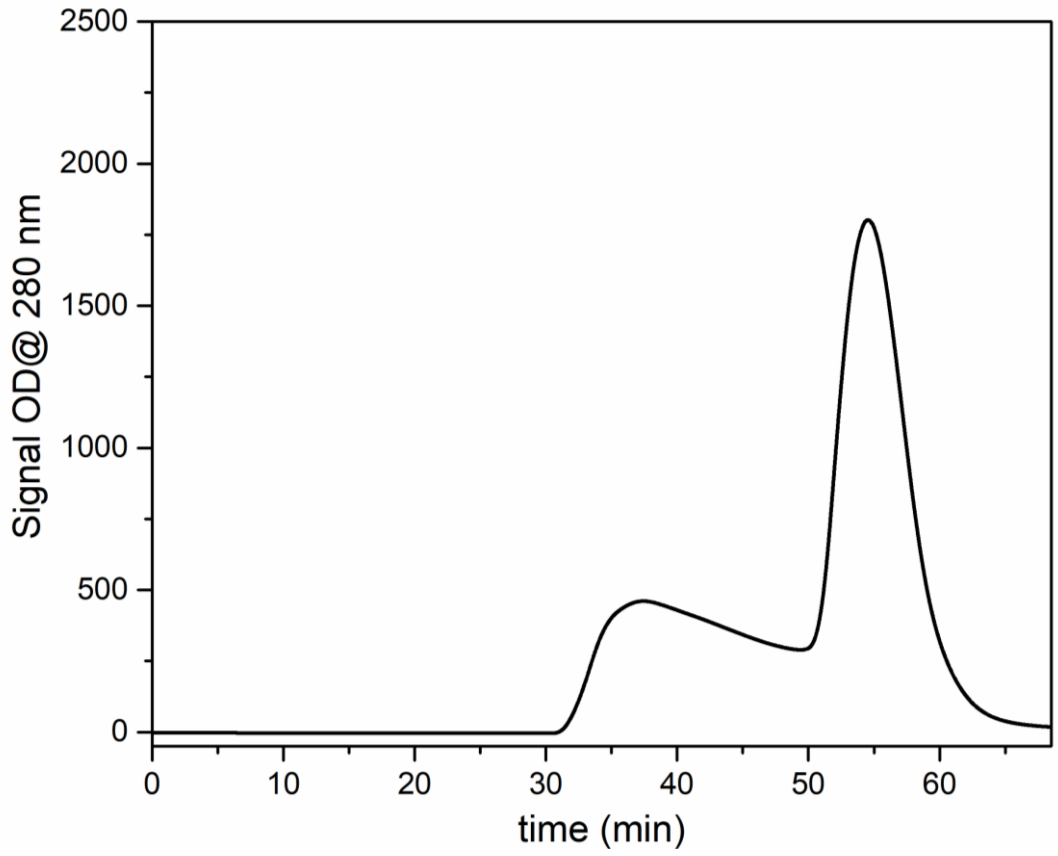

Figure 3 - 10 *Chromatogram of DNA-wrapped carbon nanotubes by SEC-HPLC separation. Injection: 300 µL. Mobile phase: 10mM MOPS + 0.2 M NaCl, pH= 8. Acid treatment: HiPco nanotubes sonicated at 30° C with H_2SO_4/HNO_3 for 15min.*

Fractions were collected each minute from min 33 to min 44 and UV-Vis-NIR absorption analysis was then performed for each fraction (Figure 3 – 11) to confirm the presence of SWCNTs and no changes in their optical properties after oxidation.

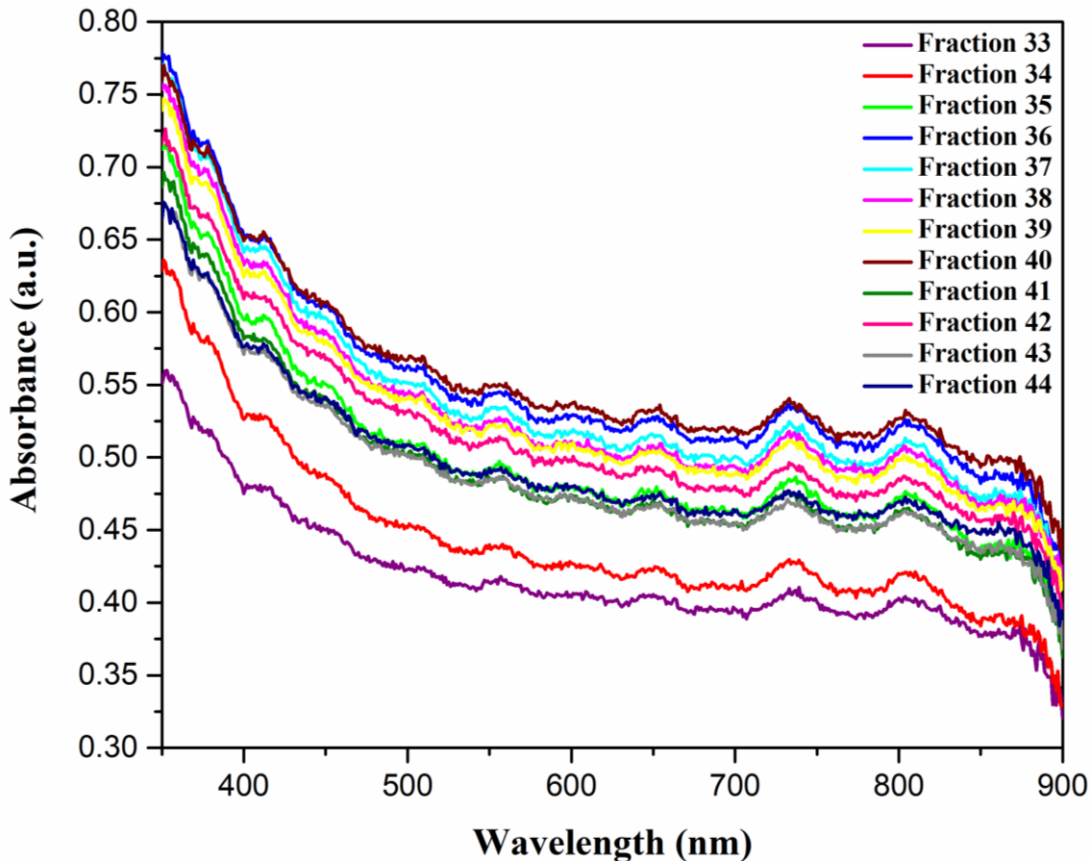

Figure 3 - 11 *UV-Vis-NIR absorption spectra of fractions 33 to 44 from the SEC-HPLC separation described in the text.*

AFM images and corresponding length distribution of fractions 36, 38 and 42 are shown in Figure 3 – 12. The three DNA-wrapped SWCNT fractions exhibit an average length and standard deviation of 329 ± 125 nm, 247 ± 99 nm and 123 ± 59 nm, respectively for fraction 36, 38 and 42. A comparison of the tube average length of the three fractions confirms that the tubes eluted first are longer than tubes eluted after. Relative frequency in the plots is defined as the number of carbon nanotube counted and measured.

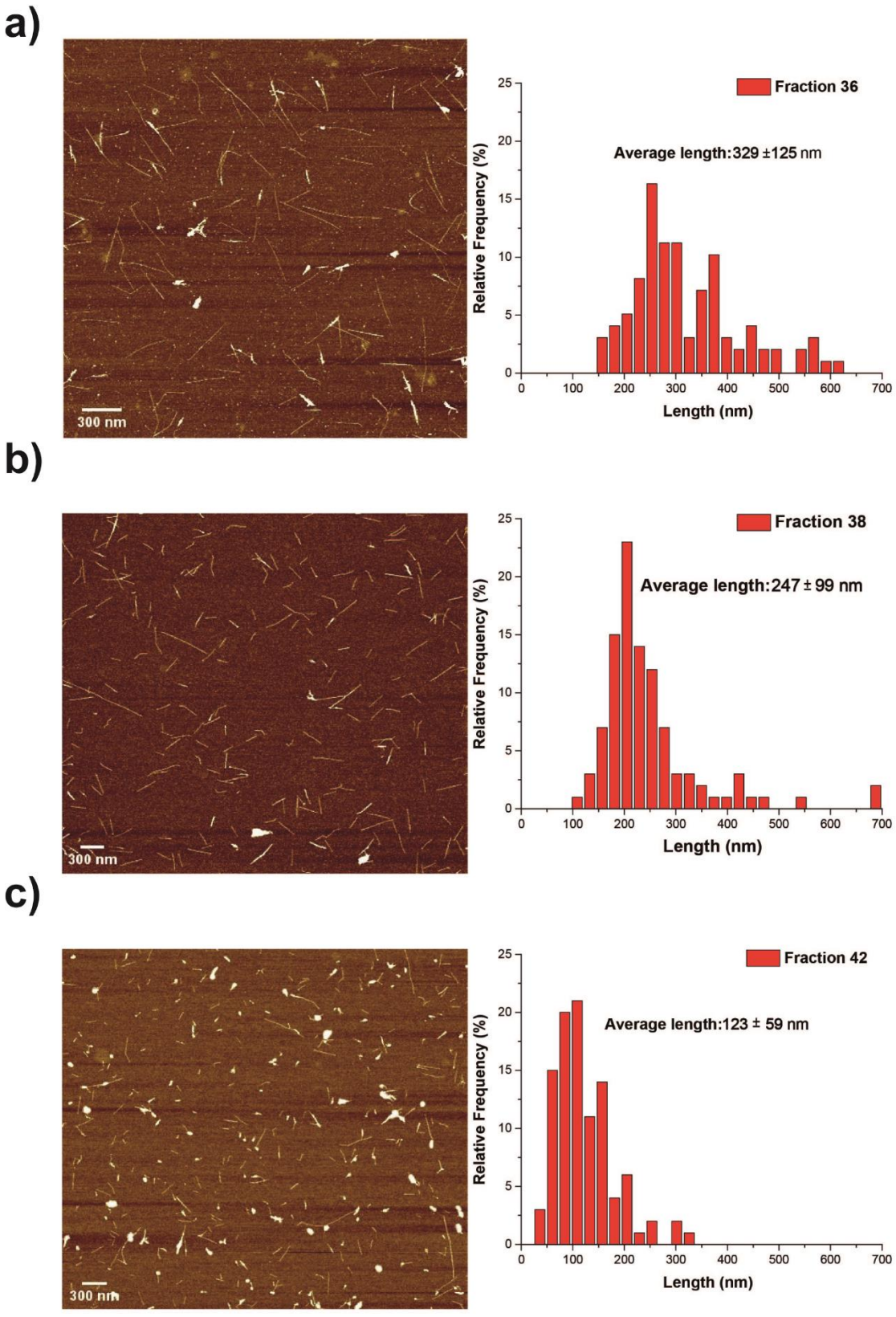

Figure 3 - 12 *a) AFM image of fraction minute 36 (left), statistical analysis of SWCNT length distribution results in 329 ±125 nm (right); b) AFM image of fraction minute 38 (left), statistical analysis of SWCNT length distribution results in 247 ± 99 nm (right); and c) AFM image of fraction minute 42 (left), statistical analysis of SWCNT length distribution results in 123 ±59 nm (right).*

Finally, a statistical analysis of the SWCNT lengths distribution was performed from 100 randomly chosen carbon nanotubes for each fraction to confirm a uniform distribution. In Table 3 is reported the average tube length of fractions from minute 33 to minute 44, where longer SWCNTs are eluted earlier than shorter SWCNTs. This confirms the possibility of separating the DNA-wrapped SWCNTs by length with our improved SEC-HPLC method.

Table 3 *Average length and standard deviation of sorted DNA-wrapped carbon nanotubes. Injection: 300 µL. Mobile phase: 10mM MOPS + 0.2 M NaCl, pH= 8. Acid treatment: HiPco nanotubes sonicated at 30° C with H_2SO_4/HNO_3 for 15min.*

Sample	Average length (nm)
Fraction 33	413 ± 100
Fraction 34	388 ± 148
Fraction 35	351 ± 106
Fraction 36	329 ± 125
Fraction 37	258 ± 60
Fraction 38	247 ± 99
Fraction 39	197 ± 102
Fraction 40	155 ± 79
Fraction 41	130 ± 61
Fraction 42	123 ± 59
Fraction 43	121 ± 77
Fraction 44	123 ± 75

3.2 SWCNT JUNCTION FORMATION

3.2.1 Direct Amidation

To form SWCNT junctions , a EDC/Sulfo-NHS strategy was undertaken as reported in published procedures.[105,124] The mild oxidative treatment generates carboxyl groups on the carbon nanotube surface, which react with primary amines resulting in a covalent amide bond. The DNA-wrapping strategy protects the nanotube side-walls and polyamine molecules would then link SWCNT tips to form end-to-end junctions *via* amidation reaction. SWCNT junctions were formed as described in Chapter 2, then solutions were drop-cast onto mica disks and imaged *via* AFM. AFM images were analysed by measuring the lengths of DNA-wrapped SWCNTs with image-J software.

The carbon nanotubes employed for the experiments were dispersed and length-sorted in aqueous solution as explained in paragraph 3.1. The average nanotube length before junction formation was of 247 ± 99 nm (Fraction 38 in Table 3).

The polyamine linkers, here employed as SWCNT molecular junctions, are as follows: 4,4``-diamino-p-terphenyl, 1,3,5-Tris(4-aminophenyl)benzene and 5,10,15,20-Tetrakis(4-aminophenyl)porphyrin (see Figure 3 – 13).

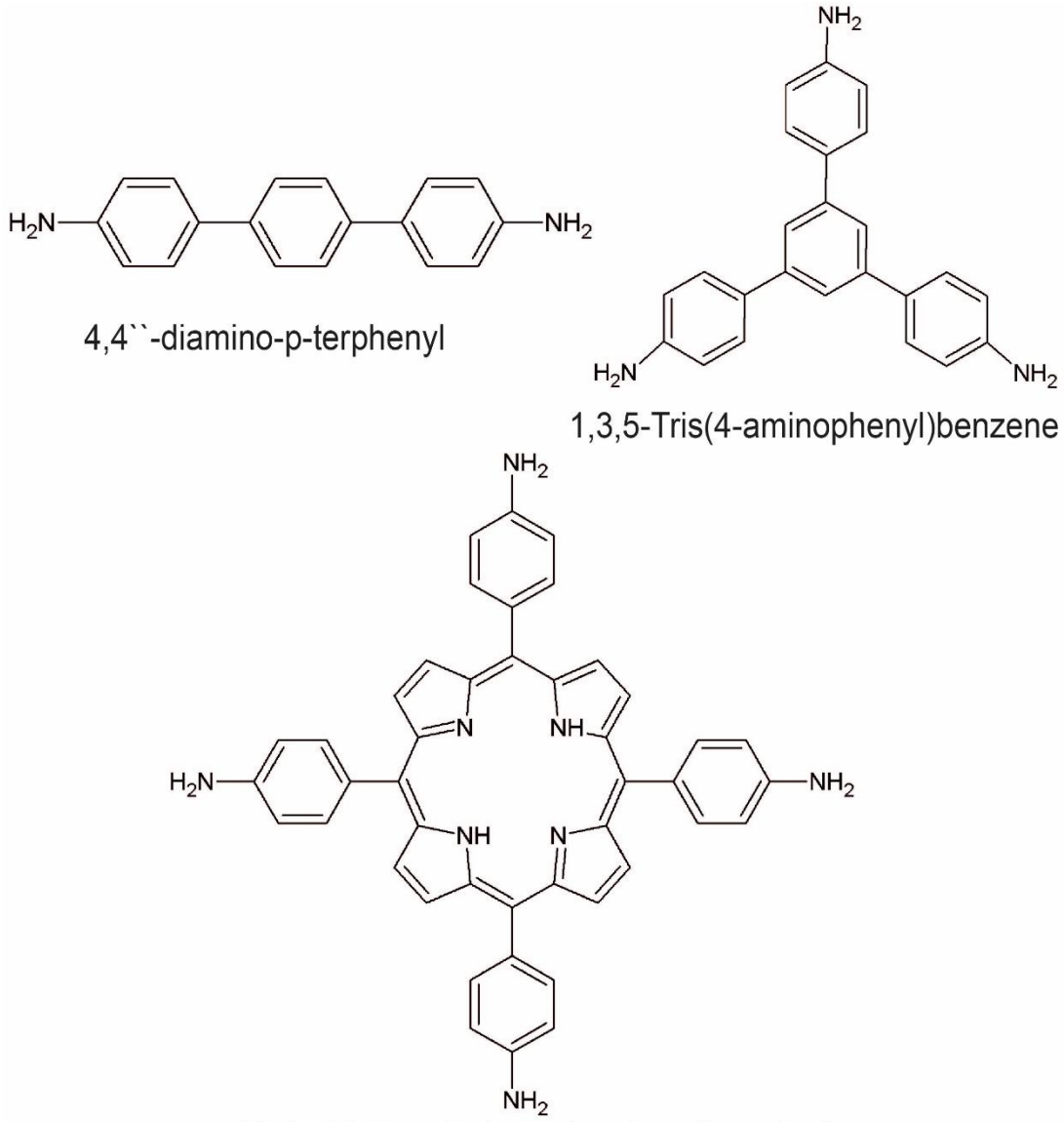

Figure 3 - 13 *The three different molecules employed as linkers: 4,4``-diamino-p-terphenyl, 1,3,5-Tris(4-aminophenyl)benzene and 5,10,15,20-Tetrakis(4-aminophenyl)porphyrin.*

3.2.1.1 Linker: 4,4``-diamino-p-terphenyl

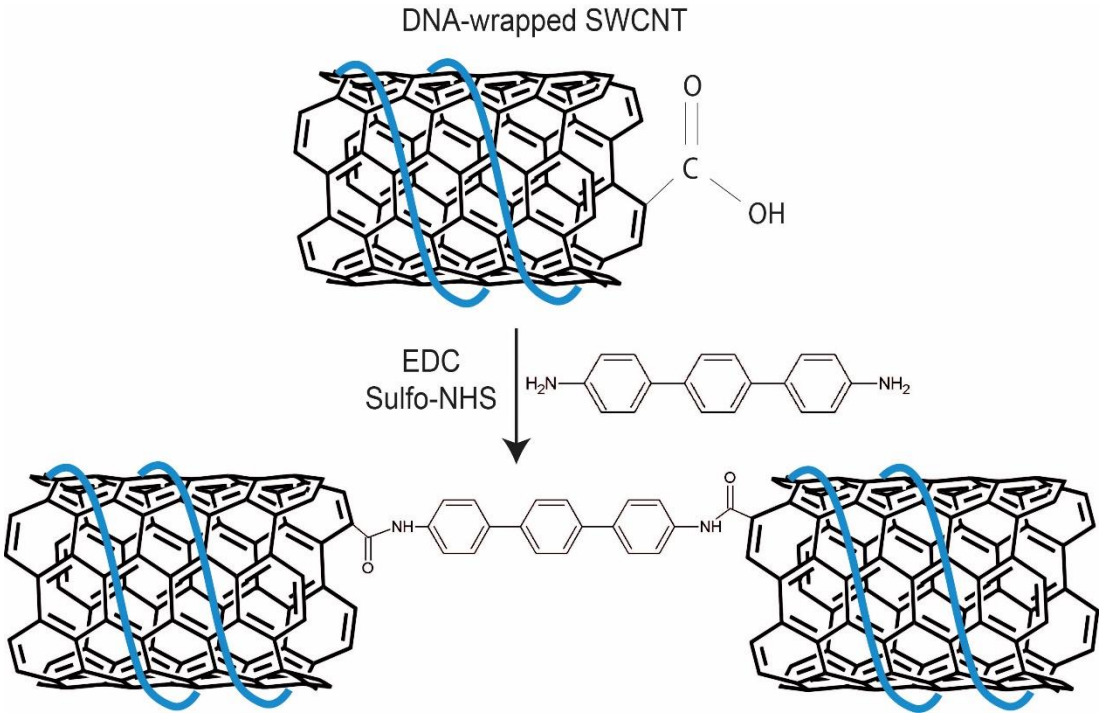

Figure 3 - 14 *Schematic pathway of an amidation reaction to form SWCNT static linear junctions employing a diamino linker.*

In Figure 3 – 14 is described the schematic mechanism to form SWCNT static linear junctions employing 4,4``-diamino-p-terphenyl molecule as diamino linker. The carboxyl groups present at the nanotube ends are activated by EDC/Sulfo-NHS and the tips of two SWCNTs are bridged by a diamino linker.

Figure 3 – 15 shows the AFM image of the assembled carbon nanotubes and the corresponding tube length distribution. The average length of the DNA-wrapped SWCNT segments is found to increase from 247 ± 99 nm for the SWCNT starting material to 387 ± 213 nm when reacted with 4,4``-diamino-p-terphenyl molecule in solution. This increase in average nanotube length indicates the formation of SWCNT linear junctions.

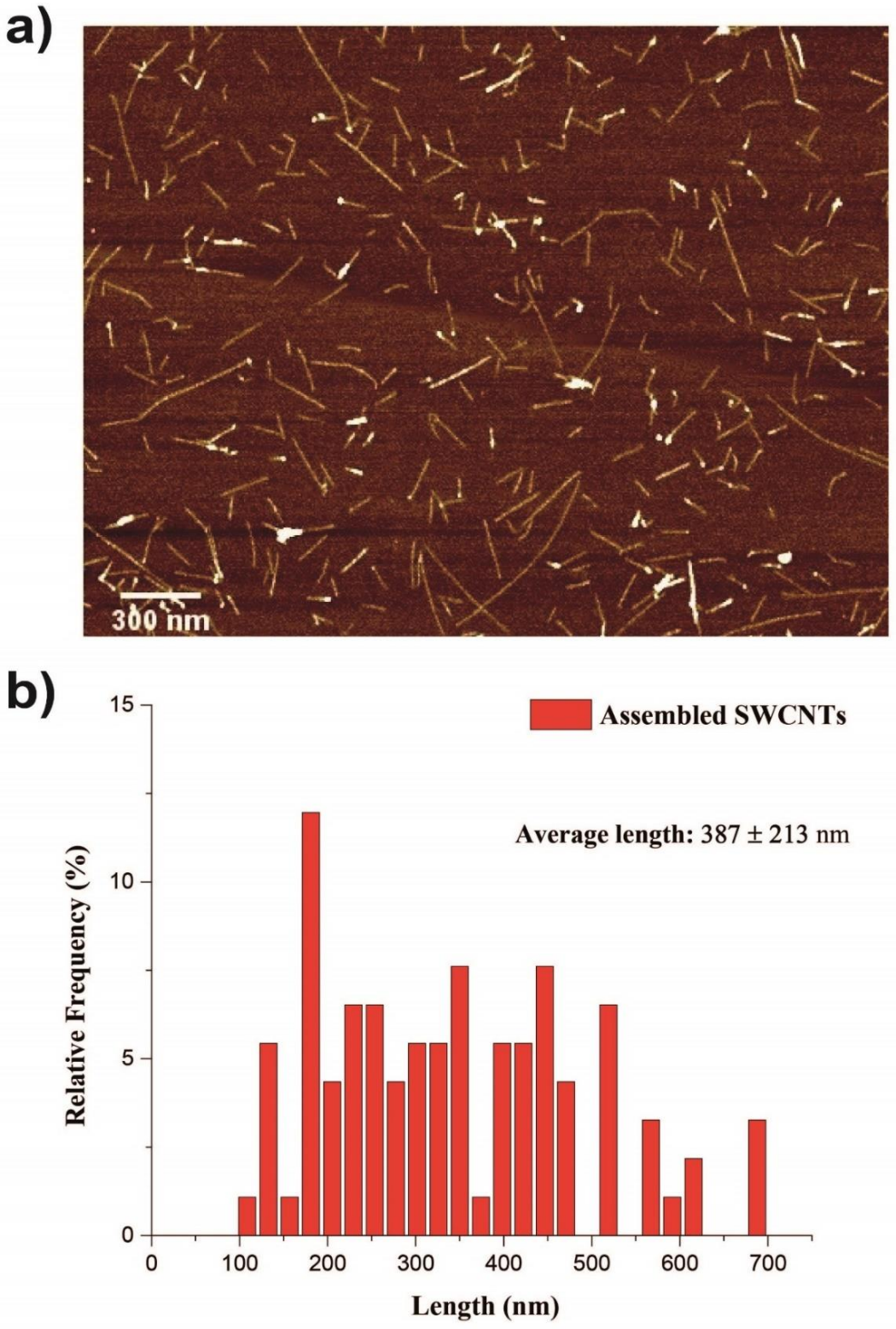

Figure 3 - 15 *(a) AFM topographical image and (b) length distribution of DNA-wrapped SWCNTs linked with 4,4``-diamino-p-terphenyl molecule.*

3.2.1.2 Linker: 1,3,5-Tris(4-aminophenyl)benzene

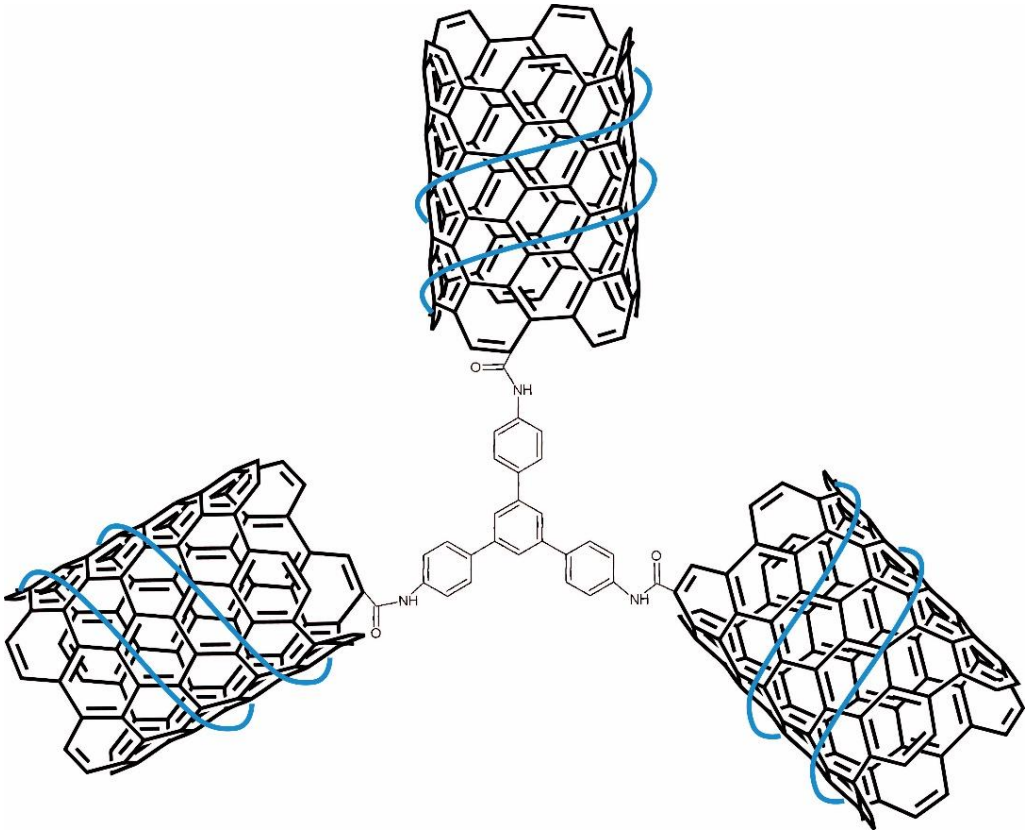

Figure 3 - 16 *Schematic of a three-terminal molecular junction employing a triamino linker.*

In order to create Y-shaped end-to-end SWCNT junctions, a triamino molecule was employed to interconnected SWCNT tips *via* amidation reaction (see Figure 3 – 16). The AFM image and length distribution plot shown in Figure 3 – 17 arise from nanotubes assembled by employing 1,3,5-Tris(4-aminophenyl)benzene as triamino linker. The average length of carbon nanotube segments is found to increase from 247 ± 99 nm for the SWCNT starting material to 409 ± 265 nm. The increased average tube length and increased standard deviation suggest the successful formation of SWCNT static junctions. The higher average tube length compared to that of SWCNTs assembled by using a diamino linker may be associated to the increased number of amino groups in the molecular linker. However, the almost total absence of a Y-shape configuration indicates that three-terminal junctions were not formed, probably due to the steric hindrance from DNA-wrapped carbon nanotubes.

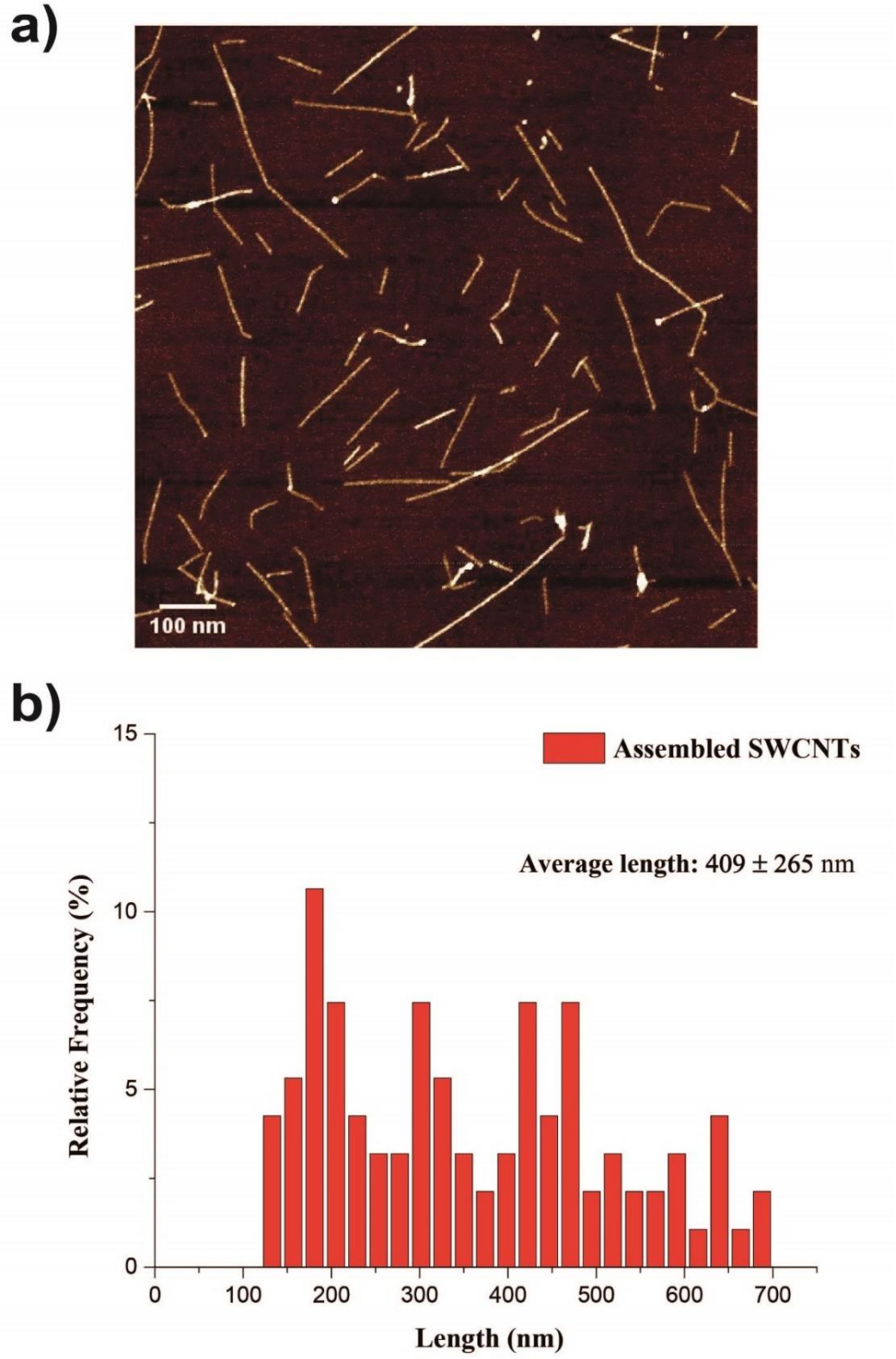

Figure 3 - 17 *(a) AFM topographical image and (b) length distribution of DNA-wrapped SWCNTs linked with 1,3,5-Tris(4-aminophenyl)benzene molecule.*

3.2.1.3 Linker: 5,10,15,20-Tetrakis(4-aminophenyl)porphyrin

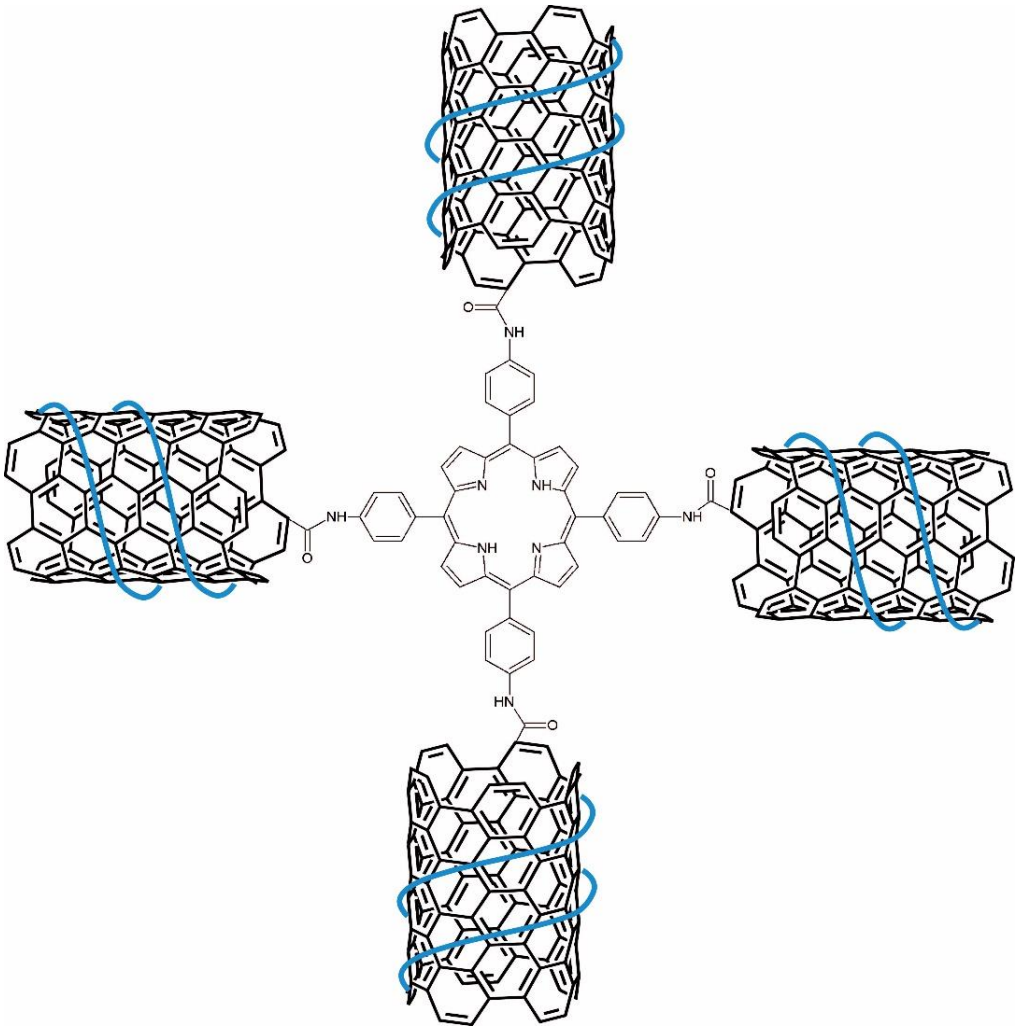

Figure 3 - 18 *Schematic of a four-terminal molecular junction employing a tetra-amino linker.*

Therefore, increasing the molecular linker size and the number of amino groups may improve the possibility of multi-terminal junctions. Porphyrin macrocycles can be modified with four amino groups and this could facilitate the formation of multi-SWCNTs end-connected to a single molecular linker (Figure 3 – 18). In this regard, a 5,10,15,20-Tetrakis(4-aminophenyl)porphyrin molecule was employed as tetra-amino linker. Figure 3 – 19 shows DNA-wrapped SWCNTs to be significant longer (average length of 329 ± 265 nm) than starting material. This indicates the formation of SWCNT junctions. The lower average tube length compared to that of nanotubes assembled by using diamino and triamino linkers may be associated to the increased number of SWCNT branched junctions.

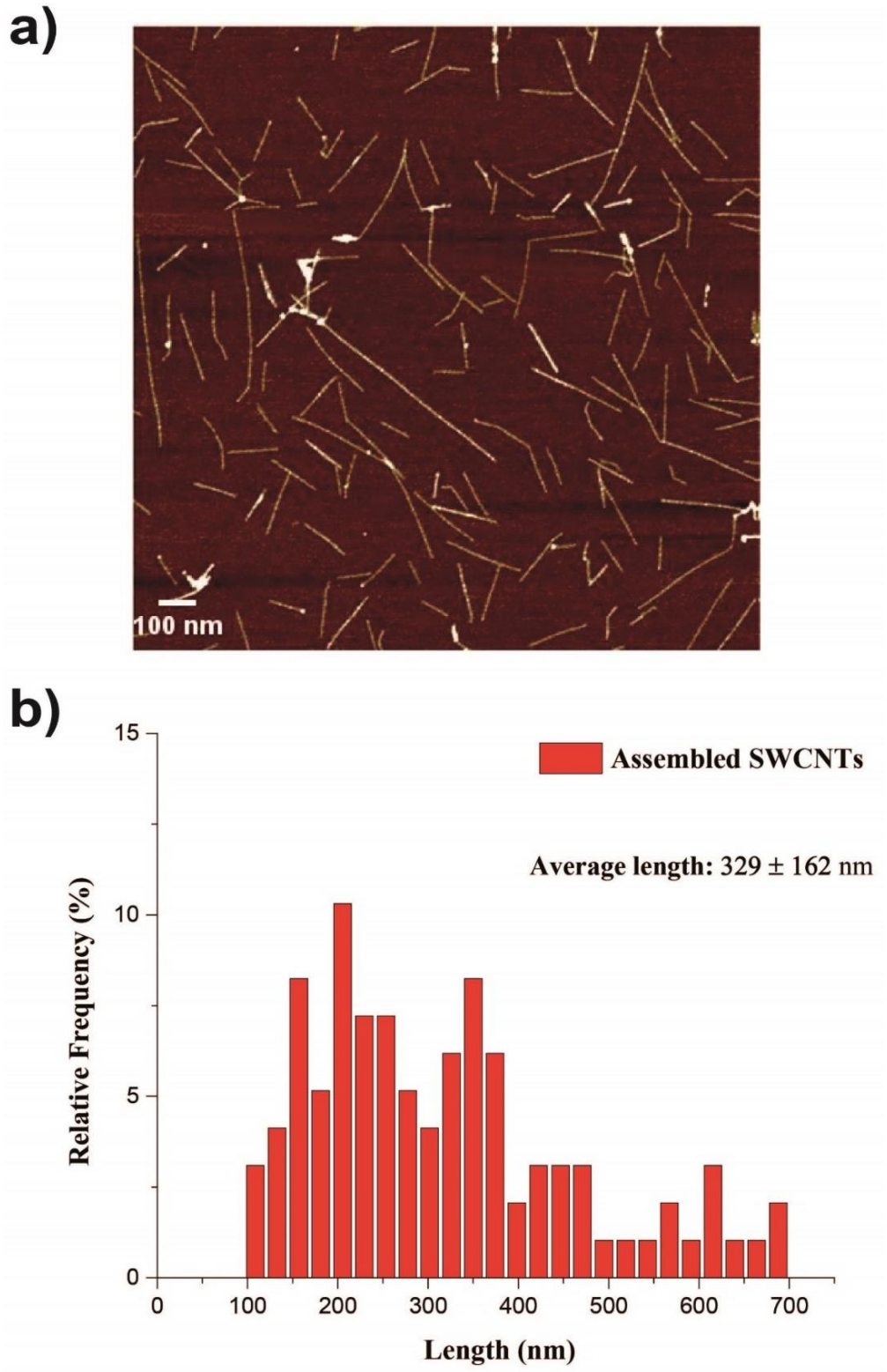

Figure 3 - 19 *(a) AFM topographical image and (b) length distribution of DNA-wrapped SWCNTs linked with 5,10,15,20-Tetrakis(4-aminophenyl)porphyrin macro-molecule.*

3.2.2 "Click" Junctions

An improved approach for the formation of SWCNT junctions was developed by means of a copper-free click chemistry strategy. The DNA-wrapped SWCNTs employed as starting materials for these experiments are the same employed in paragraph 3.2.1. Here, the carboxyl groups present on the carbon nanotube tips reacted with primary amines bearing cyclooctyne or azide functional groups *via* amidation reaction. This results in the formation of azido or cyclooctyne end-functionalised SWCNTs. Upon mixing azido and cyclooctyne end-functionalised SWCNTs, carbon nanotubes were end-to-end linked by the formation of triazole conjugates as described in Chapter 2. SWCNT "click" junctions were verified by AFM imaging and statistical analysis of the average tube length. Figure 3 – 20 shows the azido and cyclooctyne molecules employed in this study: 4-azidoaniline hydrochloride, DBCO-amine and BCN-amine respectively.

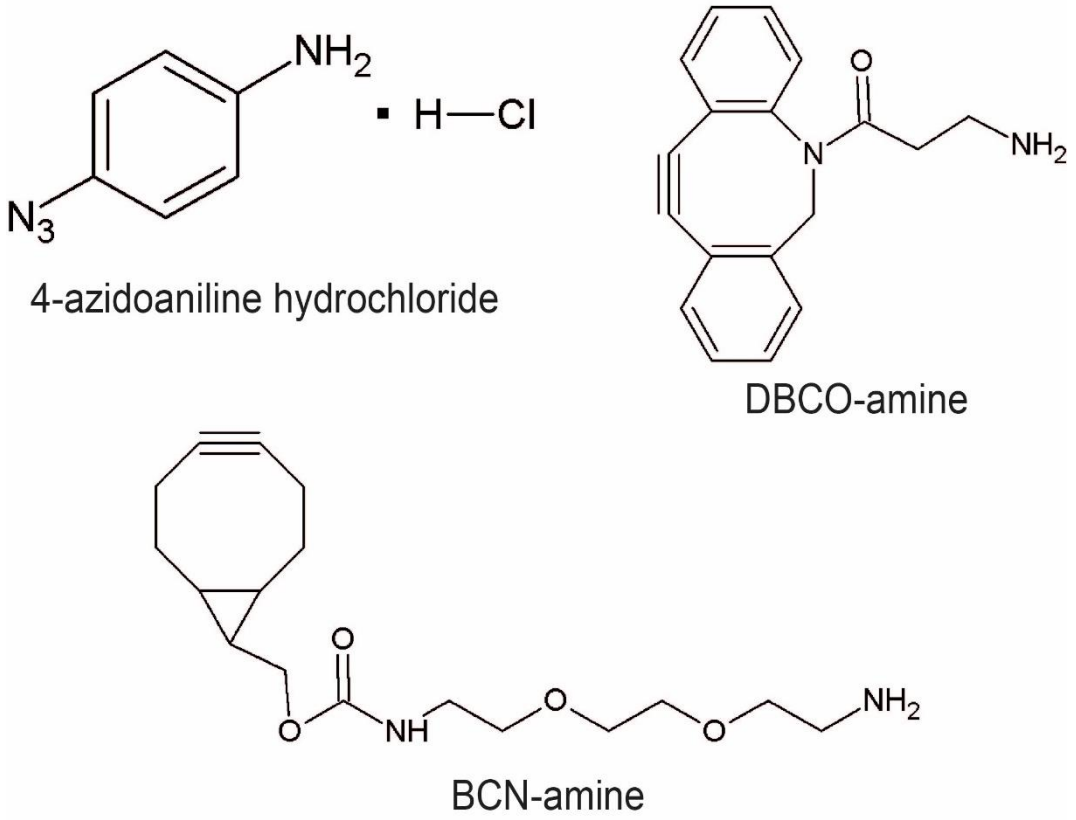

Figure 3 - 20 *The three different molecules employed for the SWCNT "click" junction formation are: 4-azidoaniline hydrochloride, DBCO-amine and BCN-amine.*

3.2.2.1 DBCO and azido end-functionalised SWCNTs

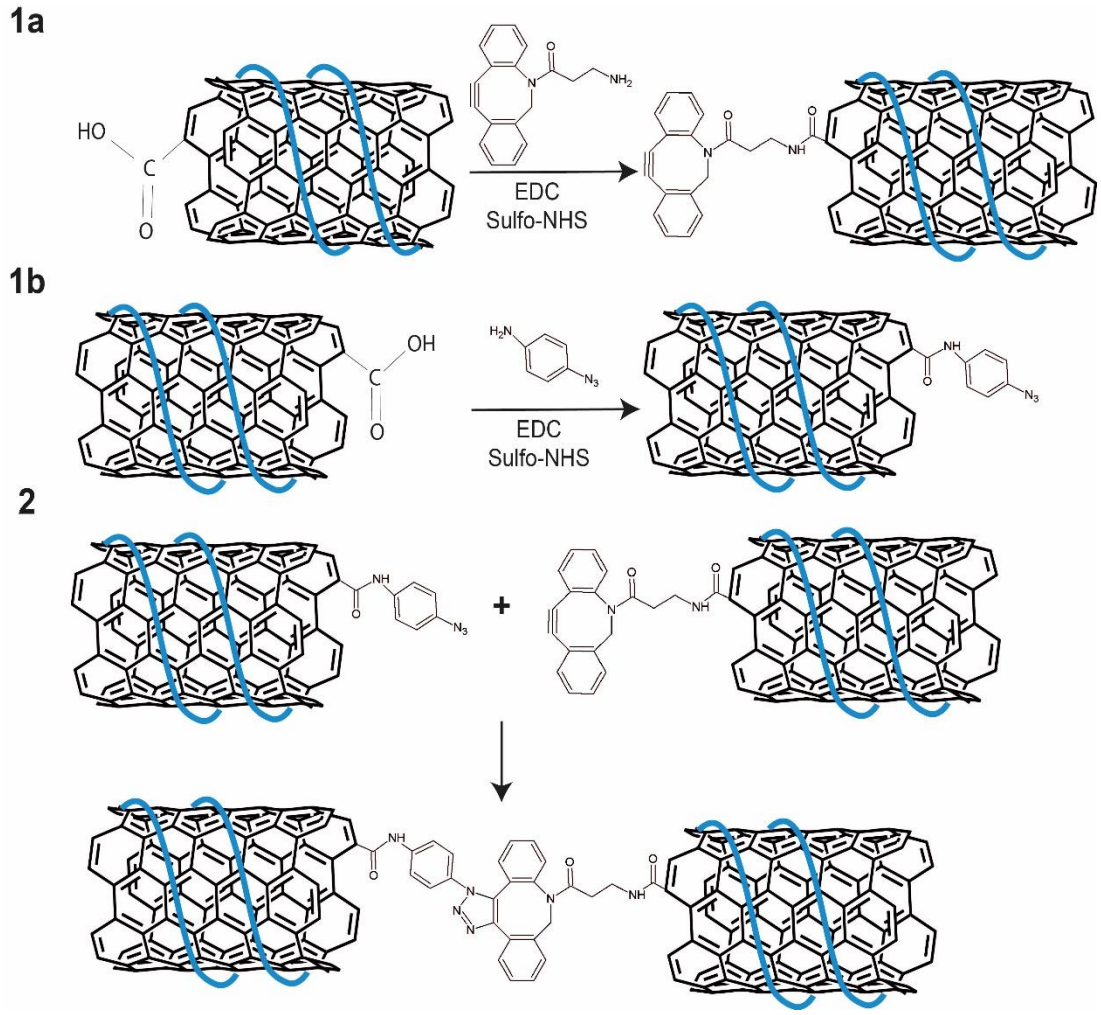

Figure 3 - 21 *Schematic pathway for the formation of SWCNT "click" junctions. 1a) end-functionalisation of SWCNTs with DBCO-amine; 1b) end-functionalisation of SWCNTs with 4-azidoaniline hydrochloride; 2) SWCNT "click" junction formation by mixing DBCO and azido end-functionalised SWCNTs.*

Figure 3 – 21 describes the schematic pathway for the formation of SWCNT "click" junctions employing 4-azidoaniline hydrochloride and DBCO-amine molecules. DNA-wrapped SWCNTs solution was divided in two aliquots: the first aliquot was end-functionalised with 4-azidoaniline hydrochloride, while the second one with DBCO-amine *via* amidation reaction. The two aliquots were then mixed and SWCNTs were assembled by the formation of triazole conjugates. The increased average SWCNT length of 371 ± 209 shown in Figure 3 – 22 suggests the end-to-end junction formation by copper-free click chemistry.

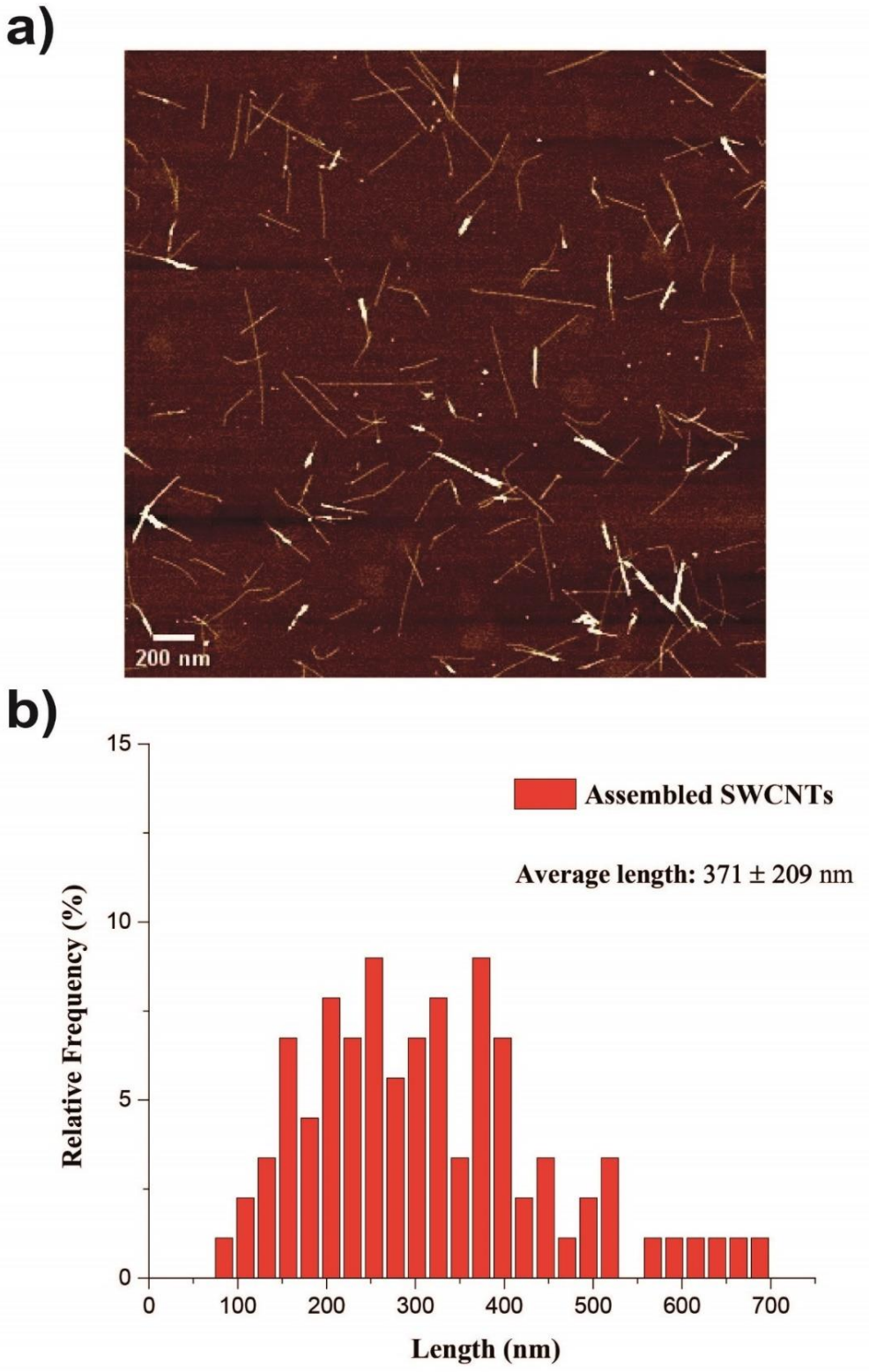

Figure 3 - 22 *(a) AFM topographical image and (b) length distribution of DNA-wrapped SWCNTs end-to-end assembled by copper-free click chemistry, employing DBCO and azido end-functionalised nanotubes.*

3.2.2.2 BCN and azido end-functionalised SWCNTs

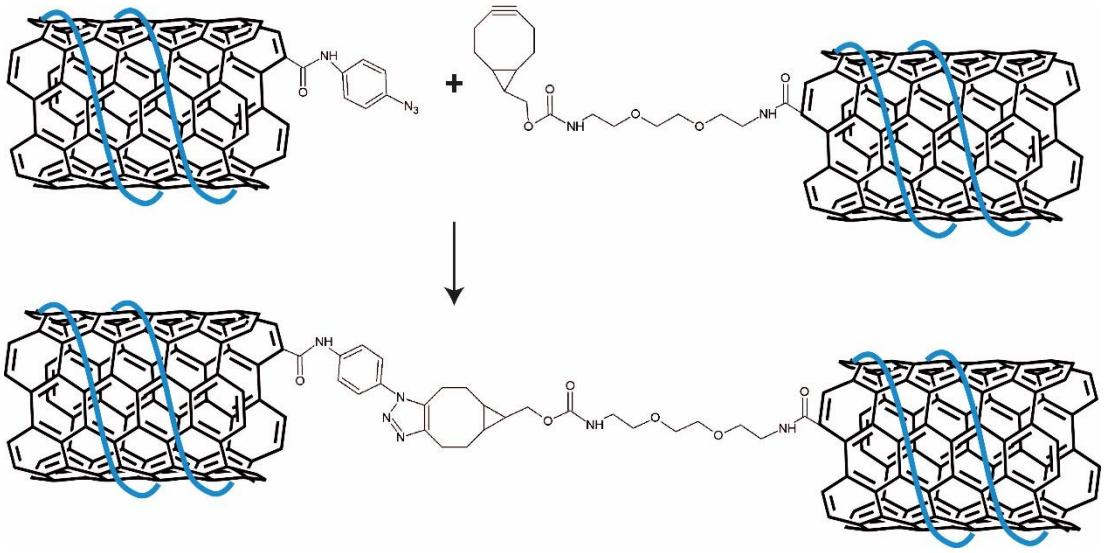

Figure 3 - 23 *Schematic pathway for the formation of SWCNT "click" junction formation obtained by mixing BCN and azido end-functionalised SWCNTs.*

As the SWCNT steric hindrance may affect junction formation, a longer molecule at the nanotube tips could facilitate the SWCNT linking. For this reason, a third SWCNT aliquot was end-functionalised with BCN-amine, which contains a longer and flexible chain, *via* amidation reaction. As shown in Figure 3 – 23, azido and BCN end-functionalised nanotubes were then mixed and DNA-wrapped SWCNTs were linked by the formation of a new triazole conjugate. Figure 3 – 24 shows the AFM image of the assembled carbon nanotubes and the corresponding tube length distribution plot. The average SWCNT length is found to increase from 247 ± 99 nm for the starting material to 509 ± 242 nm after triazole conjugate formation. This increase in average nanotube length strongly indicates the formation of SWCNT static linear junctions.

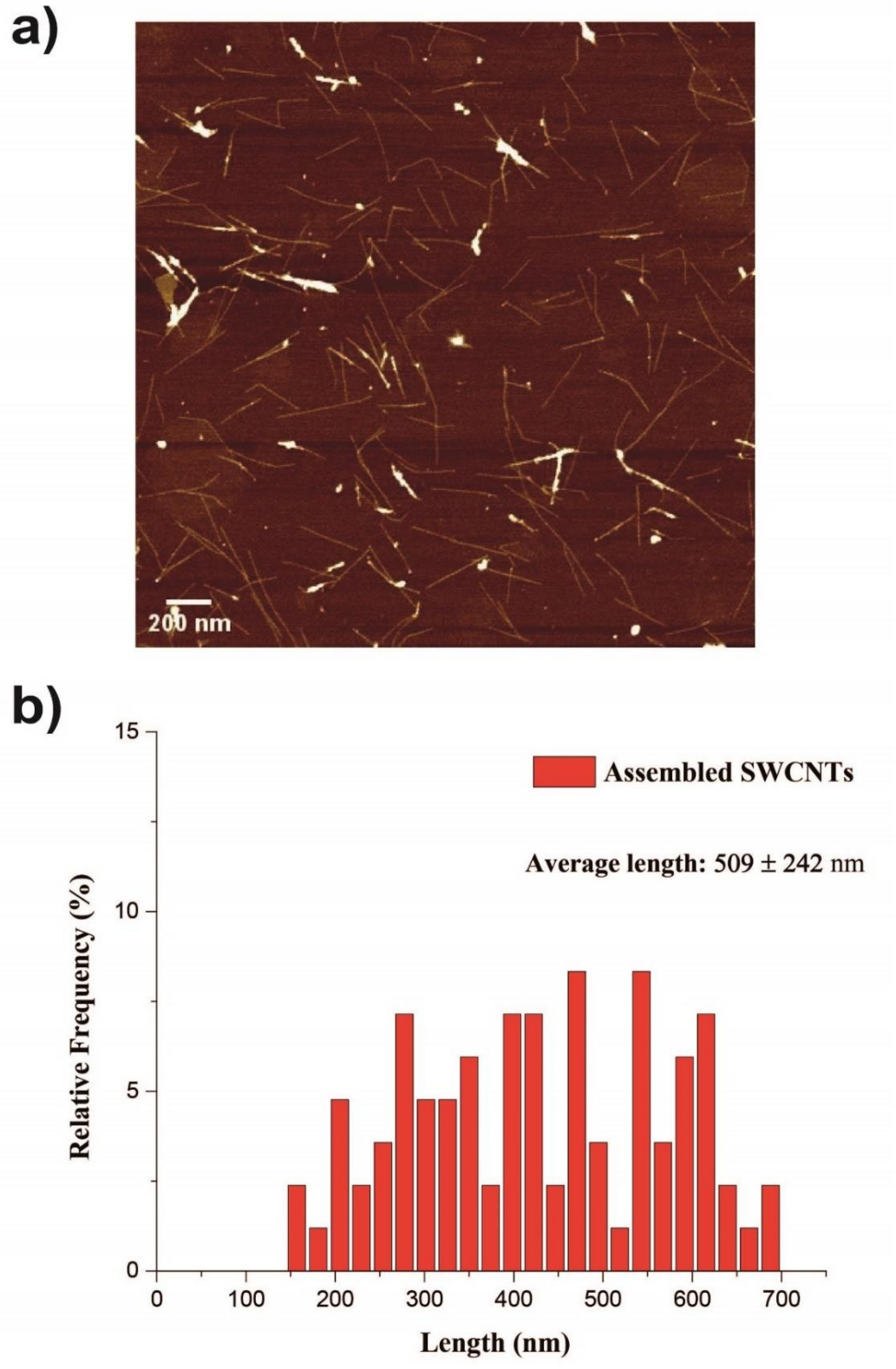

Figure 3 - 24 *(a) AFM topographical image and (b) length distribution of DNA-wrapped SWCNTs end-to-end assembled by copper-free click chemistry, employing BCN and azido end-functionalised nanotubes.*

3.3 SWCNT/QD HETEROSTRUCTURES

Length sorted acid-cut DNA-wrapped SWCNTs produced in paragraph 3.1 were also employed for the formation of nano-heterostructures in collaboration with Dr Mark Freeley, postdoctoral research associate in the Palma group.[126] As confirmed in the AFM image shown in Figure 3 – 25, we assembled individual SWCNTs with QDs by means of dsDNA as molecular linkers. The dsDNA linkers contain an amino group, used for the end-functionalisation of SWCNTs, and a biotin moiety for the interaction with streptavidin-modified QDs. In order to regulate the SWCNT/QD distance, we changed the number of bases in the double-stranded DNA linker. In particular, 10, 20 and 30 base-pair DNA linker were employed.

Furthermore, reconfigurable SWCNT/QD heterostructures were constructed, where a Guanine(G)-rich sequence was employed as molecular linker. The QD distance from the end of the SWCNT could then be varied by the addition of K^+, which induces the folding of the DNA strand into a G-quadruplex (G4) structure. The process was reverted by introducing into the system a cryptand 222, which possesses a strong affinity for K^+. Indeed, when Cryptand 222 is added to the system, it removes the K^+ from the G4 DNA linker. Removal of the metal cation permitted to bring the DNA linker back to its original extended conformation and to restore the distance between SWCNT and QD. The reversibility of the system was then confirmed by continuous fluorescence measurements, obtained while KCl and cryptand 222 were added one after the other. The fluorescence intensity was measured at 585 nm. When 2 µL of a 1 M solution of KCl was added, the fluorescence signal dropped. The emission intensity was finally recovered by adding 1.25 µl of a 1 M solution of cryptand 222 into the SWCNT/QD solution.

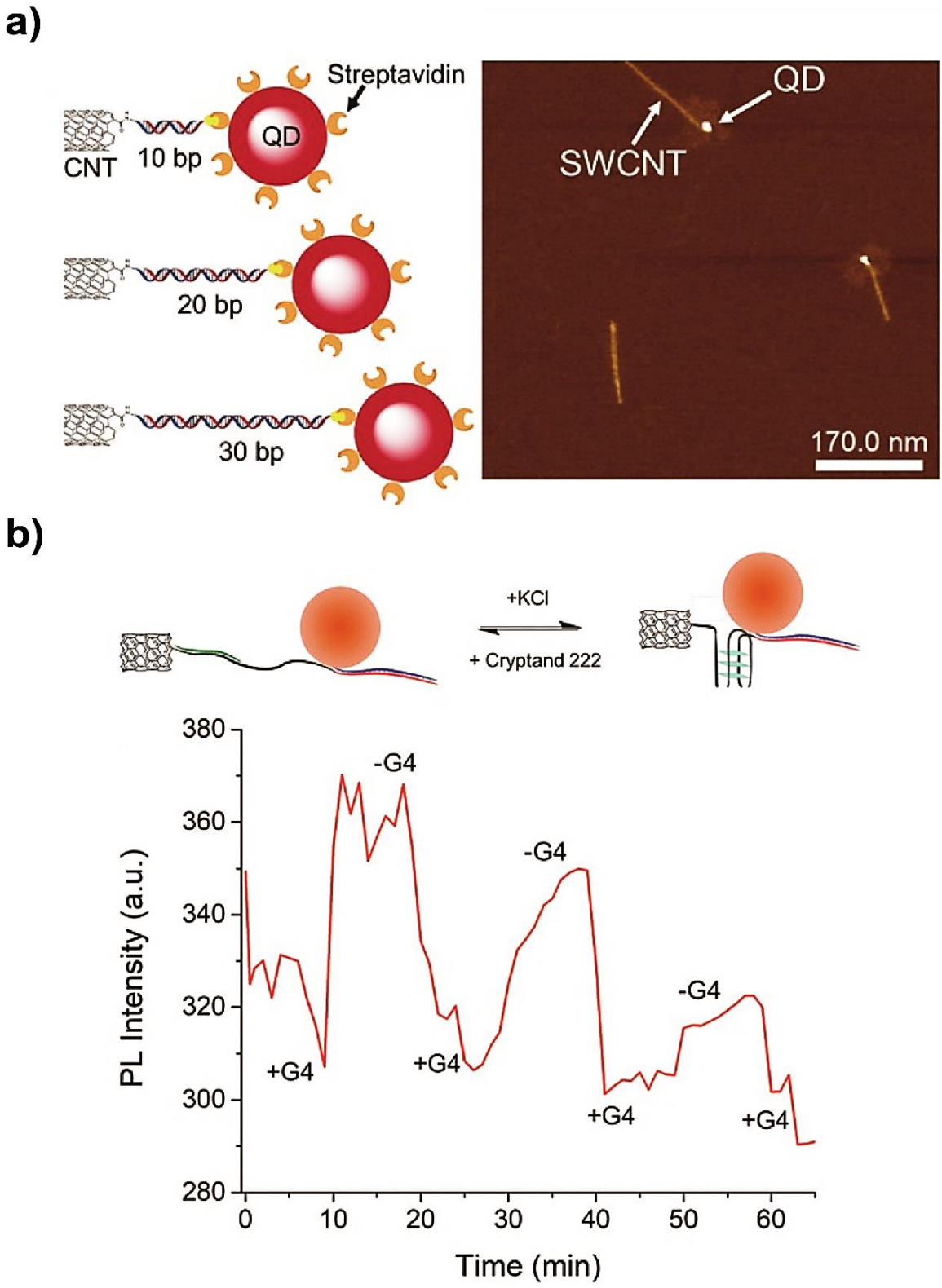

Figure 3 - 25 *a) Schematic and AFM image for the SWCNT/QD heterostructures with three DNA linkers of different length; b) Scheme for the conformational changes of the SWCNT/QD nanohybrid with G4 DNA linker upon subsequentially addition of K^+ and cryptand 222, and corresponding PL intensity measurements. Taken (adapted) from reference 126.*[126]

3.4 CONCLUDING REMARKS

In summary, we have presented the controlled static linear assembly of individual SWCNTs *via* in-solution approaches. Pristine carbon nanotubes were oxidised through a mild acid cutting process that generates carboxyl defects on the nanotube surface. Specifically, HiPco nanotubes were sonicated at 30° C for 15 min in a 3:1 volume ratio of H_2SO_4:HNO_3 solution and then dispersed in water by means of ssDNA that wraps around the tube. This also allows to protect SWCNT surface from secondary reactions, leaving nanotube tips free for specific end-functionalisation. In addition, dispersed SWCNTs were length sorted by a size-exclusion technique. The separation process uses three specially designed Sepax CNT-SEC columns in series, with different pore size, mounted on an HPLC system. DNA-wrapped SWCNTs were eluted with a pH 8 mobile phase, containing 10mM MOPS and 0.2M NaCl, and fractions were collected each minute from min 33 to min 44. Uniform length distribution of the fractions was then confirmed by AFM imaging and statistical analysis of the SWCNT length. The end-to-end assembly strategy used in this chapter relies on the covalent attachment of molecular linkers at the SWCNT ends *via* amidation reactions between the activated carboxyl groups on nanotube tips and amino functionalised linkers. In Table 4 are listed the molecular linkers employed for SWCNT linear junction formation with corresponding length. The average length of the SWCNTs used as starting material for junction formation is of 247 ± 99 nm, corresponding to Fraction 38 (highlighted in orange). Static linear SWCNT junctions were obtained with two strategies: direct amidation and copper-free click chemistry.

Table 4 *List of molecular linkers employed for SWCNT static linear junctions. Highlights: no linker (orange), direct amidation (yellow), copper-free click chemistry (green).*

Molecular linker	Average SWCNT length (nm)
none	247 ± 99
4,4``-diamino-p-terphenyl	387 ± 213
1,3,5-Tris(4-aminophenyl)benzene	409 ± 265
5,10,15,20-Tetrakis(4-aminophenyl)porphyrin	329 ± 162
DBCO-amine + 4-azidoanaline hydrochloride	371 ± 209
BCN-amine + 4-azidoanaline hydrochloride	509 ± 242

For the direct amidation, SWCNT ends were bridged by the use of poly-amine linkers (highlighted in yellow). When 4,4``-diamino-p-terphenyl is employed as diamino linker, the carbon nanotube length increases from 247 ± 99 nm for the SWCNT starting material to 387 ± 213 nm after the assembly; this increase in length suggests the formation of SWCNT linear junctions. The average SWCNT length further increase to a value of 409 ± 265 nm for assembled nanotubes after junction formation when 1,3,5-Tris(4-aminophenyl)benzene is used as triamino linker. Although the increased tube length indicates the formation of SWCNT static junctions, the almost total absence of a Y-shape configuration suggests that only linear junctions were formed, probably due to steric effects. Conversely, an increased number of branched junctions were observed when 5,10,15,20-Tetrakis(4-aminophenyl)porphyrin molecule was employed as tetra-amino linker; in this case, the SWCNT average length results to be of 329 ± 265 nm and this may be associated to the increased number of amino groups on the molecular linker.

Building upon the SWCNT junction formation *via* direct amidation, an improved copper-free click chemistry strategy was successful. In this case, SWCNT ends were functionalised with amine molecules bearing cyclooctyne or azide functional groups (highlighted in green) *via* amidation reaction, resulting in azido or cyclooctyne end-functionalised SWCNTs. Upon mixing azido and cyclooctyne end-functionalised SWCNTs, static linear SWCNT junctions were obtained by the formation of triazole conjugates that link carbon nanotube tips. In our first experiment, DBCO-amine was employed as cyclooctyne molecule and the average SWCNT length resulted to be of 371 ± 209 nm after junction formation. However, the best results were achieved by using BCN-amine as cyclooctyne molecule, where the carbon nanotube length increased to a value of 509 ± 242 nm. This is probably due to the high reactivity of the click chemistry reaction and the longer carbon chain between the amino group and the BCN ring in the linker, which overcomes the steric hindrance issue of the nanotubes.

The formation of SWCNT linear junctions paves the way for the next generations of single-molecule nano-electronic devices using a facile, environmentally friendly and low-cost in-solution strategy. Moreover, the formation of SWCNT multiple-junctions

will allow to fabricate SWCNT-based three terminal systems that imitate the function of a transistor.

Finally, to the best of our knowledge, the first example of DNA-controlled assembly of individual SWCNTs with QDs, in one-to-one ratio, was presented *via* the use of differing lengths DNA strands (10, 20 and 30 base-pair) as molecular linkers to tune the distance between the nanotube and the QD. In addition, a dynamic behaviour was introduced to the system where the SWCNT-QD distance was modulated by adding and removing K^+. Specifically, upon introduction of K^+ cations, a G-quadruplex DNA structure is formed and the distance between the QD and SWCNT decreases, resulting in the quenching of QD fluorescence. This process was then reverted by removing K^+ cations with the aid of a cryptand 222, which has a strong affinity for K^+. This opens the possibility of using DNA as molecular linker for carbon nanotube junction formation, and also of implementing a dynamic behaviour to our system. The formation of SWCNT dynamic linear junctions will be in-depth explored in the next chapter.

CHAPTER 4: SWCNT Dynamic Linear Junctions

In the previous chapter, we have discussed the in-solution SWCNT static linear junctions formation and its importance for nano-technological applications. The aim of the study here presented is to introduce a dynamic behaviour to the SWCNT junctions, which plays an important role in the fabrication of SWCNT-based stimuli-responsive molecular systems. Indeed, the ability to switch the coupling between single SWCNT segments, forming individual junctions, is of great importance for their future implementation in nano- and molecular-electronic smart devices.[282,292–294] Although different technologically-relevant nanomaterials have been designed to respond to changes in the surrounding medium,[295,296] the in-solution SWCNT reversibly reconfigurable linear junctions formation has yet to be proved. As demonstrated in Paragraph 3.3, DNA is an interesting biopolymer for the implementation of a dynamic behaviour in nanomechanical architectures[122,286] because of its well-known chemistry (i.e., several modifications are available for the attachment of functionalities or nanoparticles) and the ability to act as an actuator that responds to a number of different stimuli, depending on its nucleotide sequence. Several studies reported the use of DNA as the molecular material for the construction of designed nano-objects[297,298] or as a scaffold for the assembly of nanoparticles with precise spatial arrangement.[299,300] Furthermore, various response mechanisms to different stimuli were demonstrated to be available for the activation of the dynamics of specific DNA sequences, including strand-displacement,[301] ligand–aptamer complex formation,[302] noncanonical base-pairing,[303] and 3D motif formation (e.g., G-quadruplex and i-motif).[304,305]

In this chapter, we present a strategy for the SWCNT dynamic linear junctions formation in aqueous solution, employing DNA as a molecular linker: the dynamic behaviour of the SWCNT junctions is controlled by the interaction of the DNA specific sequences with selected external stimuli. Specifically, we fabricated linear assemblies of individual DNA-wrapped SWCNTs by their end-functionalisation with two partly

complementary azido-modified single strands of DNA. The strands can hybridise to form a partial duplex under neutral pH conditions, thus forming SWCNT linear junctions. The formed SWCNT junctions were disassembled by changing the pH of the solution from 7 to 5, *via* the formation of a more stable i-motif structure at acidic pH, hence destabilising the DNA partial duplex linking the nanotubes. The individual SWCNTs were then subjected to neutral pH, to restore the DNA duplex junctions, thus demonstrating the reversibility of the system.

Additionally, we extended the study demonstrating the construction of SWCNT dynamic junctions that operate *via* the strand-displacement mechanism. The approaches developed in this work allowed us to obtain SWCNT reconfigurable linear junctions, as indicated by AFM morphological analysis and further supported by time-dependent fluorescence characterisations.

4.1 COVALENT DNA-FUNCTIONALISATION

HiPco SWCNTs were used in this study and were dispersed as-purchased in aqueous solutions *via* DNA wrapping procedure described in Paragraph 2.2.2. The starting DNA-wrapped SWCNTs had an average length of 131 ± 72 nm as determined by AFM analysis and statistical analysis of the nanotube length distribution (see Figure 4 – 1).

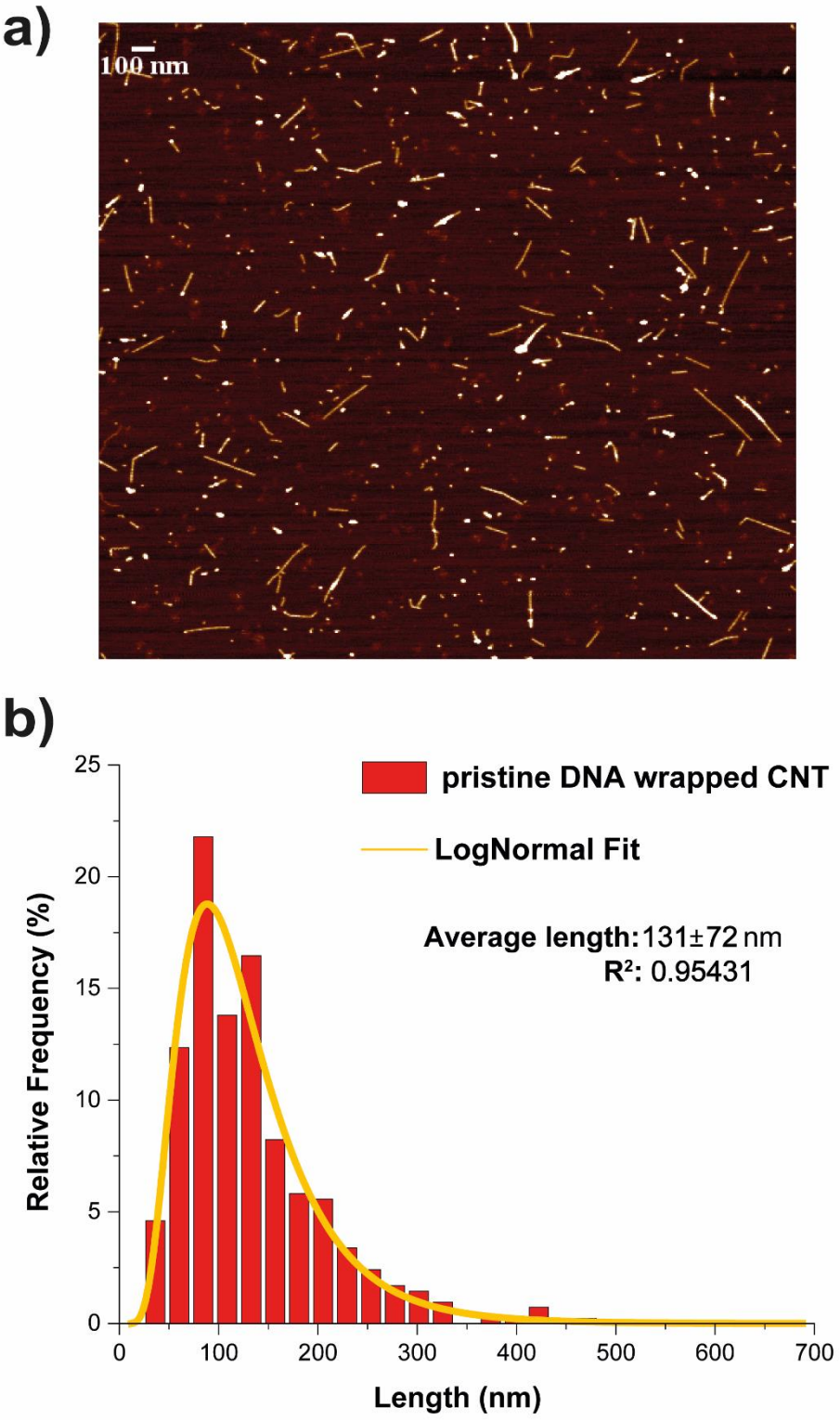

Figure 4 - 1 *(a) AFM topographical image and (b) length distribution with fitted curve of DNA-wrapped SWCNTs (data size: 413 counts).*

The solution containing the DNA-wrapped SWCNTs was mixed with methanol in a water-methanol 1:20 final ratio; this solution was divided in two aliquots, and while DNA sequence (**1**) was added to the first one, DNA sequence (**2**) was added to the second aliquot (all DNA sequences used in this study are listed in Table 1 in Paragraph 2.1). DNA sequences (**1**) and (**2**) are 5'-azido-modified oligonucleotide strands that include in their sequences a cytosine (C)-rich or guanine (G)-rich domain, respectively, that are partially complementary to one another. In order to covalently functionalise the ends of the nanotubes with DNA, the two nanotube solutions were UV-irradiated with a medium pressure immersion mercury lamp to promote the formation of reactive nitrene groups, which in proximity of the free-SWCNT-tips form aziridine photoadducts by a cycloaddition reaction,[68,306,307] as shown in Figure 4 – 2. After centrifugal filtration to remove the unreacted excess of (**1**) and (**2**) DNA strands, and subsequent re-dispersion of the modified carbon nanotubes in aqueous solution, (**1**)-functionalised and (**2**)-functionalised SWCNTs were obtained. This functionalisation procedure generates single-walled carbon nanotubes that are covalently and region-specifically linked to the DNA strands: precisely, the SWCNTs carry single DNA molecules at the nanotube ends.[124]

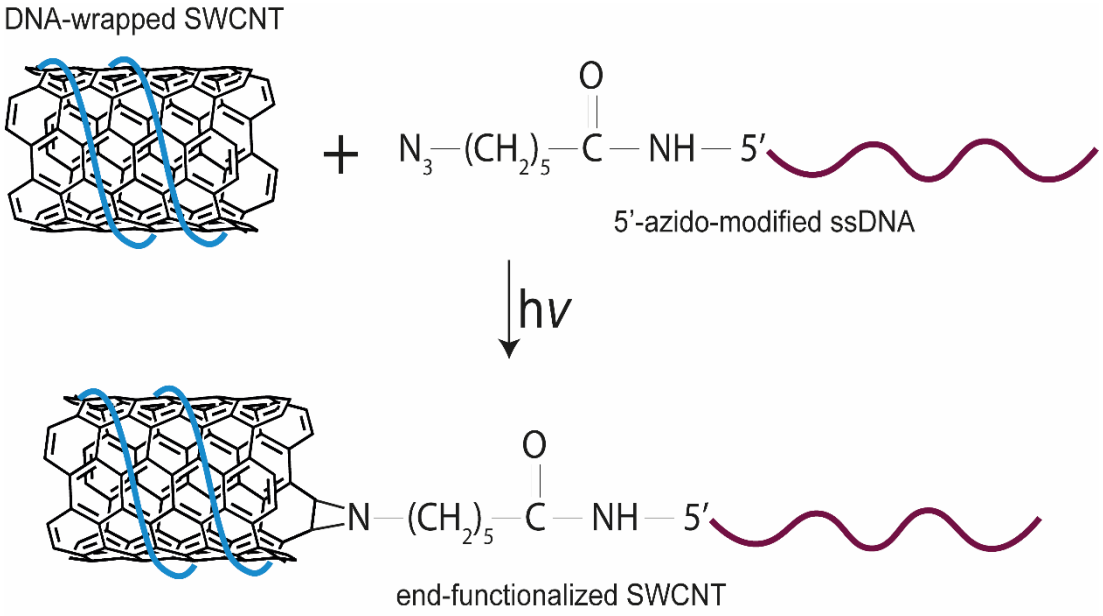

Figure 4 - 2 Schematic end-functionalisation of DNA-wrapped SWCNT.

In order to quantify the amount of azido-DNA reacted with the carbon nanotubes, the concentration of DNA in the filtered solutions was estimated by spectrophotometry: readings were taken at a wavelength equal to 260 nm. The initial concentration of both (**1**) and (**2**) in the solutions before irradiation with the mercury lamp was 2 μM, whereas the concentration of the removed and unreacted DNA in the filtered solution was found to be equal to 0.19 and 0.17 μM for (**1**) and (**2**), respectively (see Figure 4 – 3). Although most of the DNA seemed to have reacted, a direct quantification of the DNA coupled to the SWCNT ends is, at the moment, still under investigation.

As previously discussed, the DNA wrapping strategy protects the nanotube side-walls, leaving only the tube-ends available for further functionalisation: this method thus provides an easier and one-step strategy, for the selective functionalisation of SWCNT termini with azido-modified DNA strands, over the amidation strategy described in Chapter 3.

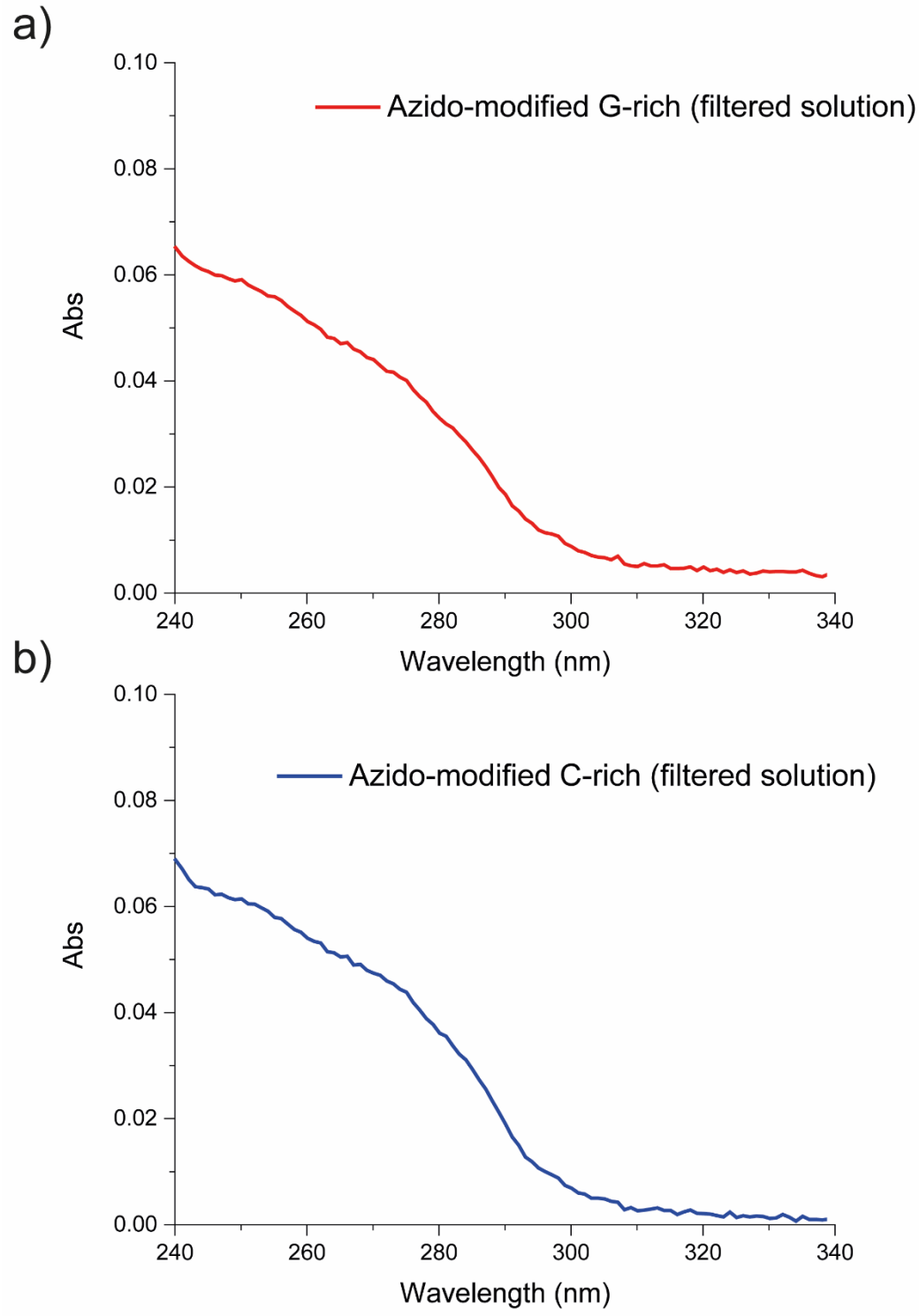

Figure 4 - 3 *(a) UV absorbance spectrum of azido-modified G-rich DNA solution in the filtered solution. Estimated concentration in the supernatant: 0.17 µM; calculated extinction coefficient: 301,800 L/(mole·cm). (b) UV absorbance spectrum of azido-modified C-rich DNA solution in the filtered solution. Estimated concentration in the supernatant: 0.17 µM; calculated extinction coefficient: 285,000 L/(mole·cm).*

4.2 pH-Responsive SWCNT JUNCTIONS

The aforementioned (**1**)-functionalised and (**2**)-functionalised SWCNTs were employed as the building blocks for the formation of DNA-linked SWCNTs. In particular, (**1**) and (**2**) can hybridise at neutral pH forming a partial DNA duplex (calculated Tm = 34 °C). In order to direct the assembly of the DNA-functionalised carbon nanotubes, (**1**)-functionalised and (**2**)-functionalised SWCNTs were then mixed in equal amounts at pH = 7 in a solution containing MOPS (2 mM) and NaCl (400 mM); this leads to the (**1**)/(**2**)-linked SWCNTs formation *via* DNA hybridisation that results in the duplex (**1**)/(**2**), as shown in Figure 4 – 4.

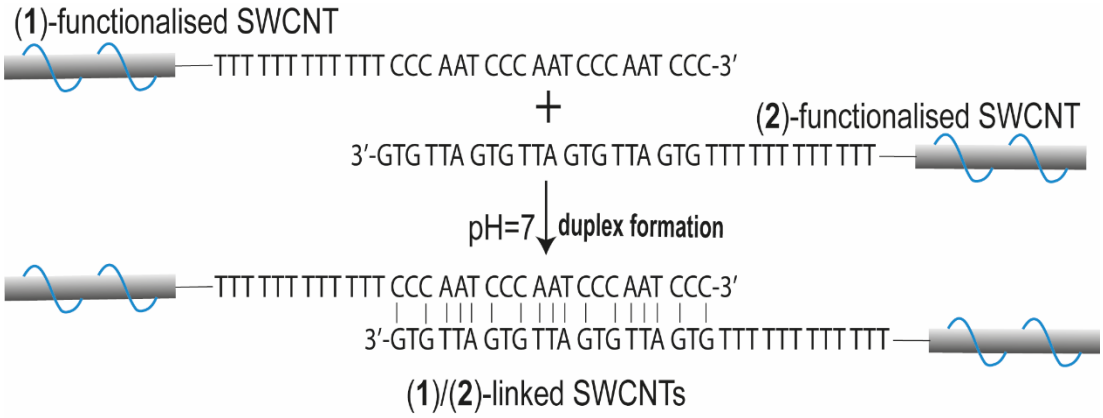

Figure 4 - 4 *Schematic SWCNTs junction formation via DNA hybridisation.*

To demonstrate and monitor the formation of the SWCNT junctions at pH = 7, diluted (**1**)/(**2**)-linked SWCNTs solution was cast on mica and the substrate was imaged with AFM. We performed a statistical analysis of the average tube length; the average length of the (**1**)/(**2**)-linked SWCNTs was found to be 184 ± 97 nm (see Figure 4 – 5). In line with our previous SWCNT length analysis of junction formation in Chapter 3, the increase in the SWCNT average length from 131 ± 72 (SWCNT starting material) to 184 ± 97 nm (assembled DNA-wrapped SWCNTs) indicates the formation of the junctions at pH = 7.

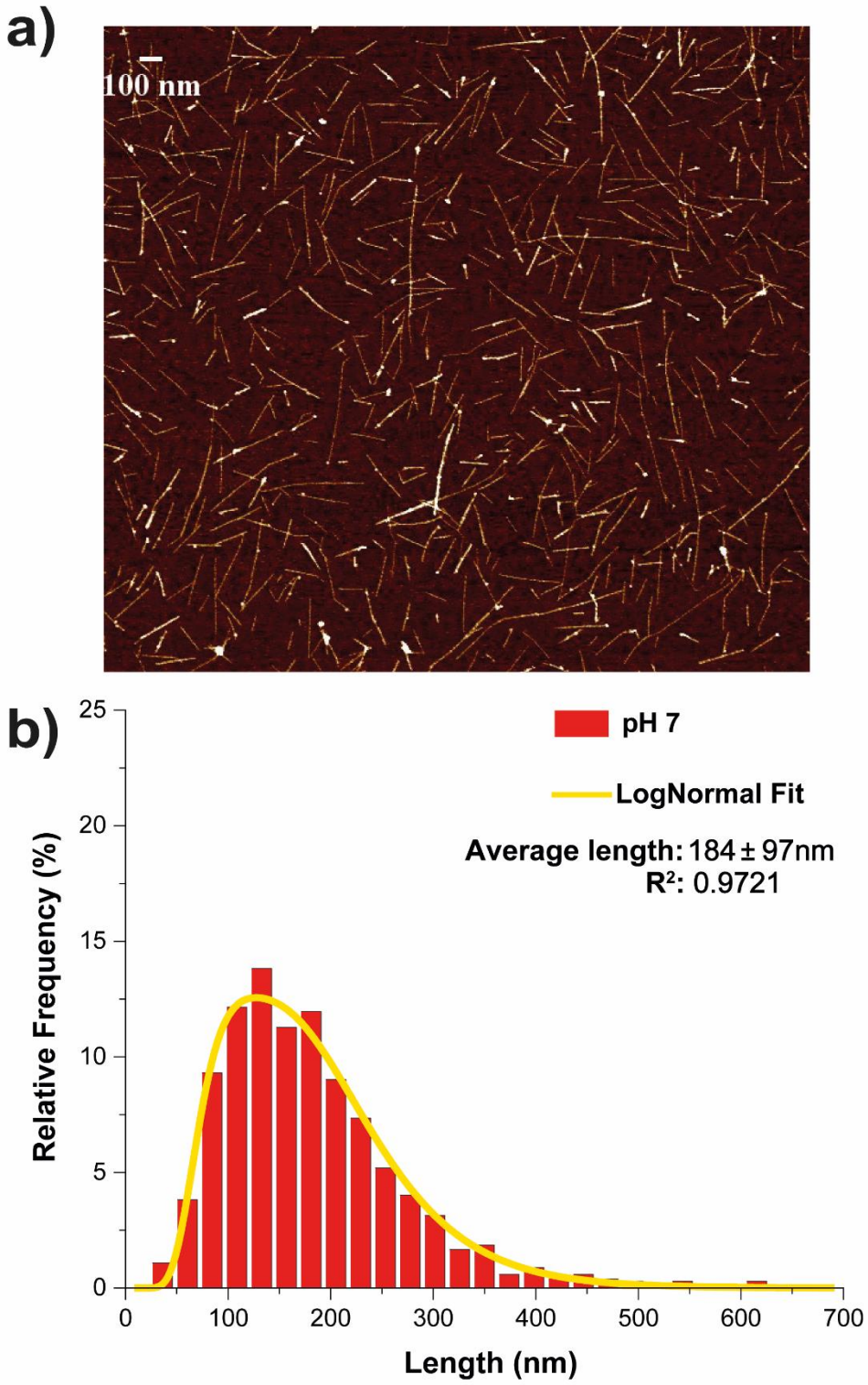

Figure 4 - 5 *(a) AFM image and (b) length distribution with fitted curve of assembled SWCNTs at pH 7 (data size: 500 counts).*

Both (**1**) and (**2**) DNA strands contain different domains: a domain that forms the DNA partial duplex (**1**)/(**2**) and a thymine-rich region. By mixing the so-formed junctions with a biotin-modified adenine-rich (**3**) DNA sequence, which is complementary to the thymine-region, we could introduce biotin functionalities at the site of the junction formation. The presence of the biotin between the two SWCNT segments in the junctions was then exploited to label the junction site *via* the addition of streptavidin that strongly and specifically interacts with biotin. This allowed us to unequivocally locate the site of the junction formation *via* AFM imaging, hence, further demonstrating the successful SWCNT assembly.

For this purpose, we drop-cast low-coverage films of (**1**)/(**2**)-linked SWCNTs solution at pH = 7 on muscovite mica, then drop-cast a streptavidin solution (500 nM), and after washing off the streptavidin excess with distilled water, the mica substrate was imaged by AFM.

Figure 4 – 6 shows a representative AFM image and respective height profiles of a streptavidin-labelled SWCNT junction, corresponding to the expected nanotube and protein sizes: this confirms junction formation.

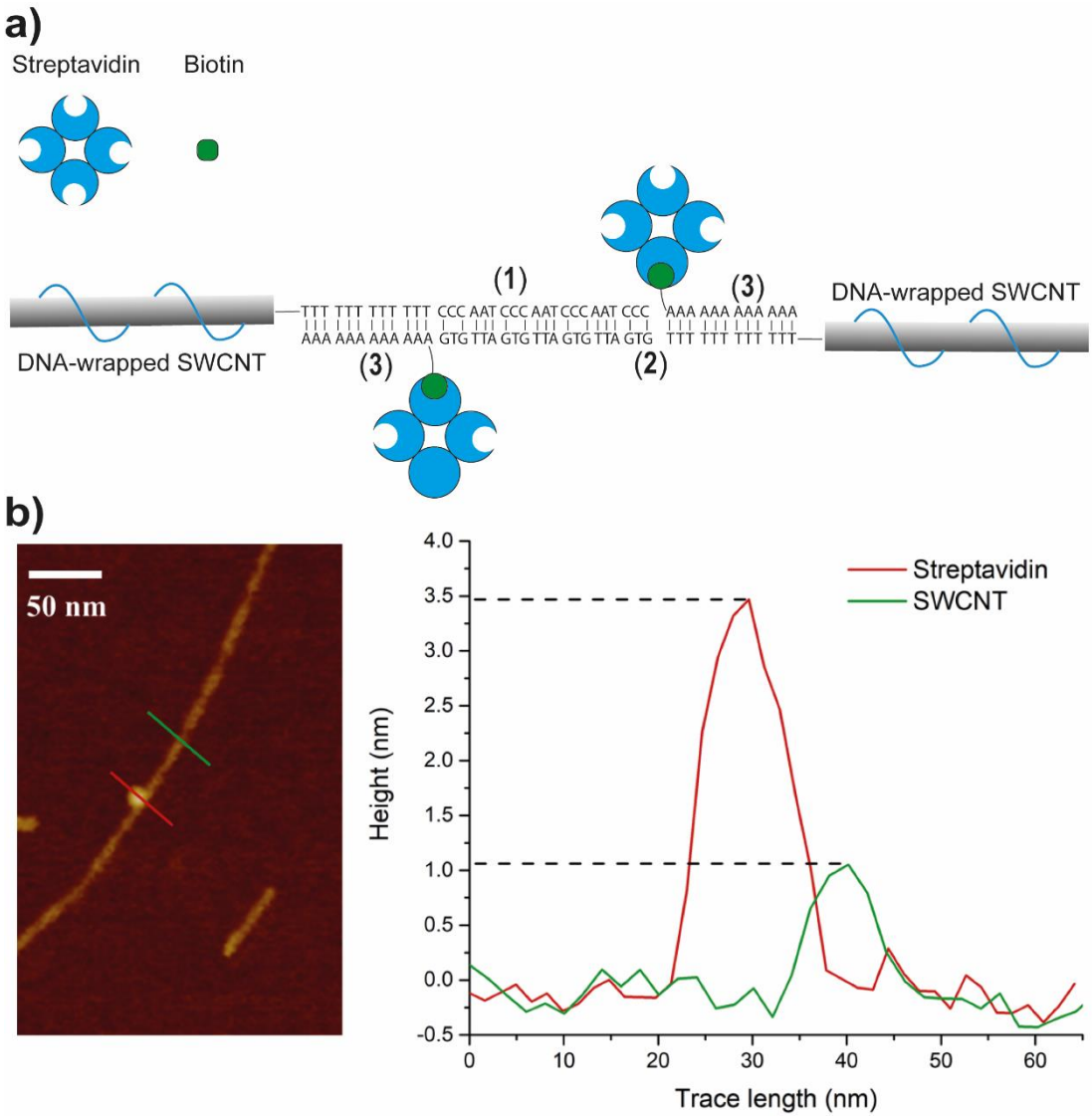

Figure 4 - 6 *In situ streptavidin-biotin labelling: (a) schematic of the streptavidin-biotin labelled site of the junction formation (b) representative topographical AFM image of a biotin-streptavidin labelled (**1**)/(**2**)-linked SWCNTs with corresponding AFM height analysis.*

It is worth mentioning that although at the junction point two biotin-labelled oligonucleotides are hybridised, it is assumed that only one streptavidin can bind to the site because of steric hindrance; this assumption is confirmed by AFM analysis of the junctions (see Figure 4 – 7).

Although the AFM image in Figure 4 – 6b shows a straight junction, bent junctions are present in all our AFM images; this is clear from the AFM images presented in Figure 4 – 5 and Figure 4 – 7. This is likely an effect of the physisorption of the SWCNT junctions from solution to surfaces, as previously observed by us and others.[122,123]

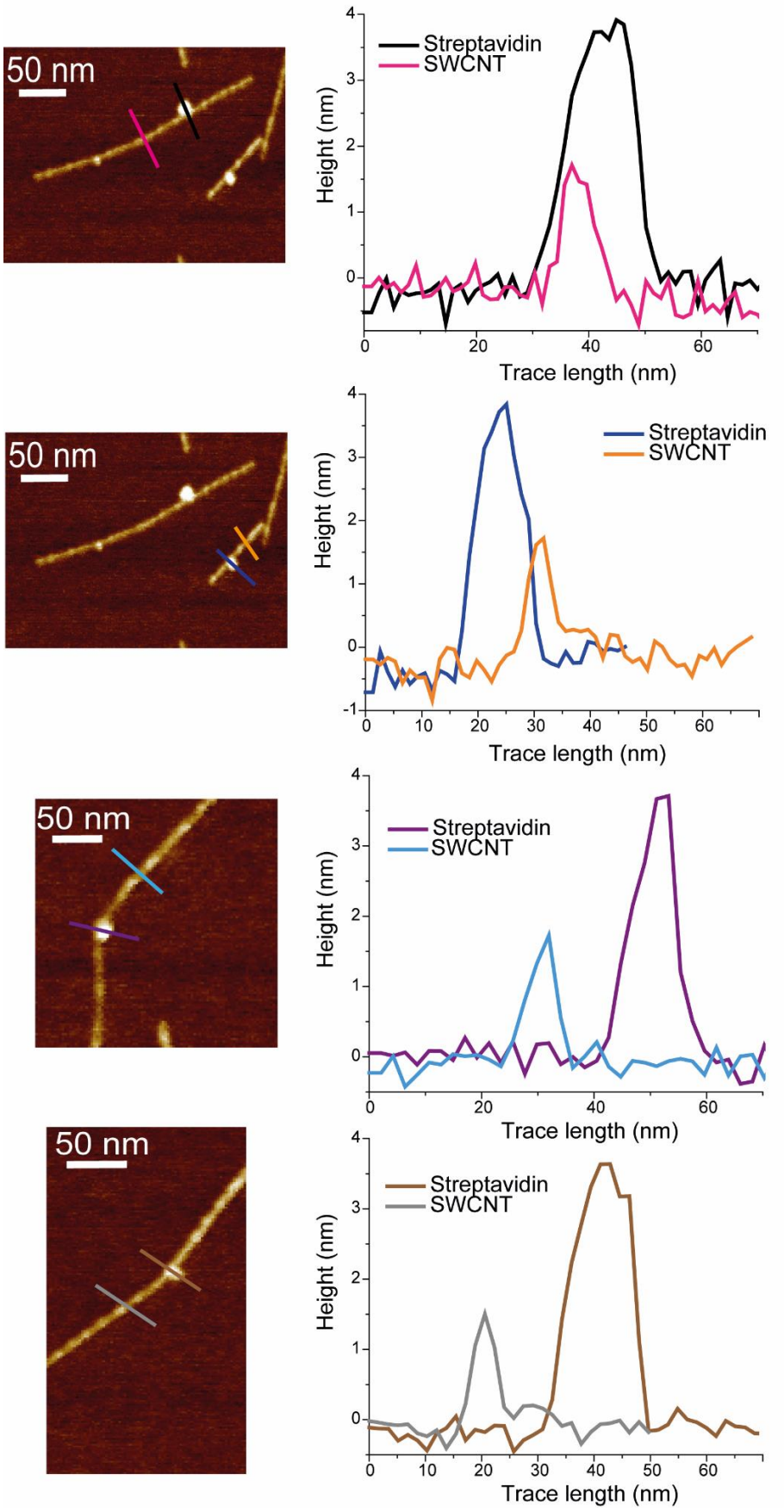

Figure 4 - 7 *Representative topographical AFM images of biotin-streptavidin labelled DNA-SWCNT junctions with corresponding AFM height analysis.*

At neutral pH, DNA strand (**1**) is available for duplex formation and consequently can hybridise with its complementary DNA strand (**2**) forming nanotube junctions. Conversely, when the pH of the solution is acidic (pH = 5), (**1**) forms an intercalated motif (*i*-motif structure),[129,304,308] leading to the disassembly of the DNA-linked SWCNT junctions. This behaviour can then be exploited for the pH-controlled assembly/disassembly of SWCNT junctions.

It should be noted that it was necessary to introduce mismatches in the DNA duplex forming the carbon nanotube junction in order to generate similar levels of thermal stability between the partial duplex (**1**)/(**2**) and the competing i-motif structure, which would be too unstable compared to the complete duplex (**1**)/(**2**), otherwise resulting in an inefficient separation of the junction at pH = 5.

To demonstrate and monitor the disassembly of the DNA-linked SWCNT junctions as a function of pH, we cast acidic solutions (pH = 5) on mica and imaged the substrates with AFM. The average length of the SWCNT junctions after changing the pH of the solution from 7 to 5 was found to decrease to 148 ± 80 nm (see Figure 4 – 8), suggesting the separation of the junctions upon reducing the pH from 7 to 5.

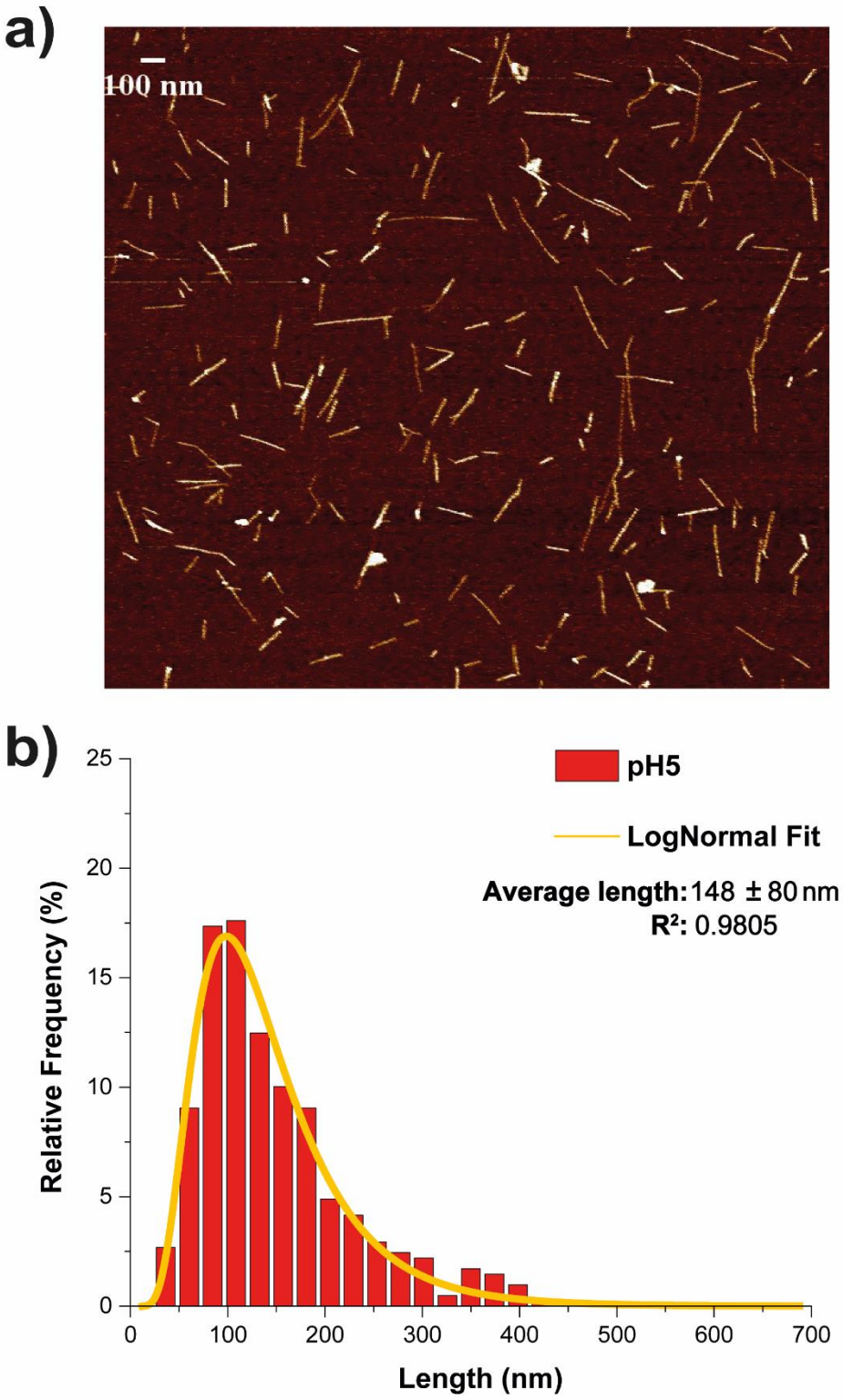

Figure 4 - 8 *(a) AFM image and (b) length distribution with fitted curve of disassembled SWCNT after acidification of the solution to pH= 5 (data size: 409 counts).*

To further prove the successful pH-controlled assembly/disassembly of SWCNT junctions, time-dependent fluorescence analysis of the nanostructures was performed. We mixed (**1**)-functionalised and (**2**)-functionalised SWCNTs in equal amounts at pH = 7 in a solution containing MOPS (2 mM) and NaCl (400 mM), as previously described, to form the junctions and added a quencher (Q)-modified DNA sequence (**4**), which is complementary to the thymine-domain and binds at the junction site. We then added to this solution a cyanine 3 (Cy3)-modified DNA (**5**), which is partially complementary to (**2**).

Figure 4 – 9 shows the pH-controlled mechanism of the SWCNT–DNA junction assembly/ disassembly, in the presence of the quencher and fluorophore labels (**4**) and (**5**), respectively.

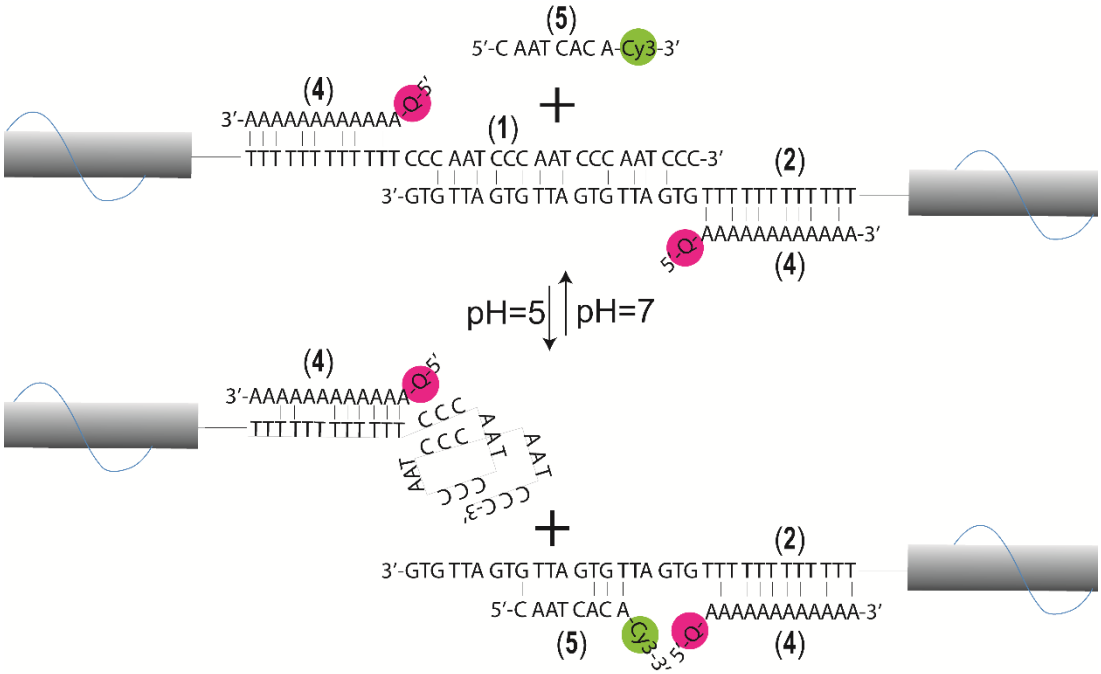

Figure 4 - 9 *Schematic of the pH-controlled system in the presence of quencher and fluorophore labels for time-dependent fluorescence analysis.*

At pH = 7, (**5**) is free in solution as (**2**) is not available due to a more stable (**1**)/(**2**) duplex structure; when the pH is decreased from 7 to 5, the disassembly of the junction frees (**2**), allowing it to hybridise with (**5**); this in turn results in the quenching of Cy3 because of its proximity to Q.

The sequences (**4**) and (**5**) were designed to position the Q and Cy3 functionalities at a specific separating distance. From geometric considerations of the DNA molecule, we calculated the distance separating Cy3 and the quencher in the duplex structure (**2**)/(**4**)/(**5**) to be equal to 1.7 nm. This results in the efficient quenching of the fluorescence emission at pH = 7, whereas at pH = 5, the large separating distance between Cy3 and Q in the single-strand (**5**) and duplex (**2**)/(**4**) results in the inefficient quenching of the fluorophore.

We monitored this change in fluorescence in real-time, by varying the pH from 7 to 5 in multiple cycles, and recording the fluorescence emission of Cy3, as shown in Figure 4 – 10. When 0.6 µL of a acetic acid (10% vol/vol) was added, the fluorescence signal dropped, while the emission intensity was finally recovered by adding 0.75 µL of ammonia solution (1M) into the SWCNT pH system. This allowed us to confirm the reversible pH-dependent assembly/disassembly of the DNA−SWCNTs.

It is worth mentioning that Cy3 fluorophore emission is insensitive to pH changes in the interval pH = 5 to pH = 7 thus in the described analysis the Cy3 emission intensity changes depend only on the average distance separating the fluorophore-quencher pair.

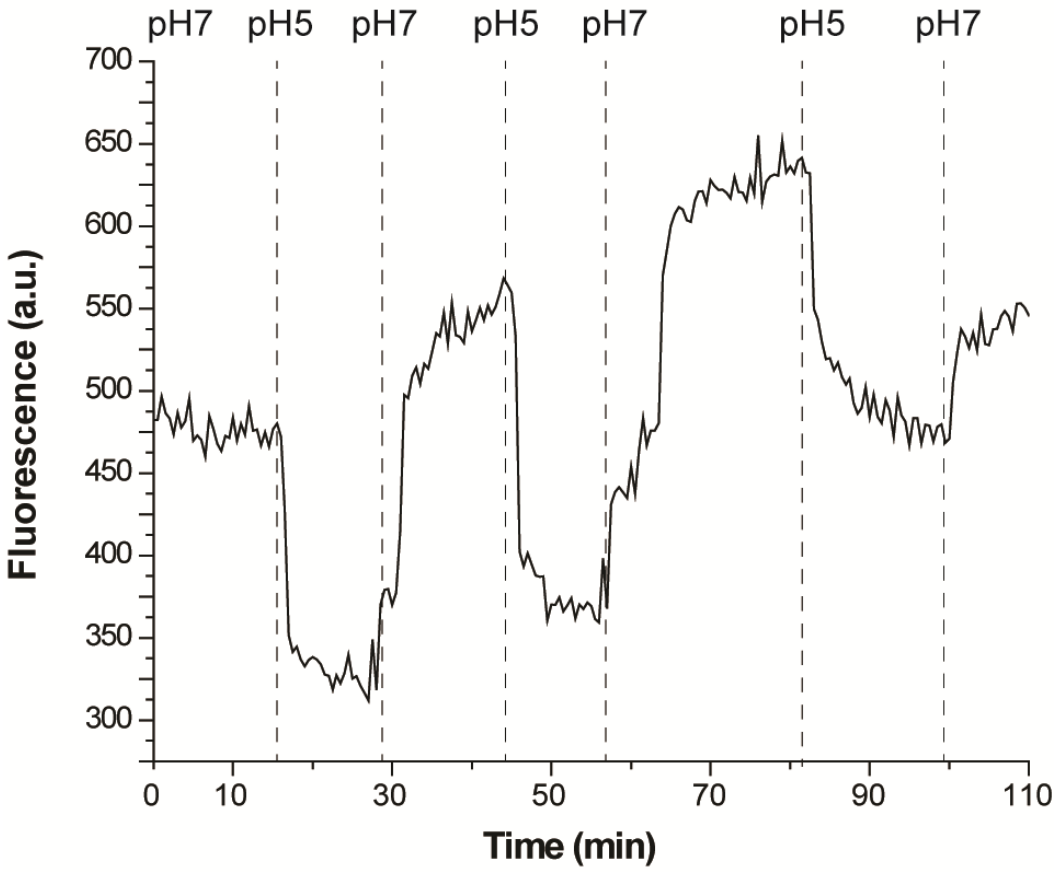

Figure 4 - 10 *Real-time fluorescence changes of the pH-controlled DNA−SWCNT junctions. The fluorescence emission of Cy3 is monitored while reversibly varying the pH between 7 and 5 in multiple cycles. High fluorescence emission corresponds to the formed DNA− SWCNT junctions at pH = 7 [where Cy3-modified strand (**5**) is free in solution], whereas low fluorescence emission corresponds to the separation of the DNA−SWCNT junctions at pH = 5 [where the Cy3-functionalized (**5**) is quenched by the Q-modified strand (**4**)].*

It should be noted that the incremental drift in the fluorescence intensity is likely due to the slow aggregation and precipitation of the SWCNTs; this results in a time-dependent proportional decrease in optical density of the mixture and increased collected emission from the fluorophore. Additionally, small deviations are observed due to the manual operation and by small volume additions of concentrated acid/base.

To prove that the quenching effect of the carbon nanotubes on the fluorophores is not significant, in the pH-responsive system, we performed the same experiment in the absence of SWCNTs (see Figure 4 – 11).

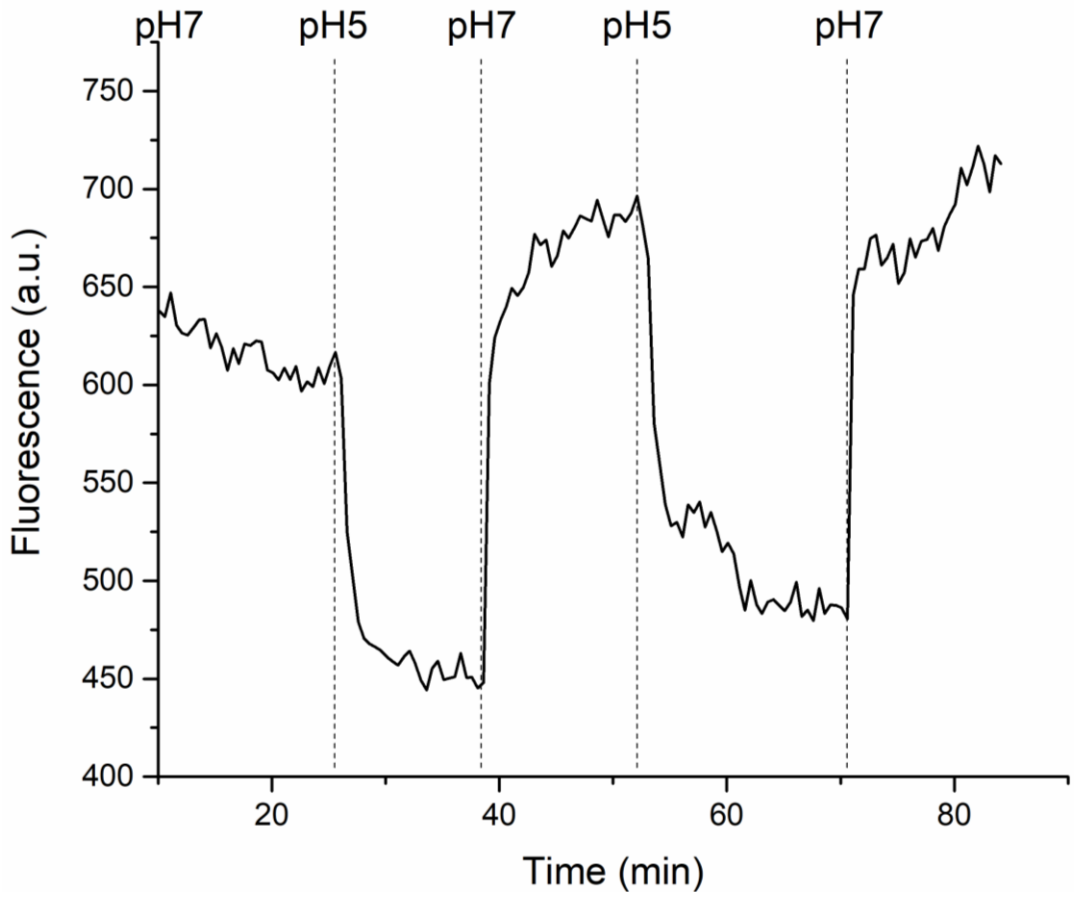

Figure 4 - 11 *Real-time fluorescence changes of the pH-switch system in absence of SWCNTs. The fluorescence emission of Cy3 is monitored while reversibly varying the pH between 7 and 5, in multiple cycles.*

Additionally, to confirm the selectivity of this pH system, we assembled nanotube junctions employing a dsDNA, as a linker, which is not affected by changes in pH. As previously described, we functionalised SWCNT with 5'-azido-modified (**1'**), we mixed (**1**')-functionalised and (**2**)-functionalised SWCNTs in equal amounts at pH = 7, and we then acidified the solution to pH = 5. Figure 4 – 12 shows how the average length of (**1'**)/(**2**)-linked SWCNTs does not vary from pH 7 to 5.

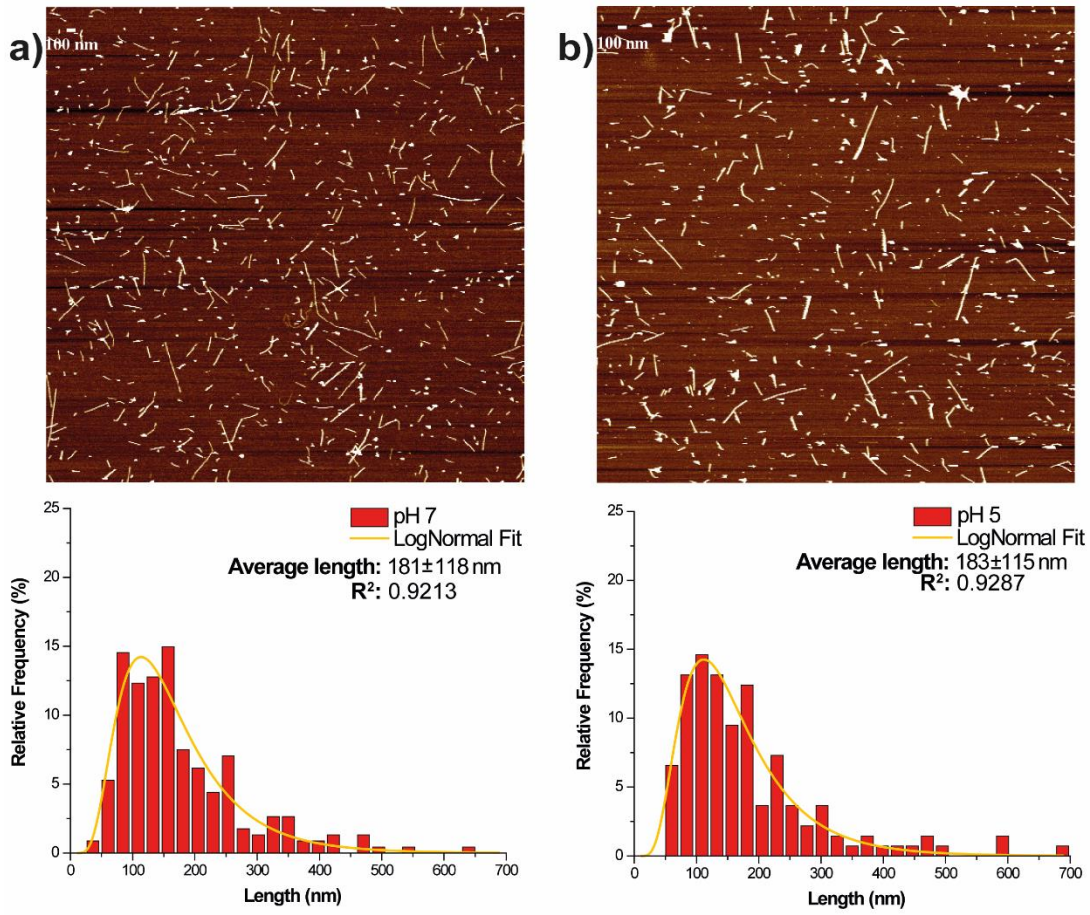

Figure 4 - 12 *AFM images of DNA-linked SWCNTs junctions not affected by changes in pH (a) at pH= 7 with corresponding length distribution of the fitted curves, data size: 228 counts; (b) at pH= 5 with corresponding length distribution of the fitted curves, data size: 137 counts.*

4.3 Strand-Displacement SWCNT JUNCTIONS

In order to explore the versatility of the approach developed here, we extended our studies by inducing the disassembly of DNA-SWCNT junctions with a different stimulus. A fuel DNA sequence (**SD1**), a DNA sequence that activates the disassembly process, was designed to be capable of destabilising the DNA duplex forming the DNA-SWCNT junction, *via* strand-displacement.[301,309,310]

Upon addition of the designed fuel DNA strand (**SD1**) to the DNA-linked SWCNT junctions solution at neutral pH, strand (**2**) is displaced from duplex (**1**)/(**2**) by (**SD1**), resulting in a new duplex (**1**)/(**SD1**) and free DNA strand (**2**). AFM images of disassembled SWCNT junctions by strand-displacement were taken after the addition of (**SD1**) to the SWCNT junctions: the disassembly was confirmed by statistical analysis of the average tube length, which was found to be 141 ± 79 nm (see Figure 4 – 13), in accordance with the results obtained for the disassembled SWCNT junctions at acidic pH (148 ± 80 nm).

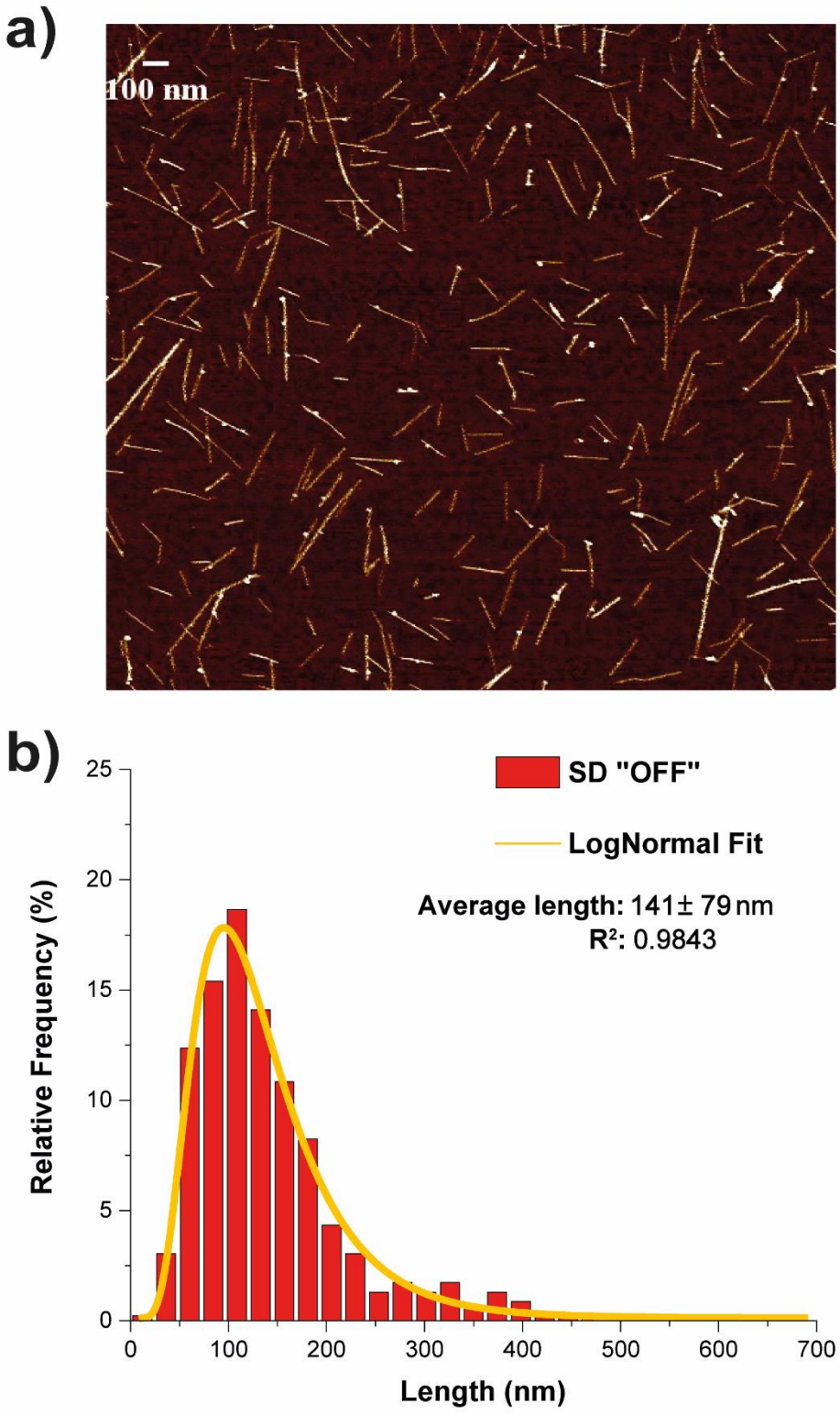

Figure 4 - 13 *(a) AFM image and (b) length distribution with fitted curve of disassembled SWCNT upon addition of (**SD1**) to SWCNT junctions solution (data size: 461 counts).*

To make this new system reversible, we introduced an anti-fuel DNA strand (**SD2**), a DNA sequence that reactivates the assembly process, which promotes the recovery of the assembly of DNA-SWCNT junctions by a second strand-displacement event. This was confirmed by time-dependent fluorescence measurements, as shown in Figure 4 – 14.

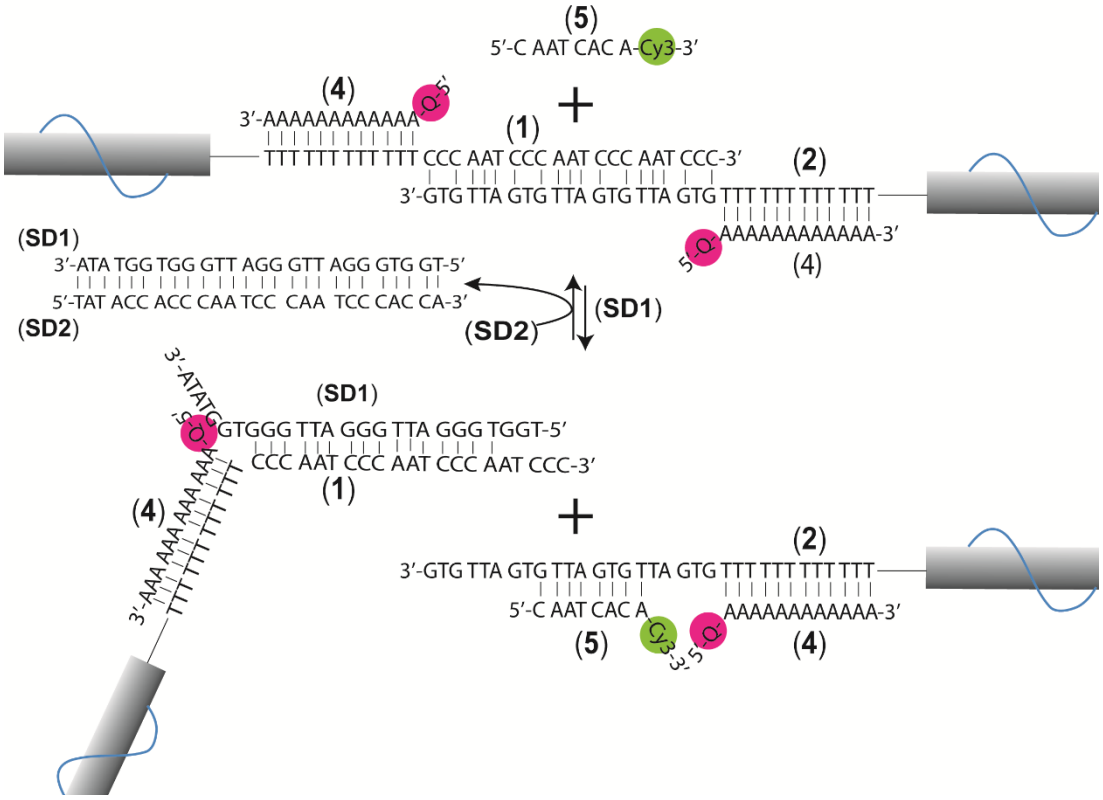

Figure 4 - 14 *Schematic of the strand-displacement system in the presence of quencher and fluorophore labels for time-dependent fluorescence analysis.*

Quencher-labelled DNA-SWCNT junctions were mixed together at pH = 7 with (**5**); at neutral pH, (**1**)-functionalised and (**2**)-functionalised SWCNTs form SWCNT junctions and the solution is characterised by a high fluorescence intensity because of the free Cy3-modified DNA (**5**) in solution. Upon addition of (**SD1**), the junction is separated and (**5**) binds to (**2**), resulting in the close proximity of Cy3 to Q and the low emission of fluorescence of Cy3. The following addition of (**SD2**) displaces (**SD1**) from the duplex (**1**)/ (**SD1**), resulting in the new duplex (**SD1**)/(**SD2**), and the restoration of the original SWCNT junction *via* the duplex (**1**)/(**2**). The concomitant release in solution of the fluorophore-modified strand (**5**) recovers the original high level fluorescence emission from Cy3 because of the large spatial separation from the quencher unit.

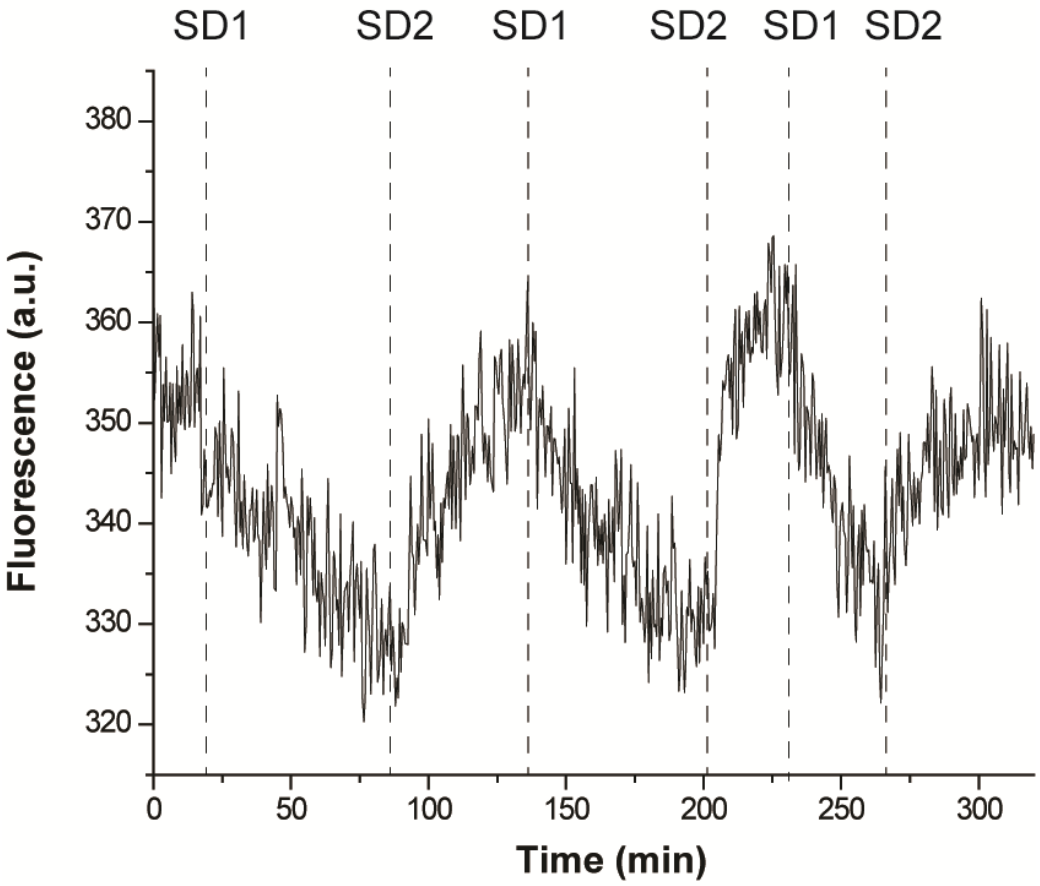

Figure 4 - 15 *Real-time fluorescence changes of the strand-displacement controlled DNA−SWCNT junctions in the presence of Q-modified oligonucleotide (**4**) and Cy3-modified strand (**5**). Addition of (**SD1**) and (**SD2**) strands, in multiple cycles, results in the separation and recovery of the junction assembly, respectively. High fluorescence emission corresponds to the free Cy3-modified strand (**5**) in solution; whereas low fluorescence emission corresponds to the quenching of Cy3-(**5**) upon separation of the DNA−SWCNT junctions.*

Upon cyclic sequential addition in solution of (**SD1**) and (**SD2**) strands, the reversible assembly and disassembly of the DNA-SWCNT junctions is demonstrated by the low and high level of emission from Cy3-modified strand (**5**). Although a high level of fluorescence characterises the free fluorophore (formed DNA-SWCNT junction), the close proximity of the fluorophore-quencher pair functionalities in the separated junctions is characterised by low fluorescence.

Figure 4 – 15 shows the time-dependent fluorescence changes of the strand-displacement controlled SWCNT junction assembly/disassembly system, in the presence of the quencher and fluorophore labels (**4**) and (**5**).

As per the pH-responsive system, to verify that the quenching effect of the SWCNTs on the Cy3 is not significant, we performed the same experiment in the absence of SWCNTs for the strand-displacement system, as shown in Figure 4 – 16.

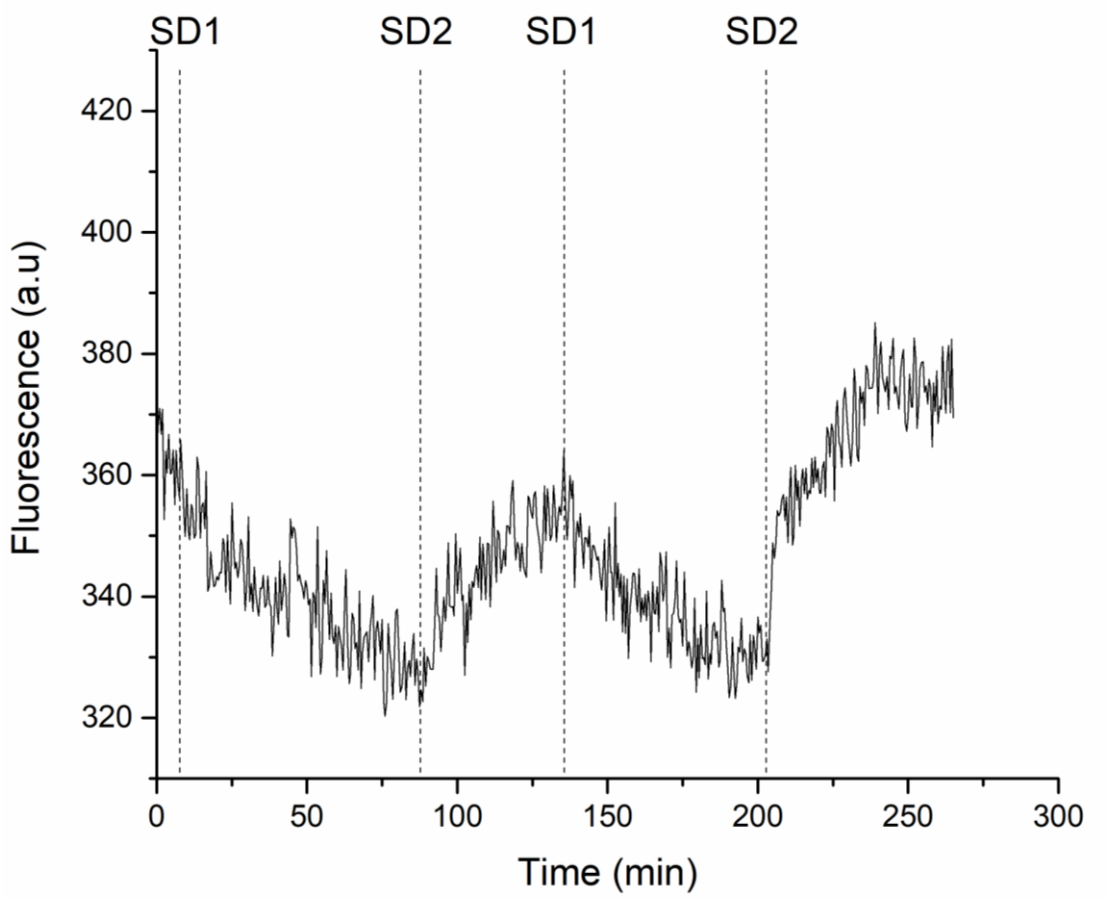

Figure 4 - 16 *Real-time fluorescence changes of the strand-displacement system in absence of SWCNTs. The fluorescence emission of Cy3 is monitored while reversibly adding (**SD1**) and (**SD2**) DNA strands, in multiple cycles.*

4.4 CONCLUDING REMARKS

In summary, we have presented a strategy for the controlled and reversible assembly of SWCNT dynamic linear junctions under different stimuli. This was achieved by exploiting the molecular recognition of DNA complementary sequences employed here as linkers. SWCNTs were covalently end-functionalised with azido-modified ssDNA in a one-pot reaction, under UV light. In Table 5 are listed the average tube length of the SWCNTs employed for stimuli-responsive linear junctions formation. The average length of the pristine DNA-wrapped SWCNTs used as starting material for junction formations is of 131 ± 72 nm (highlighted in grey).

Table 5 *List of average SWCNT lengths. Highlights: pristine DNA-wrapped SWCNTs (grey), assembly at pH 7 (green), disassembly at pH 5 (yellow) and disassembly by strand-displacement mechanism (pink).*

SWCNTs	Average SWCNT length (nm)
Pristine DNA-wrapped SWCNTs	131 ± 72
Assembly at pH = 7	184 ± 97
Disassembly at pH = 5	148 ± 80
Disassembly by strand-displacement	141 ± 79

SWCNT assembly was driven at neutral pH by the hybridisation between complementary DNA strands at the nanotube termini. The carbon nanotube length increases from 131 ± 72 nm for the starting material to 184 ± 97 nm after DNA hybridisation at pH 7 (highlighted in green); this increase in length suggests the formation of SWCNT linear junctions. Junction formation was further confirmed by streptavidin-labelling at the site of the SWCNT junction formation. Employing at the junction site a C-rich domain, the SWCNT disassembly was obtained by *i*-motif formation at pH 5; as consequence the nanotube average length decreases to a value of 148 ± 80 nm (highlighted in yellow).

Additionally, we designed the system for the controlled disassembly of SWCNT junctions *via* strand-displacement mechanisms; this resulted in average SWCNT length of 141 ± 79 nm (highlighted in pink). This further demonstrates the versatility of the approach presented here, for the dynamic tuning of DNA-SWCNT junction formation *via* different stimuli. The reversible assembly/disassembly of DNA-SWCNT

junctions, for both the pH-responsive and strand-displacement systems, was controlled by varying the pH or adding fuel/anti-fuel DNA strands; this was confirmed by real-time fluorescence investigations.

The study presented in this work is of interest for the fabrication of solution-processable and stimuli-responsive SWCNT-based systems, also of higher complexity. Moreover, it paves the way for controlling the assembly of other nano-structured materials *via* DNA hybridisation. In this regard, in the next chapter will be discussed the use of DNA as molecular linker for the formation of both static and dynamic MoS_2 layer-by-layer junctions.

CHAPTER 5: MoS_2 LbL Assembly: Static and Dynamic Junctions

DNA is a powerful molecule for the assembly of nanoarchitectures with precise spatial arrangement,[299,300,311–316] and it has been employed in different nanomaterials, from 0-D to 3-D.[317,318] Moreover, DNA allows the formation of dynamic architectures, due to its ability to reconfigure, as a response to different stimuli, depending on the nucleotide sequence.[207,313] Several dynamic DNA-based nano-mechanisms were demonstrated, including non-canonical base-pairing, strand-displacement, 3-D motif formation and ligand−aptamer complex formation; these have further been employed in the assembly of nanostructures exhibiting a dynamic behaviour.[126,127,313,319] In this context, controlling the assembly of molybdenum disulfide (MoS_2) layers into static and dynamic superstructures can impact on their use in optoelectronics, energy, and drug delivery. A further development for the aforementioned applications relies on the control of MoS_2 surface functionalisation, which directly affects its electronic properties and the distance between layers. In this regard, different strategies have been pursued to functionalise exfoliated MoS_2.[208,228,232,253,254,256,320–322] In this chapter, we present a strategy for the controlled layer-by-layer assembly of exfoliated MoS_2 in aqueous solution, employing DNA as molecular linker. We demonstrate the functionalisation of exfoliated MoS_2 layers with thiol-modified DNA, and their assembly *via* DNA hybridisation. Furthermore, to implement a dynamic response, MoS_2 surface was functionalised with specific DNA sequences that reconfigures as a response to specific external stimuli. The DNA-functionalised MoS_2 layers were then assembled into multi-layered MoS_2 nanostructures *via* hybridisation of the DNA complementary linkers, under basic pH conditions. The disassembly process was triggered by the formation of an intramolecular *i*-motif structure, within the DNA tethers, at acidic pH. To demonstrate the versatility of our approach, we also induced the disassembly of the DNA-linked MoS_2 layers *via* a strand-displacement mechanism. This proves the applicability of DNA as linker to drive both the assembly of MoS_2 layers and to implement in their structure a dynamic molecular component.

5.1 MoS_2 STATIC JUNCTIONS

Figure 5 – 1 shows the Raman spectrum of bulk 2H-MoS_2 employed for our experiments: the peak at 383 cm^{-1} corresponds to the in-plane vibration mode of Mo and S atoms in the basal plane (E_{2g}^1), while the peak at 408 cm^{-1} corresponds to the out-of-plane mode of S atoms (A_{1g}).

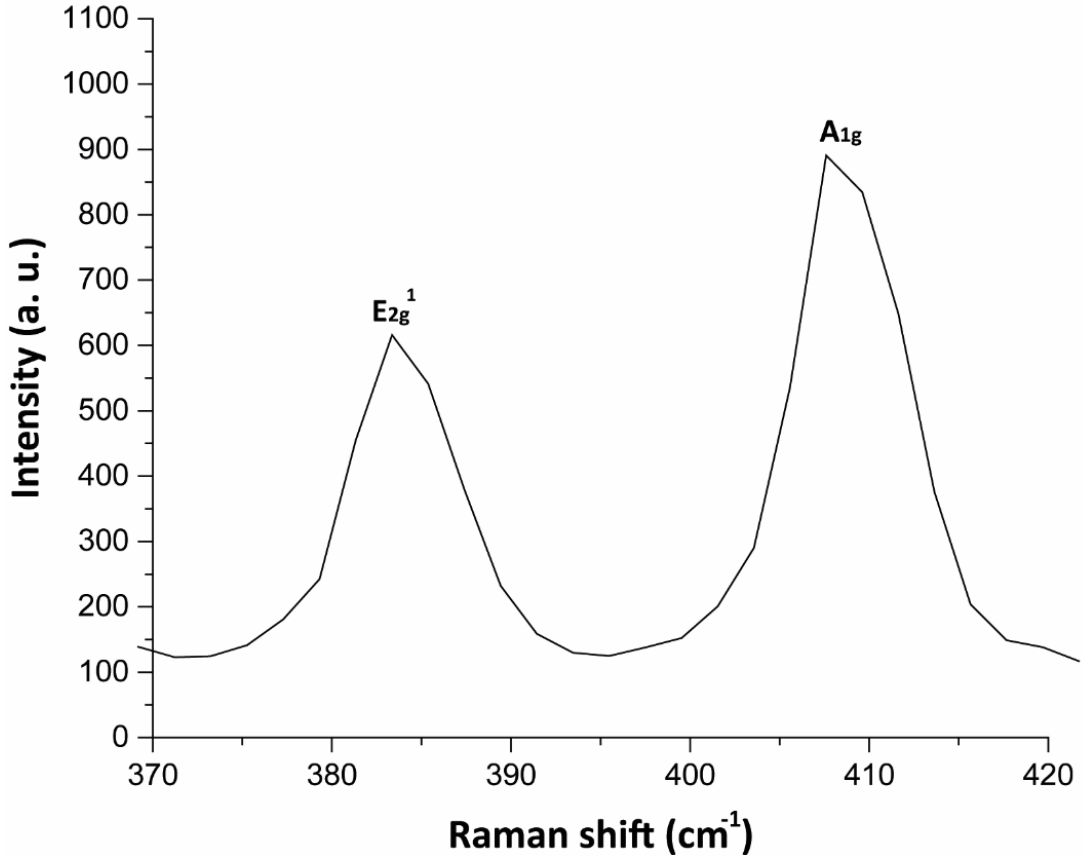

Figure 5 - 1 *Raman spectrum of bulk 2H-MoS_2 showing the typical in-plane vibration mode (E_{2g}^1) at 383 cm^{-1} and the out-of-plane mode (A_{1g}) among the S atoms at 408 cm^{-1}.*

Exfoliated 2H-MoS_2 was obtained by sonicating MoS_2-bulk powder in aqueous sodium cholate solution. The successful exfoliation of bulk 2H-MoS_2 was verified spectroscopically, and through morphological characterisation (Figure 5 – 2).

Raman spectroscopy characterisation shows two strong peaks, corresponding to the in-plane vibration mode (E_{2g}^1) at 385 cm^{-1} and the out-of-plane mode (A^{1g}) of the S atoms, at 410 cm^{-1}, of exfoliated 2H-MoS_2 . The exfoliation also results in the shift of the Raman peaks: as the number of layers decreases, the wavenumber of the E_{2g}^1 mode and the wavenumber of the A_{1g} mode shift to higher frequencies.

In the optical absorption spectrum, the presence of the four peaks further confirms the band structure of exfoliated MoS_2: the A and B peaks, characteristic for MoS_2 dispersions, arise from the interband excitonic transitions at the K point of the Brillouin zone, while the C and D peaks can be assigned to the direct excitonic transition of the M point.

In addition, TEM imaging for the exfoliated MoS_2 nanosheets indicates that the sample exhibits a sheet-like structure.

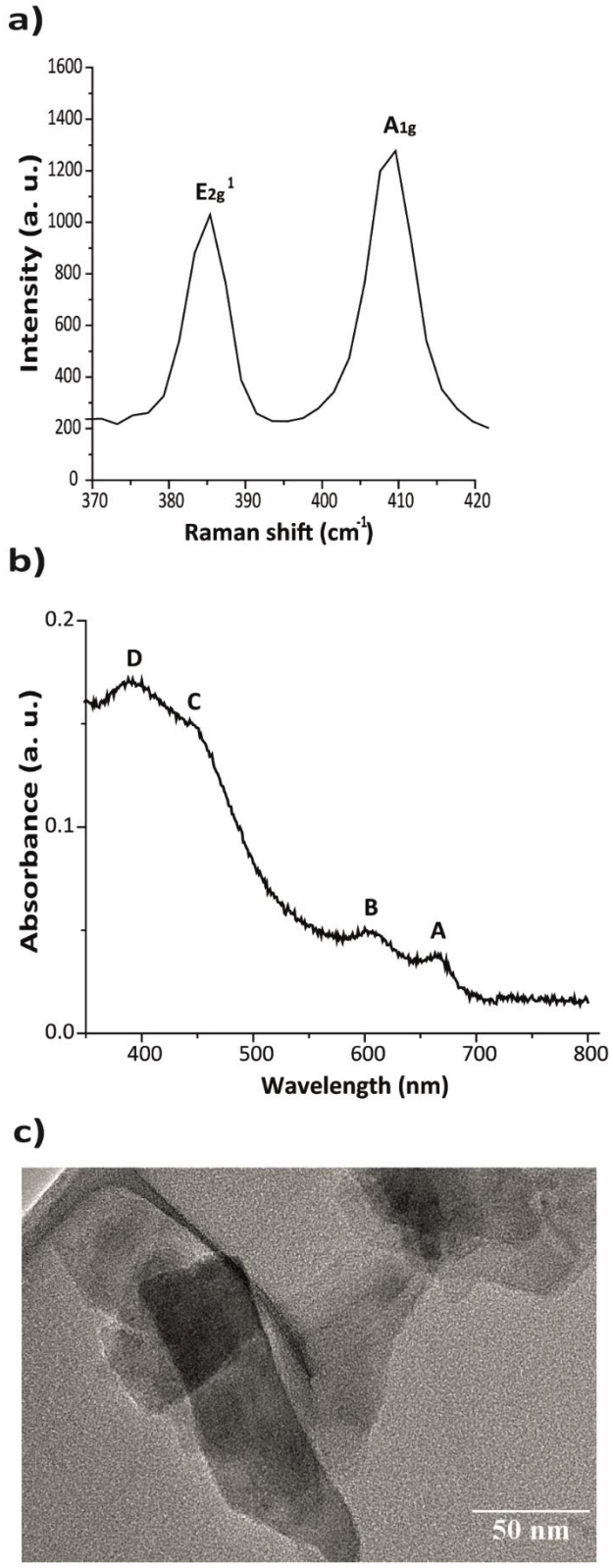

Figure 5 - 2 *Exfoliated MoS_2 obtained by sonicating MoS_2-bulk powder in aqueous sodium cholate. (a) Raman spectrum showing the in-plane vibration mode (E_{2g}^1) and the out-of-plane vibration mode (A_{1g}) of the S atoms; (b) The four absorption peaks confirm the band structure of exfoliated MoS_2: the A and B peaks arise from the interband excitonic transitions at the K point of the Brillouin zone, while the C and D peaks can be assigned to the direct excitonic transition of the M point; (c) representative TEM image of the exfoliated MoS_2.*

In order to drive the assembly, MoS_2 surface was first functionalised with DNA sequences (**1'**) and (**2**). The as-prepared exfoliated MoS_2 solution was divided in two aliquots: DNA sequence (**1'**) was added to the first aliquot, and DNA sequence (**2**) to the second one. DNA sequences (**1'**) and (**2**) are thiolated DNA strands that can be anchored to the intrinsic sulphur defects on MoS_2 surfaces. This functionalisation process produces (**1'**)-functionalised MoS_2 and (**2**)-functionalised MoS_2.

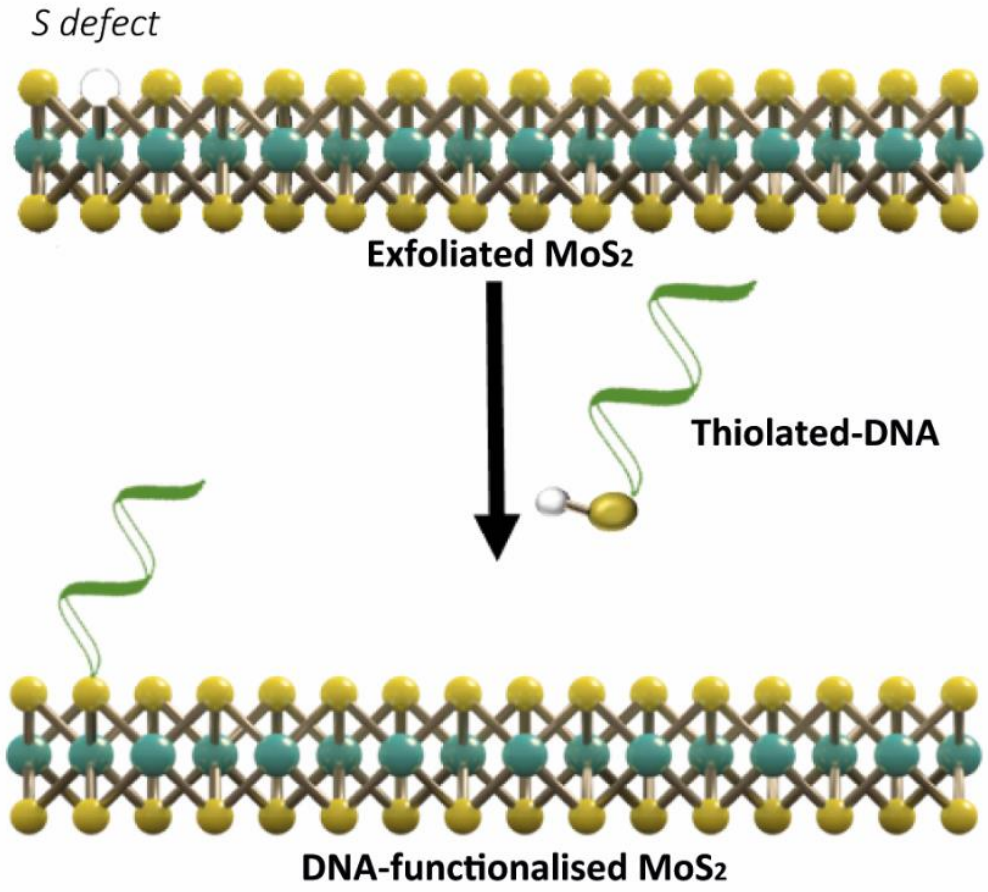

Figure 5 - 3 *Schematic illustration of DNA functionalisation of exfoliated MoS_2 surface employing a thiolated-DNA strand.*

To verify the functionalisation of exfoliated MoS_2 surface, the concentration of the DNA strands in (**1'**)-functionalised and (**2**)-functionalised MoS_2 was estimated by spectrophotometry (see Figure 5 – 4). Readings were taken at 260 nm and the concentration of DNA strands (**1'**) and (**2**) was found to be 0.54 μM and 0.65 μM, respectively; these values were then used to estimate the number of DNA strands per exfoliated MoS_2 structure, which resulted to be 61 in (**1'**)-functionalised MoS_2 and 73 in (**2**)-functionalised MoS_2.

The number of DNA strands attached per MoS_2 was estimated by assuming MoS_2 as a geometric cylinder with a density of 5.06 g/mL and molecular weight (MW) of 160.07 g/mol. The DNA MWs employed for MoS_2 functionalisation are 13,093.8 Da and 10,532.1 Da, respectively for thiol-(**1'**) and thiol-(**2**); and the number of DNA strands attached for every S atom was calculated to be $4.3 \cdot 10^{-5}$ in (**1'**)-functionalised MoS_2 and $5.16 \cdot 10^{-5}$ in (**2**)-functionalised MoS_2.

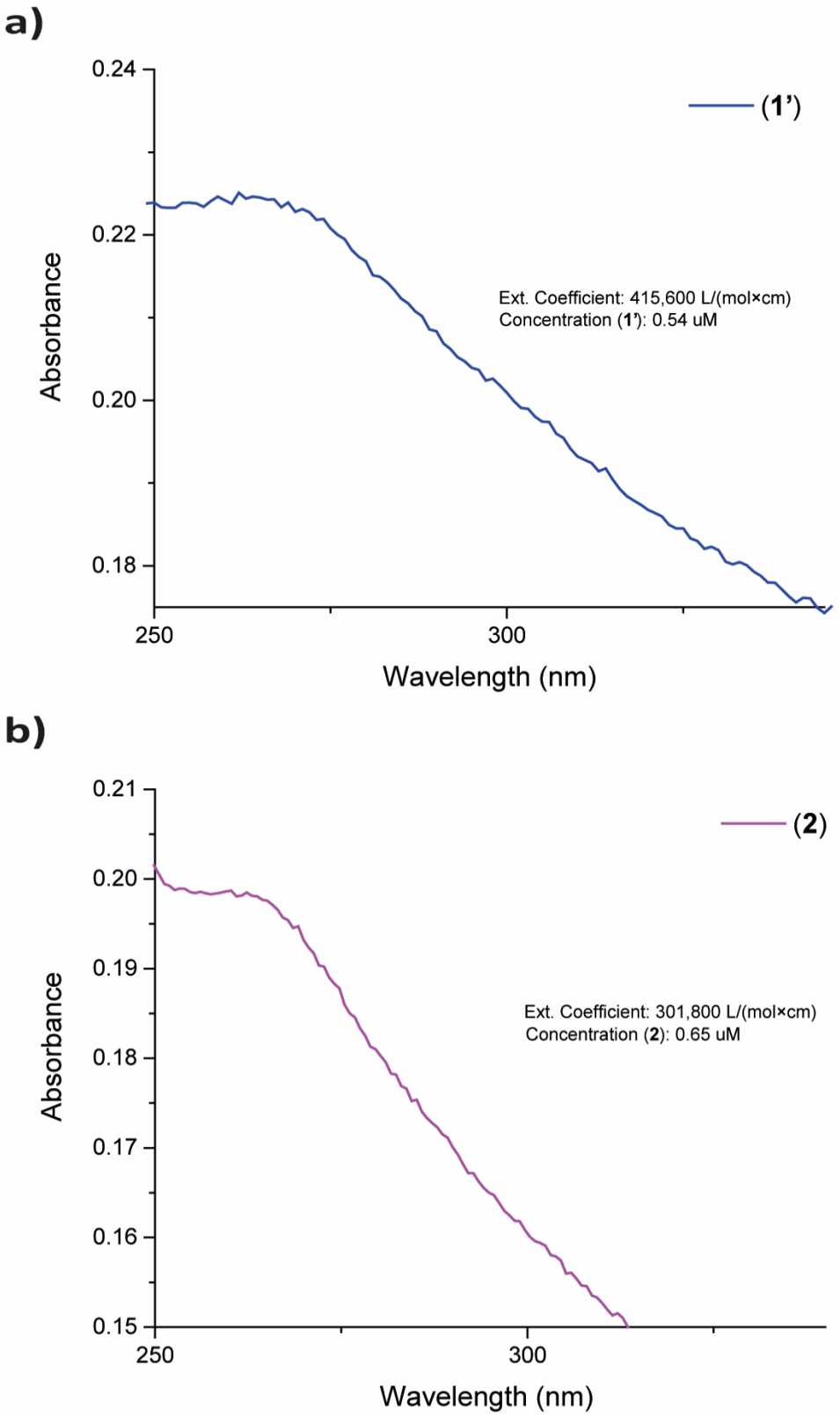

Figure 5 - 4 *UV absorbance spectra of (a) thiolated (**1'**) DNA sequence in (**1'**)-functionalised MoS_2. Calculated extinction coefficient: 415600 L/(mole*cm); Estimated concentration of (**1'**) in (**1'**)-functionalised MoS_2: 0.54 µM. (b) thiolated (**2**) DNA sequence in (**2**)-functionalised MoS_2. Calculated extinction coefficient: 301800 L/(mole*cm); Estimated concentration of (**2**) in (**2**)-functionalised MoS_2: 0.65 µM.*

(**1'**)-functionalised and (**2**)-functionalised MoS_2 were then mixed together in a solution containing NaCl (400 nM) and MOPS (2 mM), and the MoS_2 layers were assembled *via* DNA hybridisation of the complementary oligonucleotides strands (**1'**) and (**2**), as shown in Figure 5 – 5a, resulting in DNA-linked MoS_2 layers.

The Raman spectrum of the DNA-assembled MoS_2 layers (Figure 5 – 5b) shows that the E_{2g}^1 peak is shifted to lower frequencies (379 cm^{-1}) as well as the A_{1g} peak is shifted to lower frequencies (402 cm^{-1}) compared to the exfoliated MoS_2 Raman peaks shown in Figure 5 – 2a.

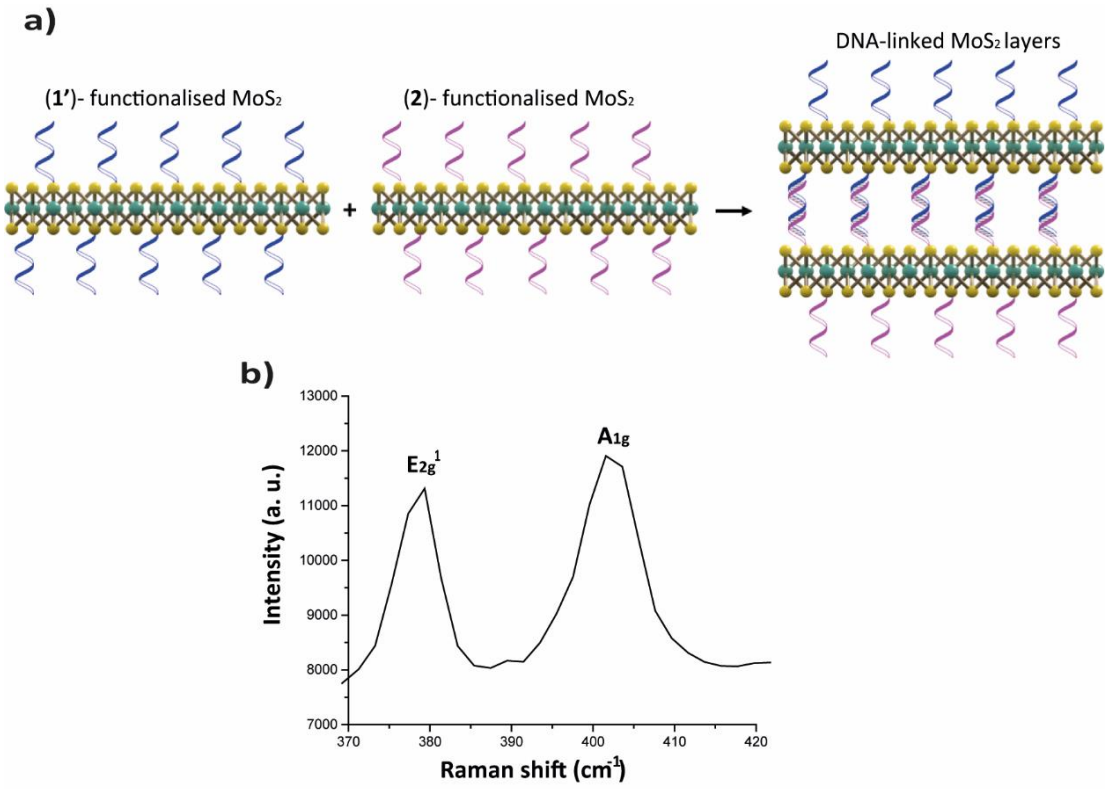

Figure 5 - 5 *Formation of DNA-linked MoS_2 layers via DNA hybridisation. (a) Schematic of the DNA-driven assembly process, (b) Raman spectrum showing the E_{2g}^1 peak at 379 cm^{-1} the A_{1g} peak at 402 cm^{-1}.*

To demonstrate the successful assembly of MoS_2 layers, AFM characterisation was carried out on samples obtained by casting the MoS_2 solutions on muscovite mica. Figure 5 – 6 shows the corresponding AFM topographical images and the height profiles of exfoliated MoS_2 and DNA-linked MoS_2 layers physisorbed on mica. The lateral size and thickness of the exfoliated material was found to be 94.9 ± 26.9 nm and 5.3 ±2.1 nm, respectively, corresponding to an average number of 8 ± 3 MoS_2 monolayers per structure. Whereas, the assembled material displays an average width of 129.6 ± 53.1 nm and a height of 17.9 ± 7.0 nm, suggesting that the assembly has taken place. The number of monolayers in the superstructures was calculated to be of 16 ± 5. This was estimated by considering the distance between the assembled layers equals to the length of the dsDNA connecting two surfaces of exfoliated MoS_2. However, it is worth mentioning that rather than only perpendicular linkers, other states are possible such as bent, compressed and free linkers.[323]

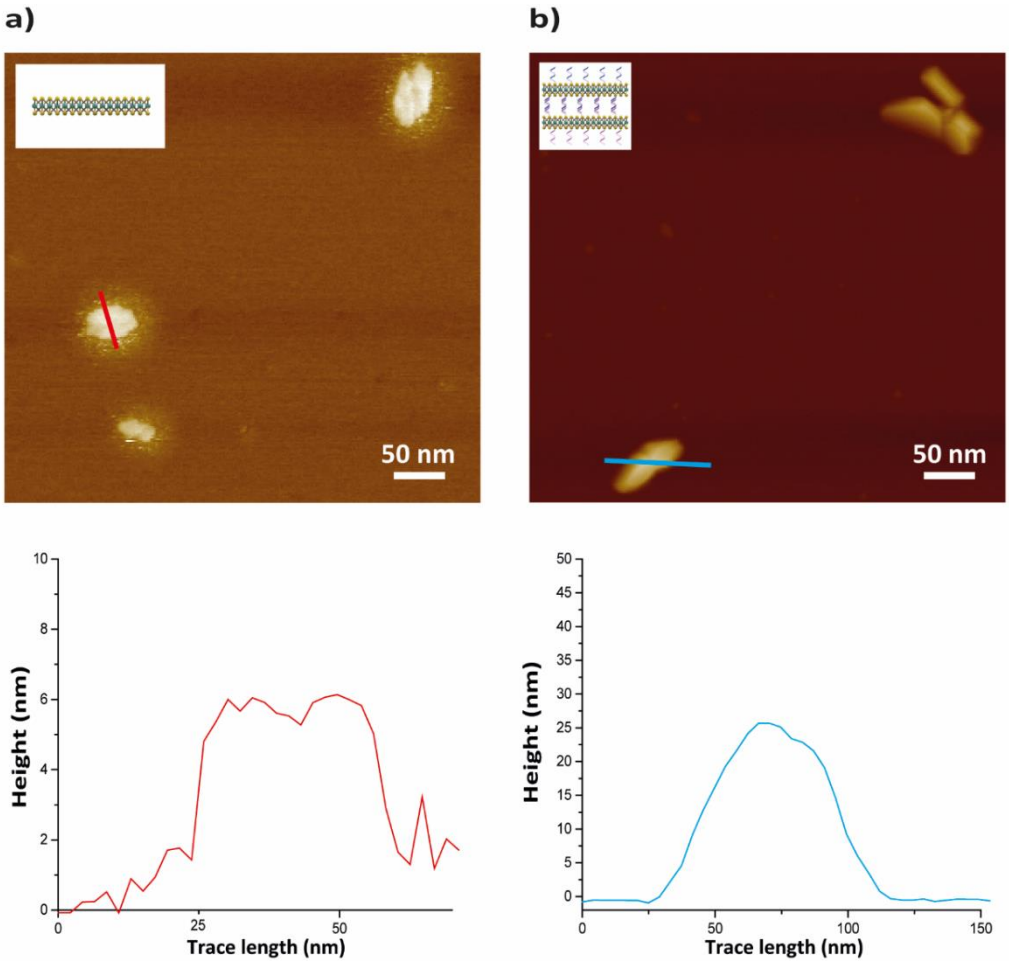

Figure 5 - 6 *(a) AFM topographical image and respective height profile of the starting material: DNA-functionalised MoS_2. (b) AFM topographical image and respective height profile of DNA-linked MoS_2 superstructures assembled via DNA hybridisation.*

Additionally, to confirm that exfoliated MoS_2 can assemble only when functionalised with complementary DNA strands, we carried out a morphological characterisation of samples obtained by casting solutions of MoS_2 functionalised with DNA strands that cannot form a DNA duplex. Specifically, we functionalised exfoliated MoS_2 with thiolated-(**1**) DNA strand and we then mixed (**1**)-functionalised and (**1'**)-functionalised MoS_2, as previously described. Figure 5 – 7a shows that the measured height of mixed (**1**)-functionalised and (**1'**)-functionalised MoS_2, which is comparable to that obtained for the exfoliated MoS_2, hence indicating that no assembly has taken place. In a similar way, if an amino-modified DNA strand (**2**) incapable of functionalising MoS_2 surface is employed, no evidence of assembly was observed (see Figure 5 – 7b).

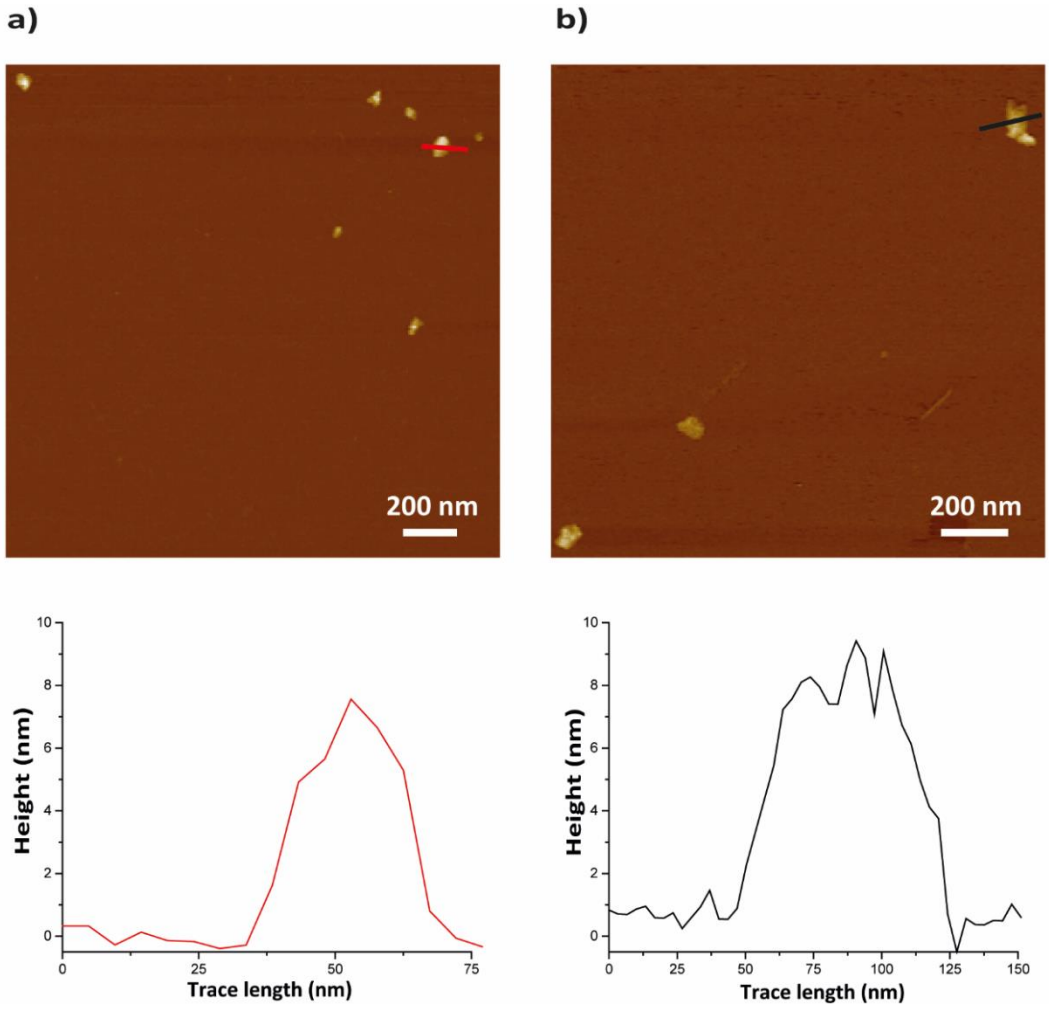

Figure 5 - 7 *AFM topographical images and respective height profiles of: (a) a solution containing (**1**)-functionalised MoS_2 and (**1'**)-functionalised MoS_2, with an average MoS_2 height= 7.5 ± 3.1 nm; and (b) a solution containing exfoliated MoS_2 and amino-modified (**2**), not capable of functionalising MoS_2 surface, with an average MoS_2 height= 7.9 ± 2.8 nm. In both samples, no evidence of assembly was observed.*

5.2 MoS_2 DYNAMIC JUNCTIONS

In order to exploit the ability of DNA to induce a stimuli responsive behaviour in the DNA-linked nanostructures,[127,319] we introduced a cytosine-rich DNA sequence, (**1**), and its partly complementary strand (**2**), as the molecular linkers of choice in the assembly of MoS_2 layers. Similarly to the experiments carried out in Chapter 4, DNA sequence (**1**) is capable to reconfigure in response to a pH change in the buffer solution. For this purpose, we functionalised MoS_2 surface with thiol modified (**1**), forming (**1**)-functionalised MoS_2. The concentration of DNA in (**1**)-functionalised MoS_2 was estimated by UV-vis analysis, as shown in Figure 5 – 8, and it was found to be 0.71 µM, while 80 DNA strands were estimated to be present per MoS_2 structure [thiol-(**1**) MW= 10,178.9 Da, number of DNA strands for S atom= $5.65 \cdot 10^{-5}$.

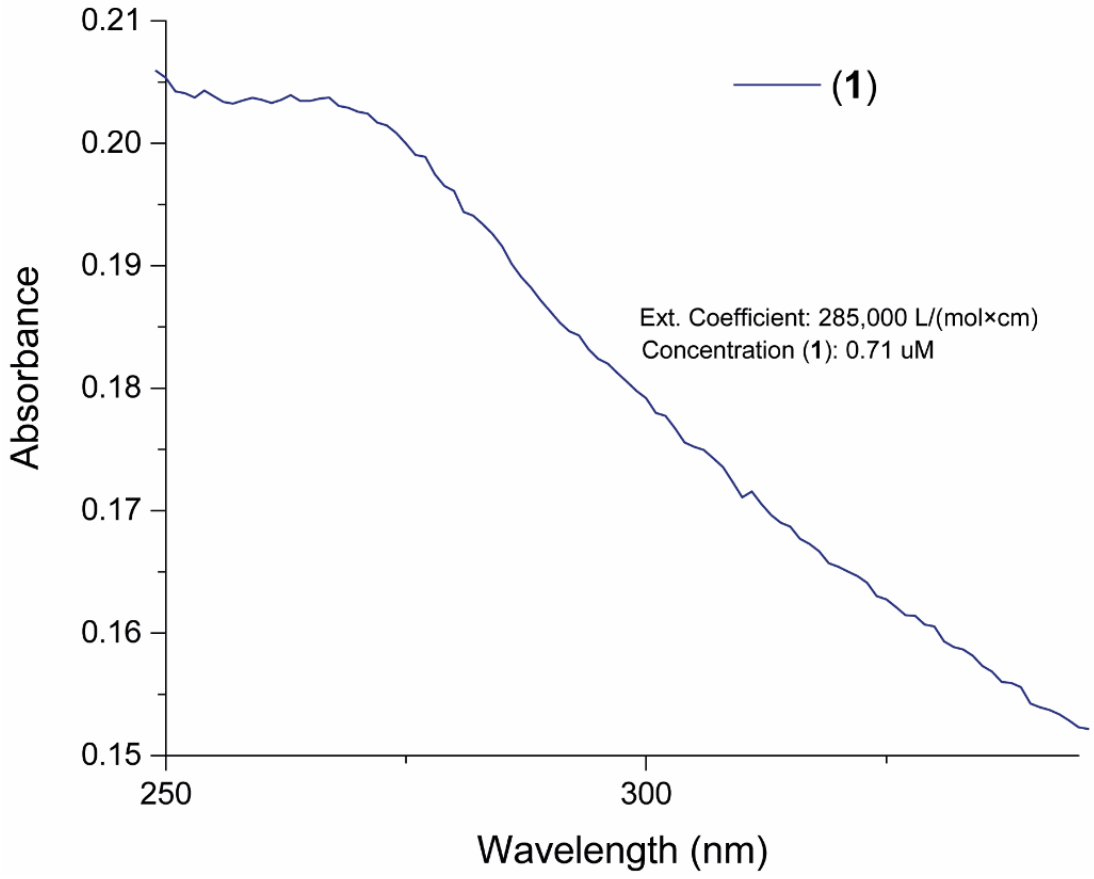

Figure 5 - 8 *UV absorbance spectrum of thiolated (**1**) in (**1**)-functionalised MoS_2. Calculated extinction coefficient: 285000 L/(mole*cm), estimated DNA concentration= 0.71 µM.*

Upon mixing of (**1**)-functionalised and (**2**)-functionalised MoS_2 at basic pH, DNA sequence (**1**) hybridises with its complementary DNA (**2**) forming a partial DNA duplex (**2**)/(**3**), leading to the assembly of MoS_2 layers. When the pH of the buffer is changed to acidic conditions, (**1**) forms a four-stranded intramolecular quadruplex DNA structure (*i*-motif).[304] The formation of this secondary DNA structure allows the disassembly of DNA-linked MoS_2 superstructures.

Figure 5 – 9 shows the schematic assembly/disassembly of MoS_2, by varying pH values, and Raman characterisation of samples at pH 8 and pH 5.5.

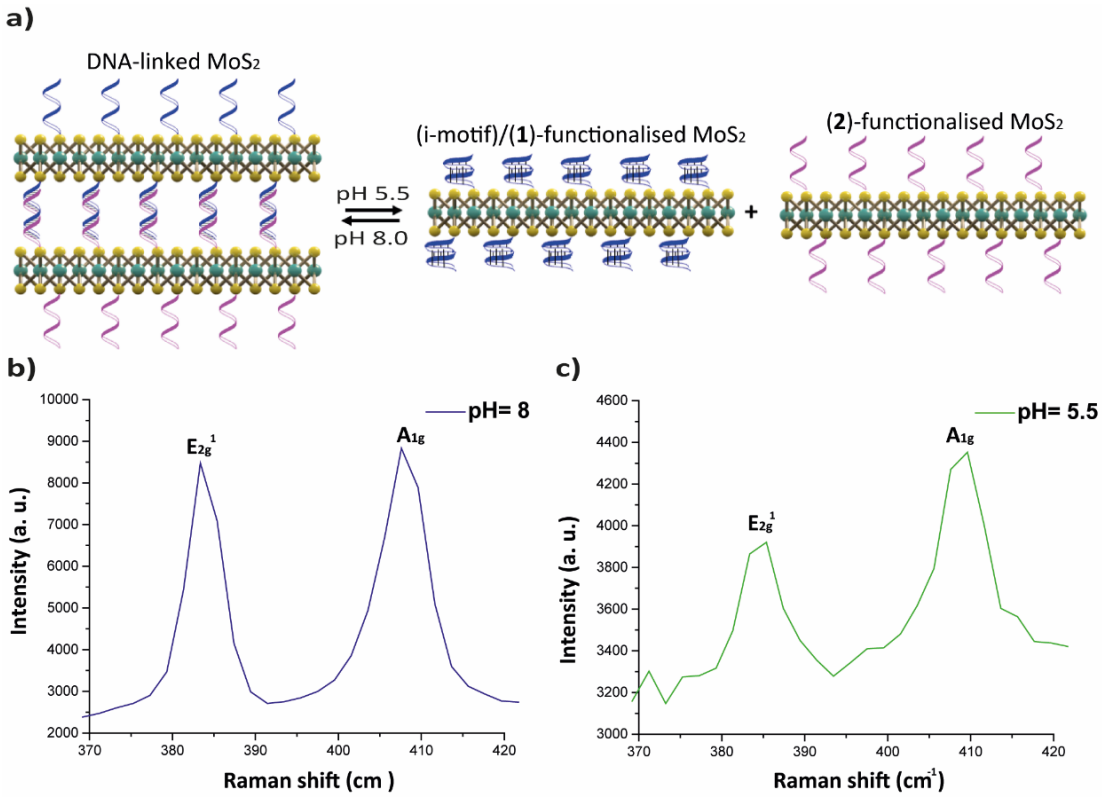

Figure 5 - 9 *Controlled disassembly of DNA-linked MoS_2 by i-motif formation: (a) scheme of the pH-driven disassembly; Raman spectra of MoS_2 solution (b) at pH= 8, showing E_{2g}^1=383 cm^{-1} and A_{1g}= 408 cm^{-1}; (c) at pH= 5.5, showing E_{2g}^1= 385 cm^{-1} and A_{1g}= 410 cm^{-1}.*

To confirm the nanosheet disassembly as a result of the pH change, we compared the size of the assembled MoS_2 nanostructures with the corresponding disassembled nanostructures. This was done *via* AFM topographical imaging of solutions cast on mica (Figure 5 – 10). The DNA-linked MoS_2 structures exhibit a lateral size and thickness of 338.2 ±117.7 nm and 40.4 ±18.9 nm, respectively, suggesting that they consist of an average number of monolayers equal to 31 ± 12. Differently, the lateral size and height of the corresponding disassembled MoS_2 nanostructures were found to be 144.8 ± 88.1 nm and 5.4 ± 3.3 nm, respectively, in line with the presence of an average number of monolayers equal to 9 ± 5, i.e. comparable to the starting exfoliated MoS_2, prior to any DNA-driven assembly. This difference in height strongly suggests that the disassembly of MoS_2 can indeed be controlled by employing a specific DNA sequence capable of forming an i-motif structure at pH 5.5.

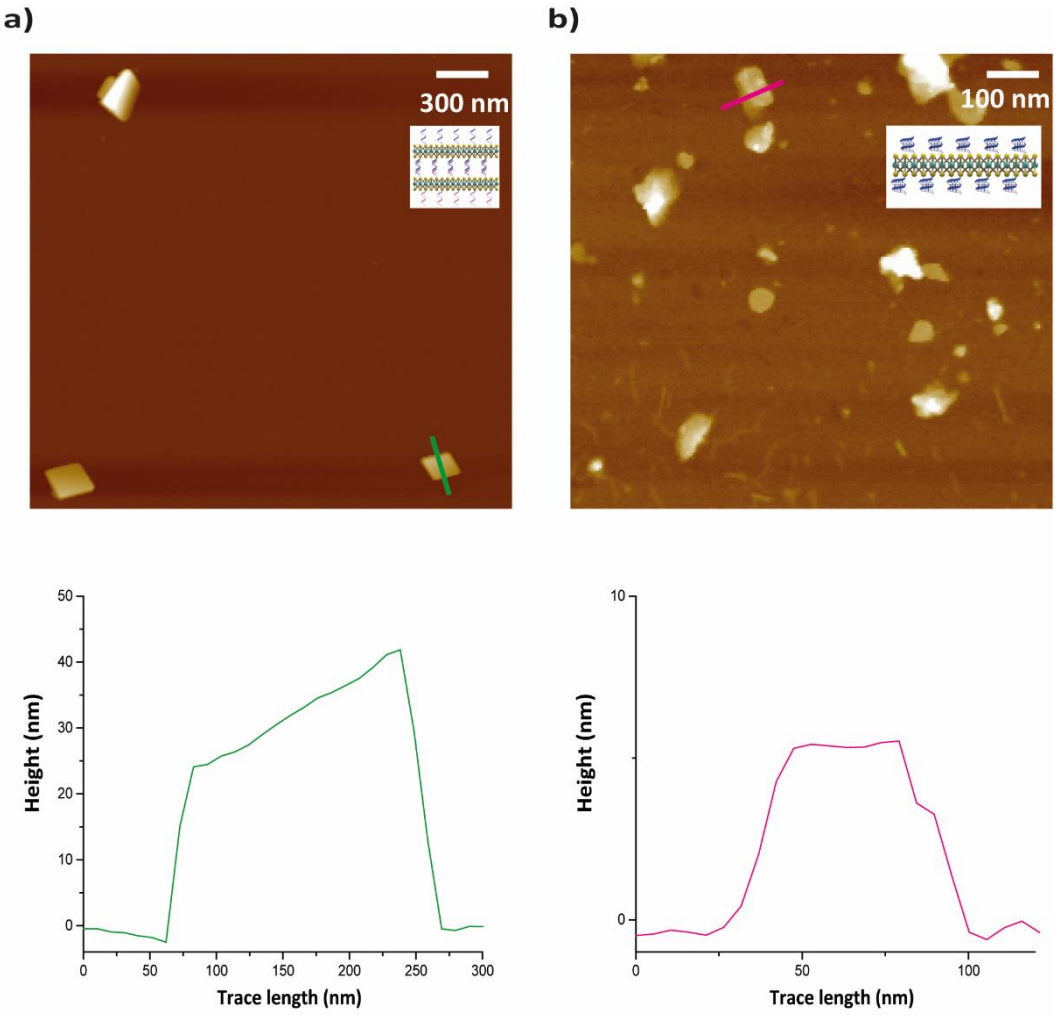

Figure 5 - 10 *AFM topographical image of (a) assembled and (b) disassembled MoS_2 with the corresponding height profiles.*

To further explore the versatility of our approach, we induced the disassembly of DNA-linked MoS_2 *via* a strand-displacement mechanism.[301] Upon introduction of strand (**SD1**), the partial duplex (**1**)/(**2**) is separated, to form the more stable duplex (**1**)/(**SD1**), resulting in the release of strand (**2**) in solution, and leading to the disassembly of MoS_2 superstructure into isolated MoS_2 nanostructures. Schematic of the disassembly process and Raman characterisation are shown in Figure 5 – 11.

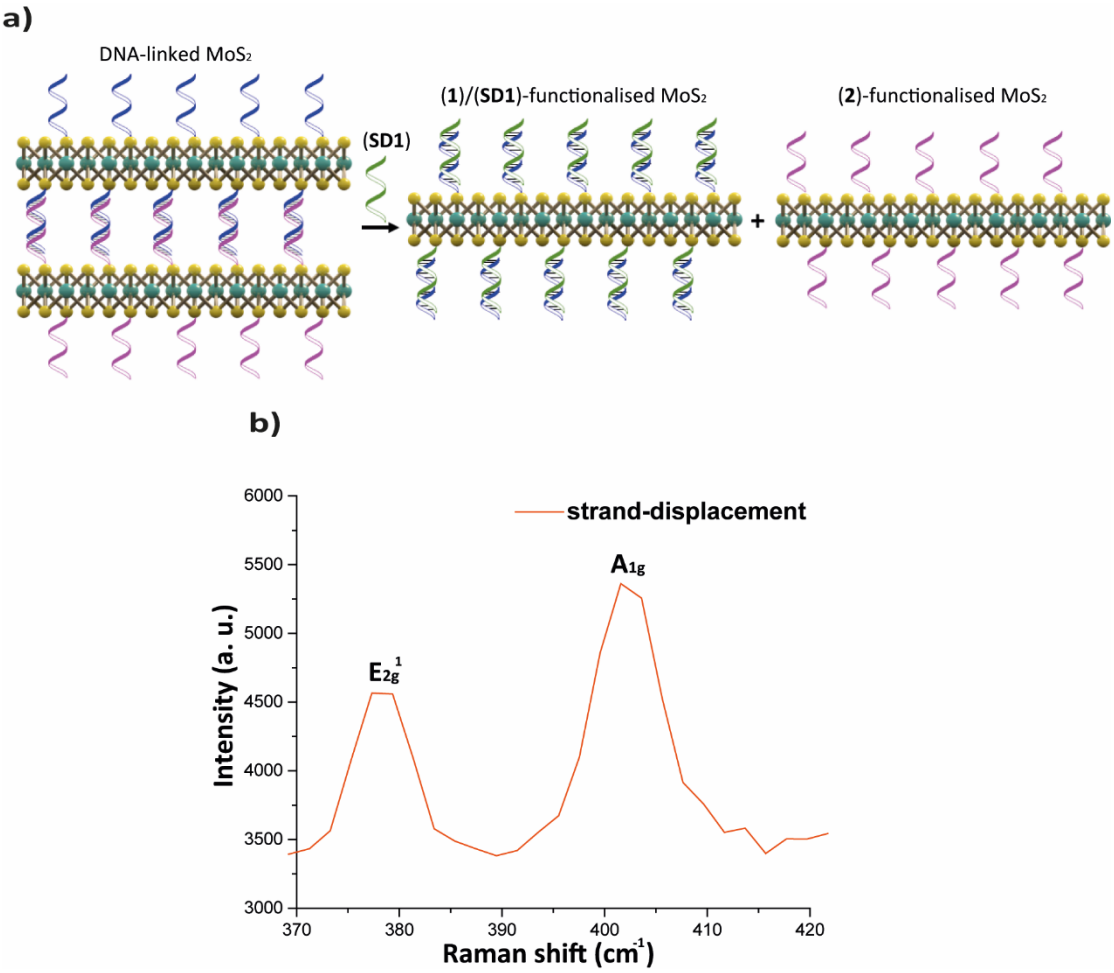

Figure 5 - 11 *Controlled disassembly of DNA-linked MoS_2 via a strand-displacement mechanism: (a) Schematic of the disassembly process; (b) Raman spectrum of sample after addition of (**SD1**), showing E_{2g}^1= 377 cm^{-1} and A_{1g}= 402 cm^{-1}.*

The disassembly was verified by statistical analysis of the average MoS_2 height and length as measured *via* AFM (Figure 5 – 12): the width and thickness of the disassembled MoS_2 structures were found to be 101.6 ±52.4 nm and 11.3 ±5.7 nm, respectively, suggesting that these structures consist of an average number of monolayers equal to 18 ± 9. The difference in thickness indicates that a disassembly process of the DNA-linked MoS_2 can take place employing an additional DNA sequence capable of destabilising the (**1**)/(**2**)-linker joining MoS_2 surfaces.

This strategy exhibited a lower efficiency compared to the aforementioned approach employing the *i*-motif strand, likely due to the limited access of DNA strand (**SD1**) in the duplex (**1**)/(**2**) located between MoS_2 layers. Moreover, conversely to the experiment carried out in paragraph 4.3, the introduction of the anti-fuel (**SD2**) DNA strand did not lead the recovery of the assembled MoS_2 superstructure.

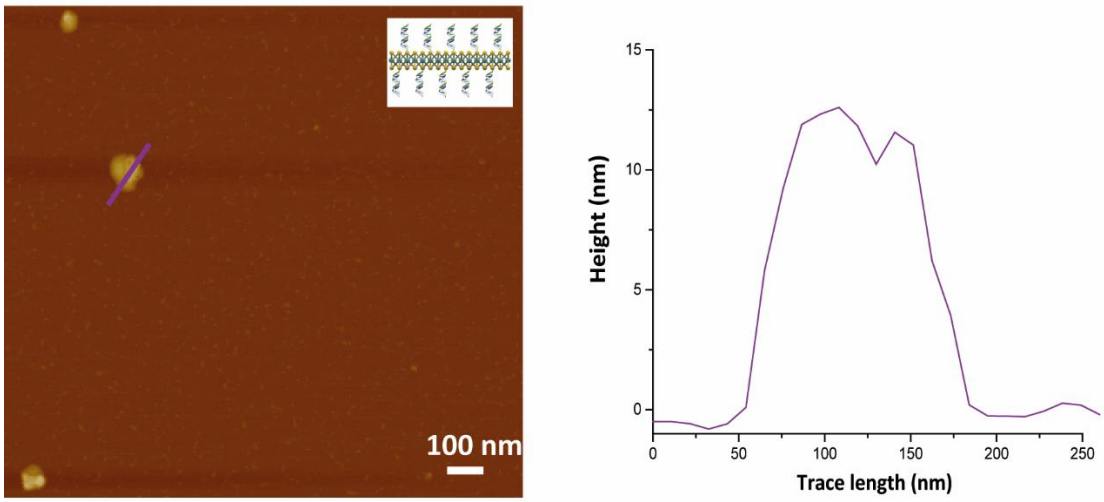

Figure 5 - 12 *AFM topographical image of MoS_2 nanostructures disassembled via strand-displacement mechanism with corresponding MoS_2 height profile.*

Finally, to prove that the disassembly occurs only when a fuel DNA strand is employed, we performed the same experiment using DNA sequence (**6**), incapable of displacing (**2**) in the DNA duplex joining the MoS_2 layers. Figure 5 – 13, shows that the disassembly does not take place in this case.

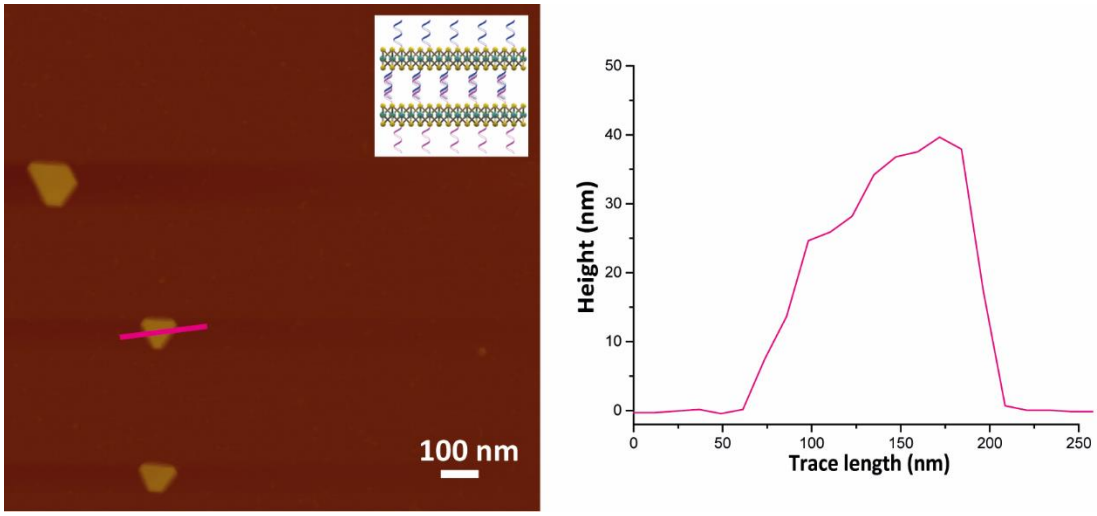

Figure 5 - 13 *AFM topographical image and respective height profile of MoS_2 solution after addition of DNA strand (**6**); average MoS_2 nanosheets height: 39.6 ± 13.5 nm. No evidence of disassembly was observed.*

5.3 CONCLUDING REMARKS

We demonstrated a strategy to drive the layer-by-layer assembly of exfoliated MoS_2 and their disassembly under different stimuli. In Table 6 are listed the average heights and later sizes of the MoS_2 employed in this work.

Table 6 *List of average lengths and lateral sizes. Highlights: exfoliated 2H-MoS_2 (orange), static assembly (green), dynamic assembly at pH 8 (blue), disassembly at pH 5.5 (yellow) and disassembly by strand-displacement mechanism (pink).*

MoS_2	Height (nm)	Lateral Size (nm)
Exfoliated 2H-MoS_2	5.3 ± 2.1	94.9 ± 26.9
Static Assembly	17.9 ± 7.0	129.6 ± 53.1
Dynamic Assembly at pH = 8	40.4 ± 18.9	338.2 ± 117.7
Disassembly at pH = 5.5	5.4 ± 3.3	144.8 ± 88.1
Disassembly by strand-displacement	11.3 ± 5.7	101.6 ± 52.4

Exfoliated 2H-MoS_2 nanostructures were obtained by sonicating bulk 2H-MoS_2 powder in aqueous sodium cholate solution. The average height of the used as starting material is MoS_2 surfaces were functionalised with thiolated-DNA strands, using the S defects in the exfoliated material, and then assembled *via* base-complementary of the DNA sequences. The successful layer-by-layer assembly was verified by AFM morphological characterisation, comparing the heights of exfoliated 2H-MoS_2 (5.3 ± 2.1 nm, highlighted in orange) and assembled MoS_2 superstructures (17.9 ± 7.0 nm, highlighted in green) .

Furthermore, we demonstrated the disassembly of DNA-linked MoS_2 by changing the pH of the solution. This was achieved by employing a cytosine-rich DNA sequence that reconfigures into an intramolecular i-motif structure at acidic pH, and separates the DNA duplex linking the MoS_2 surfaces. The successful disassembly process was verified by morphological characterisation, comparing the heights of MoS_2 solutions at pH 8 (40.4 ± 18.9 nm, highlighted in blue) and at pH 5.5 (5.4 ± 3.3 nm, highlighted in yellow).

Finally, we tested the versatility of our approach by driving the disassembly of the dynamic-assembled MoS_2 superstructures *via* a strand-displacement mechanism. This resulted in an average MoS_2 height of 101.6 ± 52.4 nm (highlighted in pink).

The strategy presented in this study is of interest for controlling the static and dynamic assembly of exfoliated MoS_2 in aqueous solution, and can be used for optoelectronic and biotechnology applications,[213,234,265] as well as for the assembly of 2-D materials into laminar membranes.[209,210]

CHAPTER 6: Conclusions and Future Challenges

In this thesis, we have presented the controlled self-assembly of 1-D and 2-D nanomaterials by the formation of both static and dynamic junctions with chemical or biological linkers. In this regard, precisely controlling the assembly of individual nanomaterials directly in solution allows to investigate and exploit their properties for the fabrication of solution-processable nano-devices.

The first main focus of the work presented here was the formation SWCNT junctions in environmentally friendly aqueous solution. Single-walled carbon nanotubes are a class 1-D nanomaterials of nano-technological interest because of their nanoscale diameter and exceptional thermal, mechanical, and electrical properties. However, the in-solution construction of SWCNT junctions is limited by their poor dispersibility in both aqueous and organic solvents. To overcome this problem, we took advantage of the capability of ssDNA to wrap around nanotube surface by π-π stacking interactions between the DNA aromatic hydrophobic bases and the SWCNT sidewall. The benefits of the DNA-wrapping strategy are the efficient dispersion of the nanotubes in bio-compatible aqueous solutions as well as the ability of DNA strands of protecting SWCNT surface, which leaves the nanotube termini available for end-functionalisation. As the dispersion process produces DNA-wrapped carbon nanotubes of different length, DNA-wrapped SWCNTs were separated by SEC-HPLC, a technique that allows to separate DNA-wrapped SWCNTs by their length.

In this study, the formation of SWCNT junctions relies on the functionalisation of SWCNT ends. Static linear junctions were obtained with two strategies: in the direct amidation strategy, SWCNT termini were joined by di, tri or tetra-amine linkers *via* amidation reaction; while in the copper-free click chemistry strategy, SWCNT ends were first functionalised with amino-functionalised cyclooctyne or azide molecules (*via* amidation reaction) and static linear junctions were then obtained by the formation of 1,2,3-triazole linkers, after mixing azido and cyclooctyne-functionalised single-walled carbon nanotubes.

In addition, static and dynamic hetero-systems were obtained by DNA-linking a single QD to the end of an individual SWCNT.[126] This opens the possibility of using biological linkers and also of implementing dynamic behaviours to SWCNT self-assemblies.

Another accomplishment of this work is indeed the formation SWCNT dynamic linear junctions, where DNA is employed as molecular linker.[127] In particular, DNA-wrapped SWCNTs were covalently functionalised at their terminal-ends with azido-modified ssDNA sequences. The assembly was then achieved *via* DNA hybridisation upon mixing SWCNTs, end-functionalised with complementary DNA strands, at neutral pH. A dynamic behaviour was implemented to the system by employing a DNA sequence containing a cytosine-rich domain, which leads to the disassembly of SWCNT junctions by *i*-motif formation at acidic pH. We further extended our study by controlling the disassembly of DNA-linked SWCNTs *via* a strand-displacement mechanisms upon addition of fuel/anti-fuel DNA strands. This demonstrates the possibility of inducing a dynamic behaviour to the SWCNT junctions with different stimuli.

In addition to the work on 1-D single-walled carbon nanotubes, we also explored the assembly of exfoliated molybdenum disulfide.[324] In this work, the exfoliation of MoS_2 was achieved by sonication in aqueous sodium cholate solution of the bulk powder. Exfoliated MoS_2 is a class of 2-D layered materials that exhibits a direct band gap and strong photoluminescence, showing promise in optoelectronic applications. Moreover, these nanostructured materials have been employed as nanocarriers for drug delivery and as laminar membranes to regulate ion transport for the desalination of seawater, toward the generation of blue energy.

A further development in the use of exfoliated MoS_2 for the aforementioned applications relies on the control of their surface functionalisation, which directly affects their electronic properties as well as the distance between layers. In this regard, the surface of exfoliated MoS_2 was functionalised with thiolated-DNA strands, exploiting the sulphur defects generated during the exfoliation process. Subsequentially, after mixing MoS_2 functionalised with complementary DNA strands, the layer-by-layer assembly was obtained *via* DNA hybridisation.

Furthermore, a stimuli-responsive behaviour was implemented by employing a C-rich DNA sequence in the MoS_2 junction, which leads to the separation the assembled MoS_2 structures by *i*-motif structure formation at acidic pH. We also demonstrated the disassembly of the DNA-linked MoS_2 superstructures *via* strand-displacement. This confirms the possibility of using DNA as molecular linker to induce the static and dynamic assembly of exfoliated MoS_2 in solution.

The formation of SWCNT linear junctions presented in this study could facilitate the development of novel single-molecule nano-devices[124,279,281–283] employing a facile, low-cost[288,289] and environmentally friendly in-solution strategy.[123] Moreover, the use of DNA as linker holds great potential for the fabrication of opto-electronic devices,[122,325] such as employing G-rich DNA sequences as active components, and sensing platforms *via* the use of oligonucleotide aptamer DNA sequences, where single-walled carbon nanotubes can be employed as switchable nano-electrodes.[282,292] The DNA-linking strategy developed in this work will also allow to control the distance between MoS_2 layers, thus to tune their opto-electronic properties,[225–231] as well as to introduce a dynamic behaviour,[206,265] which can be exploited for the fabrication of stimuli-responsive MoS_2-based devices. Future work will take advantage of the knowledge here developed to precisely control designed SWCNT assemblies of higher complexity as well as it could also be extended to other 2-D layered materials.

To conclude, this has been a challenging and exciting PhD project where the assembly of 1-D and 2-D nanomaterials, specifically SWCNTs and MoS_2, has been achieved by the formation of both static and dynamic junctions in aqueous solutions. As previously mentioned, this is of (nano)technological interest for the construction of the next generation of nano-devices, which require precise control at the nanoscale to exploit the full potential of these nanostructured materials. The results here presented have shown potential to provide platforms for future studies; there is still more to be done to predict where they can play a crucial role due to the fast-paced advancement of technology.

THE END

References

1 G. Baccarani, E. Baravelli, E. Gnani, A. Gnudi and S. Reggiani, in *European Solid-State Device Research Conference*, IEEE, 2015, vol. 2015-Novem, pp. 4–9.

2 S. Karthäuser, Control of molecule-based transport for future molecular devices, *J. Phys. Condens. Matter*, 2011, **23**, 013001.

3 R. M. Bakker, H. K. Yuan, Z. Liu, V. P. Drachev, A. V. Kildishev, V. M. Shalaev, R. H. Pedersen, S. Gresillon and A. Boltasseva, Enhanced localized fluorescence in plasmonic nanoantennae, *Appl. Phys. Lett.*, 2008, **92**, 043101.

4 T. W. Odom, J. L. Huang, P. Kim and C. M. Lieber, Atomic structure and electronic properties of single-walled carbon nanotubes, *Nature*, 1998, **391**, 62–64.

5 M. J. Allen, V. C. Tung and R. B. Kaner, Honeycomb Carbon: A Review of Graphene, *Chem. Rev.*, 2010, **110**, 132–145.

6 M. Ouyang, J.-L. Huang and C. M. Lieber, Fundamental Electronic Properties and Applications of Single-Walled Carbon Nanotubes, *Acc. Chem. Res.*, 2002, **35**, 1018–1025.

7 A. M. Smith and S. Nie, Semiconductor Nanocrystals: Structure, Properties, and Band Gap Engineering, *Acc. Chem. Res.*, 2010, **43**, 190–200.

8 M. A. El-Sayed, Some interesting properties of metals confined in time and nanometer space of different shapes, *Acc. Chem. Res.*, 2001, **34**, 257–264.

9 N. C. Seeman, Nanomaterials Based on DNA, *Annu. Rev. Biochem.*, 2010, **79**, 65–87.

10 P. W. K. Rothemund, Folding DNA to create nanoscale shapes and patterns, *Nature*, 2006, **440**, 297–302.

11 M. C. LeMieux, M. Roberts, S. Barman, Y. W. Jin, J. M. Kim and Z. Bao, Self-Sorted, Aligned Nanotube Networks for Thin-Film Transistors, *Science*, 2008, **321**, 101–104.

12 C. V. Nguyen, L. Delzeit, A. M. Cassell, J. Li, J. Han and M. Meyyappan, Preparation of Nucleic Acid Functionalized Carbon Nanotube Arrays, *Nano Lett.*, 2002, **2**, 1079–1081.

13 L. Zhang and T. J. Webster, *Nano Today*, 2009.

14 B. D. Malhotra and M. A. Ali, in *Nanomaterials for Biosensors*, Elsevier, 2018, pp. 1–74.

15 G. Guisbiers, S. Mejía-Rosales and F. Leonard Deepak, Nanomaterial Properties: Size and Shape Dependencies, *J. Nanomater.*, 2012, **2012**, 1–2.

16 A. A. Tseng, K. Chen, C. D. Chen and K. J. Ma, Electron beam lithography in nanoscale fabrication: Recent development, *IEEE Trans. Electron. Packag. Manuf.*, 2003, **26**, 141–149.

17 W. Lu and C. M. Lieber, Nanoelectronics from the bottom up, *Nat. Mater.*, 2007, **6**, 841–850.

18 N. C. Seeman, Structural DNA Nanotechnology: Growing Along with Nano Letters, *Nano Lett.*, 2010, **10**, 1971–1978.

19 R. Rauti, M. Musto, S. Bosi, M. Prato and L. Ballerini, Properties and behavior of carbon nanomaterials when interfacing neuronal cells: How far have we come?, *Carbon N. Y.*, 2019, **143**, 430–446.

20 M. Scarselli, P. Castrucci and M. De Crescenzi, Electronic and optoelectronic nano-devices based on carbon nanotubes, *J. Phys. Condens. Matter*, 2012, **24**, 313202.

21 D. S. Bethune, C. H. Kiang, M. S. de Vries, G. Gorman, R. Savoy, J. Vazquez and R. Beyers, Cobalt-catalysed growth of carbon nanotubes with single-atomic-layer walls, *Nature*, 1993, **363**, 605–607.

22 S. Iijima and T. Ichihashi, Single-shell carbon nanotubes of 1-nm diameter, *Nature*, 1993, **363**, 603–605.

23 S. Ijiima, Iljima, 1991, Helical microtubles of graphitic carbon, *Nature*, 1991, **354**, 56–58.

24 G. D. Nessim, Properties, synthesis, and growth mechanisms of carbon nanotubes with special focus on thermal chemical vapor deposition, *Nanoscale*, 2010, **2**, 1306.

25 C. Journet, W. K. Maser, P. Bernier, A. Loiseau, M. L. de la Chapelle, S. Lefrant, P. Deniard, R. Lee and J. E. Fischer, Large-scale production of single-walled carbon nanotubes by the electric-arc technique, *Nature*, 1997, **388**, 756–758.

26 C. D. Scott, S. Arepalli, P. Nikolaev and R. E. Smalley, Growth mechanisms for single-wall carbon nanotubes in a laser-ablation process, *Appl. Phys. A Mater. Sci. Process.*, 2001, **72**, 573–580.

27 Z. F. Ren, Synthesis of Large Arrays of Well-Aligned Carbon Nanotubes on Glass, *Science*, 1998, **282**, 1105–1107.

28 P. Nikolaev, M. J. Bronikowski, R. K. Bradley, F. Rohmund, D. T. Colbert, K. . Smith and R. E. Smalley, Gas-phase catalytic growth of single-walled carbon nanotubes from carbon monoxide, *Chem. Phys. Lett.*, 1999, **313**, 91–97.

29 A. Javey, J. Guo, Q. Wang, M. Lundstrom and H. Dai, Ballistic carbon nanotube field-effect transistors, *Nature*, 2003, **424**, 654–657.

30 L. M. Peng, Z. Zhang and S. Wang, *Mater. Today*, 2014.

31 S. Berber, Y.-K. Kwon and D. Tománek, Unusually High Thermal Conductivity of Carbon Nanotubes, *Phys. Rev. Lett.*, 2000, **84**, 4613–4616.

32 S. J. Tans, M. H. Devoret, H. Dai, A. Thess, R. E. Smalley, L. J. Geerligs and C. Dekker, Individual single-wall carbon nanotubes as quantum wires, *Nature*, 1997, **386**, 474–477.

33 L. Cao, M. J. Meziani, S. Sahu and Y. P. Sun, Photoluminescence properties of graphene versus other carbon nanomaterials, *Acc. Chem. Res.*, 2013, **46**, 171–182.

34 P. Singh, S. Campidelli, S. Giordani, D. Bonifazi, A. Bianco and M. Prato, *Chem. Soc. Rev.*, 2009.

35 Y.-L. Zhao and J. F. Stoddart, Noncovalent Functionalization of Single-Walled Carbon Nanotubes, *Acc. Chem. Res.*, 2009, **42**, 1161–1171.

36 H. Dai, Carbon Nanotubes: Synthesis, Integration, and Properties, *Acc. Chem. Res.*, 2002, **35**, 1035–1044.

37 C. Wang, K. Takei, T. Takahashi and A. Javey, *Chem. Soc. Rev.*, 2013.

38 M. F. L. De Volder, S. H. Tawfick, R. H. Baughman and A. J. Hart, Carbon Nanotubes: Present and Future Commercial Applications, *Science*, 2013, **339**, 535–539.

39 M. S. Dresselhaus, G. Dresselhaus and R. Saito, Physics of carbon nanotubes, *Carbon N. Y.*, 1995, **33**, 883–891.

40 H. Zhang, B. Wu, W. Hu and Y. Liu, Separation and/or selective enrichment of single-walled carbon nanotubes based on their electronic properties, *Chem. Soc. Rev.*, 2011, **40**, 1324–1336.

41 H. Kataura, Y. Kumazawa, Y. Maniwa, I. Umezu, S. Suzuki, Y. Ohtsuka and Y. Achiba, Optical properties of single-wall carbon nanotubes, *Synth. Met.*, 1999, **103**, 2555–2558.

42 R. B. Weisman and S. M. Bachilo, Dependence of Optical Transition Energies on Structure for Single-Walled Carbon Nanotubes in Aqueous Suspension: An Empirical Kataura Plot, *Nano Lett.*, 2003, **3**, 1235–1238.

43 C. Pintossi and L. Sangaletti, 2016, pp. 239–259.

44 S. M. Bachilo, M. S. Strano, C. Kittrell, R. H. Hauge, R. E. Smalley and R. B. Weisman, Structure-assigned optical spectra of single-walled carbon nanotubes, *Science*, 2002, **298**, 2361–2366.

45 C. Backes and I. Stemmler, Absorption Spectroscopy as a Powerful Technique for the Characterization of Single-Walled Carbon Nanotubes, *Perkinelmer.Co.Uk*, 2013, 4–9.

46 H. Dai, J. H. Hafner, A. G. Rinzler, D. T. Colbert and R. E. Smalley, Nanotubes as nanoprobes in scanning probe microscopy, *Nature*, 1996, **384**, 147–150.

47 A. C. Dillon, K. M. Jones, T. A. Bekkedahl, C. H. Kiang, D. S. Bethune and M. J. Heben, Storage of hydrogen in single-walled carbon nanotubes, *Nature*, 1997, **386**, 377–379.

48 R. H. Baughman, Carbon Nanotubes--the Route Toward Applications, *Science*, 2002, **297**, 787–792.

49 Y.-P. Sun, K. Fu, Y. Lin and W. Huang, Functionalized Carbon Nanotubes: Properties and Applications, *Acc. Chem. Res.*, 2002, **35**, 1096–1104.

50 A. Noy, Bionanoelectronics, *Adv. Mater.*, 2011, **23**, 807–820.

51 R. Rao, C. L. Pint, A. E. Islam, R. S. Weatherup, S. Hofmann, E. R. Meshot, F. Wu, C. Zhou, N. Dee, P. B. Amama, J. Carpena-Nuñez, W. Shi, D. L. Plata, E. S. Penev, B. I. Yakobson, P. B. Balbuena, C. Bichara, D. N. Futaba, S. Noda, H. Shin, K. S. Kim, B. Simard, F. Mirri, M. Pasquali, F. Fornasiero, E. I. Kauppinen, M. Arnold, B. A. Cola, P. Nikolaev, S. Arepalli, H.-M. Cheng, D. N. Zakharov, E. A. Stach, J. Zhang, F. Wei, M. Terrones, D. B. Geohegan, B. Maruyama, S. Maruyama, Y. Li, W. W. Adams and A. J. Hart, Carbon Nanotubes and Related Nanomaterials: Critical Advances and Challenges for Synthesis toward Mainstream Commercial Applications, *ACS Nano*, 2018, **12**, 11756–11784.

52 J. Appenzeller, Carbon Nanotubes for High-Performance Electronics—Progress and Prospect, *Proc. IEEE*, 2008, **96**, 201–211.

53 M. M. Shulaker, G. Hills, N. Patil, H. Wei, H. Y. Chen, H. S. P. Wong and S. Mitra, Carbon nanotube computer, *Nature*, 2013, **501**, 526–530.

54 E. R. Aurand, S. Usmani, M. Medelin, D. Scaini, S. Bosi, F. B. Rosselli, S. Donato, G. Tromba, M. Prato and L. Ballerini, Nanostructures to Engineer 3D Neural-Interfaces: Directing Axonal Navigation toward Successful Bridging of Spinal Segments, *Adv. Funct. Mater.*, 2018, **28**, 1700550.

55 O. S. Kwon, H. S. Song, T. H. Park and J. Jang, Conducting Nanomaterial Sensor Using Natural Receptors, *Chem. Rev.*, 2019, **119**, 36–93.

56 V. Schroeder, S. Savagatrup, M. He, S. Lin and T. M. Swager, Carbon Nanotube Chemical Sensors, *Chem. Rev.*, 2019, **119**, 599–663.

57 M. Melchionna, S. Marchesan, M. Prato and P. Fornasiero, Carbon nanotubes and catalysis: the many facets of a successful marriage, *Catal. Sci. Technol.*, 2015, **5**, 3859–3875.

58 L. Dai, Y. Xue, L. Qu, H.-J. Choi and J.-B. Baek, Metal-Free Catalysts for Oxygen Reduction Reaction, *Chem. Rev.*, 2015, **115**, 4823–4892.

59 D. Tasis, N. Tagmatarchis, A. Bianco and M. Prato, Chemistry of Carbon Nanotubes, *Chem. Rev.*, 2006, **106**, 1105–1136.

60 Y. Chen, R. C. Haddon, S. Fang, A. M. Rao, P. C. Eklund, W. H. Lee, E. C. Dickey, E. A. Grulke, J. C. Pendergrass, A. Chavan, B. E. Haley and R. E. Smalley, Chemical Attachment of Organic Functional Groups to Single-walled Carbon Nanotube Material, *J. Mater. Res.*, 1998, **13**, 2423–2431.

61 K. J. Ziegler, Z. Gu, H. Peng, E. L. Flor, R. H. Hauge and R. E. Smalley, Controlled Oxidative Cutting of Single-Walled Carbon Nanotubes, *J. Am. Chem. Soc.*, 2005, **127**, 1541–1547.

62 T. Saito, K. Matsushige and K. Tanaka, Chemical treatment and modification of multi-walled carbon nanotubes, *Phys. B Condens. Matter*, 2002, **323**, 280–283.

63 A. M. Kamil, F. H. Hussein, A. F. Halbus and D. W. Bahnemann, Preparation, characterization, and photocatalytic applications of MWCNTs/TiO2 composite, *Int. J. Photoenergy*, 2014, **2014**, 1–8.

64 J. L. Delgado, P. de la Cruz, A. Urbina, J. T. López Navarrete, J. Casado and F. Langa, The first synthesis of a conjugated hybrid of C60-fullerene and a single-wall carbon nanotube, *Carbon N. Y.*, 2007, **45**, 2250–2252.

65 D. Baskaran, J. W. Mays, X. P. Zhang and M. S. Bratcher, Carbon Nanotubes with Covalently Linked Porphyrin Antennae: Photoinduced Electron Transfer, *J. Am. Chem. Soc.*, 2005, **127**, 6916–6917.

66 S. Cosnier and M. Holzinger, Design of carbon nanotube-polymer frameworks by electropolymerization of SWCNT-pyrrole derivatives, *Electrochim. Acta*, 2008, **53**, 3948–3954.

67 J. Chen, Solution Properties of Single-Walled Carbon Nanotubes, *Science*, 1998, **282**, 95–98.

68 M. J. Moghaddam, S. Taylor, M. Gao, S. Huang, L. Dai and M. J. McCall, Highly Efficient Binding of DNA on the Sidewalls and Tips of Carbon Nanotubes Using Photochemistry, *Nano Lett.*, 2004, **4**, 89–93.

69 W. Huang, S. Taylor, K. Fu, Y. Lin, D. Zhang, T. W. Hanks, A. M. Rao and Y.-P. Sun, Attaching Proteins to Carbon Nanotubes via Diimide-Activated Amidation, *Nano Lett.*, 2002, **2**, 311–314.

70 S. E. Baker, W. Cai, T. L. Lasseter, K. P. Weidkamp and R. J. Hamers, Covalently Bonded Adducts of Deoxyribonucleic Acid (DNA) Oligonucleotides with Single-Wall Carbon Nanotubes: Synthesis and Hybridization, *Nano Lett.*, 2002, **2**, 1413–1417.

71 F. Pompeo and D. E. Resasco, Water Solubilization of Single-Walled Carbon Nanotubes by Functionalization with Glucosamine, *Nano Lett.*, 2002, **2**, 369–373.

72 J. L. Bahr, J. Yang, D. V. Kosynkin, M. J. Bronikowski, R. E. Smalley and J. M. Tour, Functionalization of carbon nanotubes by electrochemical reduction of aryl diazonium salts: A bucky paper electrode, *J. Am. Chem. Soc.*, 2001, **123**, 6536–6542.

73 C. A. Dyke and J. M. Tour, Solvent-Free Functionalization of Carbon Nanotubes, *J. Am. Chem. Soc.*, 2003, **125**, 1156–1157.

74 M. S. Strano, Electronic Structure Control of Single-Walled Carbon Nanotube Functionalization, *Science*, 2003, **301**, 1519–1522.

75 M. Pandurangappa and G. Kempegowda, in *Carbon Nanotubes Applications on Electron Devices*, InTech, 2011.

76 P. Salice, E. Fabris, C. Sartorio, D. Fenaroli, V. Figà, M. P. Casaletto, S. Cataldo, B. Pignataro and E. Menna, An insight into the functionalisation of carbon nanotubes by diazonium chemistry: Towards a controlled decoration, *Carbon N. Y.*, 2014, **74**, 73–82.

77 H. Peng, P. Reverdy, V. N. Khabashesku and J. L. Margrave, Sidewall functionalization of single-walled carbon nanotubes with organic peroxides, *Chem. Commun.*, 2003, **3**, 362–363.

78 P. Umek, J. W. Seo, K. Hernadi, A. Mrzel, P. Pechy, D. D. Mihailovic and L. Forró, Addition of Carbon Radicals Generated from Organic Peroxides to Single Wall Carbon Nanotubes, *Chem. Mater.*, 2003, **15**, 4751–4755.

79 E. M. Pérez and N. Martín, π–π interactions in carbon nanostructures, *Chem. Soc. Rev.*, 2015, **44**, 6425–6433.

80 T. Fujigaya and N. Nakashima, Non-covalent polymer wrapping of carbon nanotubes and the role of wrapped polymers as functional dispersants, *Sci. Technol. Adv. Mater.*, 2015, **16**, 024802.

81 D. Tuncel, Non-covalent interactions between carbon nanotubes and conjugated polymers, *Nanoscale*, 2011, **3**, 3545–3554.

82 J. A. Fagan, Aqueous two-polymer phase extraction of single-wall carbon nanotubes using surfactants, *Nanoscale Adv.*, 2019, **1**, 3307–3324.

83 V. C. Moore, M. S. Strano, E. H. Haroz, R. H. Hauge, R. E. Smalley, J. Schmidt and Y. Talmon, Individually Suspended Single-Walled Carbon Nanotubes in Various Surfactants, *Nano Lett.*, 2003, **3**, 1379–1382.

84 M. Zheng, A. Jagota, E. D. Semke, B. A. Diner, R. S. McLean, S. R. Lustig, R. E. Richardson and N. G. Tassi, DNA-assisted dispersion and separation of carbon nanotubes, *Nat. Mater.*, 2003, **2**, 338–342.

85 F. Balavoine, P. Schultz, C. Richard, V. Mallouh, T. W. Ebbesen and C. Mioskowski, Helical crystallization of proteins on carbon nanotubes: A first step towards the development of new biosensors, *Angew. Chemie - Int. Ed.*, 1999, **38**, 1912–1915.

86 B. Z. Tang and H. Xu, Preparation, Alignment, and Optical Properties of Soluble Poly(phenylacetylene)-Wrapped Carbon Nanotubes, *Macromolecules*, 1999, **32**, 2569–2576.

87 Z. Jin, X. Sun, G. Xu, S. H. Goh and W. Ji, Nonlinear optical properties of some polymer/multi-walled carbon nanotube composites, *Chem. Phys. Lett.*, 2000, **318**, 505–510.

88 H. W. Goh, S. H. Goh, G. Q. Xu, K. P. Pramoda and W. D. Zhang, Crystallization and dynamic mechanical behavior of double-C60-end-capped poly(ethylene oxide)/multi-walled carbon nanotube composites, *Chem. Phys. Lett.*, 2003, **379**, 236–241.

89 H. S. Woo, R. Czerw, S. Webster, D. L. Carroll, J. Ballato, A. E. Strevens, D. O'Brien and W. J. Blau, Hole blocking in carbon nanotube–polymer composite organic light-emitting diodes based on poly (m -phenylene vinylene-co-2, 5-dioctoxy- p -phenylene vinylene), *Appl. Phys. Lett.*, 2000, **77**, 1393–1395.

90 S. A. Curran, P. M. Ajayan, W. J. Blau, D. L. Carroll, J. N. Coleman, A. B. Dalton, A. P. Davey, A. Drury, B. McCarthy, S. Maier and A. Strevens, A Composite from Poly(m-phenylenevinylene-co-2,5-dioctoxy-p-phenylenevinylene) and Carbon Nanotubes: A Novel Material for Molecular Optoelectronics, *Adv. Mater.*, 1998, **10**, 1091–1093.

91 N. Nakashima, Y. Tomonari and H. Murakami, Water-Soluble Single-Walled Carbon Nanotubes via Noncovalent Sidewall-Functionalization with a Pyrene-Carrying Ammonium Ion, *Chem. Lett.*, 2002, **31**, 638–639.

92 K. Besteman, J.-O. Lee, F. G. M. Wiertz, H. A. Heering and C. Dekker, Enzyme-Coated Carbon Nanotubes as Single-Molecule Biosensors, *Nano Lett.*, 2003, **3**, 727–730.

93 R. J. Chen, Y. Zhang, D. Wang and H. Dai, Noncovalent Sidewall Functionalization of Single-Walled Carbon Nanotubes for Protein Immobilization, *J. Am. Chem. Soc.*, 2001, **123**, 3838–3839.

94 G. K. C. Lee, C. Sach, M. L. H. Green, L. Wong and C. G. Salzmann, Mixtures of oppositely charged polypeptides as high-performance dispersing agents for single-wall carbon nanotubes, *Chem. Commun.*, 2010, **46**, 7013–7015.

95 M. Zheng and E. D. Semke, Enrichment of single chirality carbon nanotubes, *J. Am. Chem. Soc.*, 2007, **129**, 6084–6085.

96 V. A. Karachevtsev, A. Y. Glamazda, V. S. Leontiev, O. S. Lytvyn and U. Dettlaff-Weglikowska, Glucose sensing based on NIR fluorescence of DNA-wrapped single-walled carbon nanotubes, *Chem. Phys. Lett.*, 2007, **435**, 104–108.

97 Y. Xu, P. E. Pehrsson, L. Chen, R. Zhang and W. Zhao, Double-stranded DNA single-walled carbon nanotube hybrids for optical hydrogen peroxide and glucose sensing, *J. Phys. Chem. C*, 2007, **111**, 8638–8643.

98 Z. Liang, R. Lao, J. Wang, Y. Liu, L. Wang, Q. Huang, S. Song, G. Li and C. Fan, Solubilization of single-walled carbon nanotubes with single-stranded DNA generated from asymmetric PCR, *Int. J. Mol. Sci.*, 2007, **8**, 705–713.

99 Y. Ma, S. R. Ali, A. S. Dodoo and H. He, Enhanced Sensitivity for Biosensors: Multiple Functions of DNA-Wrapped Single-Walled Carbon Nanotubes in Self-Doped Polyaniline Nanocomposites, *J. Phys. Chem. B*, 2006, **110**, 16359–16365.

100 C. Hu, Y. Zhang, G. Bao, Y. Zhang, M. Liu and Z. L. Wang, DNA Functionalized Single-Walled Carbon Nanotubes for Electrochemical Detection, *J. Phys. Chem. B*, 2005, **109**, 20072–20076.

101 S. Viswanathan, H. Radecka and J. Radecki, Electrochemical biosensor for pesticides based on acetylcholinesterase immobilized on polyaniline deposited on vertically assembled carbon nanotubes wrapped with ssDNA, *Biosens. Bioelectron.*, 2009, **24**, 2772–2777.

102 C. Staii, A. T. Johnson, M. Chen and A. Gelperin, DNA-decorated carbon nanotubes for chemical sensing, *Nano Lett.*, 2005, **5**, 1774–1778.

103 R. J. Chen and Y. Zhang, Controlled precipitation of solubilized carbon nanotubes by delamination of DNA, *J. Phys. Chem. B*, 2006, **110**, 54–57.

104 J. Y. Lee, H. Y. Shin, S. W. Kang, C. Park and S. W. Kim, Use of bioelectrode containing DNA-wrapped single-walled carbon nanotubes for enzyme-based biofuel cell, *J. Power Sources*, 2010, **195**, 750–755.

105 E. Penzo, M. Palma, D. A. Chenet, G. Ao, M. Zheng, J. C. Hone and S. J. Wind, Directed Assembly of Single Wall Carbon Nanotube Field Effect Transistors, *ACS Nano*, 2016, **10**, 2975–2981.

106 M. Zheng, Structure-Based Carbon Nanotube Sorting by Sequence-Dependent DNA Assembly, *Science*, 2003, **302**, 1545–1548.

107 X. Tu, S. Manohar, A. Jagota and M. Zheng, DNA sequence motifs for structure-specific recognition and separation of carbon nanotubes, *Nature*, 2009, **460**, 250–253.

108 Q. H. Yang, Q. Wang, N. Gale, C. J. Oton, L. Cui, I. S. Nandhakumar, Z. Zhu, Z. Tang, T. Brown and W. H. Loh, Loosening the DNA wrapping around single-walled carbon nanotubes by increasing the strand length, *Nanotechnology*, 2009, **20**, 195603.

109 S. R. Vogel, M. M. Kappes, F. Hennrich and C. Richert, An Unexpected New Optimum in the Structure Space of DNA Solubilizing Single-Walled Carbon Nanotubes, *Chem. - A Eur. J.*, 2007, **13**, 1815–1820.

110 S. Ghosh, N. Patel and R. Chakrabarti, Probing the Salt Concentration Dependent Nucleobase Distribution in a Single-Stranded DNA–Single-Walled Carbon Nanotube Hybrid with Molecular Dynamics, *J. Phys. Chem. B*, 2016, **120**, 455–466.

111 X. Qiu, F. Ke, R. Timsina, C. Y. Khripin and M. Zheng, Attractive Interactions between DNA-Carbon Nanotube Hybrids in Monovalent Salts, *J. Phys. Chem. C*, 2016, **120**, 13831–13835.

112 J. K. Streit, J. A. Fagan and M. Zheng, A Low Energy Route to DNA-Wrapped Carbon Nanotubes via Replacement of Bile Salt Surfactants, *Anal. Chem.*, 2017, **89**, 10496–10503.

113 R. Saito, G. Dresselhaus and M. S. Dresselhaus, *Physical Properties of Carbon Nanotubes*, PUBLISHED BY IMPERIAL COLLEGE PRESS AND DISTRIBUTED BY WORLD SCIENTIFIC PUBLISHING CO., 1998.

114 S. K. Doorn, R. E. Fields, H. Hu, M. A. Hamon, R. C. Haddon, J. P. Selegue and V. Majidi, High Resolution Capillary Electrophoresis of Carbon Nanotubes, *J. Am. Chem. Soc.*, 2002, **124**, 3169–3174.

115 S. K. Doorn, M. S. Strano, M. J. O'Connell, E. H. Haroz, K. L. Rialon, R. H. Hauge and R. E. Smalley, Capillary Electrophoresis Separations of Bundled and Individual Carbon Nanotubes, *J. Phys. Chem. B*, 2003, **107**, 6063–6069.

116 D. A. Heller, R. M. Mayrhofer, S. Baik, Y. V. Grinkova, M. L. Usrey and M. S. Strano, Concomitant Length and Diameter Separation of Single-Walled Carbon Nanotubes, *J. Am. Chem. Soc.*, 2004, **126**, 14567–14573.

117 X. Huang, R. S. Mclean and M. Zheng, High-Resolution Length Sorting and Purification of DNA-Wrapped Carbon Nanotubes by Size-Exclusion Chromatography, *Anal. Chem.*, 2005, **77**, 6225–6228.

118 G. Ao, C. Y. Khripin and M. Zheng, DNA-controlled partition of carbon nanotubes in polymer aqueous two-phase systems, *J. Am. Chem. Soc.*, 2014, **136**, 10383–10392.

119 A. P. Eskelinen, A. Kuzyk, T. K. Kaltiaisenaho, M. Y. Timmermans, A. G. Nasibulin, E. I. Kauppinen and P. Törmä, Assembly of single-walled carbon nanotubes on DNA-origami templates through streptavidin-biotin interaction, *Small*, 2011, **7**, 746–750.

120 J. McMorrow, M. Freeley and M. Palma, DNA-Wrapped Single-Walled Carbon Nanotube Assemblies, *Ind. Eng. Chem. Res.*, 2017, **56**, 5302–5308.

121 S. P. Han, H. T. Maune, R. D. Barish, M. Bockrath and W. A. Goddard, DNA-linker-induced surface assembly of ultra dense parallel single walled carbon nanotube arrays, *Nano Lett.*, 2012, **12**, 1129–1135.

122 Y. Weizmann, D. M. Chenoweth and T. M. Swager, Addressable terminally linked DNA-CNT nanowires, *J. Am. Chem. Soc.*, 2010, **132**, 14009–14011.

123 M. Palma, W. Wang, E. Penzo, J. Brathwaite, M. Zheng, J. Hone, C. Nuckolls and S. J. Wind, Controlled Formation of Carbon Nanotube Junctions via Linker-Induced Assembly in Aqueous Solution, *J. Am. Chem. Soc.*, 2013, **135**, 8440–8443.

124 J. Zhu, J. McMorrow, R. Crespo-Otero, G. Ao, M. Zheng, W. P. Gillin and M. Palma, Solution-Processable Carbon Nanoelectrodes for Single-Molecule Investigations, *J. Am. Chem. Soc.*, 2016, **138**, 2905–2908.

125 P. Clément, P. Trinchera, K. Cervantes-Salguero, Q. Ye, C. R. Jones and M. Palma, A One-Step Chemical Strategy for the Formation of Carbon Nanotube Junctions in Aqueous Solution: Reaction of DNA-Wrapped Carbon Nanotubes with Diazonium Salts, *Chempluschem*, 2019, **84**, 1235–1238.

126 M. Freeley, A. Attanzio, A. Cecconello, G. Amoroso, P. Clement, G. Fernandez, F. Gesuele and M. Palma, Tuning the Coupling in Single-Molecule Heterostructures: DNA-Programmed and Reconfigurable Carbon Nanotube-Based Nanohybrids, *Adv. Sci.*, 2018, **5**, 1800596.

127 G. Amoroso, Q. Ye, K. Cervantes-Salguero, G. Fernández, A. Cecconello and M. Palma, DNA-Powered Stimuli-Responsive Single-Walled Carbon Nanotube Junctions, *Chem. Mater.*, 2019, **31**, 1537–1542.

128 Y. Li, X. Han and Z. Deng, Grafting Single-Walled Carbon Nanotubes with Highly Hybridizable DNA Sequences: Potential Building Blocks for DNA-Programmed Material Assembly, *Angew. Chemie Int. Ed.*, 2007, **46**, 7481–7484.

129 Y. Wan, G. Liu, X. Zhu and Y. Su, PH induced reversible assembly of DNA wrapped carbon nanotubes, *Chem. Cent. J.*, 2013, **7**, 14.

130 C. Tan, X. Cao, X. J. Wu, Q. He, J. Yang, X. Zhang, J. Chen, W. Zhao, S. Han, G. H. Nam, M. Sindoro and H. Zhang, *Chem. Rev.*, 2017.

131 Z. Dong, H. Xu, F. Liang, C. Luo, C. Wang, Z.-Y. Cao, X.-J. Chen, J. Zhang and X. Wu, Raman Characterization on Two-Dimensional Materials-Based Thermoelectricity, *Molecules*, 2018, **24**, 88.

132 M. Chhowalla, H. S. Shin, G. Eda, L. J. Li, K. P. Loh and H. Zhang, The chemistry of two-dimensional layered transition metal dichalcogenide nanosheets, *Nat. Chem.*, 2013, **5**, 263–275.

133 K. S. Novoselov, Electric Field Effect in Atomically Thin Carbon Films, *Science*, 2004, **306**, 666–669.

134 K. S. Novoselov, V. I. Fal'Ko, L. Colombo, P. R. Gellert, M. G. Schwab and K. Kim, A roadmap for graphene, *Nature*, 2012, **490**, 192–200.

135 H. Zhang, Ultrathin Two-Dimensional Nanomaterials, *ACS Nano*, 2015, **9**, 9451–9469.

136 A. K. Geim and K. S. Novoselov, The rise of graphene, *Nat. Mater.*, 2007, **6**, 183–191.

137 J. Lu, K. Zhang, X. Feng Liu, H. Zhang, T. Chien Sum, A. H. Castro Neto and K. P. Loh, Order–disorder transition in a two-dimensional boron–carbon–nitride alloy, *Nat. Commun.*, 2013, **4**, 2681.

138 T. T. Lv, Y. X. Li, H. F. Ma, Z. Zhu, Z. P. Li, C. Y. Guan, J. H. Shi, H. Zhang and T. J. Cui, Hybrid metamaterial switching for manipulating chirality based on VO2 phase transition, *Sci. Rep.*, 2016, **6**, 23186.

139 Z. Zhang, Y. Liu, L. Ren, H. Zhang, Z. Huang, X. Qi, X. Wei and J. Zhong, Three-dimensional-networked Ni-Co-Se nanosheet/nanowire arrays on carbon cloth: A flexible electrode for efficient hydrogen evolution, *Electrochim. Acta*, 2016, **200**, 142–151.

140 B. Radisavljevic, A. Radenovic, J. Brivio, V. Giacometti and A. Kis, Single-layer MoS2 transistors, *Nat. Nanotechnol.*, 2011, **6**, 147–150.

141 Z. Guo, S. Chen, Z. Wang, Z. Yang, F. Liu, Y. Xu, J. Wang, Y. Yi, H. Zhang, L. Liao, P. K. Chu and X.-F. Yu, Metal-Ion-Modified Black Phosphorus with Enhanced Stability and Transistor Performance, *Adv. Mater.*, 2017, **29**, 1703811.

142 S. Zhao, B. Dong, H. Wang, H. Wang, Y. Zhang, Z. V. Han and H. Zhang, In-plane anisotropic electronics based on low-symmetry 2D materials: progress and prospects, *Nanoscale Adv.*, 2020, **2**, 109–139.

143 L. D. Zhao, S. H. Lo, Y. Zhang, H. Sun, G. Tan, C. Uher, C. Wolverton, V. P. Dravid and M. G. Kanatzidis, Ultralow thermal conductivity and high thermoelectric figure of merit in SnSe crystals, *Nature*, 2014, **508**, 373–377.

144 Z. Zhu, X. Lin, J. Liu, B. Fauqué, Q. Tao, C. Yang, Y. Shi and K. Behnia, Quantum oscillations, thermoelectric coefficients, and the fermi surface of semimetallic WTe2, *Phys. Rev. Lett.*, 2015, **114**, 176601.

145 L. D. Zhao, G. Tan, S. Hao, J. He, Y. Pei, H. Chi, H. Wang, S. Gong, H. Xu, V. P. Dravid, C. Uher, G. J. Snyder, C. Wolverton and M. G. Kanatzidis, Ultrahigh power factor and thermoelectric performance in hole-doped single-crystal SnSe, *Science*, 2016, **351**, 141–144.

146 G. Qiu, S. Huang, M. Segovia, P. K. Venuthurumilli, Y. Wang, W. Wu, X. Xu and P. D. Ye, Thermoelectric Performance of 2D Tellurium with Accumulation Contacts, *Nano Lett.*, 2019, **19**, 1955–1962.

147 Y. Chen, C. Zhao, S. Chen, J. Du, P. Tang, G. Jiang, H. Zhang, S. Wen and D. Tang, Large energy, wavelength widely tunable, topological insulator Q-switched erbium-doped fiber laser, *IEEE J. Sel. Top. Quantum Electron.*, 2014, **20**, 315–322.

148 Y. Chen, M. Wu, P. Tang, S. Chen, J. Du, G. Jiang, Y. Li, C. Zhao, H. Zhang and S. Wen, The formation of various multi-soliton patterns and noise-like pulse in a fiber laser passively mode-locked by a topological insulator based saturable absorber, *Laser Phys. Lett.*, 2014, **11**, 055101.

149 S. Zhang, J. Yang, R. Xu, F. Wang, W. Li, M. Ghufran, Y. W. Zhang, Z. Yu, G. Zhang, Q. Qin and Y. Lu, Extraordinary photoluminescence and strong temperature/angle-dependent raman responses in few-layer phosphorene, *ACS Nano*, 2014, **8**, 9590–9596.

150 Peiguang Yan, Rongyong Lin, Hao Chen, Han Zhang, Aijiang Liu, Haipeng Yang and Shuangchen Ruan, Topological Insulator Solution Filled in Photonic Crystal Fiber for Passive Mode-Locked Fiber Laser, *IEEE Photonics Technol. Lett.*, 2015, **27**, 264–267.

151 H. Mu, Z. Wang, J. Yuan, S. Xiao, C. Chen, Y. Chen, Y. Chen, J. Song, Y. Wang, Y. Xue, H. Zhang and Q. Bao, Graphene–Bi 2 Te 3 Heterostructure as Saturable Absorber for Short Pulse Generation, *ACS Photonics*, 2015, **2**, 832–841.

152 J. Liu, Y. Chen, P. Tang, C. Xu, C. Zhao, H. Zhang and S. Wen, Generation and evolution of mode-locked noise-like square-wave pulses in a large-anomalous-dispersion Er-doped ring fiber laser, *Opt. Express*, 2015, **23**, 6418.

153 P. Hu, J. Zhang, M. Yoon, X.-F. Qiao, X. Zhang, W. Feng, P. Tan, W. Zheng, J. Liu, X. Wang, J. C. Idrobo, D. B. Geohegan and K. Xiao, Highly sensitive phototransistors based on two-dimensional GaTe nanosheets with direct bandgap, *Nano Res.*, 2014, **7**, 694–703.

154 W. Han, C. Zang, Z. Huang, H. Zhang, L. Ren, X. Qi and J. Zhong, Enhanced photocatalytic activities of three-dimensional graphene-based aerogel embedding TiO2 nanoparticles and loading MoS2 nanosheets as Co-catalyst, *Int. J. Hydrogen Energy*, 2014, **39**, 19502–19512.

155 X. Ren, J. Zhou, X. Qi, Y. Liu, Z. Huang, Z. Li, Y. Ge, S. C. Dhanabalan, J. S. Ponraj, S. Wang, J. Zhong and H. Zhang, Few-Layer Black Phosphorus Nanosheets as Electrocatalysts for Highly Efficient Oxygen Evolution Reaction, *Adv. Energy Mater.*, 2017, **7**, 1700396.

156 P. Wan, X. Wen, C. Sun, B. K. Chandran, H. Zhang, X. Sun and X. Chen, Flexible Transparent Films Based on Nanocomposite Networks of Polyaniline and Carbon Nanotubes for High-Performance Gas Sensing, *Small*, 2015, **11**, 5409–5415.

157 T. Wang, Y. Guo, P. Wan, H. Zhang, X. Chen and X. Sun, Flexible Transparent Electronic Gas Sensors, *Small*, 2016, **12**, 3748–3756.

158 S. Yang, Y. Liu, W. Chen, W. Jin, J. Zhou, H. Zhang and G. S. Zakharova, High sensitivity and good selectivity of ultralong MoO3 nanobelts for trimethylamine gas, *Sensors Actuators B Chem.*, 2016, **226**, 478–485.

159 J. Shao, L. Tong, S. Tang, Z. Guo, H. Zhang, P. Li, H. Wang, C. Du and X. F. Yu, PLLA nanofibrous paper-based plasmonic substrate with tailored hydrophilicity for focusing SERS detection, *ACS Appl. Mater. Interfaces*, 2015, **7**, 5391–5399.

160 B. Zhang, F. Lou, R. Zhao, J. He, J. Li, X. Su, J. Ning and K. Yang, Exfoliated layers of black phosphorus as saturable absorber for ultrafast solid-state laser, *Opt. Lett.*, 2015, **40**, 3691.

161 H.-D. Wang, D. K. Sang, Z.-N. Guo, R. Cao, J.-L. Zhao, M. N. Ullah Shah, T.-J. Fan, D.-Y. Fan and H. Zhang, Black phosphorus-based field effect transistor devices for Ag ions detection, *Chinese Phys. B*, 2018, **27**, 087308.

162 K. S. Novoselov, D. Jiang, F. Schedin, T. J. Booth, V. V. Khotkevich, S. V. Morozov and A. K. Geim, Two-dimensional atomic crystals, *Proc. Natl. Acad. Sci.*, 2005, **102**, 10451–10453.

163 A. H. Castro Neto, F. Guinea, N. M. R. Peres, K. S. Novoselov and A. K. Geim, The electronic properties of graphene, *Rev. Mod. Phys.*, 2009, **81**, 109–162.

164 F. Bonaccorso, L. Colombo, G. Yu, M. Stoller, V. Tozzini, A. C. Ferrari, R. S. Ruoff and V. Pellegrini, Graphene, related two-dimensional crystals, and hybrid systems for energy conversion and storage, *Science*, 2015, **347**, 1246501.

165 A. S. Mayorov, R. V. Gorbachev, S. V. Morozov, L. Britnell, R. Jalil, L. A. Ponomarenko, P. Blake, K. S. Novoselov, K. Watanabe, T. Taniguchi and A. K. Geim, Micrometer-Scale Ballistic Transport in Encapsulated Graphene at Room Temperature, *Nano Lett.*, 2011, **11**, 2396–2399.

166 C. Lee, X. Wei, J. W. Kysar and J. Hone, Measurement of the Elastic Properties and Intrinsic Strength of Monolayer Graphene, *Science*, 2008, **321**, 385–388.

167 A. A. Balandin, Thermal properties of graphene and nanostructured carbon materials, *Nat. Mater.*, 2011, **10**, 569–581.

168 J. S. Bunch, S. S. Verbridge, J. S. Alden, A. M. van der Zande, J. M. Parpia, H. G. Craighead and P. L. McEuen, Impermeable Atomic Membranes from Graphene Sheets, *Nano Lett.*, 2008, **8**, 2458–2462.

169 D. C. Elias, R. R. Nair, T. M. G. Mohiuddin, S. V. Morozov, P. Blake, M. P. Halsall, A. C. Ferrari, D. W. Boukhvalov, M. I. Katsnelson, A. K. Geim and K. S. Novoselov, Control of graphene's properties by reversible hydrogenation: Evidence for graphane, *Science*, 2009, **323**, 610–613.

170 K. P. Loh, Q. Bao, P. K. Ang and J. Yang, The chemistry of graphene, *J. Mater. Chem.*, 2010, **20**, 2277.

171 R. R. Nair, W. Ren, R. Jalil, I. Riaz, V. G. Kravets, L. Britnell, P. Blake, F. Schedin, A. S. Mayorov, S. Yuan, M. I. Katsnelson, H.-M. Cheng, W. Strupinski, L. G. Bulusheva, A. V. Okotrub, I. V. Grigorieva, A. N. Grigorenko, K. S. Novoselov and A. K. Geim, Fluorographene: A Two-Dimensional Counterpart of Teflon, *Small*, 2010, **6**, 2877–2884.

172 W. Choi, I. Lahiri, R. Seelaboyina and Y. S. Kang, Synthesis of Graphene and Its Applications: A Review, *Crit. Rev. Solid State Mater. Sci.*, 2010, **35**, 52–71.

173 G. Eda, H. Emrah Unalan, N. Rupesinghe, G. A. J. Amaratunga and M. Chhowalla, Field emission from graphene based composite thin films, *Appl. Phys. Lett.*, 2008, **93**, 233502.

174 D. Wang, D. Choi, J. Li, Z. Yang, Z. Nie, R. Kou, D. Hu, C. Wang, L. V. Saraf, J. Zhang, I. A. Aksay and J. Liu, Self-Assembled TiO 2 –Graphene Hybrid Nanostructures for Enhanced Li-Ion Insertion, *ACS Nano*, 2009, **3**, 907–914.

175 K. S. Kim, Y. Zhao, H. Jang, S. Y. Lee, J. M. Kim, K. S. Kim, J.-H. Ahn, P. Kim, J.-Y. Choi and B. H. Hong, Large-scale pattern growth of graphene films for stretchable transparent electrodes, *Nature*, 2009, **457**, 706–710.

176 J. Eichler and C. Lesniak, Boron nitride (BN) and BN composites for high-temperature applications, *J. Eur. Ceram. Soc.*, 2008, **28**, 1105–1109.

177 T. Sekine, H. Kanda, Y. Bando, M. Yokoyama and K. Hojou, A graphitic carbon nitride, *J. Mater. Sci. Lett.*, 1990, **9**, 1376–1378.

178 A. Thomas, A. Fischer, F. Goettmann, M. Antonietti, J.-O. Müller, R. Schlögl and J. M. Carlsson, Graphitic carbon nitride materials: variation of structure and morphology and their use as metal-free catalysts, *J. Mater. Chem.*, 2008, **18**, 4893.

179 Y. Zheng, J. Liu, J. Liang, M. Jaroniec and S. Z. Qiao, Graphitic carbon nitride materials: controllable synthesis and applications in fuel cells and photocatalysis, *Energy Environ. Sci.*, 2012, **5**, 6717.

180 M. Inagaki, T. Tsumura, T. Kinumoto and M. Toyoda, Graphitic carbon nitrides (g-C3N4) with comparative discussion to carbon materials, *Carbon N. Y.*, 2019, **141**, 580–607.

181 B. Li, C. Lai, G. Zeng, D. Huang, L. Qin, M. Zhang, M. Cheng, X. Liu, H. Yi, C. Zhou, F. Huang, S. Liu and Y. Fu, *Small*, 2019.

182 X. Zhang, H. Xie, Z. Liu, C. Tan, Z. Luo, H. Li, J. Lin, L. Sun, W. Chen, Z. Xu, L. Xie, W. Huang and H. Zhang, Black Phosphorus Quantum Dots, *Angew. Chemie Int. Ed.*, 2015, **54**, 3653–3657.

183 L. Cartz, S. R. Srinivasa, R. J. Riedner, J. D. Jorgensen and T. G. Worlton, Effect of pressure on bonding in black phosphorus, *J. Chem. Phys.*, 1979, **71**, 1718–1721.

184 A. Brown and S. Rundqvist, Refinement of the crystal structure of black phosphorus, *Acta Crystallogr.*, 1965, **19**, 684–685.

185 O. Mashtalir, K. M. Cook, V. N. Mochalin, M. Crowe, M. W. Barsoum and Y. Gogotsi, Dye adsorption and decomposition on two-dimensional titanium carbide in aqueous media, *J. Mater. Chem. A*, 2014, **2**, 14334–14338.

186 C. E. Ren, K. B. Hatzell, M. Alhabeb, Z. Ling, K. A. Mahmoud and Y. Gogotsi, Charge- and Size-Selective Ion Sieving Through Ti3C2Tx MXene Membranes, *J. Phys. Chem. Lett.*, 2015, **6**, 4026–4031.

187 P. Salles, D. Pinto, K. Hantanasirisakul, K. Maleski, C. E. Shuck and Y. Gogotsi, Electrochromic Effect in Titanium Carbide MXene Thin Films Produced by Dip-Coating, *Adv. Funct. Mater.*, 2019, **29**, 1809223.

188 J. Chen, K. Chen, D. Tong, Y. Huang, J. Zhang, J. Xue, Q. Huang and T. Chen, CO2 and temperature dual responsive 'smart' MXene phases, *Chem. Commun.*, 2015, **51**, 314–317.

189 P. Khakbaz, M. Moshayedi, S. Hajian, M. Soleimani, B. B. Narakathu, B. J. Bazuin, M. Pourfath and M. Z. Atashbar, Titanium Carbide MXene as NH 3 Sensor: Realistic First-Principles Study, *J. Phys. Chem. C*, 2019, **123**, 29794–29803.

190 K. Chaudhuri, M. Alhabeb, Z. Wang, V. M. Shalaev, Y. Gogotsi and A. Boltasseva, Highly Broadband Absorber Using Plasmonic Titanium Carbide (MXene), *ACS Photonics*, 2018, **5**, 1115–1122.

191 A. Sarycheva, T. Makaryan, K. Maleski, E. Satheeshkumar, A. Melikyan, H. Minassian, M. Yoshimura and Y. Gogotsi, Two-Dimensional Titanium Carbide (MXene) as Surface-Enhanced Raman Scattering Substrate, *J. Phys. Chem. C*, 2017, **121**, 19983–19988.

192 Y. Dong, S. Chertopalov, K. Maleski, B. Anasori, L. Hu, S. Bhattacharya, A. M. Rao, Y. Gogotsi, V. N. Mochalin and R. Podila, Saturable Absorption in 2D Ti 3 C 2 MXene Thin Films for Passive Photonic Diodes, *Adv. Mater.*, 2018, **30**, 1705714.

193 Y. Dong, S. S. K. Mallineni, K. Maleski, H. Behlow, V. N. Mochalin, A. M. Rao, Y. Gogotsi and R. Podila, Metallic MXenes: A new family of materials for flexible triboelectric nanogenerators, *Nano Energy*, 2018, **44**, 103–110.

194 N. Driscoll, A. G. Richardson, K. Maleski, B. Anasori, O. Adewole, P. Lelyukh, L. Escobedo, D. K. Cullen, T. H. Lucas, Y. Gogotsi and F. Vitale, Two-Dimensional Ti3C2 MXene for High-Resolution Neural Interfaces, *ACS Nano*, 2018, **12**, 10419–10429.

195 A. D. Dillon, M. J. Ghidiu, A. L. Krick, J. Griggs, S. J. May, Y. Gogotsi, M. W. Barsoum and A. T. Fafarman, Highly Conductive Optical Quality Solution-Processed Films of 2D Titanium Carbide, *Adv. Funct. Mater.*, 2016, **26**, 4162–4168.

196 A. I. Khan and D. O'Hare, Intercalation chemistry of layered double hydroxides: recent developments and applications, *J. Mater. Chem.*, 2002, **12**, 3191–3198.

197 R. Uppuluri, A. Sen Gupta, A. S. Rosas and T. E. Mallouk, Soft chemistry of ion-exchangeable layered metal oxides, *Chem. Soc. Rev.*, 2018, **47**, 2401–2430.

198 S. Balendhran, S. Walia, H. Nili, J. Z. Ou, S. Zhuiykov, R. B. Kaner, S. Sriram, M. Bhaskaran and K. Kalantar-zadeh, Two-Dimensional Molybdenum Trioxide and Dichalcogenides, *Adv. Funct. Mater.*, 2013, **23**, 3952–3970.

199 K. Kalantar-zadeh, J. Z. Ou, T. Daeneke, A. Mitchell, T. Sasaki and M. S. Fuhrer, Two dimensional and layered transition metal oxides, *Appl. Mater. Today*, 2016, **5**, 73–89.

200 F. Diao and Y. Wang, Transition metal oxide nanostructures: premeditated fabrication and applications in electronic and photonic devices, *J. Mater. Sci.*, 2018, **53**, 4334–4359.

201 C. N. R. Rao and A. K. Cheetham, Giant Magnetoresistance in Transition Metal Oxides, *Science*, 1996, **272**, 369–370.

202 P. Poizot, S. Laruelle, S. Grugeon, L. Dupont and J.-M. Tarascon, Nano-sized transition-metal oxides as negative-electrode materials for lithium-ion batteries, *Nature*, 2000, **407**, 496–499.

203 X. Xie, Y. Li, Z.-Q. Liu, M. Haruta and W. Shen, Low-temperature oxidation of CO catalysed by Co3O4 nanorods, *Nature*, 2009, **458**, 746–749.

204 D. Voiry, J. Yang and M. Chhowalla, Recent Strategies for Improving the Catalytic Activity of 2D TMD Nanosheets Toward the Hydrogen Evolution Reaction, *Adv. Mater.*, 2016, **28**, 6197–6206.

205 J. Kibsgaard, Z. Chen, B. N. Reinecke and T. F. Jaramillo, Engineering the surface structure of MoS2 to preferentially expose active edge sites for electrocatalysis, *Nat. Mater.*, 2012, **11**, 963–969.

206 F. Bian, L. Sun, L. Cai, Y. Wang, Y. Zhao, S. Wang and M. Zhou, Molybdenum disulfide-integrated photonic barcodes for tumor markers screening, *Biosens. Bioelectron.*, 2019, **133**, 199–204.

207 W. Ji, D. Li, W. Lai, X. Yao, M. F. Alam, W. Zhang, H. Pei, L. Li and A. R. Chandrasekaran, PH-Operated Triplex DNA Device on MoS 2 Nanosheets, *Langmuir*, 2019, **35**, 5050–5053.

208 Y. Zhao, S. Ippolito and P. Samorì, Functionalization of 2D Materials with Photosensitive Molecules: From Light-Responsive Hybrid Systems to Multifunctional Devices, *Adv. Opt. Mater.*, 2019, **7**, 1900286.

209 Y. Kang, Y. Xia, H. Wang and X. Zhang, 2D Laminar Membranes for Selective Water and Ion Transport, *Adv. Funct. Mater.*, 2019, **29**, 1902014.

210 W. Li, Y. Yang, J. K. Weber, G. Zhang and R. Zhou, Tunable, Strain-Controlled Nanoporous MoS 2 Filter for Water Desalination, *ACS Nano*, 2016, **10**, 1829–1835.

211 Q. H. Wang, K. Kalantar-Zadeh, A. Kis, J. N. Coleman and M. S. Strano, Electronics and optoelectronics of two-dimensional transition metal dichalcogenides, *Nat. Nanotechnol.*, 2012, **7**, 699–712.

212 M. Osada and T. Sasaki, Exfoliated oxide nanosheets: New solution to nanoelectronics, *J. Mater. Chem.*, 2009, **19**, 2503–2511.

213 S. Witomska, T. Leydecker, A. Ciesielski and P. Samorì, Production and Patterning of Liquid Phase–Exfoliated 2D Sheets for Applications in Optoelectronics, *Adv. Funct. Mater.*, 2019, **29**, 1901126.

214 A. B. Kaul, Two-dimensional layered materials: Structure, properties, and prospects for device applications, *J. Mater. Res.*, 2014, **29**, 348–361.

215 G. H. Han, D. L. Duong, D. H. Keum, S. J. Yun and Y. H. Lee, Van der Waals Metallic Transition Metal Dichalcogenides, *Chem. Rev.*, 2018, **118**, 6297–6336.

216 W. Zhao, J. Pan, Y. Fang, X. Che, D. Wang, K. Bu and F. Huang, Metastable MoS 2 : Crystal Structure, Electronic Band Structure, Synthetic Approach and Intriguing Physical Properties, *Chem. - A Eur. J.*, 2018, **24**, 15942–15954.

217 G. Eda, T. Fujita, H. Yamaguchi, D. Voiry, M. Chen and M. Chhowalla, Coherent Atomic and Electronic Heterostructures of Single-Layer MoS 2, *ACS Nano*, 2012, **6**, 7311–7317.

218 T. Cao, G. Wang, W. Han, H. Ye, C. Zhu, J. Shi, Q. Niu, P. Tan, E. Wang, B. Liu and J. Feng, Valley-selective circular dichroism of monolayer molybdenum disulphide, *Nat. Commun.*, 2012, **3**, 887.

219 H. Zeng, J. Dai, W. Yao, D. Xiao and X. Cui, Valley polarization in MoS2 monolayers by optical pumping, *Nat. Nanotechnol.*, 2012, **7**, 490–493.

220 K. F. Mak, K. He, J. Shan and T. F. Heinz, Control of valley polarization in monolayer MoS2 by optical helicity, *Nat. Nanotechnol.*, 2012, **7**, 494–498.

221 M. Li, J. Shi, L. Liu, P. Yu, N. Xi and Y. Wang, Experimental study and modeling of atomic-scale friction in zigzag and armchair lattice orientations of MoS 2, *Sci. Technol. Adv. Mater.*, 2016, **17**, 189–199.

222 M. R. Vazirisereshk, A. Martini, D. A. Strubbe and M. Z. Baykara, Solid Lubrication with MoS2: A Review, *Lubricants*, 2019, **7**, 57.

223 C. Donnet, J. M. Martin, T. Le Mogne and M. Belin, Super-low friction of MoS2 coatings in various environments, *Tribol. Int.*, 1996, **29**, 123–128.

224 K. F. Mak, C. Lee, J. Hone, J. Shan and T. F. Heinz, Atomically thin MoS2: A new direct-gap semiconductor, *Phys. Rev. Lett.*, 2010, **105**, 136805.

225 Q. Tang and D. Jiang, Stabilization and Band-Gap Tuning of the 1T-MoS 2 Monolayer by Covalent Functionalization, *Chem. Mater.*, 2015, **27**, 3743–3748.

226 R. Ganatra and Q. Zhang, Few-layer MoS2: A promising layered semiconductor, *ACS Nano*, 2014, **8**, 4074–4099.

227 D. M. Sim, M. Kim, S. Yim, M. J. Choi, J. Choi, S. Yoo and Y. S. Jung, Controlled Doping of Vacancy-Containing Few-Layer MoS2 via Highly Stable Thiol-Based Molecular Chemisorption, *ACS Nano*, 2015, **9**, 12115–12123.

228 A. Hirsch and F. Hauke, Post-Graphene 2D Chemistry: The Emerging Field of Molybdenum Disulfide and Black Phosphorus Functionalization, *Angew. Chemie - Int. Ed.*, 2018, **57**, 4338–4354.

229 H. Li, Q. Zhang, C. C. R. Yap, B. K. Tay, T. H. T. Edwin, A. Olivier and D. Baillargeat, From bulk to monolayer MoS 2: Evolution of Raman scattering, *Adv. Funct. Mater.*, 2012, **22**, 1385–1390.

230 G. Eda, H. Yamaguchi, D. Voiry, T. Fujita, M. Chen and M. Chhowalla, Photoluminescence from Chemically Exfoliated MoS 2, *Nano Lett.*, 2011, **11**, 5111–5116.

231 Z.-Y. Zhao and Q.-L. Liu, Study of the layer-dependent properties of MoS 2 nanosheets with different crystal structures by DFT calculations, *Catal. Sci. Technol.*, 2018, **8**, 1867–1879.

232 D. Voiry, A. Goswami, R. Kappera, C. D. C. C. E. Silva, D. Kaplan, T. Fujita, M. Chen, T. Asefa and M. Chhowalla, Covalent functionalization of monolayered transition metal dichalcogenides by phase engineering, *Nat. Chem.*, 2015, **7**, 45–49.

233 A. M. van der Zande, P. Y. Huang, D. A. Chenet, T. C. Berkelbach, Y. You, G.-H. Lee, T. F. Heinz, D. R. Reichman, D. A. Muller and J. C. Hone, Grains and grain boundaries in highly crystalline monolayer molybdenum disulphide, *Nat. Mater.*, 2013, **12**, 554–561.

234 S. Bertolazzi, M. Gobbi, Y. Zhao, C. Backes and P. Samorì, Molecular chemistry approaches for tuning the properties of two-dimensional transition metal dichalcogenides, *Chem. Soc. Rev.*, 2018, **47**, 6845–6888.

235 I. Song, C. Park and H. C. Choi, Synthesis and properties of molybdenum disulphide: from bulk to atomic layers, *RSC Adv.*, 2015, **5**, 7495–7514.

236 C. Ataca, H. Şahin and S. Ciraci, Stable, Single-Layer MX 2 Transition-Metal Oxides and Dichalcogenides in a Honeycomb-Like Structure, *J. Phys. Chem. C*, 2012, **116**, 8983–8999.

237 J. Heising and M. G. Kanatzidis, Structure of Restacked MoS 2 and WS 2 Elucidated by Electron Crystallography, *J. Am. Chem. Soc.*, 1999, **121**, 638–643.

238 F. Wypych and R. Schöllhorn, 1T-MoS2, a new metallic modification of molybdenum disulfide, *J. Chem. Soc. Chem. Commun.*, 1992, 1386–1388.

239 Y. Yu, G. H. Nam, Q. He, X. J. Wu, K. Zhang, Z. Yang, J. Chen, Q. Ma, M. Zhao, Z. Liu, F. R. Ran, X. Wang, H. Li, X. Huang, B. Li, Q. Xiong, Q. Zhang, Z. Liu, L. Gu, Y. Du, W. Huang and H. Zhang, High phase-purity 1T′-MoS2- and 1T′-MoSe2-layered crystals, *Nat. Chem.*, 2018, **10**, 638–643.

240 C. Lee, H. Yan, L. E. Brus, T. F. Heinz, J. Hone and S. Ryu, Anomalous Lattice Vibrations of Single- and Few-Layer MoS 2, *ACS Nano*, 2010, **4**, 2695–2700.

241 U. Gupta, B. S. Naidu, U. Maitra, A. Singh, S. N. Shirodkar, U. V. Waghmare and C. N. R. Rao, Characterization of few-layer 1T-MoSe 2 and its superior performance in the visible-light induced hydrogen evolution reaction, *APL Mater.*, 2014, **2**, 092802.

242 G. Pagona, C. Bittencourt, R. Arenal and N. Tagmatarchis, Exfoliated semiconducting pure 2H-MoS2 and 2H-WS2 assisted by chlorosulfonic acid, *Chem. Commun.*, 2015, **51**, 12950–12953.

243 J. Pu, Y. Yomogida, K.-K. Liu, L.-J. Li, Y. Iwasa and T. Takenobu, Highly Flexible MoS 2 Thin-Film Transistors with Ion Gel Dielectrics, *Nano Lett.*, 2012, **12**, 4013–4017.

244 S. Bertolazzi, J. Brivio and A. Kis, Stretching and Breaking of Ultrathin MoS 2, *ACS Nano*, 2011, **5**, 9703–9709.

245 R. Yan, J. R. Simpson, S. Bertolazzi, J. Brivio, M. Watson, X. Wu, A. Kis, T. Luo, A. R. Hight Walker and H. G. Xing, Thermal Conductivity of Monolayer Molybdenum Disulfide Obtained from Temperature-Dependent Raman Spectroscopy, *ACS Nano*, 2014, **8**, 986–993.

246 J. Sun, X. Li, W. Guo, M. Zhao, X. Fan, Y. Dong, C. Xu, J. Deng and Y. Fu, Synthesis methods of two-dimensional MoS2: A brief review, *Crystals*, 2017, **7**, 198.

247 X. Zhang, H. Nan, S. Xiao, X. Wan, X. Gu, A. Du, Z. Ni and K. (Ken) Ostrikov, Transition metal dichalcogenides bilayer single crystals by reverse-flow chemical vapor epitaxy, *Nat. Commun.*, 2019, **10**, 598.

248 O. Lopez-Sanchez, D. Lembke, M. Kayci, A. Radenovic and A. Kis, Ultrasensitive photodetectors based on monolayer MoS2, *Nat. Nanotechnol.*, 2013, **8**, 497–501.

249 X. Fan, P. Xu, D. Zhou, Y. Sun, Y. C. Li, M. A. T. Nguyen, M. Terrones and T. E. Mallouk, Fast and Efficient Preparation of Exfoliated 2H MoS 2 Nanosheets by Sonication-Assisted Lithium Intercalation and Infrared Laser-Induced 1T to 2H Phase Reversion, *Nano Lett.*, 2015, **15**, 5956–5960.

250 R. J. Smith, P. J. King, M. Lotya, C. Wirtz, U. Khan, S. De, A. O'Neill, G. S. Duesberg, J. C. Grunlan, G. Moriarty, J. Chen, J. Wang, A. I. Minett, V. Nicolosi and J. N. Coleman, Large-Scale Exfoliation of Inorganic Layered Compounds in Aqueous Surfactant Solutions, *Adv. Mater.*, 2011, **23**, 3944–3948.

251 B. L. Li, L. X. Chen, H. L. Zou, J. L. Lei, H. Q. Luo and N. B. Li, Electrochemically induced Fenton reaction of few-layer MoS 2 nanosheets: preparation of luminescent quantum dots via a transition of nanoporous morphology, *Nanoscale*, 2014, **6**, 9831–9838.

252 M. Makarova, Y. Okawa and M. Aono, Selective adsorption of thiol molecules at sulfur vacancies on MoS 2(0001), followed by vacancy repair via S-C dissociation, *J. Phys. Chem. C*, 2012, **116**, 22411–22416.

253 S. S. Chou, M. De, J. Kim, S. Byun, C. Dykstra, J. Yu, J. Huang and V. P. Dravid, Ligand conjugation of chemically exfoliated MoS2, *J. Am. Chem. Soc.*, 2013, **135**, 4584–4587.

254 K. C. Knirsch, N. C. Berner, H. C. Nerl, C. S. Cucinotta, Z. Gholamvand, N. McEvoy, Z. Wang, I. Abramovic, P. Vecera, M. Halik, S. Sanvito, G. S. Duesberg, V. Nicolosi, F. Hauke, A. Hirsch, J. N. Coleman and C. Backes, Basal-Plane Functionalization of Chemically Exfoliated Molybdenum Disulfide by Diazonium Salts, *ACS Nano*, 2015, **9**, 6018–6030.

255 G. Tuci, D. Mosconi, A. Rossin, L. Luconi, S. Agnoli, M. Righetto, C. Pham-Huu, H. Ba, S. Cicchi, G. Granozzi and G. Giambastiani, Surface Engineering of Chemically Exfoliated MoS2 in a 'click': How to Generate Versatile Multifunctional Transition Metal Dichalcogenides-Based Platforms, *Chem. Mater.*, 2018, **30**, 8257–8269.

256 C. Backes, N. C. Berner, X. Chen, P. Lafargue, P. LaPlace, M. Freeley, G. S. Duesberg, J. N. Coleman and A. R. McDonald, Functionalization of liquid-exfoliated two-dimensional 2H-MoS2, *Angew. Chemie - Int. Ed.*, 2015, **54**, 2638–2642.

257 M. Vera-Hidalgo, E. Giovanelli, C. Navío and E. M. Pérez, Mild Covalent Functionalization of Transition Metal Dichalcogenides with Maleimides: A "Click" Reaction for 2H-MoS 2 and WS 2, *J. Am. Chem. Soc.*, 2019, **141**, 3767–3771.

258 Z. Tang, Y. Wang, P. Podsiadlo and N. A. Kotov, Biomedical Applications of Layer-by-Layer Assembly: From Biomimetics to Tissue Engineering, *Adv. Mater.*, 2006, **18**, 3203–3224.

259 J. J. Richardson, M. Björnmalm and F. Caruso, Technology-driven layer-by-layer assembly of nanofilms, *Science*, 2015, **348**, aaa2491–aaa2491.

260 K. Kang, K.-H. Lee, Y. Han, H. Gao, S. Xie, D. A. Muller and J. Park, Layer-by-layer assembly of two-dimensional materials into wafer-scale heterostructures, *Nature*, 2017, **550**, 229–233.

261 P. Joo, K. Jo, G. Ahn, D. Voiry, H. Y. Jeong, S. Ryu, M. Chhowalla and B. S. Kim, Functional polyelectrolyte nanospaced MoS2 multilayers for enhanced photoluminescence, *Nano Lett.*, 2014, **14**, 6456–6462.

262 J. Shen, Y. Pei, P. Dong, J. Ji, Z. Cui, J. Yuan, R. Baines, P. M. Ajayan and M. Ye, Layer-by-layer self-assembly of polyelectrolyte functionalized MoS 2 nanosheets, *Nanoscale*, 2016, **8**, 9641–9647.

263 I. E. Ushakov, A. S. Goloveshkin, N. D. Lenenko, M. G. Ezernitskaya, A. A. Korlyukov, V. I. Zaikovskii and A. S. Golub, Hydrogen Bond-Driven Self-Assembly between Single-Layer MoS2 and Alkyldiamine Molecules, *Cryst. Growth Des.*, 2018, **18**, 5116–5123.

264 K. Pramoda, U. Gupta, I. Ahmad, R. Kumar and C. N. R. Rao, Assemblies of covalently cross-linked nanosheets of MoS 2 and of MoS 2 –RGO: synthesis and novel properties, *J. Mater. Chem. A*, 2016, **4**, 8989–8994.

265 B. L. Li, M. I. Setyawati, L. Chen, J. Xie, K. Ariga, C.-T. Lim, S. Garaj and D. T. Leong, Directing Assembly and Disassembly of 2D MoS2 Nanosheets with DNA for Drug Delivery, *ACS Appl. Mater. Interfaces*, 2017, **9**, 15286–15296.

266 H. C. Kolb, M. G. Finn and K. B. Sharpless, Click Chemistry: Diverse Chemical Function from a Few Good Reactions, *Angew. Chemie Int. Ed.*, 2001, **40**, 2004–2021.

267 G. Binnig, C. F. Quate and C. Gerber, Atomic Force Microscope, *Phys. Rev. Lett.*, 1986, **56**, 930–933.

268 G. Binnig, C. Gerber, E. Stoll, T. R. Albrecht and C. F. Quate, Atomic resolution with atomic force microscope, *Surf. Sci.*, 1987, **189**–**190**, 1–6.

269 L. Daccache, S. Zeller and T. Jacob, Capturing Irradiation with Nanoantennae: Plasmon-Induced Enhancement of Photoelectrolysis, *ChemPhysChem*, 2017, **18**, 1578–1585.

270 A. L. Robinson, Electron microscope inventors share nobel physics prize, *Science*, 1986, **234**, 821–822.

271 C. V. Raman and K. S. Krishnan, A new type of secondary radiation [11], *Nature*, 1928, **121**, 501–502.

272 R. H. Baughman, Carbon Nanotubes--the Route Toward Applications, *Science*, 2002, **297**, 787–792.

273 A. A. Balandin, Thermal properties of graphene and nanostructured carbon materials, *Nat. Mater.*, 2011, **10**, 569–581.

274 Y. Zhen, H. W. C. Postma, L. Balents and C. Dekker, Carbon nanotube intramolecular junctions, *Nature*, 1999, **402**, 273–276.

275 M. S. Fuhrer, J. Nygård, L. Shih, M. Forero, Y. G. Yoon, M. S. C. Mazzoni, H. J. Choi, J. Ihm, S. G. Louie, A. Zettl and P. L. McEuen, Crossed nanotube junctions, *Science*, 2000, **288**, 494–497.

276 H. Park, A. Afzali, S. J. Han, G. S. Tulevski, A. D. Franklin, J. Tersoff, J. B. Hannon and W. Haensch, High-density integration of carbon nanotubes via chemical self-assembly, *Nat. Nanotechnol.*, 2012, **7**, 787–791.

277 Q. Cao and J. A. Rogers, Ultrathin films of single-walled carbon nanotubes for electronics and sensors: A review of fundamental and applied aspects, *Adv. Mater.*, 2009, **21**, 29–53.

278 S. Park, M. Vosguerichian and Z. Bao, A review of fabrication and applications of carbon nanotube film-based flexible electronics, *Nanoscale*, 2013, **5**, 1727.

279 M. Freeley, H. L. Worthy, R. Ahmed, B. Bowen, D. Watkins, J. E. Macdonald, M. Zheng, D. D. Jones and M. Palma, Site-Specific One-to-One Click Coupling of Single Proteins to Individual Carbon Nanotubes: A Single-Molecule Approach, *J. Am. Chem. Soc.*, 2017, **139**, 17834–17840.

280 A. Attanzio, A. Sapelkin, F. Gesuele, A. van der Zande, W. P. Gillin, M. Zheng and M. Palma, Carbon Nanotube-Quantum Dot Nanohybrids: Coupling with Single-Particle Control in Aqueous Solution, *Small*, 2017, **13**, 1603042.

281 A. K. Feldman, M. L. Steigerwald, X. Guo and C. Nuckolls, Molecular Electronic Devices Based on Single-Walled Carbon Nanotube Electrodes, *Acc. Chem. Res.*, 2008, **41**, 1731–1741.

282 X. Guo, Single-molecule electrical biosensors based on single-walled carbon nanotubes, *Adv. Mater.*, 2013, **25**, 3397–3408.

283 D. Xiang, X. Wang, C. Jia, T. Lee and X. Guo, Molecular-Scale Electronics: From Concept to Function, *Chem. Rev.*, 2016, **116**, 4318–4440.

284 C. Jin, K. Suenaga and S. Iijima, Plumbing carbon nanotubes, *Nat. Nanotechnol.*, 2008, **3**, 17–21.

285 B. Oruc, S. Celik, S. Hayat Soytas and H. Unal, DNA Directed Self-Assembly of Single Walled Carbon Nanotubes into Three-Way Junction Nanostructures, *ACS Omega*, 2018, **3**, 4157–4162.

286 S. J. Wind, E. Penzo, M. Palma, R. Wang, T. Fazio, D. Porath, D. Rotem, G. Livshits and A. Stern, Integrating DNA with Functional Nanomaterials, *J. Self-Assembly Mol. Electron.*, 2013, **1**, 177–194.

287 X. Xu, P. Clément, J. Eklöf-Österberg, N. Kelley-Loughnane, K. Moth-Poulsen, J. L. Chávez and M. Palma, Reconfigurable Carbon Nanotube Multiplexed Sensing Devices, *Nano Lett.*, 2018, **18**, 4130–4135.

288 M. L. Geier, J. J. McMorrow, W. Xu, J. Zhu, C. H. Kim, T. J. Marks and M. C. Hersam, Solution-processed carbon nanotube thin-film complementary static random access memory, *Nat. Nanotechnol.*, 2015, **10**, 944–948.

289 G. J. Brady, A. J. Way, N. S. Safron, H. T. Evensen, P. Gopalan and M. S. Arnold, Quasi-ballistic carbon nanotube array transistors with current density exceeding Si and GaAs, *Sci. Adv.*, 2016, **2**, e1601240.

290 M. Kaempgen, M. Lebert, M. Haluska, N. Nicoloso and S. Roth, Sonochemical Optimization of the Conductivity of Single Wall Carbon Nanotube Networks, *Adv. Mater.*, 2008, **20**, 616–620.

291 P. Riesz and T. Kondo, Free radical formation induced by ultrasound and its biological implications, *Free Radic. Biol. Med.*, 1992, **13**, 247–270.

292 R. Zhuravel, A. Stern, N. Fardian-Melamed, G. Eidelshtein, L. Katrivas, D. Rotem, A. B. Kotlyar and D. Porath, Advances in Synthesis and Measurement of Charge Transport in DNA-Based Derivatives, *Adv. Mater.*, 2018, **30**, 1706984.

293 X. Guo, A. A. Gorodetsky, J. Hone, J. K. Barton and C. Nuckolls, Conductivity of a single DNA duplex bridging a carbon nanotube gap., *Nat. Nanotechnol.*, 2008, **3**, 163–7.

294 H. Wang, N. B. Muren, D. Ordinario, A. A. Gorodetsky, J. K. Barton and C. Nuckolls, Transducing methyltransferase activity into electrical signals in a carbon nanotube-DNA device, *Chem. Sci.*, 2012, **3**, 62–65.

295 A. P. Alivisatos, Semiconductor Clusters, Nanocrystals, and Quantum Dots, *Science*, 1996, **271**, 933–937.

296 S. N. Baker and G. A. Baker, Luminescent Carbon Nanodots: Emergent Nanolights, *Angew. Chemie Int. Ed.*, 2010, **49**, 6726–6744.

297 C.-H. Lu, A. Cecconello and I. Willner, Recent Advances in the Synthesis and Functions of Reconfigurable Interlocked DNA Nanostructures, *J. Am. Chem. Soc.*, 2016, **138**, 5172–5185.

298 P. W. K. Rothemund, Folding DNA to create nanoscale shapes and patterns, *Nature*, 2006, **440**, 297–302.

299 R. J. Macfarlane, B. Lee, M. R. Jones, N. Harris, G. C. Schatz and C. A. Mirkin, Nanoparticle superlattice engineering with DNA, *Science*, 2011, **334**, 204–208.

300 A. Cecconello, L. V. Besteiro, A. O. Govorov and I. Willner, Chiroplasmonic DNA-based nanostructures, *Nat. Rev. Mater.*, 2017, **2**, 17039.

301 D. Y. Zhang and E. Winfree, Control of DNA Strand Displacement Kinetics Using Toehold Exchange, *J. Am. Chem. Soc.*, 2009, **131**, 17303–17314.

302 T. Hermann and D. Patel, Adaptive Recognition by Nucleic Acid Aptamers, *Science*, 2000, **287**, 820–825.

303 Y. Hu, A. Cecconello, A. Idili, F. Ricci and I. Willner, Triplex DNA Nanostructures: From Basic Properties to Applications, *Angew. Chemie Int. Ed.*, 2017, **56**, 15210–15233.

304 K. Gehring, J. L. Leroy and M. Guéron, A tetrameric DNA structure with protonated cytosine-cytosine base pairs, *Nature*, 1993, **363**, 561–565.

305 A. Siddiqui-Jain, C. L. Grand, D. J. Bearss and L. H. Hurley, Direct evidence for a G-quadruplex in a promoter region and its targeting with a small molecule to repress c-MYC transcription, *Proc. Natl. Acad. Sci.*, 2002, **99**, 11593–11598.

306 K. M. Lee, L. Li and L. Dai, Asymmetric end-functionalization of multi-walled carbon nanotubes, *J. Am. Chem. Soc.*, 2005, **127**, 4122–4123.

307 M. J. Moghaddam, W. Yang, B. Bojarski, T. R. Gengenbach, M. Gao, H. Zareie and M. J. McCall, Azide photochemistry for facile modification of graphitic surfaces: Preparation of DNA-coated carbon nanotubes for biosensing, *Nanotechnology*, 2012, **23**, 425503.

308 J.-L. Leroy, M. Guéron, J.-L. Mergny and C. Hélène, Intramolecular folding of a fragment of the cytosine-rich strand of telomeric DNA into an i-motif, *Nucleic Acids Res.*, 1994, **22**, 1600–1606.

309 G. Seelig, D. Soloveichik, D. Y. Zhang and E. Winfree, Enzyme-Free Nucleic Acid Logic Circuits, *Science*, 2006, **314**, 1585–1588.

310 F. C. Simmel, B. Yurke and H. R. Singh, Principles and Applications of Nucleic Acid Strand Displacement Reactions, *Chem. Rev.*, 2019, **119,** 6326–636.

311 H. Pei, R. Sha, X. Wang, M. Zheng, C. Fan, J. W. Canary and N. C. Seeman, Organizing End-Site-Specific SWCNTs in Specific Loci Using DNA, *J. Am. Chem. Soc.*, 2019, **141**, 11923–11928.

312 G. P. Acuna, F. M. Möller, P. Holzmeister, S. Beater, B. Lalkens and P. Tinnefeld, Fluorescence enhancement at docking sites of DNA-directed self-assembled nanoantennas, *Science*, 2012, **338**, 506–510.

313 K. Qu, J. Ren and X. Qu, PH-responsive, DNA-directed reversible assembly of graphene oxide, *Mol. Biosyst.*, 2011, **7**, 2681–2687.

314 D. Huang, M. Freeley and M. Palma, DNA-Mediated Patterning of Single Quantum Dot Nanoarrays: A Reusable Platform for Single-Molecule Control, *Sci. Rep.*, 2017, **7**, 45591.

315 D. Huang, K. Patel, S. Perez-Garrido, J. F. Marshall and M. Palma, DNA Origami Nanoarrays for Multivalent Investigations of Cancer Cell Spreading with Nanoscale Spatial Resolution and Single-Molecule Control, *ACS Nano*, 2019, **13**, 728–736.

316 W. Hawkes, D. Huang, P. Reynolds, L. Hammond, M. Ward, N. Gadegaard, J. F. Marshall, T. Iskratsch and M. Palma, Probing the nanoscale organisation and multivalency of cell surface receptors: DNA origami nanoarrays for cellular studies with single-molecule control, *Faraday Discuss.*, 2019, **219**, 203–219.

317 Q. Y. Lin, J. A. Mason, Z. Li, W. Zhou, M. N. O'Brien, K. A. Brown, M. R. Jones, S. Butun, B. Lee, V. P. Dravid, K. Aydin and C. A. Mirkin, Building superlattices from individual nanoparticles via template-confined DNA-mediated assembly, *Science*, 2018, **359**, 669–672.

318 M. R. Jones, N. C. Seeman and C. A. Mirkin, Programmable materials and the nature of the DNA bond, *Science*, 2015, **347**, 1260901–1260901.

319 B. Yurke, A. J. Turberfield, A. P. Mills, F. C. Simmel and J. L. Neumann, A DNA-fuelled molecular machine made of DNA, *Nature*, 2000, **406**, 605–608.

320 S. G. McAdams, E. A. Lewis, J. R. Brent, S. J. Haigh, A. G. Thomas, P. O'Brien, F. Tuna and D. J. Lewis, Dual Functionalization of Liquid-Exfoliated Semiconducting 2 H- MoS 2 with Lanthanide Complexes Bearing Magnetic and Luminescence Properties, *Adv. Funct. Mater.*, 2017, **27**, 1703646.

321 S. Presolski and M. Pumera, Covalent functionalization of MoS2, *Mater. Today*, 2016, **19**, 140–145.

322 X. Chen and A. R. McDonald, Functionalization of Two-Dimensional Transition-Metal Dichalcogenides, *Adv. Mater.*, 2016, **28**, 5738–5746.

323 L. Parolini, B. M. Mognetti, J. Kotar, E. Eiser, P. Cicuta and L. Di Michele, Volume and porosity thermal regulation in lipid mesophases by coupling mobile ligands to soft membranes, *Nat. Commun.*, 2015, **6**, 5948.

324 G. Amoroso, A. Sapelkin, Q. Ye, V. Araullo-Peters, A. Cecconello, G. Fernandez and M. Palma, DNA-Driven Dynamic Assembly of MoS2 Nanosheets, *Faraday Discuss.*, 2020, DOI:10.1039/c9fd00118b.

325 Y. Weizmann, D. M. Chenoweth and T. M. Swager, DNA-CNT nanowire networks for DNA detection, *J. Am. Chem. Soc.*, 2011, **133**, 3238–3241.